# Development of an efficient level set framework for the full field modeling recrystallization in 3D

Benjamin Scholtes

▶ **To cite this version:**

Benjamin Scholtes. Development of an efficient level set framework for the full field modeling recrystallization in 3D. Materials. Université Paris sciences et lettres, 2016. English. NNT : 2016PSLEM083 . tel-01719664

**HAL Id: tel-01719664**
**https://pastel.hal.science/tel-01719664**

Submitted on 28 Feb 2018

**HAL** is a multi-disciplinary open access archive for the deposit and dissemination of scientific research documents, whether they are published or not. The documents may come from teaching and research institutions in France or abroad, or from public or private research centers.

L'archive ouverte pluridisciplinaire **HAL**, est destinée au dépôt et à la diffusion de documents scientifiques de niveau recherche, publiés ou non, émanant des établissements d'enseignement et de recherche français ou étrangers, des laboratoires publics ou privés.

# THÈSE DE DOCTORAT

de l'Université de recherche Paris Sciences et Lettres
PSL Research University

**Préparée à MINES ParisTech**

# Development of an efficient level set framework for the full field modeling of recrystallization in 3D

## Développement d'un modèle level set performant pour la modélisation de la recristallisation en 3D

**Ecole doctorale n°364** Sciences fondamentales et appliquées
**Spécialité** Mécanique Numérique et Matériaux

**COMPOSITION DU JURY :**

M. Ingo STEINBACH
ICAMS, Président du jury

M. Håkan Hallberg
Lund University, Rapporteur

M. Roland LOGÉ
EPFL, Rapporteur

M. Marc BERNACKI
MINES ParisTech, Examinateur

M. Carl E. KRILL III
University of Ulm, Examinateur

M. Lukasz MADEJ
AGH, Examinateur

M. Anthony D. ROLLETT
Carnegie Mellon University, Examinateur

M. Amico SETTEFRATI
Transvalor SA, Examinateur

Soutenue par **Benjamin SCHOLTES**
le **5 décembre 2016**

Dirigée par **Marc BERNACKI**

MINES ParisTech | PSL RESEARCH UNIVERSITY PARIS

# Contents


**1 Modeling of recrystallization and grain growth** **19**

1.1 Introduction . . . . . 21

1.2 Constitutive equations for the migration of grain boundaries . . . . . 21

1.3 Macroscopic models . . . . . 23

1.3.1 Physical laws and analytical models of recrystallization and grain growth . . . . . 24

1.3.2 Enriched mean field models . . . . . 33

1.4 Full field models . . . . . 37

1.4.1 Stochastic approaches . . . . . 37

1.4.2 Deterministic approaches . . . . . 41

1.5 The level set approach, state of the art concerning the modeling of polycrystals . . . . . 48

1.5.1 Generation and immersion of virtual polycrystals within unstructured finite element meshes . . . . . 49

1.5.2 Migration of the grain boundaries . . . . . 58

1.5.3 Limitations of the existing implementation . . . . . 63

**2 Development of a new direct and parallel reinitialization method** **67**

2.1 Introduction . . . . . 69

2.2 A review of numerical methods for the reinitialization of level set functions 69

2.2.1 The Fast Marching Method . . . . . 69

2.2.2 The Hamilton-Jacobi equation . . . . . 70

2.2.3 Methods without reinitialization . . . . . 72

2.2.4 Geometric reconstruction of the distance functions . . . . . 73

2.2.5 Summary on existing reinitialization methods . . . . . 74

2.3 Study of the Hamilton-Jacobi reinitialization within a continuous and linear finite element framework . . . . . 75

2.3.1 Formulation of the used finite element method . . . . . 75

2.3.2 Study of the numerical parameters of the Hamilton-Jacobi approach for fixed mesh size . . . 77
2.4 Development of a new reinitialization algorithm and comparison with other classical methods of the state of the art . . . 80
2.4.1 To a direct reinitialization method . . . 80
2.4.2 Academic benchmark and comparison with other approaches . 90
2.5 Test on realistic metallurgical cases in two and three dimensions . . . . 94

**3 Improvement of the numerical formalism based on global level set functions 99**
3.1 Introduction . . . 102
3.2 Basics about grain coloring . . . 102
3.2.1 Principle . . . 102
3.2.2 Limitations . . . 102
3.2.3 Existing situation and problem statement . . . 103
3.3 Improvement of the existing situation . . . 103
3.3.1 Literature review . . . 103
3.3.2 Development of an efficient recoloring scheme . . . 105
3.4 Evaluation of the numerical efficiency . . . 116
3.4.1 Standard benchmarks . . . 116
3.4.2 Massive grain growth computations and topological analysis . . 119
3.5 Immersion of real microstructure from experimental data . . . 126
3.5.1 Procedure . . . 126
3.5.2 Illustration . . . 132

**4 A new efficient model of static recrystallization based on stored energy field 139**
4.1 Introduction . . . 141
4.2 Modeling of static recrystallization using the level set/finite element method: first approach and limitations . . . 141
4.3 New implementation of the recrystallization model . . . 143
4.3.1 Objective . . . 143
4.3.2 Initialization of the energy fields . . . 143
4.3.3 Calculation of the recrystallization velocity field . . . 144
4.3.4 Tracking of the grain energies . . . 147
4.3.5 Improvement of the nucleation algorithm . . . 150
4.3.6 Evaluation of the numerical efficiency and comparison with the initial implementation . . . 152
4.4 Large-scale simulations of static recrystallizaton in three dimensions . 156
4.4.1 Static recrystallization simulation from a deformed state . . . 156

4.4.2 Simulation of static recrystallization in site-saturated conditions 160

**5 To an efficient modeling of microstructural evolution under consideration of Zener pinning 175**

5.1 Introduction . . . . . 177
5.2 Level set modeling of the Zener pinning phenomenon within a finite element framework . . . . . 177
5.2.1 Description of the numerical approach . . . . . 177
5.2.2 Limitations . . . . . 179
5.2.3 Improvement of the algorithm for the generation of finite element meshes . . . . . 182
5.3 Numerical investigations of the Zener pinning phenomenon . . . . . 187
5.3.1 Literature review . . . . . 187
5.3.2 Discussion of a classical limiting mean grain size equation in 2D 188
5.3.3 First 3D simulation of Zener pinnning using a level set approach within a finite element framework . . . . . 193

**6 Conclusion and outlooks 201**

6.1 Achievement . . . . . 202
6.2 Suggestions for future works . . . . . 205
6.2.1 Management of the time step in simulations . . . . . 207
6.2.2 Mesh adaptation, perspectives and challenges . . . . . 209
6.2.3 Level set modeling of the ZP phenomenon in the presence of evolving second phase precipitates . . . . . 211

**Bibliography 219**

# Nomenclature

| | |
|---|---|
| $n$D | $n$ dimension(s) |
| ReX | Recrystallization |
| DRX | Dynamic recrystallization |
| PDRX | Post-dynamic recrystallization |
| SRX | Static recrystallization |
| GG | Grain growth |
| SPP | Second phase particle |
| ZP | Zener pinning |
| EBSD | Electron backscatter diffraction |
| M&S | Modeling and simulation |
| TMT | Thermomechanical treatment |
| TT | Thermal treatment |
| HPC | High performance computing |
| FE | Finite element |
| MC | Monte Carlo |
| CA | Cellular automata |
| PCA | Probabilistic cellular automata |
| PDE | Partial differential equation |
| PF | Phase field |
| MPF | Multiphase-field |
| CPF | Continuum phase field |
| LS | Level set |
| GLS | Global level set |
| CPFEM | Crystal plasticity finite element method |
| BC | Boundary condition |
| REV | Representative elementary volume |
| VT | Voronoï tessellation |
| LVT | Laguerre-Voronoï tessellation |
| DOF | Degree of freedom |

| | |
|---|---|
| CDE | Convective-diffusive equation |
| SUPG | Streamline upwind Petrov-Galerkin |
| GMRES | Generalized minimal residual method |
| HJ | Hamilton-Jacobi |
| CPU | Central processing unit |
| FMM | Fast marching method |
| RK | Runge-Kutta |
| ENO | Essentially non-oscillatory |
| WENO | Weighted essentially non-oscillatory |
| CR | Convection-reinitialization |
| CR-DF | Convection-reinitialization with distance function |
| CR-HTDF | Convection-reinitialization with hyperbolic tangent distance function |
| DR | Direct reinitialization |
| DRT | Direction reinitialization with trees |
| NNS | Nearest neighbor search |
| SCC | Separation of connected components |
| FSN | First and second neighbors |
| CAD | Computer assisted design |
| GBMG | Geometry-based mesh generation |
| DTSA | Dynamic time step adaptation |

# General introduction

## A little bit of history...

From 7000 B.C., Men begin to hammer copper and replace their existing tools made of rock by their metal equivalents, which work as well and last far longer. Although copper is a relatively soft metal, shaping it remains mainly an art at this period... But it was without counting the great (and probably accidental) discovery of one nature's secret: the metal softens when heated. Even better, it turns to liquid whether the temperature is sufficiently high, and can then be easily cast in molds. By casting several metals as one substance, hybrid materials can be formed, the *alloys*, which are sometimes harder than the initial metals on their own. Most scientists and historians considers that the discovery of the bronze alloy, around 4000 B.C., marks the real beginning of *metallurgy*, the science of metals.

Later in the Middle Ages, blacksmiths observed that swords are harder to break when they have been rapidly cooled in water after forging. Despite this phenomenon was clearly observed and used for many years, it remained misunderstood until the emergence of optical microscopy in the 19th century. The metallurgists observed at this period that metals are actually heterogeneous materials. Their *microstructure* is an assembly of crystals, *the grains*, whose sizes are typically between 10 and 100$\mu$m. A grain is associated to a given *crystallographic orientation* which describes the spatial atom arrangement. A large heterogeneity of this orientation marks the transition from a grain to an other, and this transition zone which is typically of few nanometers is called *grain boundary*. The size, shape and orientation of the grains influence directly the capacity of the material to conduct electricity, endure high temperatures, resist to shocks... Thus when the blacksmith cools violently the burning sword in the water, he stops the evolution of the microstructure without knowing it, making finally the sword more resistant.

This ancestral example illustrates a basic but fundamental idea: **the forming pro-**

**cesses impact the grain structure and consequently the behavior of the metals, during and after the forming .** But understanding the related effects of this forming process on the microstructure is a challenging research topic of modern metallurgy, because it involves many complex and coupled phenomena.

## Annealing phenomena in metals

An important part of the energy is dissipated as heat during deformation of a metal. The remaining is stored into the microstructure in the form of crystallographic defects, mostly *dislocations*, which disturb the thermodynamic equilibrium. If the material is subsequently heated to high temperature (*annealed*), thermally activated processes such as solid state diffusion provide mechanisms whereby the defects may be removed or alternatively arranged in configurations of lower energy.

On annealing a cold worked metal at an elevated temperature, the microstruture and also the properties may be partially restored to their original values by *recovery* in which annihilation and rearrangement of the dislocations occurs. The microstructural changes during recovery are relatively homogeneous and do not usually affect the boundaries between the deformed grains [Humphreys et al. 2004]. This phenomenon results generally in the formation of a subgrain structure in the grain interior as schematically illustrated on fig. 1b.

Recovery generally involves only a partial restoration of properties because it leads to a metastable state wherein the dislocation structure is still present. A further restoration process called recrystallization (ReX) may occur in which new dislocation-free grains, the *nuclei*, are formed within the deformed or recovered structure (see fig. 1c). These new grains grow and consume the old grains, forming a new grain structure with low dislocation density as depicted on fig. 1d. Recrystallization may take place during deformation at elevated temperature and this is then termed *dynamic recrystallization* (DRX) [Humphreys et al. 2004]. It can also continue during a thermal post-treatment (post-dynamic recrystallization, PDRX), or be only initiated during this post-treatment (static recrystallization, SRX) (see fig. 2). DRX is frequently observed during the hot deformation of ordered alloys.

Although recrystallization removes the dislocations, the material still contains *grain boundaries*, which are thermodynamically unstable. Further annealing may result in *grain growth* (GG), in which the smaller grains are eliminated and the larger grains

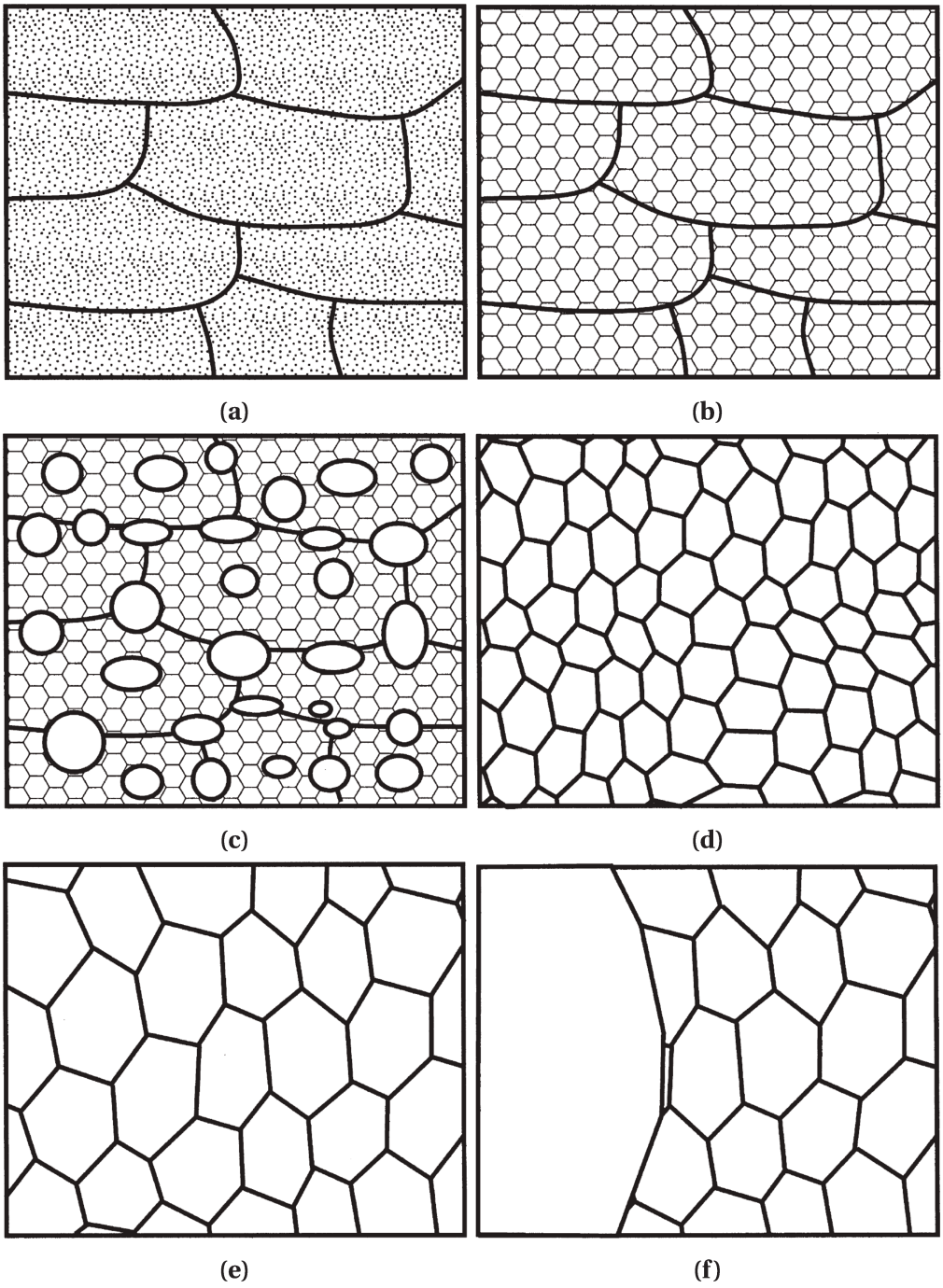


**Fig. 1** – Schematic diagram of the main annealing processes: (a) deformed state, (b) recovered, (c) partially recrystallized, (d) fully recrystallized, (e) grain growth, (f) abnormal grain growth [Humphreys et al. 2004].

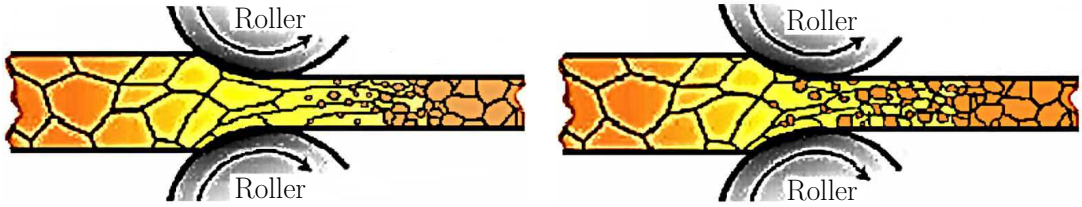


**(a)** SRX **(b)** DRX

**Fig. 2** – Schematic representation of the static (a) and dynamic (b) recrystallization regimes [Zheng et al. 2008].

grow by minimizing the energy of the grain boundary network (see fig. 1e). Consequently the mean grain size inside the material increases during GG. This effect can be slowed down or eventually hindered by adding to the alloy a solute element with low solubility which precipitates as second-phase particles (SPPs) able to pin the grain boundaries [Smith 1948; Weygand et al. 1999]. This dragging effect exerted by the SPPs is commonly referred as the *Zener pinning* (ZP) phenomenon. In certain circumstances (heterogeneous particle distribution, gradient of stored energy, advantage in size,...), some grains of the microstructure may grow preferentially, referring to *abnormal grain growth*. This phenomenon depicted on fig. 1f can have a dramatic effect on the mechanical properties of the material.

Addressing these annealing phenomena is very complex as they act together during the forming process. In the last decades, more and more sophisticated experimental techniques emerged for the characterization of material at the grain scale. Resolutions close to micron are now achieved thanks to the recent advances in the field of microscopy. Among all methods, Electron BackScatter Diffraction (EBSD) is probably the most popular and is now widely used [Alam et al. 1954]. This method provides a great description of the cutting-view of the grain structure, as illustrated on fig. 3a. Most recent methods, such as near-field high energy X-ray diffraction microscopy [Hefferan et al. 2012; Pokharel et al. 2015], X-ray diffraction contrast tomography [Syha et al. 2012; Nervo et al. 2016] or absorption-contrast X-ray microtomography [Werz et al. 2014] permit also to reconstruct precisely the 3D microstructure (see fig. 3b for an illustration). But these techniques remain quite confidential because they require complex and specific experimental facilities.

But characterizing the material at each stage of the forming process is not always possible, and evaluate the intrinsic effects of the process parameters (temperature, strain rate...) can be complex, costly and time-consuming. This is especially true

for high value-added materials. Modeling and simulation (M&S) approaches are of a valuable help in these situations for orienting the technological decisions. They can effectively be employed to quantify the intrinsic influences of the process parameters before having recourse to real materials, which limits the number of needed experiments. M&S is in that sense a potential time and money saver, and thus attracts growing interest from producers of high performance materials (ceramic, titanium alloys, superalloys...). *Numerical metallurgy* is the research field which investigates these modeling approaches. As illustrated in the next section, it is extremely active nowadays in the scientific community and widely supported by the industry.

## The DIGIMU® software

The "blacksmith's experience" taught us that mechanical and functional properties of metallic materials are strongly related to their microstructure, which are themselves inherited from the thermal and mechanical processing. The understanding of the microstructural evolutions during thermomechanical treatments (TMT) or thermal treatment (TT) is thus of prime importance for the control of the final in-use properties (mechanical strength, fatigue limit, crack resistance, stress corrosion resistance,...). Being able to accurately predict the microstructure obtained after complex forming paths became recently crucial for the metallurgy industry, and is now a real challenge in the scientific community. Addressing this challenge requires the development of numerical modeling capabilities based on a realistic description of the intricate physical phenomena undergone by the material during the forming processes.

The numerical modeling of materials and their behavior has now become a major research topic in materials science because simulations can reduce greatly the time and cost of the new material development, and help to better understand the metallurgical phenomena. From the improvement of Nickel-based superalloys used in the critical parts of engine aircraft to the stainless steel used in nuclear power plants which places unusual demands on the metallic materials, through the lightening of structures in the automotive and aeronautics industries, the needs are tremendous. So tomorrow's material will also be numeric.

Let us consider a simple example. When an aircraft takes off, its engines develop their maximal rated power. In the high-pressure compressors, the air temperature reaches 950°C and the fan blades undergo very high stress and temperature solicita-

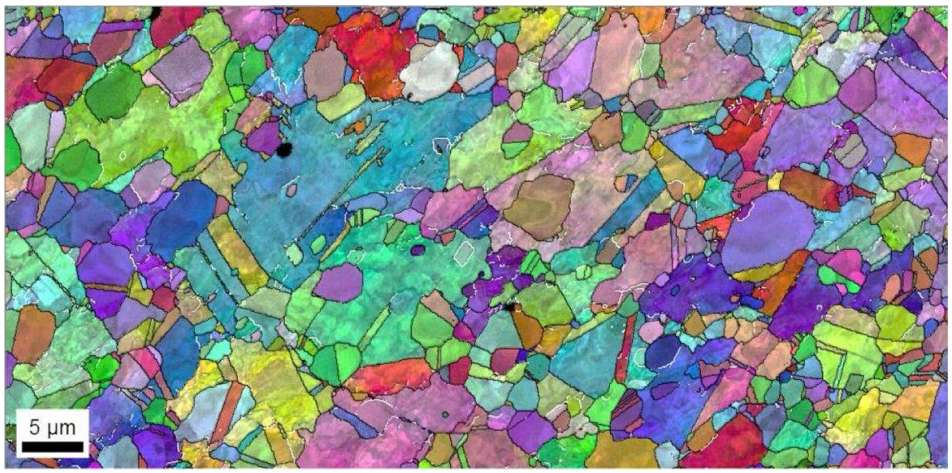


**(a)**

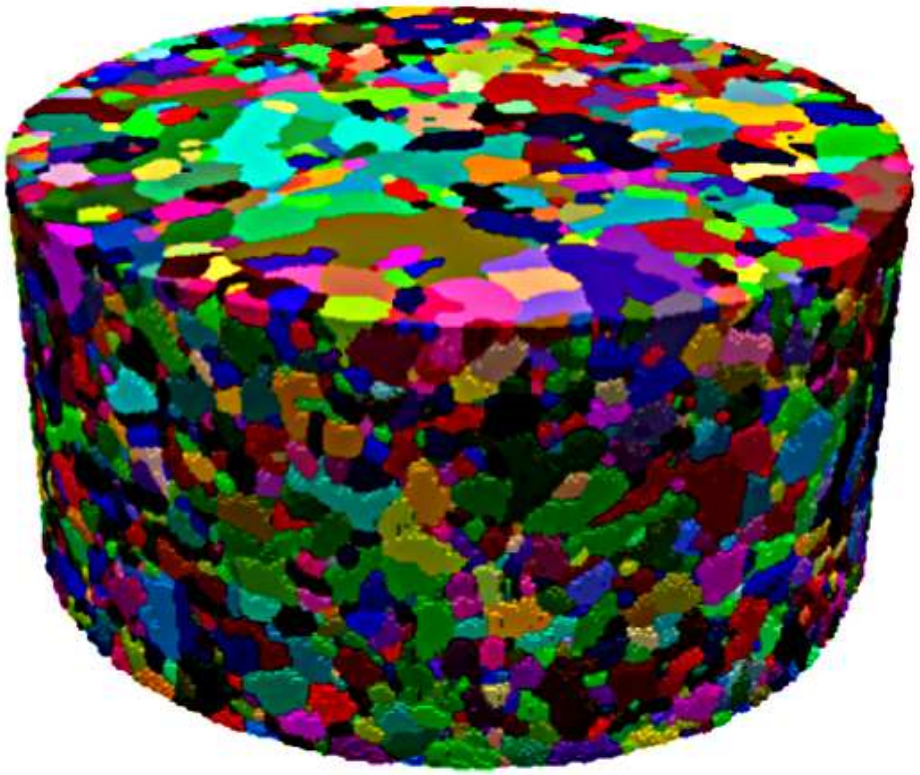

**(b)**

**Fig. 3** – (a) 2D Microstructure of a superalloy material obtained by EBSD technique (PhD work of M.A. Charpagne, MINES ParisTech, 2013-2016); (b) 3D reconstruction of a polycrystalline copper based on data obtained from near-field high-energy X-ray diffraction microscopy [Pokharel et al. 2015]. In both images the color code refers to the local crystalline orientation.

tions. There exist different materials able to tackle these extreme applications, such as titanium alloys, monocristalline alloys and finally the nickel-based superalloys which remain, at the time being, the better compromise in terms of mechanical properties and costs for civil aircraft. However the performance requirements, the environmental and profitability considerations require the aeronautics manufacturer to reduce the aircraft consumption, and this implies to increase the internal temperature in the engines. However the resistance of today's materials limit this increase in temperature. So the TMT of these superalloys must be improved.

Also in nuclear power plants, primary pipes must have high mechanical properties, especially the Yield strength at high temperature. This requires to control the grain size of the material during the forming process. But fine-grained microstructures are hard to obtain for these massive parts because of the long heating periods that have to be counterbalanced by SRX, DRX or PDRX which take place during forging and rolling.

These microstructure evolutions during TMT can be treated in an average way, by using the classical method referred to as *mean field* approach. This relies on a macroscopic description using representative material parameters (grain size, inclusions, phase fraction, precipitate size, etc.), the identification of physical laws that govern the evolution of these parameters, and their influence on the mechanical behavior [Chastel et al. 2012]. This approach is quite convenient for coupling the thermal, mechanical and physical computations but suffers from inherent limitations. Especially a large amount of experiments is generally needed for identifying the parameters of these models that describe the microstructure evolutions.

On the other hand, computations at the mesoscale are now possible and are developed for a potentially more realistic description of materials under the concept of *full field* approach. The prefix *meso-* implies being between the atomic and macroscopic scales, but the precise length or time scale where the break in understanding develops depends on the physical mechanisms of interest. Mesoscale modeling is a very active research domain nowadays, especially for polycrystals [Rollett et al. 2015], because it is potentially much more accurate. However full field modeling is also more greedy in terms of computer resources and a direct coupling with macroscopic TMT simulations seems at yet complicated, even with the recent developments of High Performance Computing (HPC).

This PhD work has two main objectives. First, contribute to the development of a unified groundbreaking and robust finite element (FE) numerical solution in order

to describe a wide range of microstructural mechanisms and, secondly, develop relevant multiscale strategies. For example full field simulations can be employed to improve the mean field models used in existing FE software packages working at the macroscale. It is also possible to simulate very precisely, at the microscale, a set of specific interesting zones of the material during a macroscale simulation in order to describe the local evolution. This work is part of a global trend towards a better control of the industrial forming processes dealing with metallic products in order to improve their reliability and their performance while limiting the production costs. Our central objective is to provide precise numerical models able to predict the final microstructure and the material behavior before they can be processed, in order to improve the reactivity to new markets and increase our confidence in the proposed manufacturing sequences and parameters.

In such context the recent report of the European Commission entitled *Metallurgy made in and for Europe* should be cited [Metallurgy made in and for Europe 2014]. The purpose of this report is to set a roadmap concerning the development of materials science and metallurgy in EU for the next 10-20 years and beyond, and the way to promote this thematic which carries crucial economic and societal impacts. If conclusions of this document emphasize that "... Europe plays world-wide leading roles in computational materials science..." and the importance of developing "...strong modeling capacities..." in this field, it highlights also the emergency to promote the following key challenge: "...Moving from "Modelling for industry" to "Modelling by industry", which means shifting efforts from laboratory-centred modelling activities to helping industry equip itself with advanced modelling tools and skills". Through the development of HPC in metallurgy and the integration of these developments within an industrial software package called DIGIMU® , the purpose of this PhD work is then fully in line with these recommendations.

Thanks to the explosion of computer capacities and the better understanding of physical phenomena, several mesoscale numerical models have been proposed to simulate ReX and GG during the last decades. Probabilistic voxel-based approaches such as Monte Carlo (MC) and cellular automata (CA) are very popular. Furthermore, these methods scale extremely well with parallelization as they rely on regular grids, but the lack of physical time in the MC method and the difficulty to approximate accurately the grain boundary curvature with regular grids are still open issues. There are also difficulties with these approaches to treat the polycrystal deformation and the grain boundary motion in the same numerical framework, which implies that they need to be coupled with other numerical methods, at least for problems involving large

polycrystal deformations. There are also deterministic approaches, which are more precise, as they do not rely on probabilistic laws, but also more greedy in terms of computational resources due to the fact that they involve the resolution of large systems of partial differential equations (PDEs). Thus several workers have developed the vertex method wherein the grain boundaries are defined in terms of vertices ; the interface motion is then imposed by the displacement of a set of points. The main limitation of these front-tracking approaches is the handling of topological events (grain shrinkage, appearance of a nucleus) in three dimensions, that is extremely challenging and costly from a numerical point of view. Finally, the microstructural evolution can also be modeled using a phase field (PF) or a level set (LS) description of the interfaces, in a FE framework or in the context of uniform grids with Fourier transform resolution. The FE-LS and FE-PF methods are actually quite close and share some common features (front-capturing approaches, deterministic approach lying on the solving of PDE systems, high numerical cost). Although the PF method lies on strong physical and thermodynamical foundations, its formulation introduces purely numerical parameters (like the grain boundary width). On the other hand, the LS method only requires measurable quantities which have a direct physical interpretation, making it more simple to use *a priori*. Also the interest of using a FE framework instead of uniform grids relies on the possibility to handle large polycrystal deformations with the well-known Crystal Plasticity Finite Element Method (CPFEM) and to deal with a global resolution framework concerning the modeling of the thermomechanical treatments and their subsequent microstructure evolutions.

This brief review of the existing methods show that they all have advantages and limitations, that will be further detailed in the first chapter of this manuscript. However it is worth noting that, for the time being, there is no global method able to treat the successive steps required to model at the mesoscale the different mechanisms involved during ReX for hot metal forming. These remarks have led us to develop a LS numerical formalism working within a FE framework. Although this approach is not perfect, especially concerning the numerical cost as it will be detailed later, it seems to us the most promising candidate to address the considered problematic.

The present LS-FE model has been developed around the C++ library *Cimlib* developed at the Center for Materials forming - MINES ParisTech (CEMEF) [Digonnet et al. 2007]. The Cimlib library contains many numerical tools that can be directly used in the context of this work (solvers, mesh adaptation algorithms,...). Recent studies have demonstrated the very interesting potential of the LS-FE approach for the modeling of SRX [Bernacki et al. 2008; Bernacki et al. 2009] and GG [Bernacki et al. 2011; Cruz-

Fabiano et al. 2014]. However it remains rather inefficient from a numerical point of view and several weeks of computations on a lab supercomputer (cluster) are sometimes needed to complete the simulations, even in two dimensions (2D) [Agnoli et al. 2014]. It is obvious that companies do not have access to such computational facilities and the simulation times must be drastically reduced in order to make DIGIMU® attractive for industrials. The three dimensional aspect must also be considered, as specific metallurgical phenomena require to be treated in three dimensions (3D) like the crystal plasticity, but also to avoid the use of a 2D paradigm. But predicting finely the microstructural evolutions in 3D within reasonable computation times is a real challenge, which requires major improvements of the existing implementations. One main objective of this PhD work, and more generally of the industrial ANR Chair DIGIMU started in October 2016 at the CEMEF, is therefore to increase drastically the numerical efficiency of the LS-FE numerical model used by DIGIMU® in order to make possible this transition from 2D to 3D. GG and SRX are particularly considered in this manuscript to evaluate the quality of the new developments. However it must be highlighted that these developments are completely generic and can be (*or* are already) used for a large variety of front-capturing problems based on a LS description of the interfaces.

Finally due to the limited time, some topics have not been investigated in the context of this work. Especially we focused on the development and improvement of the considered LS-FE model. Even if a mean field model [Bernard et al. 2011] available at the lab has been used to validate the full field predictions and for comparison, no development has been carried out on this mean field model. Moreover the resolution of the PDE systems has not been particularly studied in this work, as we simply used the existing FE solvers available in the Cimlib library [Basset 2006]. The algorithms used for the statistical generation of polycrystals, that will be introduced in the first chapter, have been developed in the context of previous studies [Hitti 2011; Hitti et al. 2012; Fabiano 2013]. In the same manner, the CPFEM code [Delannay et al. 2006; Logé et al. 2008; Resk et al. 2009] used in the fourth chapter to provide inputs for the SRX simulations has been used as it is, without any modification. The mesh adaptation algorithms were also provided by the Cimlib library [Mesri et al. 2008; Shakoor et al. 2015a]. Finally the problem of the boundary conditions (BCs) applied to solve the FE problems has not been investigated and we used null Neumann BCs in all simulations. Obviously the choice of working with this kind of BCs can be discussed. Periodic BCs are effectively preferred in most works from the state of the art because they enable to limit the domain-size effects in an optimal way. They thus permit to limit the sizes of the representative elementary volumes (REVs) used in the simula-

tions, the number of considered grains, and consequently to save computation time. On the other hand, periodic BCs impose to use a polycrystal and a mesh which are also periodic. When simulations are performed from an experimental image of a real material, as it will be presented in the third chapter of this manuscript, this condition of polycrystal periodicity is not satisfied and periodic BCs are not relevant in this case. Also, even if regular Cartesian grids are naturally periodic, maintaining the periodicity of unstructured FE meshes is much more complex, especially when anisotropic remeshing is performed. The numerical tools available in our library, and especially the remeshing algorithms, are not able to tackle this problem for the time being. So in this work, we made the choice to work with null Neumann BCs and consequently, not minimal REV size concerning convergence aspects. Even if it is not optimal in terms of numerical efficiency as it requires larger polycrystals, this solution presents the advantage of being sufficiently versatile to simulate also non-periodic polycrystals (possibly obtained from experimental data) and to deal easily with anisotropic mesh adaptation thanks to our current numerical facilities. But let us keep in mind that the ideal approach remains to have both methods (periodic and null Neumann BCs) and to choose the most relevant according to the expectations and the configuration. Future works have therefore been already planned in the context of the DIGIMU Chair to integrate periodic BCs in the considered LS-FE numerical formalism and meshing/remeshing algorithms.

## Layout of the thesis

The manuscript is organized in five chapters. The first chapter introduces the existing modeling approaches and highlights the advantages/limitations of the numerical formalism employed in the state of the art. Two central algorithms which address these limitations are then introduced in the second and third chapters. Different benchmarks are used to quantify the gains achieved in terms of numerical efficiency. The last two chapters present finally new numerical strategies for the efficient modeling of SRX in 3D and for the consideration of inert precipitates inside the material:

Chapter 1 first covers the existing models for GG and ReX at the macroscopic and polycrystal scales. The main features, assumptions and limitations of these approaches are thoroughly detailed. Special attention is paid to the LS method used in the present work.

Chapter 2 introduces a direct algorithm for reconstructing (*i.e. reinitializing*) analytically a signed distance function based on its front. This algorithm is

especially employed in the present model to restore the metric property of the LS functions during the GG/ReX simulations. By taking full advantage of the parallel FE environment of Cimlib, this algorithm permits acceleration factors up to 70 in 2D and 5 in 3D for polycrystal simulations, compared with the existing reinitialization method.

Chapter 3 details the implementation of an efficient recoloring scheme working on a FE mesh. The latter detects and handles dynamically the risks of contacts between grains represented by the same LS function during a simulation. Thus it prevents numerical issues and enables to use far less LS functions, especially in 3D, which permits computation time and memory savings. Moreover a new method is presented for immersing real polycrystal within a LS-FE framework based on experimental images.

Chapter 4 presents a new implementation of the numerical formalism introduced in [Bernacki et al. 2008; Bernacki et al. 2009] for the modeling of SRX with nucleation within a LS-FE framework. This new implementation takes advantage of the numerical tools introduced in the two previous chapters and is demonstrated far more efficient than the existing one from a computational point of view, with acceleration factors close from 700 for realistic large scale 3D SRX simulations.

Chapter 5 proposes an improvement of the numerical strategy presented in [Agnoli et al. 2014] for the modeling of GG with inert SPPs. Especially we apply the previous numerical developments to ZP simulations and introduce a new method for generating the specific FE meshes needed in these simulations, which results in excellent acceleration of the simulation times. A classical 2D limiting mean grain size equation is then discussed and improved thanks to the full field simulation results. Finally a first 3D LS-FE simulation of the ZP phenomenon is performed, which was hardly possible before this thesis work.

# Oral and written communications

The work of this thesis has contributed to the following written communications:

### Articles

- Improvement of 3-D mean field models for pure grain growth based on full field simulations, L. Maire, B. Scholtes, C. Moussa, D. Pino Muñoz, N. Bozzolo, M.

Bernacki, Journal of Materials Science, vol. 51(24), pp. 10970-10981, 2016.

- 3D level set modeling of static recrystallization considering stored energy fields, B. Scholtes, R. Boulais-Sinou, A. Settefrati, D. Pino Muñoz, I. Poitrault, A. Montouchet, N. Bozzolo, Computational Materials Science, vol. 122, pp. 57-71, 2016.

- An efficient and parallel reinitialization method - Application to micromechanics and microstructural evolutions, M. Shakoor, B. Scholtes, P.-O. Bouchard, M. Bernacki, Applied Mathematical Modelling, vol. 39, pp. 7291-7302, 2015.

- New finite element developments for the full field modeling of microstructural evolutions using the level set method, B. Scholtes, M. Shakoor , A. Settefrati, P.-O. Bouchard, N. Bozzolo, M. Bernacki, Computational Materials Science, vol. 109, pp. 388-398, 2015.

- Advances in level-set modeling of recrystallization at the polycrystal scale - Development of the Digi-$\mu$ software, B. Scholtes, M. Shakoor , A. Settefrati, P.-O. Bouchard, N. Bozzolo, M. Bernacki, Key Engineering Materials, 651-653:617-623, 2015.

**Conference proceedings**

- Full field modeling of recrystallization and grain growth thanks to a level set approach: towards modeling by industry, M. Bernacki, B. Scholtes, A. Settefrati, N. Bozzolo, C. Moussa, D. Pino Muñoz, Y. Zhan, E. Rigal, C. Dumont, R. Besnard, I. Poitrault, J. Demurger, A. Montouchet, I. Bobin, J.-M. Franchet, in MATCH newsletter, 2016.

- Large scale FE simulations of recrystallization and grain growth thanks to a level set approach, illustrations in context of industrial forming processes, B. Scholtes, A. Settefrati, N. Bozzolo, E. Perchat, J.-L. Chenot, and M. Bernacki, in Proceedings of NUMIFORM 2016, 2016.

- A new numerical framework for the full field modeling of dynamic recrystallization, application to 304L stainless steel, R. Boulais-Sinou, B. Scholtes, D. Pino Muñoz, C. Moussa, I. Poitrault, I. Bobin, A. Montouchet, and M. Bernacki, in Proceedings of NUMIFORM 2016, 2016.

- Full field modeling of the Zener pinning phenomenon in a level set framework - discussion of classical limiting mean grain size equation, B. Scholtes, D. Ilin,

A. Settefrati, N. Bozzolo, A. Agnoli, M. Bernacki, in Proceedings of SuperAlloys 2016: the 13th International Symposium on Superalloys, 2016.

- P. De Micheli, A. Settefrati, S. Marie, J. Barlier, P. Lasne, B. Scholtes, M. Bernacki, and F. Bay. Towards the simulation of the whole manufacturing chain processes with Forge. In Proceedings of NEMU 2015: New Developments in Forging Technology, 2015.

And the following oral communications:

**Conferences**

- Recent advances in the full field modeling of recrystallization and grain growth using the level set approach, M. Bernacki, N. Bozzolo, B. Scholtes, A. Settefrati. SIAM Conference on Mathematical Aspects of Materials Science, Philadelphia, USA, May 08-12 2016.

- Large scale FE simulations of recrystallization and grain growth thanks to a level set approach, illustrations in context of industrial forming processes, B. Scholtes, A. Settefrati, N. Bozzolo, E. Perchat, J.-L. Chenot, and M. Bernacki. NUMIFORM 2016, Troyes, France, July 04-07 2016.

- A new numerical framework for the full field modeling of dynamic recrystallization, application to 304L stainless steel, R. Boulais-Sinou, B. Scholtes, D. Pino-Muñoz, C. Moussa, I. Poitrault, I. Bobin, A. Montouchet, and M. Bernacki. NUMIFORM 2016, Troyes, France, July 04-07 2016.

- New finite element developments for the full field modeling of microstructural evolutions using the level set method, B. Scholtes, A. Settefrati, and M. Bernacki, in WCCM XII: The 12th world congress on computational mechanics. Seoul, Korea, July 24-27 2016.

- Full field modeling of the Zener pinning phenomenon in a level set framework - discussion of classical limiting mean grain size equation, B. Scholtes, D. Ilin, A. Settefrati, N. Bozzolo, A. Agnoli, M. Bernacki. SuperAlloys 2016, Seven Springs, USA, September 11-15 2016.

- Recrystallization and grain growth modeling at the mesoscopic scale thanks to a level-set/FE framework, B. Scholtes, R. Boulais-Sinou, A. Settefrati, N. Bozzolo, D. Pino Muñoz, C. Moussa, R. Besnard, J. Demurger, and M. Bernacki. ReX & GG 2016, Pittsburgh, USA, July 17-21 2016.

- 3D full field modeling in a level set framework, of grain growth and Zener pinning phenomenon, B. Scholtes, and M. Bernacki. EUROMAT 2015, Warsaw, Poland, September 20-24 2015.
- Recent advances in the full field modeling of recrystallization and grain growth using the level set approach, B. Scholtes, A. Settefrati, and M. Bernacki. EUROMAT 2015, Warsaw, Poland, September 20-24 2015.
- Towards the simulation of the whole manufacturing chain processes with FORGE, P. De Micheli, A. Settefrati, S. Marie, J. Barlier, P. Lasne, B. Scholtes, M. Bernacki, and F. Bay. NEMU 2015, Stuttgart, Germany, May 05-06 2015.
- Advances in level-set modelling of recrystallization at the microscopic scale - development of the Digi-$\mu$ software, B. Scholtes, M. Shakoor, N. Bozzolo, P.-O. Bouchard, A. Settefrati, and M. Bernacki. ESAFORM 2015, Graz, Austria, April 15-17 2015.
- Advances in level set modeling of recrystallization at the mesoscopic scale - development of the Digi-$\mu$ software, B. Scholtes, A. Settefrati, and M. Bernacki. CAE conference, Verona, Italy, October 27-28 2014.

**Workshops**

- Simulation de la recristallisation statique par modélisation en champ moyen et en champ complet, L. Maire, B. Scholtes, C. Moussa, N. Bozzolo, and M. Bernacki. Colloque "La métallurgie, quel avenir!", Saint-Etienne, France, June 27 - July 01 2016.
- Effect of intragranular strain heterogeneity on recrystallization kinetics assessed by numerical simulation at the mesoscopic scale, D. Ilin, B. Scholtes, N. Bozzolo, D. Pino Muñoz, and M. Bernacki. Colloque La métallurgie, quel avenir!", Saint-Etienne, France, June 27 - July 01 2016.
- Simulation en champ complet de la recristallisation dynamique par une approche level-set, R. Boulais-Sinou, B. Scholtes, D. Pino Muñoz, C. Moussa, N. Bozzolo, and M. Bernacki. Colloque "La métallurgie, quel avenir!", Saint-Etienne, France, June 27 - July 01 2016.
- Microstructural evolution prediction during forming processes: towards a modelling by industry, A. Settefrati, B. Scholtes, M. Bernacki. Colloque "La métallurgie, quel avenir!", Saint-Etienne, France, June 27 - July 01 2016.

- Établissement et évolution des interfaces lors du soudage diffusion - modélisation en champ complet du mécanisme de croissance de grains, M. Bernacki, B. Scholtes, E. Rigal, N. Bouquet, Y. Zhan, D. Piot. Colloque "La métallurgie, quel avenir!", Saint-Etienne, France, June 27 - July 01 2016.
- Level-set modelling of recrystallization and grain growth, B. Scholtes, A. Settefrati, and M. Bernacki. Workshop SF2M/MECAMAT, Paris, France, November 30 - December 01 2015.
- Advances in level set modeling of recrystallization at the mesoscopic scale, M. Bernacki, N. Bozzolo, Y. Jin, B. Scholtes, R. Boulais-Sinou, D. Polychronopoulou, and D. Ilin. 2ème Journées Matériaux Numériques, St-Aignan-sur-Cher, France, February 03-05 2015.
- Simulation en champ complet de la recristallisation et la croissance de grains par une approche level-set avec remaillage local, B. Scholtes, A. Settefrati, and M. Bernacki. 2ème Journées Matériaux Numériques, St-Aignan-sur-Cher, France, February 03-05 2015.
- Full field modeling of grain growth and Zener pinning phenomenon in a level set framework. 2ème Journées Matériaux Numériques, B. Scholtes, A. Settefrati, and M. Bernacki. Workshop SF2M/MECAMAT, Paris, France, November 30 - December 01 2015.
- Simulation en champ complet de la recristallisation et de la croissance de grains par une approche Level-Set avec remaillage local, and B. Scholtes, A. Settefrati, and M. Bernacki. Matériaux 2014, Montpellier, France, November 24-28 2014.

# Chapter 1

# Modeling of recrystallization and grain growth

## Contents


**1.1 Introduction . . . . . 21**

**1.2 Constitutive equations for the migration of grain boundaries . . . . 21**

**1.3 Macroscopic models . . . . . 23**

1.3.1 Physical laws and analytical models of recrystallization and grain growth . . . . . 24

1.3.2 Enriched mean field models . . . . . 33

**1.4 Full field models . . . . . 37**

1.4.1 Stochastic approaches . . . . . 37

1.4.2 Deterministic approaches . . . . . 41

**1.5 The level set approach, state of the art concerning the modeling of polycrystals . . . . . 48**

1.5.1 Generation and immersion of virtual polycrystals within unstructured finite element meshes . . . . . 49

1.5.2 Migration of the grain boundaries . . . . . 58

1.5.3 Limitations of the existing implementation . . . . . 63

## Résumé en français

Ce chapitre aborde la modélisation des phénomènes de recristallisation et de croissance de grains. Les modèles en champ moyen, qui reposent sur une description simplifiée de la microstructure, sont d'abord présentés. Bien qu'ils soient rapides et simples à mettre en œuvre, ces modèles homogénéisés ne permettent pas de décrire explicitement les interactions ayant lieu entre les grains. Les modèles en champ complet sont ensuite introduits. Ceux-ci sont basés sur une description du polycristal à l'échelle microscopique et décrivent son évolution au travers de lois physiques. Les principaux modèles en champ complet de la littérature sont détaillés. Un accent tout particulier est mis sur l'approche level set. Cette méthode a d'ores et déjà démontré un potentiel très intéressant pour modéliser la recristallisation statique et la croissance de grains, et des travaux sont actuellement en cours pour l'étendre au phénomène de recristallisation dynamique. On introduit les principales équations liées à cette méthode level set ainsi que l'immersion de polycristaux dans des maillages éléments finis non structurés. Une première simulation simple en deux dimensions est réalisée afin de mettre en évidence les limites de l'implémentation du modèle numérique existant au début de ce travail de thèse. On s'intéresse plus particulièrement à ces limitations dans les prochains chapitres.

## 1.1 Introduction

Choosing the appropriate modeling scale is crucial in any engineering problem. This choice is generally determined by the amount of computational resources available and the desired degree of accuracy. Metallurgical models for GG and ReX fall classically on three categories: macroscopic, mesoscopic and atomistic models.

In order to limit the thickness of the present manuscript, models based on *molecular dynamics* or *dislocation dynamics* are not considered hereafter. Effectively, consider more than one grain (or even a portion of grain) is complicated in such simulations because of the prohibitive numerical costs. So they are not compatible with the present study, which aims to provide viable numerical solutions for the industry, that are able to address the whole manufacturing process within reasonable computation times. However molecular dynamics or dislocation dynamics simulations present a great academic interest because they can help to better understand different physical phenomena that occur at a very fine scale, or to identify some material properties.

So this chapter will focus mainly on macroscopic and mesoscopic metallurgical models. But before considering precisely the existing modeling approaches, it is crucial to introduce the physical and theoretical foundations of microstructural evolutions from which most of these models are built.

## 1.2 Constitutive equations for the migration of grain boundaries

A grain boundary moves with a velocity $\vec{v}$ in response to the net pressure $p$ on the boundary. Its is generally assumed that the velocity is directly proportional to the pressure, the constant of proportionality being the mobility $M$ of the boundary, and thus:

$$\vec{v} = Mp\vec{n}, \tag{1.1}$$

where $\vec{n}$ is the unit outward vector normal to the interface. The driving pressure $p$ can also be seen as the sum of two contributions $p = p^{\mathrm{c}} + p^{\mathrm{e}}$, the former $p^{\mathrm{c}}$ depicting the capillarity effects due to the curved shape of the grains, and the second $p^{\mathrm{e}}$ which is related to the stored energy gradients across the grain boundary. The capillarity force $p^{\mathrm{c}}$ is usually assumed to be directly proportional to the *local mean curvature* of the interface, which is the trace of the curvature tensor:

$$p^{\mathrm{c}} = \gamma\kappa. \tag{1.2}$$

Here $\gamma$ is a material parameter called the grain boundary energy.

On the other hand $p^{\mathrm{e}}$ depends on the local heterogeneity of the stored deformation energy $e$:

$$p^{\mathrm{e}} = \Delta e. \tag{1.3}$$

This deformation energy is usually deduced from the dislocation density $\rho$ according to $e = \tau\rho$, with $\tau$ being the dislocation energy by unit length. Finally the velocity $\vec{v}$ in eq. (1.1) can be rewritten as follows:

$$\vec{v} = \vec{v}^{\mathrm{c}} + \vec{v}^{\mathrm{e}}, \tag{1.4}$$

where $\vec{v}^{\mathrm{c}} = M\gamma\kappa\vec{n}$ and $\vec{v}^{\mathrm{e}} = M\Delta e\vec{n}$ (see fig. 1.1).

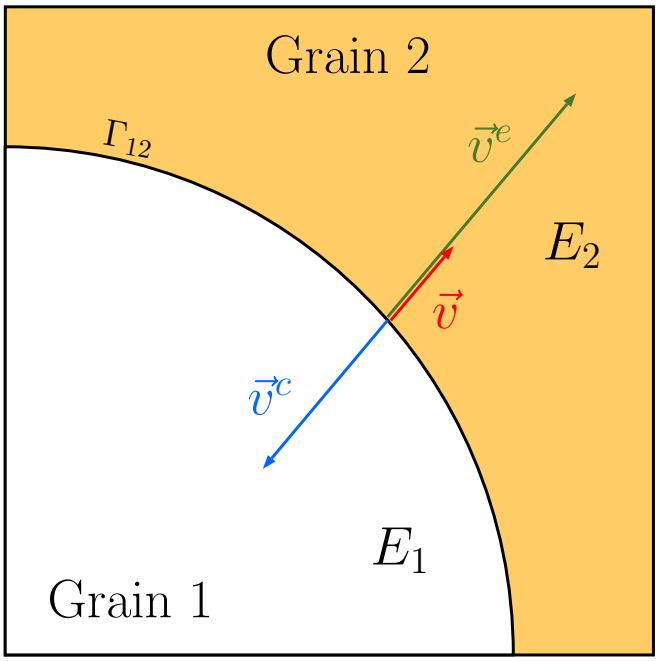


**Fig. 1.1** – Velocity $\vec{v}$ of a grain boundary consisting of a capillarity contribution $\vec{v}^{\mathrm{c}}$ and a term representing the energy jump across the interface $\vec{v}^{\mathrm{e}}$. Here, the concave shape of $\Gamma_{12}$ gives the orientation of $\vec{v}^{\mathrm{c}}$ and it is assumed that $E_1 < E_2$, explaining why the vector $\vec{v}^{\mathrm{e}}$ is oriented from $G_1$ toward $G_2$. The energy is here assumed constant by grain for simplicity.

The material parameters $M$ and $\gamma$ depend on the material, the processing conditions

and the local *misorientation* $\Delta\theta$, *i.e.* anisotropy in terms of crystalline orientation. Especially the classical Read-Schokley relationship can be used in first approximation to describe the dependence of $\gamma$ to the misorientation:

$$\gamma(\Delta\theta) = \begin{cases} \gamma_{\mathrm{m}} \dfrac{\Delta\theta}{\Delta\theta_{\mathrm{m}}} \left(1 - \ln\left(\dfrac{\Delta\theta}{\Delta\theta_{\mathrm{m}}}\right)\right) & \text{if } \Delta\theta \leq \Delta\theta_{\mathrm{m}} \\ \gamma_{\mathrm{m}} & \text{if } \Delta\theta > \Delta\theta_{\mathrm{m}}, \end{cases} \tag{1.5}$$

in which $\gamma_{\mathrm{m}}$ is the grain boundary energy in the case of large misorientation angles (*i.e.* $\Delta\theta > \Delta\theta_{\mathrm{m}}$), with $\Delta\theta_{\mathrm{m}} \approx 15°$ classically. However this expression is not valid for any kind of boundaries, especially *twin boundaries* whose interfacial energy cannot be described by eq. (1.5).

Also the mobility is usually given a temperature dependence according to an Arrhenius relation on the form [Humphreys et al. 2004]:

$$M = M_0(T) \exp\left(-\frac{Q_{\mathrm{m}}}{\mathscr{R}T}\right), \tag{1.6}$$

where $T$ is the temperature, $Q_{\mathrm{m}}$ is the activation energy for grain boundary migration and $\mathscr{R}$ corresponds to the gaz constant. The pre-exponential term $M_0$ is generally inversely proportional to the temperature, but can be reasonably considered constant for metallic materials processed at high temperature.

Most macroscopic and mesoscopic models work on these fundamental equations as it will be detailed later. However it is to note that the present work does not consider the possible anisotropy of the interface features, and more specifically of the grain boundary energy (see eq. (1.5)).

## 1.3 Macroscopic models

There exists many confidential works and published metallurgical models that are developed for specific applications and depend on the thermomechanical conditions and of the considered materials. Mention all of them would obviously be impossible. Here we focus on historic physical laws, analytic models, and recent mean field approaches based on an enriched description of the microstructure, in order to tackle the DRX, SRX and GG phenomena with possible ZP. Examples of other phenomenological ReX models can be found elsewhere [Voyiadjis et al. 2005; Estrin et al. 2007; Hallberg et al. 2010a].

### 1.3.1 Physical laws and analytical models of recrystallization and grain growth

#### Dynamic recrystallization

The metal accumulates dislocations during deformation and empirical laws are usually employed to describe the evolution of $\rho$. These are classically composed of a hardening term (+) related to Frank-Read sources of dislocations, and a softening term (−) which reflects the rearrangement and annihilation of dislocations:

$$\frac{\partial \rho}{\partial \varepsilon} = \left(\frac{\partial \rho}{\partial \varepsilon}\right)^{+} - \left(\frac{\partial \rho}{\partial \varepsilon}\right)^{+}, \tag{1.7}$$

where $\varepsilon$ is the effective plastic strain. Most-known hardening laws are summarized in table 1.1. Different dislocation species can also be considered, such as mobile and immobile dislocations. For example in [Bammann et al. 1982; Walgraef et al. 1985a; Walgraef et al. 1985b; Walgraef et al. 1985c; Hallberg et al. 2013], the evolution of mobile and immobile dislocations are described by a reaction-convection system.

| Refs. | Relation |
|---|---|
| Kocks-Mecking [Kocks 1976] | $\frac{\partial \rho}{\partial \varepsilon} = K_1\sqrt{\rho} - K_2\rho$ |
| Yoshi-Laasraoui-Jonas [Laasraoui et al. 1991] | $\frac{\partial \rho}{\partial \varepsilon} = K_1 - K_2\rho$ |
| Estrin [Estrin 1998] | $\frac{\partial \rho}{\partial \varepsilon} = K_1\sqrt{\rho} - K_2\rho - \frac{s_r}{\dot{\varepsilon}}$ |
| Montheillet [Montheillet et al. 2009] | $\frac{\partial \rho}{\partial \varepsilon} = \frac{K_1}{\rho^x}$ |

**Table 1.1** – Classical hardening laws used to describe the evolution of the dislocation density. The additional term $s_r$ refers to static recovery, while $x$ is a positive constant in the Montheillet's model.

The DRX phenomenon starts when the dislocation density reaches a critical threshold value during the deformation. This quantity is noted $\rho_{cr}^{DRX}$, and was estimated by Roberts and Ahlblom [Roberts et al. 1978]:

$$\rho_{cr}^{DRX} = \left(\frac{20K_1\gamma\dot{\varepsilon}}{3MK_3\tau}\right)^{1/3} \text{ with } K_3 = M\tau. \tag{1.8}$$

Here $\dot{\varepsilon}$ designates the plastic strain rate. The dependence of this model to strain rate and temperature is indirectly considered through the parameters $K_3$ and $K_1$. However eq. (1.8) neglects dynamic recovery, which is sometimes a strong assumption. Beltran et al. [Beltran et al. 2015] proposed recently a new expression which is valid for a wide range of thermomechanical conditions:

$$\rho_{cr}^{DRX} = \left[ \frac{-2\gamma\dot{\varepsilon}\dfrac{K_2}{K_3\tau}}{\ln\left(1-\dfrac{K_2}{K_1}\rho_{cr}^{DRX}\right)} \right]^{1/2} . \tag{1.9}$$

The term $K_2$ in this expression is related to the dislocation annihilation term in [Kocks 1976; Laasraoui et al. 1991; Estrin 1998]. After DRX is initiated, new recrystallized grains emerge in the microstructure. The nucleation rate (per surface unit) during DRX is usually related to the plastic strain rate and to the temperature according to:

$$\dot{\Upsilon} = c\dot{\varepsilon}\exp\left(\frac{Q_n}{\mathscr{R}T}\right), \tag{1.10}$$

where $c$ is a constant and $Q_n$ the activation energy for nucleation [Peczak et al. 1993; Peczak et al. 1994]. After they appear in the microstructure, the nuclei can grow or shrink, depending on the capillarity force, the local energy gradient and the mobility of the surrounding grain boundaries. Only the germs achieving a *critical size* $r_c$ survive, while the others disappear. By neglecting capillarity effects, Bailey-Hirsch [Bailey et al. 1962] estimated $r_c$ according to:

$$r_c = \frac{4\gamma}{\langle\rho\rangle\mu b^2}, \tag{1.11}$$

where $\langle\rho\rangle$ is the mean dislocation density inside the material, $\mu$ is the shear modulus and $b$ corresponds to the magnitude of the Burger's vector. Favre et al. proposed recently an extension of the previous criterion which considers also the capillarity forces [Favre et al. 2013]:

$$r_c = \frac{4\gamma}{\langle\rho\rangle\mu b^2 + \dfrac{4\gamma}{\langle R\rangle}}, \tag{1.12}$$

with $\langle R\rangle$ the mean grain size of the material.

Obviously these approaches are mainly phenomenological and experimental tests are needed to calibrate the model parameters, which depend on the material and the thermomechanical conditions.

### Static recrystallization

During SRX the nuclei grow and consume progressively the old microstructure. The type of curve shown in fig. 1.2 is typically used to describe phenomenologically the nucleation and growth processes of SRX. The early works in this area are due to Kolmogorov [Kolmogorov 1937], Johnson and Mehl [Johnson et al. 1939], and Avrami [Avrami 1939; Avrami 1940; Avrami 1941]. They gave rise to the well-known JMAK model.

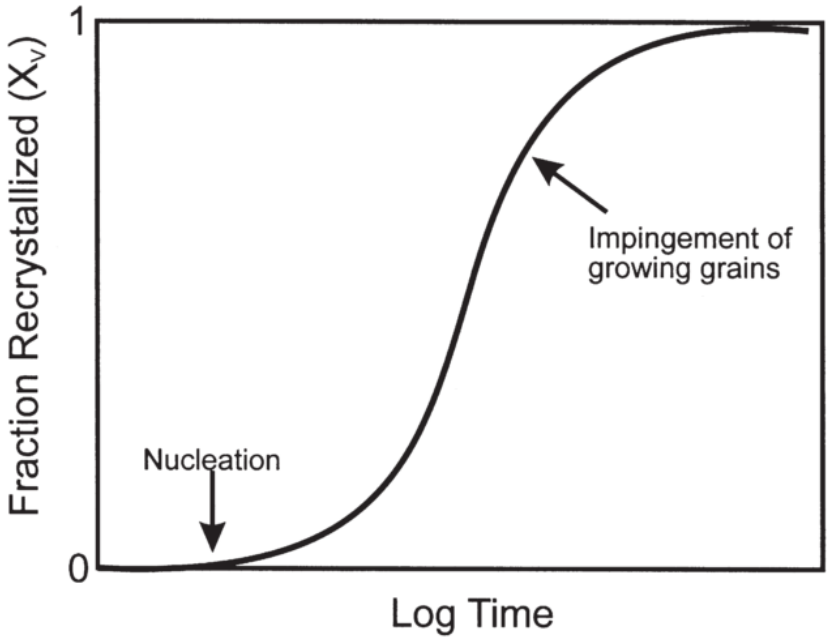


**Fig. 1.2** – Typical recrystallization kinetics during isothermal annealing [Humphreys et al. 2004].

This model is based on the assumption that nuclei are formed at a rate $\dot{N}$ and that grains grow into the deformed material at a linear rate $\dot{G}$. If the grains are spherical, their volume varies as the cube of their diameter, and the fraction of recrystallized material $X_v$ rises rapidly with time. However, the new grains will eventually impinge on each other and the rate of ReX will then decrease, tending to zero as $X_v$ approaches unity:

$$X_v = 1 - \exp\left(-Bt^n\right), \tag{1.13}$$

where $t$ is the time, $n$ is a constant called the Avrami exponent and $B$ is also a constant equals to $f\dot{N}\dot{G}^3/4$, with $f$ a shape factor equals to $4\pi/3$ for spheres.

In the theoretical case where the rates of nucleation and growth remain constant during ReX, the JMAK theory gives $n = 4$. Other configurations have been investigated by Avrami [Avrami 1939], in which the nucleation rate is not constant, but a decreasing function of time, $\dot{N}$ having a simple power law dependence on time. In this situation $n$ lies between 3 and 4, depending on the exact form of the function. A particular case is that where the nucleation rate decreases so rapidly that all nucleation events effectively occur at the start of recrystallization. This is termed *site saturated nucleation*. In this limiting case, $n$ is found to be 3.

The above analyses assume that until impingement, the grains grow isotropically in three-dimensions. If the grains are constrained either by the sample geometry or by some internal microstructural constraint to grow only in one or two-dimensions, then the JMAK exponent is lower as shown in table 1.2. Cahn [Cahn 1956] has extended the theory to include nucleation at random sites on grain boundaries and found that $n$ fell from 4 at the start of the transformation to 1 at the end. It is generally assumed that a growth direction is constrained when nucleation occurs at the grain boundaries [Fabiano 2013]. However, no general analytical treatment of non-randomly distributed nucleation sites is available because the essential feature of the JMAK approach is that the nucleation sites are assumed to be randomly distributed.

| Growth dimensionality | Site saturated nucleation | Constant nucleation rate |
|---|---|---|
| 3D | 3 | 4 |
| 2D | 2 | 3 |
| 1D | 1 | 2 |

**Table 1.2** – Ideal values of the Avrami exponent $n$ in eq. (1.13). According to [Humphreys et al. 2004].

Obviously this approach is limited because it relies on many assumptions concerning the rate of nucleation and growth which are not constant practically and can be hardly estimated. This requires a lot of experimental tests in order to calibrate the model for a given material in the considered range of themomechanical conditions. Also the JMAK theory is only valid in the case of a homogeneous distribution of the stored deformation energy.

### Pure capillarity-driven grain growth

In 1952 von Neumann discovered that the 2D growth of soap froth depends only on the number of sides. Later in 1956 Mullins [Mullins 1956] confirmed these findings by observing that the rate of area loss or gain of a given grain depends only on its topological class $n_t$, *i.e.* the number of neighbors. These investigations gave rise to the von Neumann-Mullins topological law which relates the growth rate of a grain to $n_t$:

$$\frac{dA}{dt} = 2\pi M\gamma\left(\frac{n_t}{6} - 1\right), \tag{1.14}$$

where $A$ is the instantaneous surface area of the considered grain. According to this relationship, grains that have $n_{cr} = 6$ neighbors do not grow or shrink, *i.e.* $dA/dt = 0$ in eq. (1.14).

Later in 2007 this analysis has been extended in 3D by MacPherson and Srolovitz [MacPherson et al. 2007], which gave rise to the fundamental MacPherson-Srolovitz law [MacPherson et al. 2007] that governs normal grain growth in three-dimensional isotropic polycrystalline materials. Especially this relationship describes the volume evolution of individual grains:

$$\frac{dV}{dt} = -2\pi M\gamma\left(L - \frac{1}{6}J\right), \tag{1.15}$$

where $V$ is the volume of the considered grain, $L$ is a one-dimensional measure of the grain size called the mean width, and $J$ is the sum of the lengths of all triple edges (along which three grains meet) of the grain.

Other 3D analytical models of GG have also been developed, that can be seen, more or less, like direct 3D counterparts of the von Neumann-Mullins law. Especially Mullins [Mullins 1989] developed the symmetric model of polyhedral geometry and derived an expression for the growth rate of a polyhedral grain with $n_t$ faces:

$$\frac{1}{R}\frac{dV}{dt} = M\gamma F(n_t) 5.35 n_t^{2/3}\left(\frac{n_t - 2}{2\sqrt{n_t - 1}} - \frac{3}{8}F(n_t)\right), \tag{1.16}$$

where $F(n_t)$ is given by:

$$F(n_t) = \left[\frac{\pi}{3} - 2\arctan\left(1.86\frac{\sqrt{n_t - 1}}{n_t - 2}\right)\right]. \tag{1.17}$$

This symmetric model of a polyhedron is based on the following three assumptions: (1) each face subtends an equal solid angle of $4\pi/n_t$ at the centroid of the polyhedron,

in accord with the approximate equiaxed shape of grains undergoing normal grain growth; (2) three edges of the polyhedron intersect at each vertex, in accord with the topology of a grain aggregate; (3) each face (plane) may be approximated as a pentagon, in accord with the observed polygonal face of greatest frequency [Mullins 1989].

An other equivalent model were introduced in 2006 by Rios and Glicksman [Rios et al. 2006], which is based on the so-called average $N$-hedra method developed by Glicksman [Glicksman 2005] for polycrystalline structures, and relates directly the growth rate of an individual grain to $n_t$:

$$\frac{dV^{2/3}}{dt} \approx \frac{9}{4} M\gamma \left(\sqrt{n_t} - \sqrt{n_{cr}}\right). \tag{1.18}$$

Based on their theory the critical $N$-hedra which has an equivalent zero mean curvature (zero growth rate) satisfies $n_t = n_{cr} = 13.3973$.

The main advantage of eq. (1.18) and eq. (1.16) comparatively to eq. (1.15) is that these two models enable to estimate the growth rate of a grain in pure GG condition directly as a function of the number of neighbors, which is an easily measurable quantity. On the other hand, the parameter $J$ in eq. (1.15) that represents the total length of triples edges of the considered grain can be much harder to estimate, making this law less convenient even if it is exact.

These precise analytical models are interesting because they permit to study the influence of the topology on the evolution of the individual grains during pure GG. They can also be used directly as evolution rules in numerical models of pure GG [Lazar et al. 2010; Lazar et al. 2011] or to validate new modeling approaches. However they remain rather limited, especially because they consider the grains "one by one" and do not provide directly a statistically representative representation of the microstructure, and especially of its mean grain size which determines the macroscopic behavior of the material.

In 1952 Burke & Turnbull investigated the physical mechanisms of GG and developed a model that remains probably the most widely-used model for normal GG. Based on eq. (1.2), Burke & Turnbull developed a complete theory based on two fundamental assumptions. The former is that the grains are perfectly spherical with radius $R$, so that their curvature is constant and equal to $\kappa = 2/R$ in 3D. The second assumption is that grain boundaries migrate by atom transport towards their center of curvature.

They finally deduced a parabolic law for the growth:

$$\frac{d\langle R\rangle^2}{dt} = \alpha M\gamma, \tag{1.19}$$

where $\alpha$ is a growth constant that is found to be 0.5 according to the Burke & Turnbull analysis [Burke et al. 1952]. This value were later comforted by Mullins [Mullins 1989] which found $\alpha = 0.5^{\pm 0.1}$, based of its symmetric model of polyhedral geometries and the experimental data of Hull [Hull 1988] on separated $\beta$-brass grains. The same value $\alpha \approx 0.5$ were also obtained more recently thanks to 3D PF simulations [Darvishi Kamachali et al. 2012]. The classical Burke & Turnbull law is finally obtained by integrating eq. (1.19):

$$\langle R\rangle^2 - \langle R_0\rangle^2 = \alpha M\gamma t. \tag{1.20}$$

with $\langle R_0\rangle$ the mean grain size at the early stage of GG.

However recent numerical investigations have pointed out that this model is not able to predict precisely the GG kinetics for any kind of initial grain size distribution in 2D [Cruz-Fabiano et al. 2014] or in 3D [Maire et al. 2016]. Especially in the case of very homogeneous initial distribution, the mean grain size remains globally stable during the first stage of the TT which reflects in a plateau for the mean grain size evolution. This can not be captured by eq. (1.20). Moreover it is worth noting that eq. (1.19), on which the Burke & Turnbull model is built, relies on many assumptions (homogeneous and constant grain boundary mobility and energy, self similarity of the grain size distribution, spherical grains, microstructure free of deformation energy and second phase particle) that limit its scope.

### Particle pinning

The interaction angle between a particle and a grain boundary is dictated by the respective surface tensions at the interface. Let us consider fig. 1.3 for an illustration, where $\gamma_1^p$, $\gamma_2^p$ and $\gamma$ are respectively the surface tensions associated with the interfaces $\Gamma_1^p$, $\Gamma_2^p$, $\Gamma_{12}$, and $\vec{p}$ is the unit outward vector normal to the precipitate. Here the balance of the surface tensions provides:

$$\gamma_2^p = \gamma_1^p + \gamma\sin(\alpha), \tag{1.21}$$

which can be rewritten:

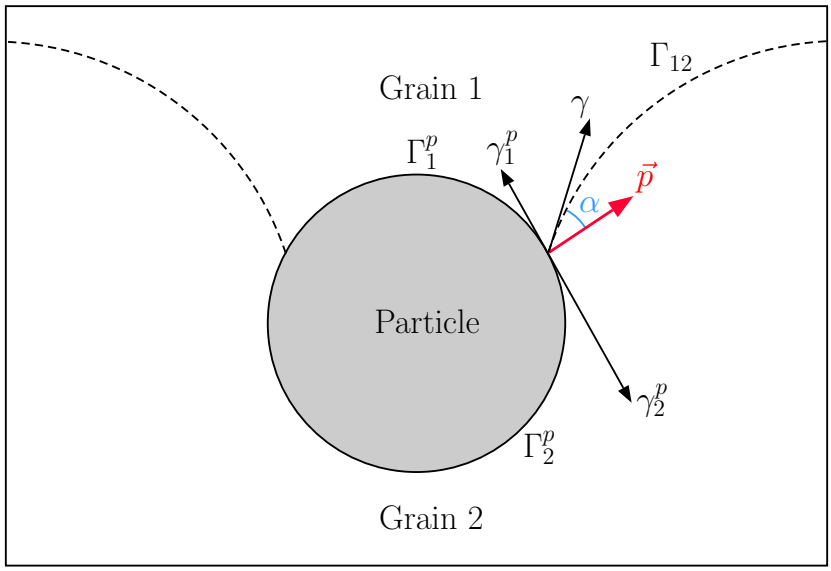


**Fig. 1.3** – Schematic illustration of the interaction between a moving grain boundary and a coherent SPP [Humphreys et al. 2004].

$$\sin(\alpha) = \frac{\gamma_2^p - \gamma_1^p}{\gamma}. \tag{1.22}$$

A particular case is obtained when the surface tensions at the particle interface are isotropic ($\gamma_1^p = \gamma_2^p$). Particles which satisfy this equilibrium are denoted *incoherent* with the matrix, and then eq. (1.22) boils down to $\alpha = 0$ (grain boundary perpendicular to the particle).

Zener & Smith were first to investigate analytically the dragging effect exerted by the SPPs [Smith 1948]. They developed a complete theory that rely on the following assumptions:

- grain boundaries are rigid,
- the mobility and energy of the grain boundary are constant and homogeneous,
- particles are incoherent with the matrix, *i.e.* $\gamma_1^p = \gamma_2^p$,
- all particles are perfectly spherical with mean radius $\langle r_\mathrm{p} \rangle$,
- each particle exerts the maximal dragging force $\pi\gamma\langle r_\mathrm{p}\rangle$ at the same time,
- particles are randomly dispersed in the microstructure (no clustering) with a given volume fraction $f_\mathrm{v}$,

- the material is free of deformation energy.

They deduced an expression for the global dragging pressure exerted by the particle cloud on the grain boundaries:

$$p^{\mathrm{z}} = -\frac{3\gamma f_{\mathrm{v}}}{2\langle r_{\mathrm{p}}\rangle}, \tag{1.23}$$

that is supposed to counterbalance the homogenized capillarity driving pressure: $p^{\mathrm{c}} = 2\gamma/\langle R\rangle$. The equilibrium of the driving and dragging forces, $p^{\mathrm{c}} + p^{\mathrm{z}} = 0$, gives finally:

$$\langle R_{\mathrm{f}}\rangle = \frac{4}{3}\frac{\langle r_{\mathrm{p}}\rangle}{f_{\mathrm{v}}}, \tag{1.24}$$

where $\langle R_{\mathrm{f}}\rangle$ designs the mean grain size achieved when normal GG is completely hindered by the particles. This equation, well-known as the Smith-Zener equation, has been widely discussed in the state of the art under the following more general form:

$$\langle R_{\mathrm{f}}\rangle = K\frac{\langle r_{\mathrm{p}}\rangle}{f_{\mathrm{v}}^{m}}, \tag{1.25}$$

where $K$ and $m$ are two fixed parameters. However these values fluctuate according to the authors and the assumptions that are made to obtain eq. (1.23). A brief overview can be found in table 1.3. Also many recent numerical investigations based on full field simulations have yielded to very different values for $K$ and $m$. This point will be further detailed in the fifth chapter.

| References | $K$ | $m$ | Remarks |
|---|---|---|---|
| [Smith 1948] | 4/3 | 1 | |
| [Gladman 1966] | $\frac{\pi}{6}\left(\frac{3}{2}-\frac{2}{Z}\right)$ | 1 | $\sqrt{2} \leq Z \leq 2$ |
| [Hellman et al. 1975] | 4/9 | 1 | |
| [Anand et al. 1975] | | 1/2 | most particles are on gain boundaries |
| [Hellman et al. 1975] | | 1/3 | most particles are at grain corners |

**Table 1.3** – Evaluation of coefficients $K$ and $m$ in eq. (1.25) according to different authors. Here $Z$ is a parameter related to the initial grain size heterogeneity [Agnoli 2013].

Finally even if eq. (1.25) has a direct practical interest because it predicts the mean grain size, there are strong limitations behind this approach. The most obvious is that the Zener model only addresses the normal GG phenomenon without stored energy. Then it can not be easily extended as such to more complex phenomena, like

SRX, DRX or PDRX. The second limitation is related to the inherent parameters in this model, that require to be calibrated. Also the large discrepancies for the $(K;m)$ values reported in the literature and very recent numerical investigations [Agnoli et al. 2014; Scholtes et al. 2016b] tend to indicate that $K$ and $m$ could actually be not considered as constant. Finally, a main limitation of this model and all other presented above, is the inability to treat the whole manufacturing process in a unified way. Effectively the material and forming processes are now extremely complex, and treating the underlying metallurgical phenomena "one by one", as it is done in these approaches, is no longer sufficient in the industry where the needs in terms of precision are increasingly important. Also some industrial applications require information about the variability of the microstructures, and not only the averaged quantities. Consequently more attention has been paid recently to new enriched macroscopic models that are based on a more accurate representation of the material microstructure and are able to treat a wide range of different metalurgical phenomena.

### 1.3.2 Enriched mean field models

Enriched mean field models are typically based on a discrete representation of the microstructure, composed of $N$ classes of spherical grains. Each class $i \in \{1,...,N\}$ is represented by a grain radius $R_i$ and eventually a dislocation density $\rho_i$, as illustrated on fig. 1.4. This description is especially employed in the recent models of Montheillet et al. [Montheillet et al. 2009] and Bernard et al. [Bernard et al. 2011].

The first historic approach of this type is due to Hillert, which proposed in 1965 an enriched mean field model for GG [Hillert 1965]. This model has been discussed in a large number of studies [Chao et al. 2004; Rios et al. 2006; Suwa et al. 2008; Darvishi Kamachali et al. 2012]. It states that the radius of each class evolves according to the following equation:

$$\frac{dR_i}{dt} = \beta M\gamma\left(\frac{1}{R_{cr}} - \frac{1}{R_i}\right) \quad \forall i \in \{1,...,N\}, \tag{1.26}$$

where $R_{cr}$ is a critical grain radius equals to $\langle R\rangle$ in 2D. In 3D it can be demonstrated that $R_{cr} = \langle R^2\rangle / \langle R\rangle$ by applying the volume conservation [Chao et al. 2004; Rios et al. 2006]. Also Hillert has shown that $R_{cr} \approx 9\langle R\rangle/8$ at steady-state [Hillert 1965]. The parameter $\beta$ refers to the inherent approximations concerning the assumed idealized geometry in the Hillert's model representation. According to Hillert $\beta = 0.5$ in 2D and $\beta = 1$ in 3D [Hillert 1965]. Other authors have nevertheless reported values above unity, such as $\beta \approx 1.25$ [Darvishi Kamachali et al. 2012] and $\beta \approx 1.1$ [Suwa et al. 2008].

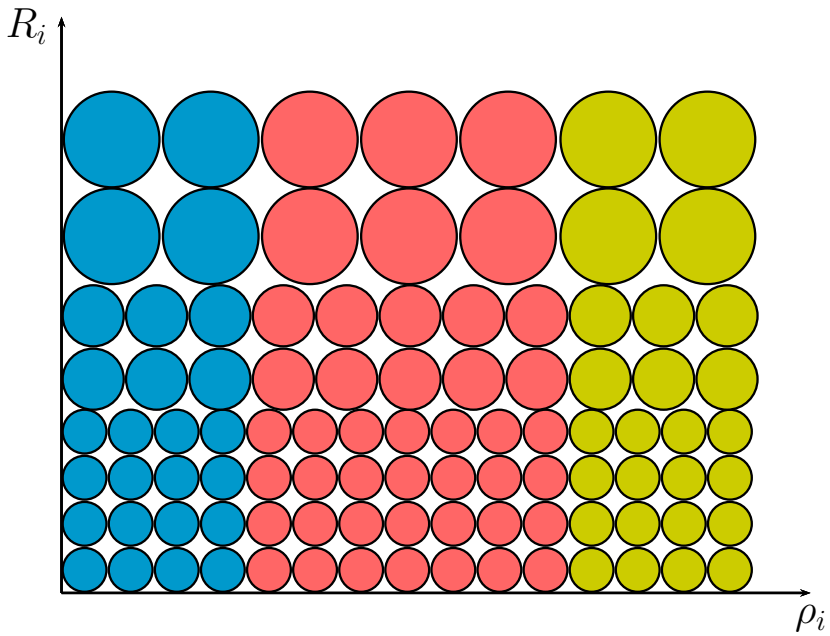


**Fig. 1.4** – Discrete representation of the microstructure in mean field models.

As it considers several grain classes, this model has the advantage of predicting the evolution of the grain size distribution. Also Fabiano et al. [Cruz-Fabiano et al. 2014] have demonstrated the ability of this model to capture correctly the GG kinetics in 2D for different initial grain size distributions.

Later Hillert extended his theory of normal grain growth to include the effects of particle pinning on the kinetics of grain growth and on grain size distribution. For this purpose, an additional dragging term was added to eq. (1.26):

$$\frac{dR_i}{dt} = \beta M\gamma\left(\frac{1}{R_{\text{cr}}} - \frac{1}{R_i} \pm \frac{z}{\beta}\right) \quad \forall i \in \{1,...,N\}\,, \tag{1.27}$$

where $z = 3f_{\text{v}}/4\langle r_{\text{p}}\rangle$. Grains in the size range $1/R \pm z/\beta$ are assumed to be pinned by the particles and do not evolve (*i.e.* $dR/dt = 0$). Grains larger or smaller than this will shrink or grow at a reduced rate.

Also in 2009 Montheillet et al. proposed an enriched mean field model of discontinuous DRX wherein each grain is assumed to be immersed in a homogeneous matrix with average dislocation density $\langle\rho\rangle$ (see fig. 1.5a). This model neglects capillarity effects which are assumed to be one order of magnitude smaller than the stored energy gradients during DRX. Then the evolution of the grain classes are simply dictated by the difference in dislocation density:

$$\frac{dR_i}{dt} = M\tau\left(\langle\rho\rangle - \rho_i\right) \quad \forall i \in \{1,...,N\}, \tag{1.28}$$

The term $\langle\rho\rangle$ is deduced from the volume conservation condition:

$$\frac{d}{dt}\left(\sum_{i=1}^{N} V_i\right) = \sum_{i=1}^{N} \frac{dV_i}{dt} = \sum_{i=1}^{N} 4\pi R_i^2 \frac{dR_i}{dt} = \sum_{i=1}^{N} S_i \frac{dR_i}{dt} = 0, \tag{1.29}$$

with $V_i$ and $S_i$ the respective volume and surface area of the $i^{th}$ grain class, given by $V_i = 4\pi R_i^3/3$ and $S_i = 4\pi R_i^2$. Finally it falls:

$$\langle\rho\rangle = \sum_{i=1}^{N} S_i\rho_i \Big/ \sum_{i=1}^{N} S_i. \tag{1.30}$$

The DRX model of Cram et al. [Cram et al. 2009], introduced in 2009, is globally similar with the exception that each grain class has here its own mechanical behavior, related to its respective orientation/Taylor factor $T_i$ (see fig. 1.5b). More recently Bernard et al. [Bernard et al. 2011] proposed a new semi-analytical model of DRX in which each grain class evolves in a matrix composed of two homogeneous equivalent media, one representing the recrystallized grains with a low dislocation density and the other one representing the deformed grains with higher dislocation density (see fig. 1.5c). These two media are considered at each time step for describing the grain migration. One advantage of this model comparatively to the ones of [Montheillet et al. 2009; Cram et al. 2009] is that it also takes into account the capillarity effects through a coupled formulation of eq. (1.26) and eq. (1.28). See [Bernard et al. 2011; Beltran et al. 2015] for more details about the evolution laws used in this model.

This model comes also with an original formulation for the nucleation rate:

$$\dot{\Upsilon}_i = K_g S_c \frac{N_i R_i^q \left(\rho_i - \rho_{cr}\right)^{b_g}}{\sum\limits_{\rho_k > \rho_c} N_k R_k^q \left(\rho_k - \rho_{cr}\right)^{b_g}}; \; K_g = K_g(T, \dot{\varepsilon}), \tag{1.31}$$

where $b_g$ is a constant close to 3 according to Montheillet et al. [Montheillet et al. 2009], $K_g$ is a probability constant depending on the processing conditions and $S_c$ is finally the total surface area of the grains satisfying $\rho_i > \rho_{cr}$. The exponent $q$ is equal to 2 or 3, depending whether it is assumed necklace or bulk nucleation [Bernard et al. 2011]. The critical dislocation density $\rho_{cr}$ in eq. (1.31) is given by eq. (1.9).

It is usually very convenient to express directly the evolution of the grains in terms of volume (respectively in terms of internal area in 2D). This can be done by derivation

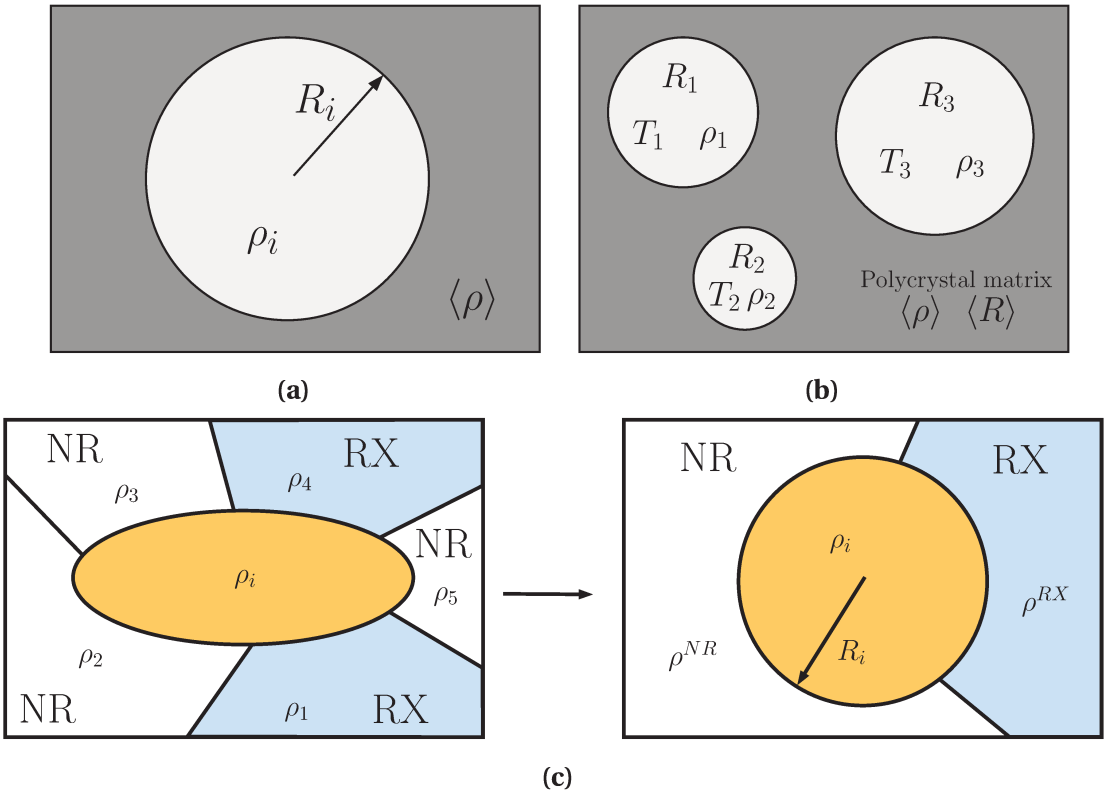


**Fig. 1.5** – Schematic microstructure representation in different enriched macroscopic models of DRX: (a) grain immersed in a homogeneous matrix [Montheillet et al. 2009]; (b) grains with different orientations/Taylor factors immersed in a homogeneous matrix [Cram et al. 2009]; (c) grain interacting with the rest of the aggregate (left) and simplified representation used in the model, considering two equivalent homogeneous media [Bernard et al. 2011].

of the internal volume $V_i$ (respectively of the internal area $A_i$ in 2D) of each class of grains [Darvishi Kamachali et al. 2012]:

$$\frac{dA_i}{dt} = 2\pi R_i \frac{dR_i}{dt} \text{ (in 2D) or } \frac{dV_i}{dt} = 4\pi R_i^2 \frac{dR_i}{dt} \text{ (in 3D)} \tag{1.32}$$

One main interest of these enriched mean field models is that they predict the grain size distribution and its evolution during the treatment. Moreover most recent models are able to account for capillarity forces, stored energy gradients and the possible dragging effect exerted by precipitates, which makes them sufficiently versatile to address a wide range of TMT/TT. Obviously the precision and the computational cost of these approaches is strongly related to the number of classes $N$ used in the simulations. But simulation times are of few minutes for most configurations, using standard laptop computers, making these models extremely effective from a numerical point of view. A less attracting feature of these models is there inability to predict the non-averagable phenomena, such as abnormal grain growth, caused by local heterogeneities of the microstructure properties that can not be captured with averaged approaches. An other issue is the lack of grain topology in the existing mean field representations. More specifically, these models do not describe how the grains are connected to each other in the aggregate which is especially problematic when the interface properties depend on the adjacent grains. The Read-Shockley equation that defines the grain boundary energy as a function of the local misorientation is a perfect example (see eq. (1.5)). Finally, even if we have presented an extension of the Hillert's model that is able to consider the ZP phenomenon (see eq. (1.27)), let us keep in mind that this approach averages the dragging effect on the whole microstructure, and can thus not account for heterogeneous non-random distributions of SPPs. Also from a more general point of view, these macroscopic models rely on many parameters (for example $\beta$ in eq. (1.26), $z$ in eq. (1.27), $c$ in eq. (1.10)) which do not have a direct physical interpretation, contrary to the parameters needed in full field models. These parameters must therefore be calibrated at a finer scale through experimental tests and/or full field simulations. We interest to these lower-scale numerical approaches in the next section.

## 1.4 Full field models

### 1.4.1 Stochastic approaches

Stochastic approaches, such as MC and CA are probably the most known and are still widely used. The former has been introduced by Potts in 1952 [Potts 1952]. MC and

CA approaches both rely on a pixelized in 2D or voxelized in 3D representation of the microstructure consisting of $P$ lattice sites (see fig. 1.6).

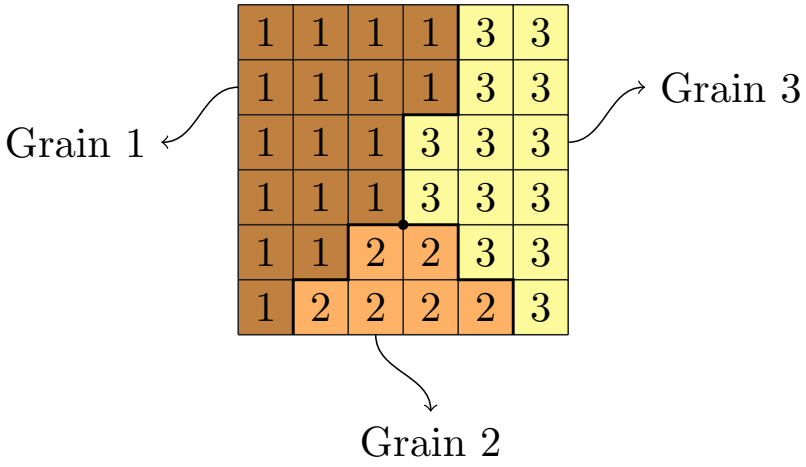


**Fig. 1.6** – Pixelized representation of the microstructure in MC and CA models. Three grains are depicted, with respective indexes 1, 2 and 3.

### Monte Carlo models

First metallurgical MC models emerged in the 1980s [Anderson et al. 1984; Srolovitz et al. 1984]. Later this method has become very popular especially through the works of Rollett et al. [Rollett et al. 1992b; Rollett et al. 1992a; Rollett 1997; Rollett et al. 2001]. At the early stage of a MC simulation, each cell of the pixelized domain is assigned an index $s_i$ (also called a *spin*) and a set of internal variables (dislocation density, crystallographic orientation,...). Then the total energy $E_{\text{mc}}$ of the initial configuration is calculated:

$$E_{\text{mc}} = \sum_{i=1}^{P} \left( \sum_{j=1}^{n_i} \frac{1}{2} \gamma(s_i, s_j) + E(s_i) \right), \tag{1.33}$$

with $n_i$ the number of neighboring lattice sites considered for each individual site $i$. The boundary energy $\gamma(s_i, s_j)$ is a function of the lattice index $s_i$ of the present site and of the neighbor site $j$. This corresponds to the boundary energy being a function of the relative crystallographic misorientation across the boundary as discussed in relation to eq. (1.5) [Rollett et al. 1989; Rollett et al. 2004; Hallberg 2011].

Next a lattice site with index $s_i$ is randomly picked in the domain and it is suggested a different index $s_{i'}$ (with $s_{i'} \neq s_i$). Due to the spin change the total energy becomes $E'_{\text{mc}}$,

and the difference $E'_{mc} - E_{mc}$ determines whether the suggested index is accepted of rejected thanks to a probabilistic law. A MC step is completed after $P$ spin changes have been tested. Obviously the morphology of the grains will be influenced by the underlying lattice onto which the microstructure is mapped. The lattice structure will be represented in the results, giving an undesired faceting of the modeled grain boundaries, which may influence the kinetics. Another major drawback of MC approaches is the lack of physical time scale in the classical formulation. Different techniques can however be employed to compare simulation and experimental results. One option is to relate the length and time scales of the simulation to their physical counterparts and perform a statistical matching of simulation and experimental results. Alternatively the parameters of the MC model can be interpreted in terms of physical quantities as in [Raabe 2000] giving correct units to the simulation. As the data structure employed in MC model is based on a regular lattice of pixels/voxels, the numerical implementation is straightforward. These models exhibit also high numerical efficiency, since they are well suitable for parallelization. On the other hand, there are inherent issues in MC models that are still regularly criticized. First the formulation of MC models does not allow to verify the linearity of the grain boundary migration velocity to the stored energy gradients during SRX. Also the influence of the underlying lattice on the kinetics and the lack of physical length and time scale (although remedies have been proposed previously) are still at the origin of many discussions in the literature, and complicate the comparison with experimental results [Rollett 1997]. Recent applications of MC approaches in the context of SRX and DRX can be found in the literature [Hore et al. 2013; Wang et al. 2014; Hore et al. 2015], although they tend to be progressively replaced by CA for these applications.

The dragging effect of SPPs can be introduced in MC models by assigning to several individual cells a particular spin, which is different of the spins used in the matrix and is not allowed to switch during the simulation [Gao et al. 1997]. Then, as the total energy of the configuration is lower when a particle meets a grain boundary compared to the situation when it is within the grain, there is a natural attraction between the particles and the grain boundaries which hinders the grain boundary displacement.

The first MC simulations of ZP date from the eighties thanks to the work of Srolovitz [Srolovitz et al. 1984] and were performed in 2D. The results of these simulations yielded values for the parameter $m$ in eq. (1.25) very different from unity ($m < 0.5$). This was due to the fact that a particle in a 2D microstructure is equivalent to a fiber in a 3D microstructure and so pinning forces are overestimated. Also successive 3D simulations yielded values of $m$ different from unity. However, it was shown that this

result is only the consequence of the artificial faceting of grain boundaries that is induced during the simulation [Miodownik et al. 1999]. Finally a large scale 3D MC simulation (with about $10^7$ voxels) where grain boundary faceting could be inhibited [Miodownik et al. 2000] confirmed the value $m = 1$ as in the original model of Zener & Smith, while $K = 0.73$ for a particle volume fraction lower than 10%. Overall, accounting for the ZP effect is straightforward in the MC formalism and can be easily implemented in 3D. However, this approach requires very fine lattice in order to counterbalance the error induced by the interface faceting, and then describe properly the grain boundary/SPP interactions.

### Cellular automata

CA were introduced by von Neumann in 1963 and later on in 1986 by Wolfram to a broader scientific public [Janssens 2010]. Then Hesselbarth [Hesselbarth et al. 1991; Hesselbarth et al. 1993], Davies [Davies 1995; Davies 1997; Davies et al. 1999] and Raabe [Raabe 1999; Raabe 2002] were first to use these models for problems involving solid-state transformations. Especially Raabe introduced the concept of probabilistic cellular automata (PCA) which are commonly used nowadays. In PCA models, the probability for a grain boundary to cover a neighboring cell is:

$$\mathscr{P}_{\text{ca}} = \frac{v}{v_{\max}}, \tag{1.34}$$

where $v$ and $v_{\max}$ are the local velocity in the considered pixel/voxel and the maximal grain boundary velocity calculated in the whole simulated domain, respectively. Then $\mathscr{P}_{\text{ca}}$ is compared with a random number comprise between 0 and 1. If it is greater, then the considered cell adopts the spin of the advancing adjacent grain, otherwise the spin remains unchanged. The cell states are updated simultaneously at the end of each time step in order to prevent multiple cell covering. Although PCA seems quite close to the MC method, these have a physical time scale because they rely on the kinetic law of eq. (1.4). This is a great advantage. Also CA scale very well with parallelization and can be easily implemented. On the other hand estimating precisely the local curvature of an interface is rather complex in a CA model because of the faceting induced by the lattice. One approach is by use of kink-templates as formulated in [Kremeyer 1998]. This method, very common in recent CA studies [Hallberg et al. 2010b; Liu et al. 2015; Lin et al. 2016], uses an extended neighborhood, *a template*, of the cell to estimate $\kappa$, based on the number of cells constituting the considered grain and the number of cells that would constitute a planar interface in the template region [Hallberg 2011]. However the precision of this approach is necessarily correlated with the resolution of the cell lattice. For small grain whose sizes are close to cell

dimensions, the number of neighboring cells in the template can be insufficient to estimate properly the local curvature. The trivial solution is therefore to refine the cell lattice in order to increase the number of cells in the template and thus the precision. But in the context of regular grids such as those used in CA models, this approach imposes to refine homogeneously (*i.e.* everywhere in the domain) the cell lattice, with potential impact on the simulation time. This is a weakness comparatively to FE approaches which permit to handle more efficiently and simply the local adaptation of the mesh and the heterogeneous mesh sizes inside the domain.

An other limitation of CA approaches, which is common with MC, is the inability to treat the microstructural evolution and the polycrystal deformation in a unified numerical framework. These are often coupled with the CPFEM [Raabe et al. 2000; Chuan et al. 2013; Lin et al. 2016; Madej et al. 2016]. Obviously coupled CA-CPFEM models come with inherent numerical difficulties such as the transport of the fields and the synchronization of the time steps. However CA remain an interesting approach for the modeling of ReX [Liu et al. 2015].

It is worth noting that MC and PCA both rely on probabilistic evolution laws. These are only statistically representative. In other words, two different PCA simulations using the same initial microstructure will not give exactly the same final result because evolution laws rely on probabilistic considerations wherein there is an inherent random aspect. This has necessarily an impact on the predictions and needs also to be taken into account.

### 1.4.2 Deterministic approaches

Recently more attention has been paid to deterministic approaches, which are more precise as they do not rely on probabilistic laws and can be used within FE meshes. However these are also largely more greedy in terms of computational resources due to the fact that they involve the resolution of large systems of PDEs. Most deterministic models concerning the simulation of microstructure evolutions fall on three categories: the front-tracking approaches, the PF approach and the LS approach.

#### Front-tracking approaches

Front-tracking methods explicitly construct and follow the motion of the grain boundaries. Based on, it is possible to use a volume discretization, as in the GRAIN3D model developed by Kuprat et al. [Kuprat 2000; Demirel et al. 2003; Gruber et al. 2005], or to

mesh only the grain boundaries, as in the Vertex method developed at the end of the 1980s [Kawasaki et al. 1989; Nakashima et al. 1989]. In Vertex models, the microstructure is discretized into a set of *real* vertices at multiple junctions. *Virtual* vertices may also be added along the grain boundaries to account for their curved shape, as depicted on fig. 1.7.

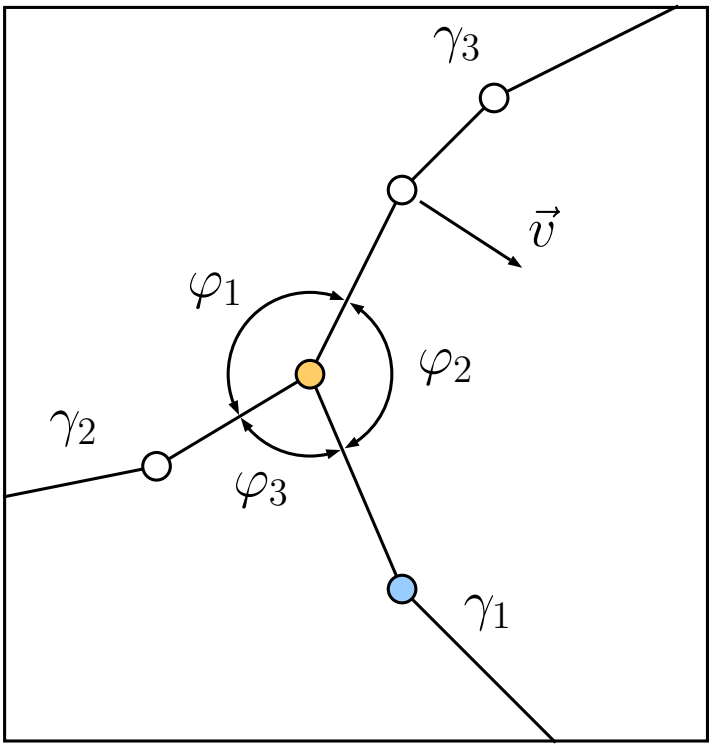


**Fig. 1.7** – Explicit representation of the grain boundary network composed of real (yellow) and virtual (blue) vertices in the Vertex method [Kawasaki et al. 1989; Nakashima et al. 1989; Hallberg 2011].

There are several ways to derive the equations describing the migration of vertices. Especially in [Kawasaki et al. 1989; Nakashima et al. 1989] it is assumed that the excess surface energy variation of the grain boundary due to the area reduction is entirely dissipated by viscous friction during the motion. This formulation results in a linear system of equations that must be solved at each time step. Most recent Vertex models of the literature are based on this formalism [Piekos et al. 2008; Toda-Caraballo et al. 2013; Mellbin et al. 2015]. Because interfaces are explicitly meshed, topological operation must be performed to ensure the FE mesh remains conform. But handling all the possible events in 3D is not straightforward and can be very demanding in terms of computational resources. See fig. 1.8 for an overview of the topological operations

that need to be handled in a 3D Vertex model. It is worth noting that these operations are immediate and irreversible in the sense that there is no progressive evolution. Let us consider for example the disappearance of a grain, as illustrated on fig. 1.8e. At the current time increment, the black grain is still present. Then, if a given arbitrary criterion is satisfied (*e.g.* minimal distance between two vertices achieved), this grain will be immediately removed from the microstructure, in sort that it will no longer be present at the next time increment. So these evolutions are not correlated with the time step of the simulation, but with an arbitrary criterion which does not have a direct physical interpretation. This may obviously impact the predictions, and especially the kinetics of the microstructure evolution.

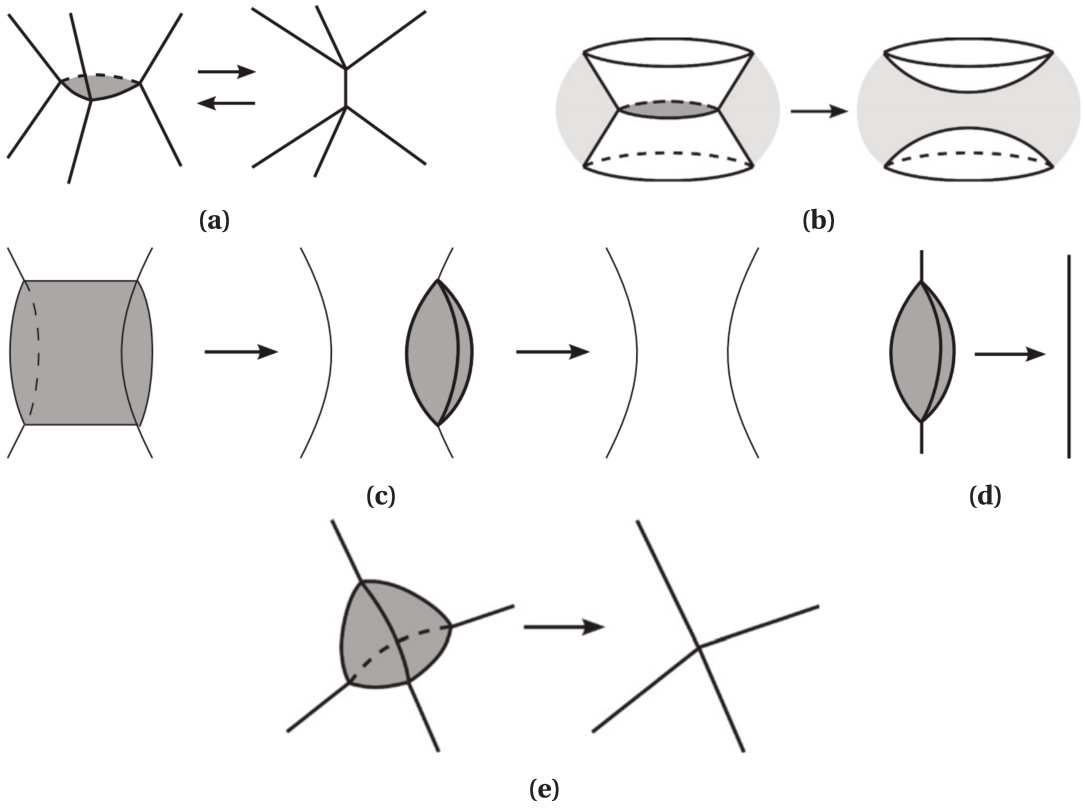


**Fig. 1.8** – (a)-(e) Some topological operations that must be handled in 3D Vertex models [Lazar et al. 2011].

Mellbin et al. [Mellbin et al. 2015] proposed recently an interesting 2D DRX model based on the Vertex approach for the description of microstructural evolutions considering nucleation events. To our knowledge there is no equivalent in 3D for the time being. Effectively handling the nucleation of a new grain, which can be interpreted as a reversed (e) operation in fig. 1.8, remains an open-issue in 3D Vertex models. It

could explain why this method seems at yet limited to GG [Syha et al. 2010; Lazar et al. 2011; Toda-Caraballo et al. 2013] or 2D ReX [Piekos et al. 2008].

The presence of particles can be simulated in Vertex models by introducing "pinning centers" in the domain, which are a new kind of vertex characterized by the maximum force $F_{\max}$ they can sustain. This force is a function of a critical unpinning angle which is imposed arbitrarily [Weygand et al. 1999]. When grain boundaries sweep an area which contains particles, the final position is chosen such that at most one particle is present in the triangular area swept. Then, the conditions for unpinning are tested: in the simplest situation, if the force acting on the particle is higher than $F_{\max}$, then grain boundary unpins. Simulations have shown that if the overall pinning force of particles $F_{\max}$ increases, then the final grain size distribution shifts from a log-normal one to a normal one. Moreover, the number of particles effectively acting as pinning centers is inversely proportional to $F_{\max}$. The effect of different particles sizes or shapes can be studied by assigning to the pinning centers different values of $F_{\max}$. Nonetheless, it remains questionable if the simulation of pinning effects, simply introduced in the model as a new kind of vertex, can be representative of real microstructures where the interactions between particles and grain boundaries can assume very complex geometries.

In 2005 Couturier et al. proposed a FE boundary tracking model which describes the interaction of a single planar grain boundary moving through a cloud of particles [Couturier et al. 2003; Couturier et al. 2005]. Here the interactions between the grain boundary and the particles are handled by applying kinematic conditions to the boundary nodes in contact with the particles so that their velocity remains tangential to a meridian of the particles. Under certain assumptions on the grain geometry during grain growth it is possible to extend the results yielded from this single grain boundary model to obtain information on the behavior of a polycrystal. The simulation results confirmed the theoretical value $m \approx 1$ in eq. (1.25) and highlighted that the effective pinning force of particles is almost two times smaller compared to the value proposed by Smith & Zener in eq. (1.23). Compared to previous approaches, this FE model allows to simulate the phenomenon in more details and on a more physically meaningful basis since the particle-grain boundary interaction is treated as a geometrical constraint to the movement. Nonetheless, up to now simulations are limited to spherical particles and do not consider the surface tension between grains and particles. Moreover, since the surface of grain boundaries is assumed to be planar with respect to particles, simulations are valid only if the ratio between the grain and particle sizes is very important. Finally, as for Vertex models, the implementation of

a full 3D simulations of a realistic polycrystal appears to be quite challenging due to the difficult treatment of topological transformations due to the explicit description of interfaces.

The boundary tracking approaches illustrate the complexity of the interface tracking problem. An alternative consists in using mathematical functions to describe implicitly the grains in the mesh. Using this approach, the handling of topological events is natural as grains can be added/removed from the simulation domain by performing simple arithmetic operations on these mathematical functions. This attractive framework based on *implicit interfaces* is at the heart of front-capturing methods, such as the PF and LS methods.

### The phase field method

The PF method employs continuous functions of spatial coordinates and time to represent the grains, the so-called PF variables. In the most basic form of PF models, the variable $\eta_i$ which represents the $i^{th}$ grain of the microstructure is equal to unity inside this grain and zero elsewhere. But this representation, illustrated in fig. 1.9a, creates sharp gradients at the boundaries which result in discontinuities and in ill-conditioned problems. To prevent this issue, grain boundaries are given implicitly by narrow regions where the PF variables change smoothly between their values in the neighboring grains [Moelans et al. 2008]. This introduces the concept of *diffuse interfaces* (see fig. 1.9b).

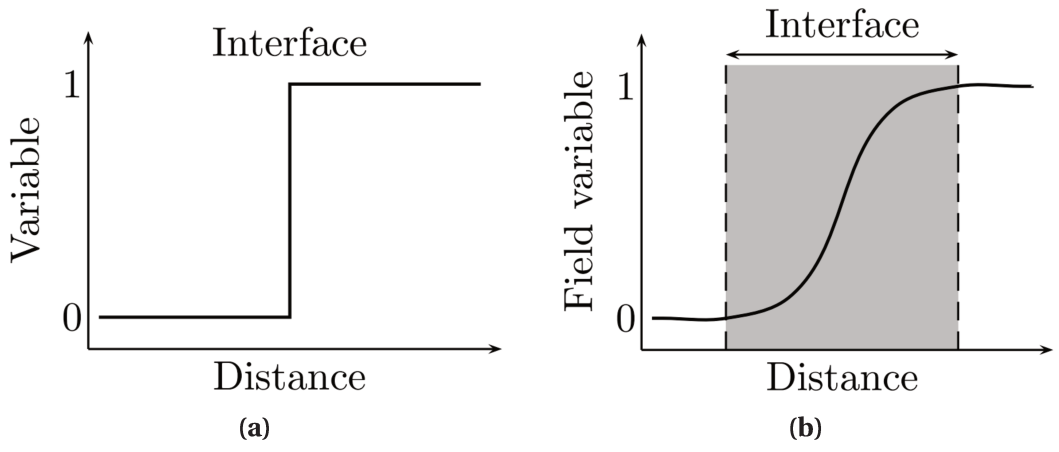


**Fig. 1.9** – Sharp and diffuse interface descriptions related to PF approaches.

At least three grid points (respectively mesh elements in a FE framework) are generally needed in the normal direction to the interface to account for this transition and

ensure numerical convergence [Darvishi Kamachali et al. 2012; Jin et al. 2015]. But the limitation in computational power forces to take the diffuse interface regions in the simulations wider than the physical grain boundary width in order to perform simulations for relevant length and time scales [Moelans et al. 2008]. The diffuse interface width is then treated as a numerical parameter that determines the accuracy of the simulation results. Finding an appropriate value for this transition thickness is a recurrent topic of discussions for PF methods [Moelans et al. 2009; Miyoshi et al. 2016].

Two variants of PF models can be found in the literature: the so-called *continuum phase field* (CPF) [Fan et al. 1997b; Fan et al. 1997a] and *multiphase-field* (MPF) [Steinbach et al. 1996; Garcke et al. 1998; Steinbach et al. 1999] models. In both methods, PF variables evolve to minimize the total free energy of the system, which is given by an integral of the local free-energy density $\hat{f}$ across the diffuse grain boundary regions. Diverse expressions can be found for $\hat{f}$ in the literature (see table 1.4 for a brief review).

| Refs. | $\hat{f}\left(\eta_i, \nabla\eta_i\right)$ | Comments |
|---|---|---|
| [Takaki et al. 2009] | $\sum_{k=1}^{N_p}\sum_{l>k}^{N_p}\left(-\frac{a_{kl}^2}{2}\nabla\eta_k\nabla\eta_l + W_{kl}\eta_k\eta_l\right) + f_e$ | 2D DRX |
| [Takaki et al. 2007] [Takaki et al. 2010] | $\sum_{k=1}^{N_p}\sum_{l>k}^{N_p}\left(-\frac{a_{kl}^2}{2}\nabla\eta_k\nabla\eta_l + W_{kl}\eta_k\eta_l\right)$ | 2D SRX |
| [Darvishi Kamachali et al. 2012] | $\sum_{k=1}^{N_p}\sum_{l>k}^{N_p}\left(\frac{4\gamma_{kl}}{\epsilon}\left\{-\frac{\epsilon^2}{\pi^2}\nabla\eta_l\nabla\eta_l + \eta_k\eta_l\right\}\right)$ | 3D normal GG |
| [Jin et al. 2015] | $\sum_{k=1}^{N_p}\sum_{l>k}^{N_p}\left(-\frac{\varepsilon_{kl}}{2}\nabla\eta_k\nabla\eta_l + w_{kl}\lvert\eta_k\rvert\lvert\eta_l\rvert\right)$ | 2D anisotropic GG |

**Table 1.4** – Few expressions of the local energy density $\hat{f}$ reported in the literature. We refer the interested reader to the related papers for more details.

CPF and MPF models are confronted in [Moelans et al. 2009] and it is demonstrated that the two formulations can predict the same steady-state microstructure, but with different kinetics. Especially authors point out the influence of the non-unique formu-

lation concerning the local free-energy density. This is obviously problematic when it comes to model real industrial processes, because many metallurgical phenomena can be involved successively or simultaneously, and the material may never achieve a steady-state. So predicting also the transient stage of microstructure evolutions is crucial for industrial applications. However, the PF method relies on strong thermodynamical foundations, making it an attractive technique. Interesting couplings with Crystal Plasticity have been proposed recently to model DRX [Zhao et al. 2016] and SRX [Chen et al. 2015] in 3D. Also it is worth mention the commercial software MICRESS® (http://web.micress.de/).

The presence of SPPs can be implemented in PF models by introducing an additional space-dependent energy term in the total free energy of the system [Moelans et al. 2005]. This additional energy term is built so that the energy difference induced by a particle placed on a grain boundary is equal to the intersection area multiplied by the surface tension. For a spherical particle that is "cut" in half by a grain boundary, the energy difference is then $\pi r^2 \gamma$. Several 3D PF simulations of ZP [Suwa et al. 2006; Vanherpe et al. 2010] yielded values for $m$ in eq. (1.25) close to unity, in accordance both with the original model of Zener & Smith and with MC/Vertex simulations. On the contrary, the values for the coefficient $K$ are more scattered, even though the order of magnitude remains the same. The effect of spheroid secondary-phase particles characterized by different aspect ratios and sizes [Vanherpe et al. 2010; Chang et al. 2009], and of cylindrical particles [Schwarze et al. 2016] have been also studied. Results show that, for the same volume fraction of particles, smaller particles are more effective in pinning grain boundaries. Moreover needle-shape particles have a stronger pinning effect than spherical ones, even though the difference remains quite limited. However these approaches rely on different assumptions in order to estimate the dragging force exerted by each particle as a function of its geometry. This approach is possible for simple analytical geometries of particles, but much more complex for particles with complex shapes, such as these present in real materials. To our knowledge there is no PF formulation able to tackle real-shape particles for the time being. Very recently a first PF approach to model the 2D interaction between a single grain boundary and an evolving particle has been proposed [Chang et al. 2015] and has shown very promising results. This model has not yet been extended in 3D for the time being.

The last major full field approach for modeling GG and ReX is the so-called LS method. As detailed in the first chapter, this approach can be used in the context of uniform grids with a finite-difference scheme or Fourier transform resolution, or within a FE

framework. The FE-LS modeling of microstructural evolutions is a very exciting research topic due to the possibility to simulate many physical phenomena (particle pinning, annealing twin development, solute drag, CPFEM and field dislocation mechanics,...). So the LS-FE approach presents very appreciable features, making it a logical technical choice for the DIGIMU® software. However, as for the PF approach, the numerical cost of LS-FE remains its main drawback, explaining why it was hardly used in 3D up to now. Our main objective in this thesis work is to make this approach much more numerically efficient in order to allow this transition from 2D to 3D. We present the approach and its related limitations in the next section.

## 1.5 The level set approach, state of the art concerning the modeling of polycrystals

The LS method is a front-capturing approach introduced by Osher and Sethian in 1988 [Osher et al. 1988], which allows to represent implicitly an (*or* a set of) object(s) and to describe its (their) evolution(s) inside a simulation domain $\Omega$. In that sense, the LS method is relatively similar to the PF field approach. Here, signed distance functions, also called LS functions, are employed to represent the interfaces instead of the PF functions. A LS function $\psi$ returns the standard Euclidean distance to the boundary $\Gamma$ of a sub-domain $\Sigma \in \Omega$, and generally a sign convention is assumed:

$$\forall t \begin{cases} \psi(x,t) = d(x,\Gamma(t)) \text{ for } X \in \Sigma \\ \psi(x,t) = -d(x,\Gamma(t)) \text{ for } X \notin \Sigma \\ \Gamma(t) = \left\{X \in \Omega, \psi(x,t) = 0\right\}, \end{cases} \tag{1.35}$$

where $d(X,\Gamma(t))$ corresponds to the Euclidean distance between a point $X \in \Omega$ with spatial coordinates $x$ and the interface $\Gamma$ of $\Sigma$. The sub-domain $\Sigma$ can be composed of one or several distinct *connected components*, as it will be presented later. Large multi-phase problems involve typically the definition of several sub-domains in the simulations. Hereafter we note $N_\mathrm{p}$ this number of sub-domains and $\psi_i$ the LS function that represents the $i^{th}$ sub-domain $\Sigma_i$, whose interface is denoted $\Gamma_i$ (with $i \in \{1,...,N_\mathrm{p}\}$). The first step of a LS simulation is to initialize the LS functions as a distance function to the object interface, represented by its zero-isovalue. For this purpose the value of each LS function is estimated at a certain number of points located inside $\Omega$. These points can be simply the grid points if regular Cartesian grids are used for the computations, or more generally the interpolation points of the mesh when the work is done within a FE framework. We detail the possible approaches to initialize the LS functions in the next section.

### 1.5.1 Generation and immersion of virtual polycrystals within unstructured finite element meshes

#### Basics about immersion

The term *polycrystal immersion* refers to the creation of a virtual representation of a microstructure that can be used to describe its evolution. This virtual polycrystal is generally referred as *fictive* when the shapes, sizes and positions of the grains are determined by the computer at the start of the simulation, while it is simply designated as *real* when it is obtained from an experimental image.

After generating a fictive or real polycrystal, this has to be linked with the FE mesh. In the context of unstructured meshes, as used in this work, different methods can be found in the literature. The most widely-used method, illustrated on fig. 1.10, consists in creating a surface mesh for each grain (coincident with the neighboring grain) and then generating a volume mesh based on these surface meshes [Rollett et al. 2004; Delannay et al. 2009; Quey et al. 2011; Dancette et al. 2016]

This approach wherein the mesh is coincident with the grain boundaries is well-suited for simulating the deformation of polycrystals. However when modeling ReX and GG, specific topological operations must be performed on the FE meshes to handle the shrinkage and nucleation events. This is exactly the same problem than for Vertex models. So using these approaches in the context of microstructural evolutions is not straightforward.

Front-capturing approaches such as the PF and LS methods avoid this problem of tracking the interfaces by using mathematical functions to represent implicitly the interfaces. However this approach requires to be able to initialize these mathematical fields (PF or LS functions) in such a way that they represent accurately the considered aggregate.

Using an experimental image as input, different techniques are possible to initialize the PF/LS fields. In [Zhao et al. 2016] the image is firstly interpolated on a homogeneous FE mesh. Then this mesh is refined in order to increase the precision at the interfaces. Finally the data from the experimental image are interpolated on the FE mesh and converted into LS functions by resolving a standard redistancing equation. In the third chapter, we will propose a new original approach, based on the development of Shakoor et al. [Shakoor et al. 2015a], that is able to tackle efficiently the

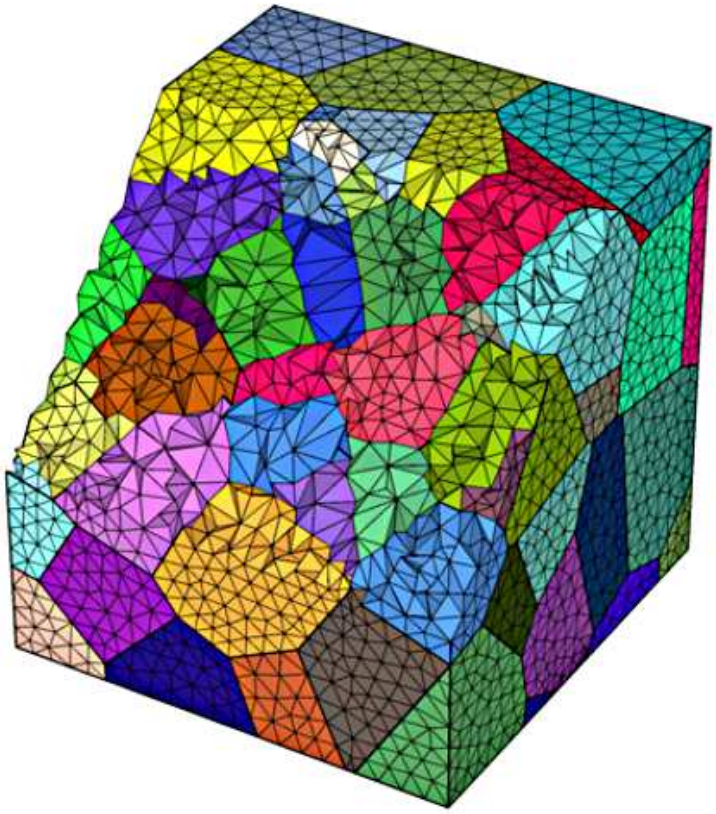

**Fig. 1.10** – FE mesh of a 100-grain polycrystal coincident with the grain boundaries [Quey et al. 2011].

immersion of real polycrystals in a LS-FE framework.

However, experimental data are not always available. Especially obtaining a 3D image of a microstructure requires specific numerical facilities. An alternative is to create a fictive polycrystal that obeys certain constraints, *e.g.* mean grain size, respect of a prescribed grain size or shape factor distribution and so on. This can be done by using specific generation techniques that will be described in the next section. Their main advantage is that they allow to modify easily the properties of the initial polycrystal. Also they do not require a lot of experimental data. Hereafter we present the principles of these approaches and how they can be used to immerse virtual polycrystals within FE meshes using the LS functions.

**Statistical generation of polycrystals and immersion**

A very popular technique for generating 2D/3D polycrystals is the *Voronoï tessellation* (VT) method [Wu et al. 2000; Bernacki et al. 2009; Quey et al. 2011; Hitti et al. 2012]. A Voronoï tesselation is fully described by a set of $N_v$ sites, noted $S_i$ with $i \in \{1,...,N_v\}$. Each nucleus $S_i$ defines a Voronoï cell $V_i$, which consists of all points closer to $S_i$ than to any other nucleus (see fig. 1.11):

$$V_i = \left\{ X \in \mathbb{R}^{d_s} / d(x,S_i) = \min_{1 \leq j \leq N_v} d(x,S_j) \right\}, \tag{1.36}$$

with $d_s$ the space dimension. From a mathematical point of view, the Voronoï diagram of a set of points is dual to its Delaunay triangulation. We note Graph($S_i$) the sites that are connected to $S_i$ in the underlying Delaunay triangulation.

Voronoï sites are generally picked randomly in the domain, which makes the VT extremely fast and simple to implement. The number of sites and the domain dimensions determine directly the mean grain size. On the other hand, this method does not allow to obey a given grain size distribution. A possible alternative is the Laguerre-Voronoï tesselation (LVT) method [Telley et al. 1996; Fan et al. 2004; Quey et al. 2011; Hitti et al. 2012; Wejrzanowski et al. 2013; Randrianalisoa et al. 2015] wherein a weight $W_i$ is also affected to each site. Here each Laguerre-Voronoï cell $L_i$ is defined by a pair $(S_i, W_i)$:

$$L_i = \left\{ X \in \mathbb{R}^{d_s} / \Pi(x,S_i) = \min_{1 \leq j \leq N_v} \Pi(x,S_j) \right\}, \text{ where } \Pi(x,S_i) = d(x,S_i)^2 - W_i^2. \tag{1.37}$$

A possible option to determine the cell weights consists in generating a dense sphere

packing with highest possible density which obeys the prescribed grain size distribution [Fan et al. 2004; Hitti et al. 2012]. Then the weight $W_i$ of the $i^{th}$ site can be seen as the radius of the corresponding sphere. But creating a dense packing is not straightforward, especially in 3D. A review of the existing methods and those implemented in the Cimlib library can be found in [Hitti 2011; Hitti et al. 2012].

A great advantage of the VT and LVT techniques is that they permit to immerse easily the generated aggregates using LS functions. Especially the LS function $\psi_i$ defining the $i^{th}$ Voronoï/Laguerre cell is given by:

$$\psi_i(x) = \min_{j \in \text{Graph}(S_i)} \left(\alpha_{ij}(x)\right), \ \forall i \in \{1, ..., N_\text{v}\}. \tag{1.38}$$

In the VT method, $\alpha_{ij}$ is the signed distance between a point $X \in \Omega$ and the perpendicular bisector of $[S_i S_j]$:

$$\alpha_{ij}(x) = \frac{1}{2}\|\overrightarrow{S_i S_j}\| - \frac{\overrightarrow{S_i S_j} \cdot \overrightarrow{S_i X}}{\|\overrightarrow{S_i S_j}\|}. \tag{1.39}$$

This function $\alpha_{ij}$ adopts a different form in the LVT method because the cells are weighted:

$$\alpha_{ij}(x) = \frac{1}{2}\left(\|\overrightarrow{S_i S_j}\| + \frac{W_i^2 - W_j^2}{\|\overrightarrow{S_i S_j}\|}\right) - \frac{\overrightarrow{S_i S_j} \cdot \overrightarrow{S_i X}}{\|\overrightarrow{S_i S_j}\|}. \tag{1.40}$$

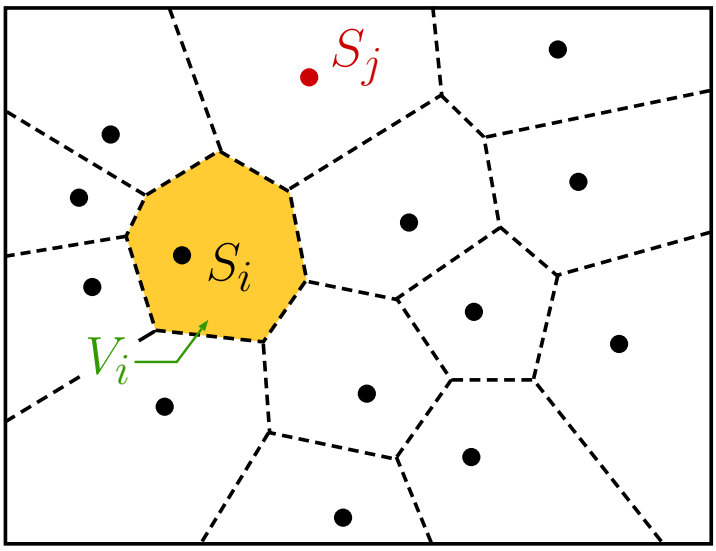


**Fig. 1.11** – A Voronoï tesselation in 2D.

In such a *monolithic* framework wherein all the phases are immersed in the same mesh, it can be useful to achieve a better precision at the interfaces. Especially we know that the velocity of the grain boundaries depends on their morphology (see eq. (1.4)). Thus achieving a correct description of the interfaces is crucial for capturing the interface kinetics. A first approach is to increase the interpolation degree. An alternative consists in adapting the spatial discretization. The simplest way is to refine homogeneously the mesh size to achieve a better description of the interface geometry (see fig. 1.12a and fig. 1.12b). But homogeneous refinement increases significantly the number of degrees of freedom (DOF) and then the numerical cost. *Local refinement* is a classical alternative, which consists in using a fine mesh size $h_n$ inside a layer $\pm E$ around the interface and a coarse mesh size $h_b$ elsewhere (see fig. 1.12c). This approach can be further optimized by employing anisotropic elements in the refined zone. This strategy of local refinement is generally more simple than using non constant order interpolation. Of course both techniques could be coupled. In this work, a constant P1 formulation is adopted with a meshing/remeshing strategy. In our GG/ReX context where grain boundaries migrate normally, the normal direction to the interface needs to be finely discretized. In other directions, the mesh can be stretched with coarse mesh sizes $h_t$, dependent of the corresponding local curvature, as illustrated on fig. 1.12d. Thus less elements and DOF are needed.

But anisotropic meshes are also more complex to generate because it requires a full control of the shape, size, stretching factor and orientation of elements. Different approaches exist, although they are generally based on local modifications of an existing mesh. Creating anisotropic meshes mainly requires to extend the way we measure lengths following the space directions. This can be done by using a *metric field* to redefine the geometric distances. Then the FE mesh is adapted according to this metric field and a mesh quality criterion. Hereafter we define the quality of a mesh element as the normalized ratio of its volume (respectively area in 2D) and perimeter squared. This indicator is equal to unity when the simplicial mesh element is a regular tetrahedron (respectively an equilateral triangle in 2D) in the considered metric field [Coupez 2011] and equal to zero for a ill-shaped tetrahedron. In this study we use the topological mesher/remesher Fitz [Shakoor et al. 2015a] to perform the mesh adaptation. This uses a nodal metric map as input which is motivated by the fact that elements are much more versatile than the nodes, and therefore defining fields on a continuous basis ease their reconstruction, interpolation and extrapolation [Coupez 2011].

A metric $\mathbb{M}$ is a real, symmetrical, positive definite $d_s \times d_s$ matrix (we recall that $d_s$

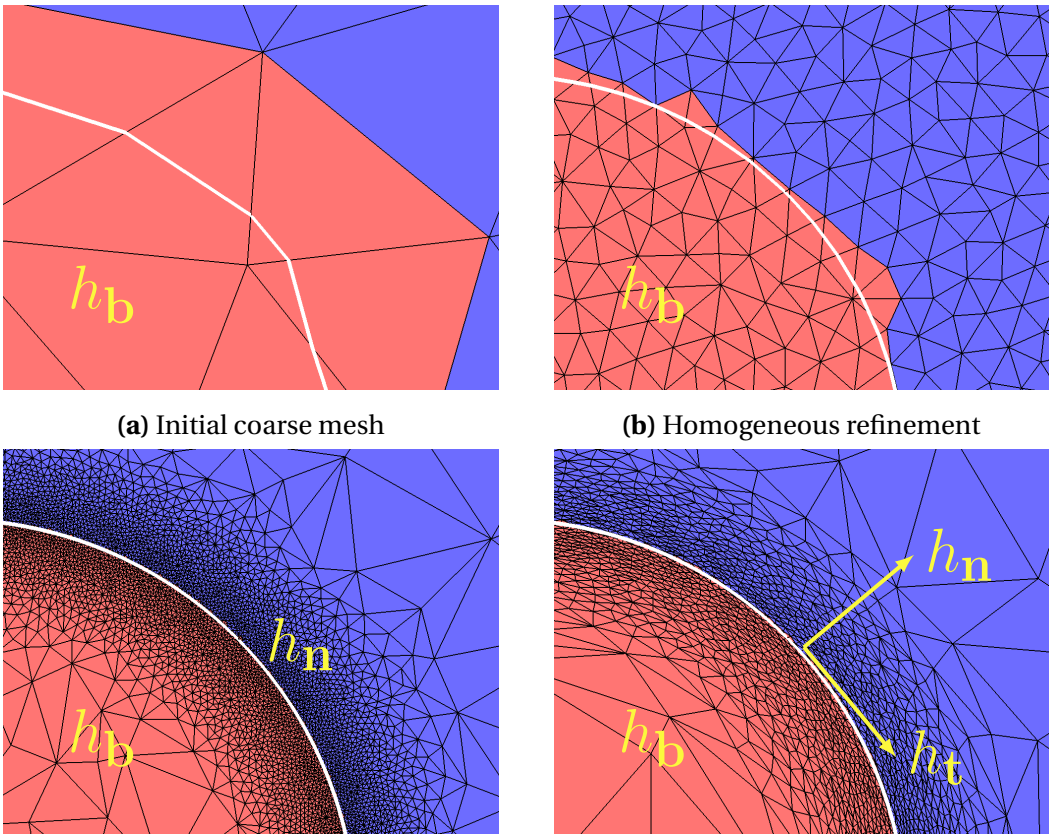


**(a)** Initial coarse mesh

**(b)** Homogeneous refinement

**(c)** Local mesh adaptation (isotropic)

**(d)** Locally mesh adaptation (anisotropic)

**Fig. 1.12** – Isotropic and anisotropic FE meshes at the interface of a spherical grain (represented by a solid white line). Elements having at least one node inside the grain are depicted in red.

is the space dimension). Since it is symmetrical, $\mathbb{M}$ can be diagonalized, and its positive definite nature ensures that the eigenvalues are strictly positive. Thus $\mathbb{M}$ can be decomposed as:

$$\mathbb{M} = R_{\mathrm{t}} \begin{bmatrix} \frac{1}{h_1^2} & & 0 \\ & \ddots & \\ 0 & & \frac{1}{h_d^2} \end{bmatrix} R_{\mathrm{t}}^{\top}, \tag{1.41}$$

where $R_{\mathrm{t}}$ is a rotation matrix whose columns are the eigenvectors of $\mathbb{M}$ and $\left(h_i^{-2}\right)_{1\leq i\leq d}$ are the corresponding eigenvalues. The $h_i$ are the mesh sizes in the basis directions defined by the eigenvectors of $\mathbb{M}$.

The metric field can be constructed manually by specifying directly the directions of refinement, and one or all the associated mesh sizes. In [Bernacki et al. 2009], an approach able to deal with multiple LS functions is proposed in the context of polycrystalline aggregates. Basically the procedure gives a metric field that is a function of the distance to the grain boundary and of the multiple junctions. More specifically, fine and possibly anisotropic mesh sizes are employed near the standard grain boundaries (*i.e.* interfaces separating two adjacent grains) and a coarse mesh size is used in the grain interior. At multiple junctions the interface is irregular. So there is no well-defined normal and tangential directions in these regions, and a fine isotropic mesh size is therefore employed in these regions. In this study the mesh size used for each direction is directly specified by the user. So all the interfaces are identically discretized in all the space directions. Figure 1.13a illustrates a part of a 2D polycrystal ($\langle R\rangle = 72\mu$m) and the related FE mesh obtained with this remeshing strategy [Resk et al. 2009]. Here the overall mesh is composed of 164,000 triangles, the thickness of the refined layer is $E = 40\mu$m and the mesh sizes are $h_{\mathrm{n}} = 2\mu$m and $h_{\mathrm{t}} = h_{\mathrm{b}} = 10\mu$m.

When the interface flow is dictated by curvature, as it is the case during normal GG, it can be useful to refine the mesh only in the regions of high interface curvature in order to save computation time. A possible approach is to define the tangential mesh sizes as a function of the local corresponding curvature. This approach, used in [Quan et al. 2014], has been proven to provide optimal convergence rates.

The main limitation of these approaches, referred to as *a priori*, is that the number of elements used in the simulation is a direct function of the interface length and cannot be easily anticipated. This can dramatically increase the computation time if

inappropriate mesh sizes are specified by the user.

The second method consists in performing an error analysis in order to create an "ideal" mesh, *i.e.* which minimizes a given error (typically the discretization error) according to a physical field $\omega$ and/or a given number of elements (or a a given precision). Here the mesh size map is directly given by the error estimator, which allocates the numerical resources preferentially in the areas and space directions that exhibit the sharpest gradients $\nabla\omega$. An important number of approaches have been proposed in recent years and we refer the interested reader to [Almeida et al. 2000; Boussetta et al. 2006; Coupez 2011; Bois et al. 2012; Rabizadeh et al. 2016] for further details. In this work we focus more precisely on the error estimator of [Almeida et al. 2000; Mesri et al. 2008], which is implemented in our FE library and allows to generate anisotropic FE meshes according to a given number of elements.

We need firstly to create a field that will support the mesh adaptation. Providing that our objective is to refine the mesh in the grain boundary area extending perpendicularly to the interfaces, the field $\omega$ can be simply defined as the global unsigned distance function of the aggregate:

$$\omega(x) = \max_{1\leq i\leq N_\mathrm{p}} \psi_i(x), \tag{1.42}$$

As this field has a discontinuity at $\omega = 0$ and is therefore not differentiable, it is firstly filtered by using a classical sinusoidal filter:

$$\omega^s(x) = \begin{cases} 0 & \text{for } \omega(x) < -E \\ 0.5\left(1 + \dfrac{\omega}{E} + \dfrac{1}{\pi}\sin\left(\pi\dfrac{\omega}{E}\right)\right) & \text{for } \|\omega(x)\| \leq E \\ 1 & \text{for } \omega(x) > E. \end{cases} \tag{1.43}$$

Contrary to $\omega$, the filtered field $\omega^s$ is smooth and can be differentiate anywhere. We use its gradient $\nabla\omega^s$ as input in the error estimator in order to compute the metric field needed for mesh adaptation. Hereafter this strategy is employed in all the simulations that use local remeshing. Figure 1.13b depicts the FE mesh obtained with this *a posteriori* method for the 2D polycrystal of fig. 1.13a. The target number of elements is set to 150,000 and $E = 5\mu$m. Based on these information and $\nabla\omega^s$, the mesh sizes in the different space directions and the related metric field are directly determined by the error estimator.

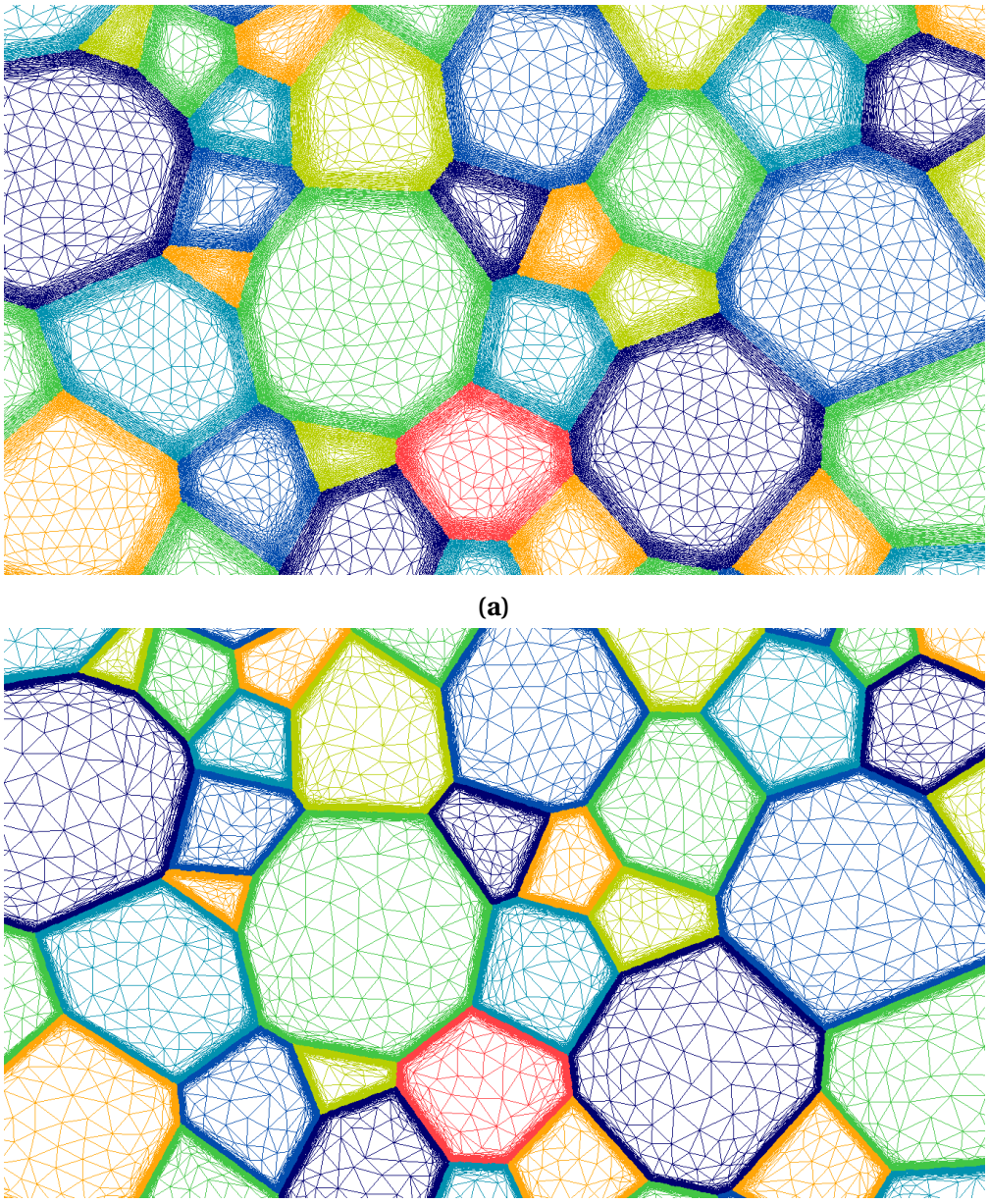

**(a)**

**(b)**

**Fig. 1.13** – Anisotropic FE meshes of a 2D polycrystal obtained through: (a) an *a priori* technique [Bernacki et al. 2009] with $E = 40\mu$m, $h_n = 2\mu$m and $h_t = h_b = 10\mu$m; (b) an *a posteriori* technique [Mesri et al. 2008] with $E = 5\mu$m and a constrained number of elements (150,000).

### 1.5.2 Migration of the grain boundaries

After initializing the distance functions and adapting the initial FE mesh, interfaces can be displaced according to a given velocity field $\vec{v}_i$ by solving a set of transport PDEs:

$$\begin{cases} \dfrac{\partial \psi_i(x,t)}{\partial t} + \vec{v}_i \cdot \nabla \psi_i = 0 \\ \psi_i(x, t=0) = \psi_i^0(x) \end{cases} \quad \forall i \in \{1, ..., N_p\}, \tag{1.44}$$

where $\psi_i^0$ is the initial value of $\psi_i$. In the considered LS framework, the terms $\vec{n}$ and $\kappa$, present in eq. (1.4), can be rewritten as follows:

$$\vec{n}_i = \frac{\nabla \psi_i}{\|\nabla \psi_i\|} \text{ and } \kappa_i = -\nabla \cdot \vec{n}_i, \tag{1.45}$$

where $\nabla\cdot$ corresponds to the divergence operator. By combining eq. (1.4), eq. (1.44) and eq. (1.45), one obtains a set of convective equations which describe the microstructure evolutions in the context of uniform grain boundary mobility and energy:

$$\begin{cases} \dfrac{\partial \psi_i(x,t)}{\partial t} - M\gamma \nabla \cdot \left( \dfrac{\nabla \psi_i}{\|\nabla \psi_i\|} \right) \dfrac{\nabla \psi_i}{\|\nabla \psi_i\|} \nabla \psi_i + \vec{v}_i^{\,e} \cdot \nabla \psi_i = 0 \\ \psi_i(x, t=0) = \psi_i^0(x) \end{cases} \quad \forall i \in \{1, ..., N_p\}, \tag{1.46}$$

If the LS functions satisfy the metric property $\|\nabla \psi_i\| = 1$ at least in a thin layer $\pm\varepsilon$ around the interface, eq. (1.46) boils down to a system of convective-diffusive equations (CDEs):

$$\begin{cases} \dfrac{\partial \psi_i(x,t)}{\partial t} - M\gamma \Delta \psi_i + \vec{v}_i^{\,e} \cdot \nabla \psi_i = 0 \\ \psi_i(x, t=0) = \psi_i^0(x) \end{cases} \quad \forall i \in \{1, ..., N_p\}, \tag{1.47}$$

We interest specifically to the term $\vec{v}_i^{\,e}$ in the fourth chapter of this manuscript. In the case of GG without stored energy (*i.e.* $\vec{v}_i^{\,e} = \vec{0} \ \ \forall i$), eq. (1.47) boils down to:

$$\begin{cases} \dfrac{\partial \psi_i(x,t)}{\partial t} - M\gamma \Delta \psi_i = 0 \\ \psi_i(x, t=0) = \psi_i^0(x) \end{cases} \quad \forall i \in \{1, ..., N_p\}, \tag{1.48}$$

In [Elsey et al. 2009; Elsey et al. 2011; Elsey et al. 2013; Mießen et al. 2015], eq. (1.47) or eq. (1.48) is solved by using a spectral method relying on Fourier transforms in the context of regular Cartesian grids. This approach has been proven extremely effective

numerically and provides very good results. However, as exposed in the introduction chapter, using regular grids presents severe limitations related to the difficulty to model the polycrystal deformation. Let us remember that our main objective is to develop a robust approach able to tackle both the problem of the polycrystal deformation and the microstructural evolutions in a unified numerical framework. For this reason, eq. (1.47) is here solved by applying a FE method, which is effectively slower than spectral methods, but also more versatile and robust in the context of large deformations. More precisely we use an implicit P1 solver with Streamline Upwinding Petrov-Garlerkin (SUPG) method for the stabilization, and the Generalized Minimal Residual Method (GMRES) for the numerical resolution of the linear system of equations. This GMRES method is referred as *iterative* because it requires a certain number of *iterations* to find a satisfactory solution of the FE problem defined by eq. (1.47) without computing the inverse matrix.

LS functions that become negative everywhere in $\Omega$ after resolving eq. (1.47) are deactivated and are no longer considered in the simulation. Hereafter we omit systematically the physical time variable $t$ in the notations although it is obvious that all considered quantities are (or can be seen as) time-dependent.

Concerning the boundary conditions, a common choice adopted in the literature for such problems consists in applying periodic BCs at the surface of the simulation domain $\partial\Omega$. This approach is straightforward to implement in the context of Cartesian grids because regular meshes are naturally periodic. On the other hand unstructured FE meshes such as employed in our approach do not satisfy any property of symmetry which makes them poorly compatible with periodic BCs. So we apply the following Neumann boundary condition:

$$\nabla\psi_i \vec{s} = \sin(\theta) \; \forall x \in \partial\Omega, \tag{1.49}$$

where $\vec{s}$ is the unit outward vector normal to $\partial\Omega$ and $\theta$ is the interaction angle between the grain boundaries and $\partial\Omega$. Hereafter it is fixed $\theta = 90°$ which corresponds to null Neumann BCs. Obviously this alters the topology and the kinetics of the grains which interact with $\partial\Omega$. Consequently the REVs employed in the simulations need to be large enough (*i.e.* with a sufficient initial number of grains) in order to be statistically representative and limit the influence of domain-size effects.

Due to numerical diffusion and the theoretically infinite curvature of the grain boundaries at multiple junctions, the resolution of eq. (1.47) may introduce kinematic in-

compatibilities between the LS functions. It can be either a node where more than one function is positive (overlap) or, on the contrary, a node where all functions are negative (vacuum). A specific strategy to deal with these kinetic incompatibilities relying on mesh adaptation can be found in [Hallberg et al. 2013]. This approach is based on an explicit representation of the multiple junctions through the FE mesh. An alternative consists in applying the following treatment [Merriman et al. 1994]:

$$\tilde{\psi}_i(x) = \frac{1}{2}\left(\psi_i(x) - \max_{j\neq i}\left(\psi_j(x)\right)\right), \tag{1.50}$$

which is valid in the context of isotropic grain boundary mobility and energy. But this treatment alters strongly the distance functions near the zero-isovalue, where their profiles become very sharp. This is particularly problematic when a specific remeshing technique depending on the distance property is used at the interface [Quan et al. 2014]. In addition, the diffusive formulation introduced in eq. (1.47) is valid only if the function $\psi_i$ is a distance function, at least in a thin layer $\pm\varepsilon$ around the interface [Bernacki et al. 2008; Cruz-Fabiano et al. 2014]. Finally, the condition number associated with our weak formulation (P1 interpolation, implicit method) depends largely on the regularity of the LS function [Shakoor et al. 2015b]. This condition number determines how much the results can change for a small variation of the input function. A FE problem is said *well-conditioned* if the condition number is low. So the LS functions used as input in eq. (1.47) must be regular enough to ensure this property.

This process of regularization of the distance function is called *reinitialization*. Given a LS function $\psi^0$, the reinitialization process finds the signed distance function $\psi$ to the interface $\Gamma^0$ of $\psi^0$, which is the viscosity solution of the following Eikonal equation [Crandall et al. 1984; Min 2010]:

$$\begin{cases} \|\nabla\psi(x)\| = 1 \\ \mathrm{sgn}(\psi) = \mathrm{sgn}(\psi^0), \end{cases} \tag{1.51}$$

where sgn denotes the sign value, taking either 1 (for $\psi^0 > 0$), -1 (for $\psi^0 < 0$), or 0 (at the interface $\Gamma^0$).

Several methods exist to restore the metric property of a distance function. They will be detailed in the second chapter of the manuscript dedicated to this topic. Here the well-known Hamilton-Jacobi (HJ) approach was used at the beginning of this work [Bernacki et al. 2011; Cruz-Fabiano et al. 2014; Agnoli et al. 2014].

We introduce the notation $N_g$ to designate the number of grains present into the

microstructure. As mentioned above, a possible modeling approach consists in representing each grain by a LS function, which leads to $N_\mathrm{p} = N_\mathrm{g}$. But the numerical costs associated with the resolution of the CDEs (see eq. (1.47)) and reinitialization is strongly related to $N_\mathrm{p}$. Then this first approach is impracticable for large-scale 3D simulations, both from the standpoint of computing time as well as the amount of memory needed to store so many floating-point values [Krill III et al. 2002]. An alternative is the use of a *coloring* technique. Thus several distinct grains of the initial microstructure can be grouped to form Global Level Set (GLS) functions. For convenience two grains represented by the same GLS function are denoted as *child grains* hereafter. In the same manner, a grain is referred as *exterior to i* if it is not represented by $\psi_i$. By employing a coloring technique, as it is done in [Hitti 2011; Cruz-Fabiano et al. 2014], the number of needed functions can be drastically reduced $N_p \ll N_g$. Especially in 2D, the *four color theorem* states than any planar map (which includes obviously 2D microstructures) is four colorable [Appel et al. 1977a; Appel et al. 1977b]. An example is depicted on fig. 1.14a wherein a microstructure of 25 grains is represented by only four colors (*i.e.* GLS functions). However, with coloring the child grains can no longer be distinguished and it is impossible to reach directly the properties of individual grains, like the grain size. But worst still is the possibility of *numerical coalescence* between child grains meeting each other, as illustrated on fig. 1.14b. Obviously, the smaller the number of GLS functions, the more often coalescence will occur, with potentially dramatic consequences for the grain topology and rate of growth of the average grain size [Krill III et al. 2002]. This point was especially verified by Fan et al. [Fan et al. 1997b] in the context of 2D PF simulations of GG. The strategy employed in [Fabiano 2013] is to delay coalescence by using a number of functions $N_\mathrm{p}^\delta$ which guarantee a minimal separation of $\delta$ exterior grains between the child grains in the initial microstructure. Obviously the greater the initial separation, the greater the number of GLS functions and the computation time. So $\delta$ must be chosen small enough to limit the computation time and sufficiently high to prevent a significant amount of coalescence. Determining an adequate value for $\delta$ becomes almost impossible to solve when it comes to simulate complex and coupled metallurgical phenomena (GG, ReX with nucleation, possible particle pinning,...). Furthermore this strategy imposes to use a number of functions which is still much greater than the minimal number of colors really needed to represent the microstructure, making it a non-optimized numerical solution in any cases. Ideally the microstructure should be initialized with a strict minimal of colors and then recoloring should be performed automatically during the simulation everytime a risk of coalescence is detected. This strategy has already been discussed in the context of regular grids [Krill III et al. 2002; Elsey et al. 2009]. But its extension to a parallel

framework using non uniform FE meshes is not straightforward. This point is further discussed in the third chapter.

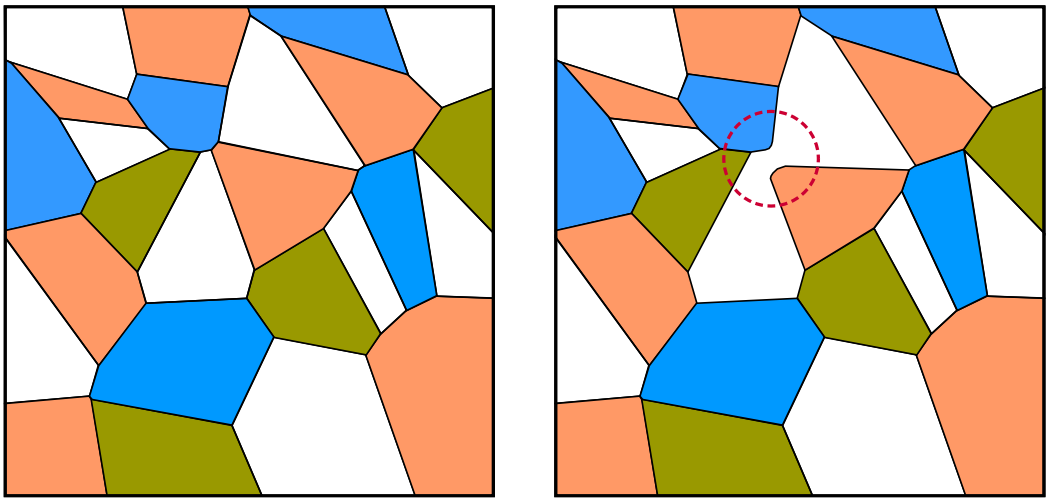

**(a)** **(b)**

**Fig. 1.14** – (a) 2D polycrystal composed of 25 grains and represented by four colors; (b) illustration of numerical coalescence between two (white) child grains.

Finally we summarize below the global algorithm for a LS simulation of SRX or GG:

1. initialize the distance functions according to a VT method, a LVT method, or based on an experimental image,
2. adapt the initial FE mesh (homogeneous or local refinement can be employed),
3. compute $\vec{v}_i^{\,e}$ (only for SRX simulations),
4. solve eq. (1.47) (SRX) or eq. (1.48) (GG) for all active GLS functions,
5. deactivate the GLS functions which are negative everywhere,
6. remove kinematic incompatibilities by performing the treatment given by eq. (1.50),
7. reinitialize the GLS functions,
8. adapt the mesh around the new interfaces (if local refinement has been chosen),
9. loop to (3) until the end of the simulation.

Recent extension of this framework to deal with DRX is still under development [Boulais-Sinou et al. 2016]. Then, the most advanced LS-FE framework to model GG/SRX has been described. Hereafter we interest to the limits of this numerical strategy.

### 1.5.3 Limitations of the existing implementation

Now the efficiency of the existing implementation is discussed through a simple GG benchmark in 2D. The simulation domain is a square with dimensions $9.2 \times 9.2\text{mm}^2$ wherein 5000 grains are generated through a VT technique, with respect to the grain size distribution measured experimentally in a 304L austenitic steel [Fabiano 2013] (see fig. 1.15).

The aggregate is submitted to a heat treatment of $t_\text{h} = 5\text{h}$ at $T = 1050°\text{C}$, which gives $M = 1.38 \times 10^{-12}\ \text{m}^4/\text{J/s}$ and $\gamma = 0.6\ \text{J/m}^2$ for the considered 304L material at this temperature [Cruz-Fabiano et al. 2014]. Local anisotropic mesh adaptation is preferred in order to achieve a precise description of the grain boundaries. The metric field is calculated *a posteriori* according to the error estimator of [Mesri et al. 2008], as discussed previously. The half thickness of the refined anisotropic layer around the interface is $E = 5\mu\text{m}$. The number of elements is around $1.5 \times 10^6$ and the time step is $\Delta t = 1\text{min}$. We set $\delta = 3$ according to [Cruz-Fabiano et al. 2014], which gives $N_\text{p}^{\delta=3} = 27$. Table 1.5 provides the distribution of the computation time obtained for this simulation using 6 Intel Xeon central processing units (CPUs). The respective contributions of the CDEs resolution (eq. (1.48)), of the HJ reinitialization described in the second chapter [Basset 2006], the mesh adaptation and the diverse post-treatment operations are noted $t_\text{resol}$, $t_\text{reinit}$, $t_\text{remesh}$ and $t_\text{other}$. Finally the global simulation time, noted $t_\text{simu}$, is the sum of the above contributions. To visualize the microstructure at a given time of the simulation, an output text file which contains the mesh and the field values needs to be created. Commonly in simulations an output file is generated every $t_\text{f}/3$ increments to limit the storage needs. The evolution of the aggregate during the treatment is depicted on fig. 1.16.

At the end of the treatment 24 GLS are still active. Almost 3 days of computations are needed for this simple 2D case (normal GG, 5h of heat treatment, 5000 initial grains), which is critically high. Especially the reinitialization step appears to be the bottleneck of the simulation because it demands almost 90% of the global computation time.

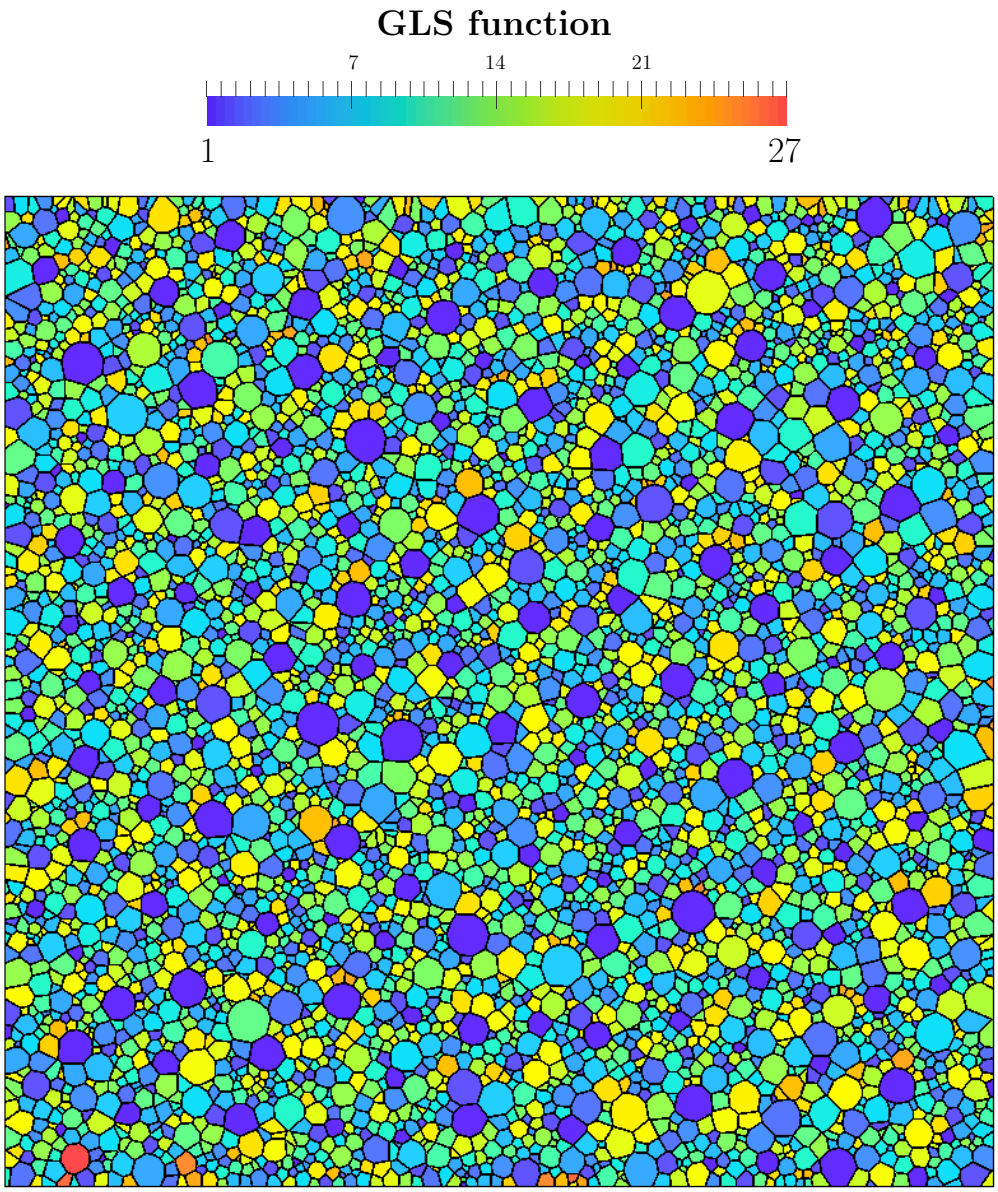


**Fig. 1.15** – 2D polycrystal containing 5000 grains, generated according to a LVT technique, and representative of a 304L austenitic steel. The color code refers to the index of the GLS functions.

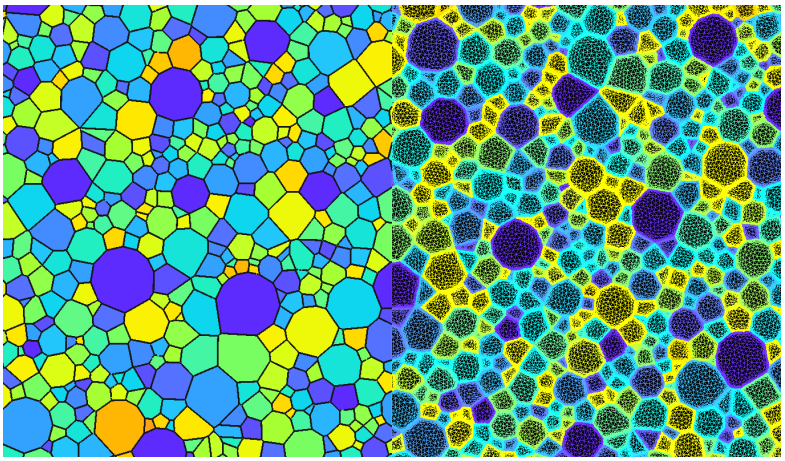

**(a)** $t = 0$ (5000 grains)

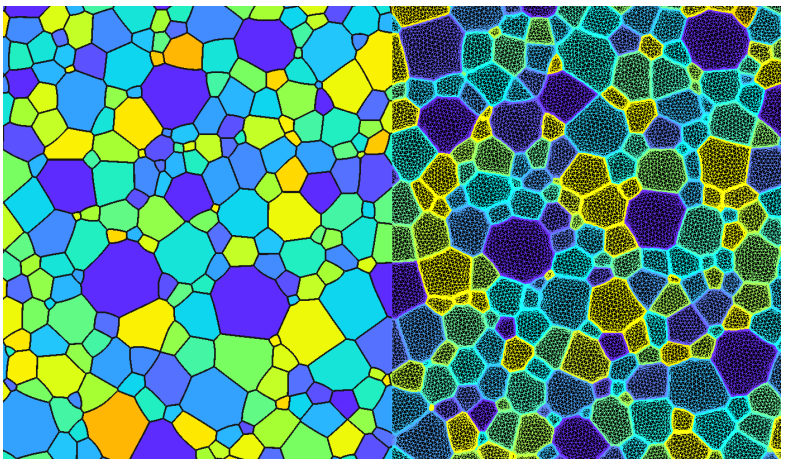

**(b)** $t = 1/2\,t_h$ (2900 grains)

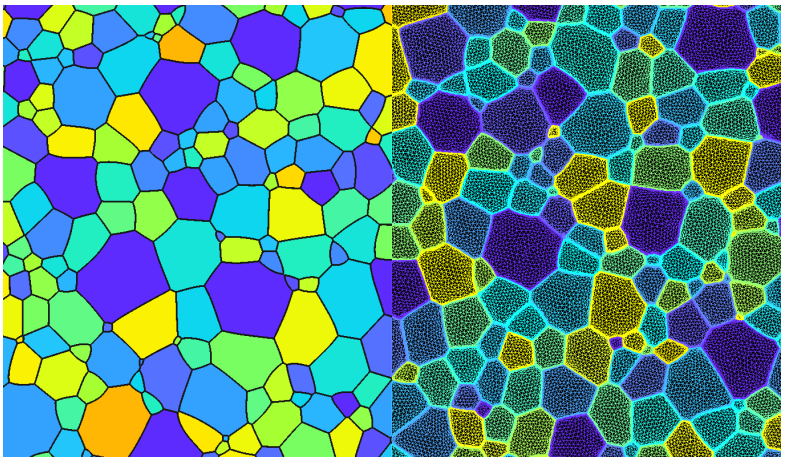

**(c)** $t = t_h$ (2100 grains)

**Fig. 1.16** – Zoom of the 2D microstructure at different stages of the heat treatment. The left side of the microstructure illustrates the grains and the right side depicts the corresponding FE mesh. The color code refers to the index of the GLS functions.

| | Existing implementation | |
|---|---|---|
| $t_{\text{remesh}}$ | 4h 11min | (6.4%) |
| $t_{\text{resol}}$ | 2h 02min | (3.1%) |
| $t_{\text{reinit}}$ | 59h 04min | (89.8%) |
| $t_{\text{other}}$ | 28min | (0.7%) |
| $t_{\text{simu}}$ | 65h 45min | |

**Table 1.5** – Distribution of the computation time for the 2D GG simulation of a 5h heat treatment at 1050°C, using the initial polycrystal of fig. 1.15 composed of 5000 grains. Simulation is performed on 6 Xeon Intel CPUs.

To summarize, the present FE-LS model has two main limitations. The former concerns the reinitialization method, which is extremely demanding in terms of computation resources and must be improved. Let us remind that this operation relies on the resolution of HJ equations for each distance function. The second limitation is related to the use of GLS functions which may introduce numerical coalescence and does not permit to assess the individual grain properties. The negative effects of numerical coalescence can be limited by employing more GLS functions but this approach is not optimal and increases the memory requirements. Also it is not systematic because the number of needed GLS functions can not be anticipated in any situations. We address these two limitations in the second and third chapters.

## Summary

In this chapter, the approaches devoted to the modeling of GG and ReX are covered. First of all, it is exposed that mean field models rely on a simplified description of the microstructure. Although they are fast and simple to implement, these homogenized models can not describe explicitly the interactions between the grains. Then full field models are introduced. These are based on a complete description of the polycrystal whose evolution is described by physical laws. Major full field approaches reported in the literature are discussed. A focus is placed on the LS approach. This approach has already been successfully employed to model GG and SRX, and is currently being extended to model also DRX. The main equations behind the LS method and the immersion of polycrystalline aggregates within FE meshes are detailed. A first 2D LS-FE simulation of GG is analyzed in order to highlight the limitations of the existing model implementation at the beginning of this thesis work. We interest to these limitations in the next chapters.

# Chapter 2

# Development of a new direct and parallel reinitialization method

## Contents


**2.1 Introduction . . . . . 69**

**2.2 A review of numerical methods for the reinitialization of level set functions . . . . . 69**

2.2.1 The Fast Marching Method . . . . . 69

2.2.2 The Hamilton-Jacobi equation . . . . . 70

2.2.3 Methods without reinitialization . . . . . 72

2.2.4 Geometric reconstruction of the distance functions . . . . . 73

2.2.5 Summary on existing reinitialization methods . . . . . 74

**2.3 Study of the Hamilton-Jacobi reinitialization within a continuous and linear finite element framework . . . . . 75**

2.3.1 Formulation of the used finite element method . . . . . 75

2.3.2 Study of the numerical parameters of the Hamilton-Jacobi approach for fixed mesh size . . . . . 77

**2.4 Development of a new reinitialization algorithm and comparison with other classical methods of the state of the art . . . . . 80**

2.4.1 To a direct reinitialization method . . . . . 80

2.4.2 Academic benchmark and comparison with other approaches 90

**2.5 Test on realistic metallurgical cases in two and three dimensions . 94**

## Résumé en français

Ce chapitre est consacré à la réinitialisation des fonctions distances. Le potentiel de la méthode de réinitialisation de type Hamilton-Jacobi dans le cadre de notre application est tout d'abord étudié. Il est démontré que cette méthode ne peut pas être améliorée sans modifications importantes du formalisme numérique. En outre, cette approche présente un défaut de robustesse et nécessite des paramètres numériques qui peuvent être difficile à calibrer. Ces limitations rendent la méthode Hamilton-Jacobi peu attrayante dans le cadre de la modélisation des évolutions microstructurales en trois dimensions avec un nombre représentatif de grains. Une nouvelle méthode de réinitialisation des fonctions distances est donc proposée et mise en œuvre dans notre modèle numérique level set/éléments finis. Celle-ci repose sur une discrétisation de l'interface et une reconstruction géométrique des fonctions distances. Elle bénéficie d'une implémentation numérique efficace reposant sur une stratégie de partitionnement de l'espace utilisant les arbres $k$-d, ainsi qu'une technique de boîtes englobantes assurant une grande efficacité numérique lors des calculs parallèles. L'algorithme a été testé avec succès et comparé à d'autres approches de réinitialisation de l'état de l'art. Des facteurs d'accélération allant jusqu'à 300 ont été obtenus par rapport à la méthode Hamilton-Jacobi. Il est également prouvé que le nouvel algorithme est beaucoup plus précis et robuste car il ne requiert aucun paramètre numérique. Enfin, cette nouvelle méthode de réinitialisation a permis d'accélérer certains cas de croissance de grains en deux dimensions par un facteur proche de 9, ainsi que d'effectuer une première simulation level set réaliste en trois dimensions avec des temps de calcul raisonnables. Ces développements ont permis la publication d'un article dans une revue internationale à comité de lecture [Shakoor et al. 2015b].

## 2.1 Introduction

In the first chapter, the reinitialization step during which the metric property of the LS functions is restored has been clearly designated as the bottleneck of this approach in 2D. This chapter aims to address this issue. First we propose a review of the state of the art concerning reinitialization methods. Their principles, advantages and limitations in the considered polycrystal context are thoroughly discussed. Then we propose a study of the HJ reinitialization method which was used in previous works at the CEMEF [Cruz-Fabiano et al. 2014; Agnoli et al. 2014; Jin et al. 2015]. Finally a new reinitialization algorithm is proposed and we detail its implementation within the present LS-FE framework. This algorithm is compared with the other methods implemented in our numerical library and demonstrates much higher numerical efficiency.

## 2.2 A review of numerical methods for the reinitialization of level set functions

Reinitialize a LS function is equivalent to find the viscosity solution of eq. (1.51). Hereafter we propose a comprehensive overview of the existing reinitialization methods.

### 2.2.1 The Fast Marching Method

The first option for reinitializing a LS function is to solve directly eq. (1.51) in a single pass, using the well-known Fast Marching Method (FMM). At the early stage, the algorithm fixes the values of a certain number of nodes, generally located in the vicinity of the interface. These nodes, referred to as the upwind nodes, are shown in black on fig. 2.1. Then a narrow band is constructed, which is composed of the downwind nodes located "close" from the upwind nodes. These are colored in grey on fig. 2.1. Then the method propagates the front from the upwind nodes by updating the values at the downwind nodes in order to ensure a gradient whose magnitude is unity. After the value of a downwind node has been updated, it swaps to a upwind node, and is next used to update the values of its neighbors, and so on. Nodes in the narrow band are visited in the order of causality to ensure consistency. The visiting order of causality is implemented by the Heap sorting algorithm. This approach was firstly formulated for regular Cartesian grids by Sethian [Sethian 1995] and used in this framework [Saye et al. 2012; Noumir et al. 2015; Treister et al. 2016; Weinbub et al. 2016]. The method has been also extended to unstructured meshes [Kimmel et al. 1998] and has

been used recently in [Gross et al. 2006; Lelièvre et al. 2011]. However its implementation becomes extremely complicated when it comes to consider anisotropic (*i.e.* obtuse) triangulations [Sethian et al. 2000] because it modifies the visiting order of causality. The implementation of a FMM-like algorithm [Elias et al. 2007] in our FE library has been attempted by Desmaison during its PhD work [Desmaison 2013] but with difficulties to exhibit a criterion for determining the visiting order of causality in the case of anisotropic FE meshes. A solution is to insert numerical supports for the obtuse triangles, but this makes the approach "cumbersome" according to [Sethian et al. 2000]. To our knowledge, this variant is not used in the recent literature. Another issue of the FMM approach is that is requires an *a priori* knowledge of the distance values at the nodes near the interface in order to initiate the front propagation. These values are used as reference and are no longer corrected during the algorithm. A common option is to use the algorithm developed by Chopp [Chopp 2001], which uses bicubic (tricubic in 3D) interpolations to accurately initialize the FMM. However, in our numerical framework where the treatment given by eq. (1.50) is performed after the solving of the CDEs, it cannot be predicted whether the nodal distance values near the interface are initially exact or no. So using this approach can compromise the values of the LS function at the interface. Finally the original FMM algorithm is inherently sequential and not well-suited with parallelization. So the algorithm needs to be performed several times on each partition in order to synchronize the values between the processors, which requires significant implementation efforts and gives modest parallel efficiency, even if recent works have significantly improve this situation [Weinbub et al. 2016]. These points make the FMM hardly compatible with our expectations.

### 2.2.2 The Hamilton-Jacobi equation

In most applications, the LS function at the current time step, obtained after solving eq. (1.44), is nearly a distance function if the function was properly reinitialized at the previous time step. For such cases there is more suitable equation for the reinitialization than the stationary eq. (1.51). Especially the time dependent Eikonal equation works very efficiently here:

$$\begin{cases} \dfrac{\partial \hat{\psi}(x,\tau)}{\partial \tau} = \operatorname{sgn}(\hat{\psi})\left(\|\nabla \hat{\psi}\| - 1\right) \\ \hat{\psi}(x,\tau=0) = \psi(x,t). \end{cases} \tag{2.1}$$

In this equation, $\tau$ designates a fictive time and $\hat{\psi}$ is the parameter function of the

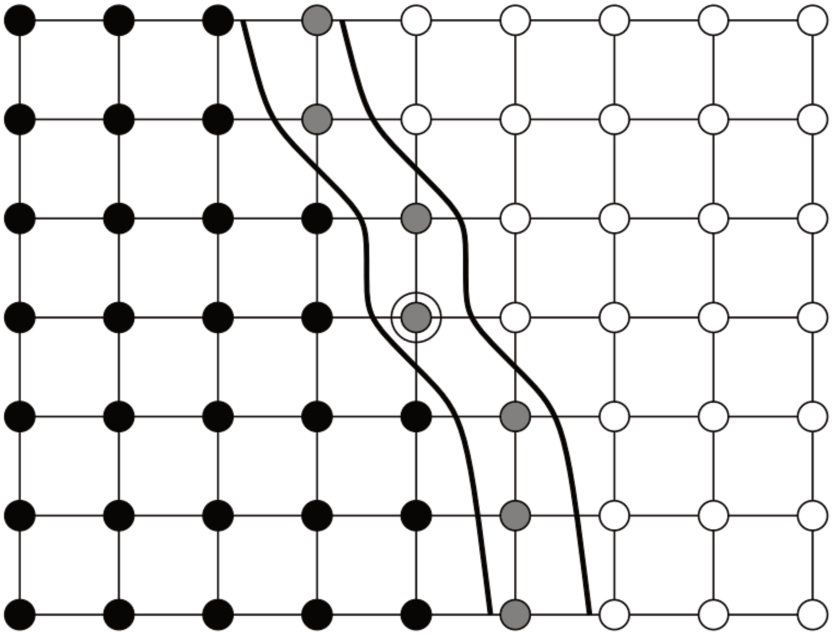

**Fig. 2.1** – Narrow band in the FFM on a 2D regular Cartesian grid whose nodes are represented by circles. Upwind nodes are shown in black and their values are blocked. Downwind nodes that are in the narrow band (colored in gray) are going to be updated.

HJ equation. Without the signum term sgn, eq. (2.1) is a Hamilton-Jacobi equation. As $\tau \to \infty$, the solution of this equation $\hat{\psi}$ converges to the signed distance function which has the same zero-isovalue than $\psi$ at the current time step.

A classical option to treat eq. (2.1) in a finite difference context is to discretize the equation with the Runge-Kutta (RK) method in time, and a Essentially Non-Oscillatory (ENO) [Osher et al. 1988; Osher et al. 1991] or Weighted Essentially Non-Oscillatory (WENO) [Jiang et al. 2000; Zhang et al. 2003] method in space [Min 2010]. The sign function sgn plays a very important role because it fixes the position of the interface. However its discontinuous nature invokes a lot of difficulties in the coupling between the second order RK and ENO schemes. In [Sussman et al. 1994] the sign function is smoothed around the interface to avoid this issue. However the artificial smearing moves the interface during the reinitialization which induces considerable volume loss. This was improved in [Sussman et al. 1999] by imposing the volume conservation in reinitialization to prevent artificial volume shrinking. Equation (2.1) can also be solve separately in the two regions defined by $\{\psi^0 > 0\}$ and $\{\psi^0 < 0\}$ using a subcell resolution technique [Harten 1989], so that it boils down to a classical HJ equation without any smoothing of the sign function [Cheng et al. 2008].

All the previous finite difference methods work efficiently on Cartesian grids, but lose the advantage of simplicity on unstructured FE meshes and are generally computationally inefficient [Abgrall 1996; Zhang et al. 2003; Cheng et al. 2014; Karakus et al. 2016]. Also treating directly eq. (2.1) in a FE framework is a complex task due to its non-linear form. Jensen et al. [Jensen et al. 2013] treated the problem as a second-order fully nonlinear equation by introducing artificial diffusion which activates in regions of degeneracy. Also recent works concerned by the FE resolution of eq. (2.1) paid more attention to the discontinuous Galerkin FE method [Hu et al. 1999; Li et al. 2005; Cheng et al. 2007; Yan et al. 2011; Chang et al. 2014; Karakus et al. 2016].

Finally the HJ equation can also be reformulated and treated directly as a purely convective linear equation in a continuous FE framework [Basset 2006]. This approach will be further detailed hereafter.

### 2.2.3 Methods without reinitialization

In the last decade, new LS models emerged wherein no reinitialization of the distance fields is needed. In these approaches, the transport is performed so that the LS functions remain distance functions. An example of variational formulation is described in [Li et al. 2005; Li et al. 2006] in which eq. (1.44) is modified to include a nonlinear term that penalizes the deviation of the LS function from the signed distance. The penalty term not only eliminates the need for reinitialization, it allows the use of a simpler and more efficient numerical scheme in the implementation than those used for conventional LS formulations. This model has been improved recently thanks to a more general formulation for the penalty coefficient in order to limit the tuning process [Touré et al. 2016]. Other works use a coupled formulation of eq. (1.44) and eq. (2.1) which enables to transport and reinitialize the LS functions simultaneously [Coupez 2007; Ville et al. 2011; Bernacki et al. 2008; Bernacki et al. 2009]. Especially in [Coupez 2007], the parameter $\lambda = d\tau/dt$ is introduced (in practice $\lambda \approx h/\Delta t$, with $h$ the local mesh size near the interface) to write the following equality:

$$\frac{\partial}{\partial \tau} = \frac{\partial t}{\partial \tau}\frac{\partial}{\partial t} + \frac{\partial x}{\partial \tau}\cdot\nabla = \frac{1}{\lambda}\left(\frac{\partial}{\partial t} + \vec{v}\cdot\nabla\right), \tag{2.2}$$

and to formulate the coupled convection-reinitialization (CR) problem:

$$\begin{cases} \dfrac{\partial \psi(x,t)}{\partial t} + \vec{w}\cdot\nabla\psi = \lambda \mathrm{sgn}(\psi) \\ \psi(x, t=0) = \psi^0(x) \end{cases} \quad \text{with } \vec{w} = \vec{v} + \lambda \mathrm{sgn}(\psi)\frac{\nabla\psi}{\|\nabla\psi\|}. \tag{2.3}$$

The main advantage of this approach compared to the HJ method is that only one solver is needed for the simulation. According to [Coupez 2007], the signed distance function can also be replaced by any smooth function which satisfies the metric property at least in a thin layer around the interface. Especially a hyperbolic tangent distance function $\tilde{\psi} = \varepsilon \tanh(\psi/\varepsilon)$ can be used advantageously. The CR methods using a classical distance function (CR-DF) and a hyperbolic tangent distance function (CR-HTDF) are both implemented within our FE library and will be considered hereafter. Although interesting these CR approaches have two main drawbacks in the considered context of microstructural evolutions. First the eq. (2.3) is purely convective, which implies that the grain boundary curvature must be explicitly computed through eq. (1.45) and can no longer be approximated with a diffusive formulation as it is done in eq. (1.47). Knowing that a linear approximation is used for the LS functions and that a P1 description of the curvature is required (since the velocity interpolation is P1), the direct use of eq. (1.4) (and then of eq. (2.3)) implies, *a priori*, two consecutive $P0 \rightarrow P1$ interpolations to estimate $\kappa$. This approach was proven poorly accurate in [Fabiano 2013]. The second issue is related to the treatment of the vacuums and overlaps, related to eq. (1.50), which is performed after the solving of eq. (1.47) and before reinitialization, according to the algorithm presented in chapter 1. If eq. (2.3) was used to transport the LS functions, it would then be necessary to perform eq. (1.50) to remove the eventual kinematic incompatibilities generated during the resolution, and finally to reinitialize again the LS functions because the previous treatment displaces the interfaces and distorts the distance fields [Bernacki et al. 2008]. This solution is therefore hardly applicable.

### 2.2.4 Geometric reconstruction of the distance functions

Finally, a natural way to reinitialize the distance functions consists in using a brute force algorithm to perform a complete reconstruction as it is done in [Merriman et al. 1994]. This technique works in two steps. Firstly the interface is discretized into a collection of simple elements. Then the Euclidean distances between each FE node and all the elements of the collection are computed and the smallest one becomes the updated value of the distance function. This Direct Reinitialization (DR) technique provides optimal accuracy and is perfectly robust because it is purely geometric. So this method deals very well with irregular functions, which can possibly be very different from a distance function initially. On the other hand the basic approach has a complexity which is a quadratic function of the number of elements in the collection $c$ and of the number of nodes in the FE mesh $\mathcal{N}$, which explains why it is generally mentioned as extremely greedy in terms of computational requirements in

the literature [Sussman et al. 1994; Elias et al. 2007]. This is mainly why these direct approaches are carefully avoided in most implementations, with the exception of [Hallberg et al. 2013]. A review of the possible improvements for this method can be found in [Jones et al. 2006], but these works address only regular grids or hierarchical meshes [Fortmeier et al. 2011]. We interest further to the DR approach in the rest of the chapter.

### 2.2.5 Summary on existing reinitialization methods

There are basically four main methods to reinitialize the LS functions that have been detailed above: the FMM method, the HJ reinitializaton method, the CR approaches and the DR methods. We have highlighted that the FMM approach is hardly compatible with our massively parallel numerical framework using anisotropic FE meshes. On the other hand, several CR solvers have been implemented within our FE library in the context of previous works [Coupez 2007; Ville et al. 2011]. These approaches have been proven able to tackle SRX without consideration of capillarity effects [Bernacki et al. 2008]. However they do not permit to model efficiently the GG phenomenon in our P1 framework. There are also geometric approaches which present many interesting features (analytic reconstruction of the LS functions, no numerical parameter, exact, conservative and robust) and could be seen as an ideal solution for the reinitialization of LS functions if their numerical costs could be significantly improved. Finally the HJ reinitialization algorithm is sufficiently versatile to tackle most problems involving LS functions, as demonstrated in previous works [Fabiano 2013; Agnoli 2013; Jin et al. 2014]. However we pointed out in section 1.5.3 that the HJ approach used in these works is rather inefficient computationally and is therefore very limiting for considering the 3D aspect. In the next section, we detail the FE formulation of the HJ problem and the way it is implemented in our numerical library [Basset 2006]. Our objective is finally to evaluate in what extent this method can be improved for the modeling of SRX and GG by studying the numerical parameters involved in the HJ formulation.

## 2.3 Study of the Hamilton-Jacobi reinitialization within a continuous and linear finite element framework

### 2.3.1 Formulation of the used finite element method

We mentioned earlier different methods for the resolution of the HJ equation given by eq. (2.1). First approach is to solve directly the nonlinear equation. The second is to use the discontinuous Galerkin finite element method. Finally a third approach consists in reformulating eq. (2.1) as a linear convective equation that can be solved more easily using standard linear and continuous FE schemes. This method has been chosen by Basset [Basset 2006] during its PhD work for the implementation of the HJ reinitialization solver in the Cimlib library. We detail this approach hereafter.

First, an implicit Euler-type scheme is use to approximate the time derivative of eq. (2.1):

$$\frac{\partial \hat{\psi}(x,\tau)}{\partial \tau} = \frac{\hat{\psi} - \hat{\psi}^-}{\Delta\tau}, \tag{2.4}$$

where $\Delta\tau$ designates a fictive time step and $\hat{\psi}^-$ is the known value of $\hat{\psi}$ at the previous increment.

Then the gradient term can be linearized as follows:

$$\|\nabla\hat{\psi}\| = \frac{\|\nabla\hat{\psi}\|^2}{\|\nabla\hat{\psi}\|} \approx \frac{\nabla\hat{\psi}\cdot\nabla\hat{\psi}^-}{\|\nabla\hat{\psi}^-\|}, \tag{2.5}$$

leading to the following convective formulation:

$$\frac{\hat{\psi} - \hat{\psi}^-}{\Delta\tau} + \vec{w}\cdot\nabla\hat{\psi} = \mathrm{sgn}(\hat{\psi}^-) \text{ with } \vec{w} = \mathrm{sgn}(\hat{\psi}^-)\frac{\nabla\psi^-}{\|\nabla\psi^-\|}, \tag{2.6}$$

which is equivalent to eq. (1.44) with an additional constant term $\mathrm{sgn}(\hat{\psi}_i^-)$. So the same P1 stabilized solver can be employed for the resolution of this equation.

Sussman et al. [Sussman et al. 1994] proposed the following approximation of the sign function:

$$\mathrm{sgn}(\hat{\psi}) = \frac{\hat{\psi}}{\hat{\psi}^2 + h^2}, \tag{2.7}$$

which works pretty well when the initial function $\hat{\psi}^-$ is neither too sharp nor too flat around the interface. Otherwise some issues may arise. Effectively if $\|\nabla\hat{\psi}\| \ll 1$, then

the propagation speed of the distance function is reduced and more increments are needed, which increases the reinitialization time. On the contrary if $\|\nabla\hat{\psi}\| \gg 1$ the sign of $\hat{\psi}$ can change, which would modify the position of the zero-isovalue during reinitialization. An other approximation has been proposed by Peng et al. [Peng et al. 1999]:

$$\mathrm{sgn}(\hat{\psi}) = \frac{\hat{\psi}}{\sqrt{\hat{\psi}^2 + \|\nabla\hat{\psi}\|^2 h^2}}, \tag{2.8}$$

which offers better performances according to [Basset 2006]. This version is therefore preferred. Finally a FE method is apply to solve eq. (2.6). At steady state, it falls $\hat{\psi} = \hat{\psi}^-$, which gives $\|\nabla\hat{\psi}\| = 1$. So the solution of eq. (2.1) is effectively a distance function with the same zero-level as the initial function $\psi$. But restoring the metric property everywhere in the domain is costly from a numerical point of view. Furthermore most applications requires only that the LS function satisfies $\|\nabla\psi\| = 1$ in the direct vicinity $\pm\varepsilon$ of the interface. Elsewhere the function can be constant:

$$\psi(x) = \begin{cases} \pm d(x,\Gamma_i) & \text{if} \quad d(x,\Gamma) < \varepsilon \\ \pm\varepsilon & \text{if} \quad d(x,\Gamma) \geq \varepsilon, \end{cases} \tag{2.9}$$

This is the *local level set method* [Chopp 1993; Adalsteinsson et al. 1997; Basset 2006]. When this formulation is adopted the reinitialization procedure can be performed only on a small interval of fictive time $\tau \in [0,\varepsilon]$. Here $\varepsilon$ can be seen as the half thickness of the layer where $\psi$ retrieves its algebraic distance property during the reinitialization stage. This presents the great advantage of reducing significantly the computation time devoted to reinitialization because only $\varepsilon/\Delta\tau$ increments of fictive time are needed to restore the distance function in the zone $d(x,\Gamma) < \varepsilon$, where $\varepsilon$ is very small compared to the dimensions of the simulation domain. Obviously the numerical cost associated with reinitialization is strongly dependent on the number of fictive time increments. So a first approach for accelerating the HJ reinitialization is basically to narrow the reinitialization band (*i.e.* reduce $\varepsilon$). However the local LS formulation creates a discontinuity at $\psi = \pm\varepsilon$ which may alter the conditioning of the FE problem if this discontinuity is very close from the interface, *i.e.* if the reinitialization layer is too tight. Moreover the diffusive formulation of eq. (1.47) is valid only if the GLS function remains a distance function within a sufficient layer around the interface. This parameter must therefore be carefully calibrated.

A second option is to increase the fictive time step. But this also complicates the resolution of eq. (2.6) and more iterations can be needed to solve the FE problem (let

us remind that we use an iterative GMRES solver to solve the equations). As each iteration represents a large number of computations, using disproportionate time steps can slow down the simulation. Using the GMRES method in such problems, a satisfactory solution is generally obtained after few iterations (typically no more than 100 iterations). Hereafter we fix the maximal number of iterations to 3000, which is far more than needed. So if the approximated solution is still not satisfactory after these 3000 iterations, one can reasonably consider that the iterative solver fails to converge. It is worth noting that non-convergence usually results in numerical instabilities and must be absolutely avoided.

Next numerical investigations are carried out in order to determine whether these two numerical parameters $(\varepsilon; \Delta\tau)$ can be optimized for our application.

### 2.3.2 Study of the numerical parameters of the Hamilton-Jacobi approach for fixed mesh size

#### The half reinitialization thickness

Firstly we interest to the half reinitialization thickness. The objective is to calibrate $\varepsilon$ and determine whether it is possible to narrow the reinitialization band without compromising the precision. For this purpose we use the same 2D GG simulation presented in section 1.5.3. In this first simulation, $\varepsilon = 4E = 20\mu$m was fixed. Next different values are tested $\varepsilon \in [0, 8E]$ and we analyze the predictions obtained in terms of mean grain size. Obviously the case wherein $\varepsilon = 0$ corresponds to a simulation without reinitialization. The results of this study are depicted on fig. 2.2.

As expected the case without reinitialization ($\varepsilon = 0$) provides catastrophic results, which illustrates the importance of restoring the metric property. Predictions converge for $\varepsilon \geq 6E$ to a final mean grain size around $135\mu$m. By using $\varepsilon = 4E$ as it was done in chapter 1 the final mean grain is slightly underestimated around 7%, which remains acceptable. For $\varepsilon < 4E$, results are more scattered and deviate from the above reference value. These investigations indicate that $\varepsilon = 4E$ is a good compromise between numerical efficiency and precision. So we adopt this value hereafter.

The results of this first study is therefore very clear: **the half reinitialization thickness can not be further optimized without degrading substantially the precision.** Next we examine the fictive time step.

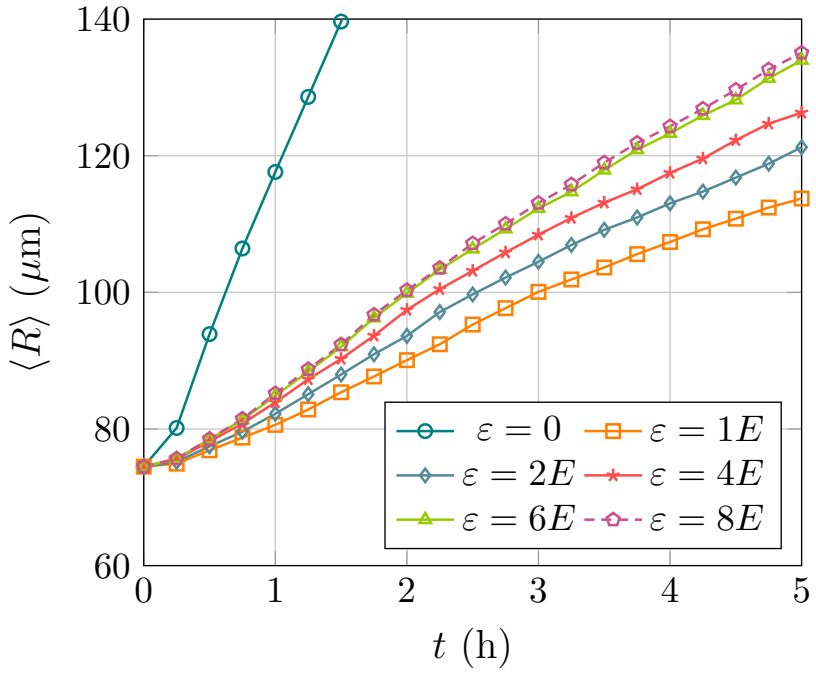


**Fig. 2.2** – Influence of the half reinitialization thickness on the numerical predictions. See section 1.5.3 for details concerning this simulation.

### The fictive time step

This second analysis focuses on the fictive time step. Finding an appropriate value for this parameter is not straightforward practically, especially because it has no physical interpretation. It must be chosen as high as possible to limit the number of fictive increments by ensuring a prompt convergence of the reinitialization solver (*i.e.* with a low number of iterations). In the 2D GG simulation of chapter one, $\Delta\tau = 4$ms was fixed, giving $\varepsilon/\Delta\tau = 5$ needed fictive time increments. We propose to challenge this value by using the following numerical experiment:

1. take the GLS functions at a given time of the simulation. Let us take $t = t_h/2$ for example,
2. solve eq. (1.48) with $M\gamma = 0$ in order to introduce numerical diffusion without *real* migration of the grain boundaries,
3. perform the treatment given by eq. (1.50),
4. reinitialize the GLS functions.

After performing this procedure, GLS functions are expected to recover approximately their initial values because $d\psi_i/dt = 0$ in eq. (1.48) for $M\gamma = 0$. Let designate by $\mathcal{N}_i$

the set of nodes where $d(n,\Gamma_i) < 4E$ is satisfied, $n$ designating a mesh node. A possible expression for the residual difference between the $\psi_i(t_\mathrm{f}/2)$ and $\psi_i(t_\mathrm{f}/2+\Delta t)$ functions is given by:

$$\mathscr{R} = \frac{1}{N_\mathrm{p}} \sum_{i=1}^{N_\mathrm{p}} \frac{\|\psi_i(t_\mathrm{h}/2+\Delta t) - \psi_i(t_\mathrm{h}/2)\|_2^{\mathcal{N}_i}}{\|\psi_i(t_\mathrm{h}/2)\|_2^{\mathcal{N}_i}} \quad \text{with} \quad \|u\|_2^{\mathcal{N}_i} = \sum_{n \in \mathcal{N}_i} u(n)^2. \tag{2.10}$$

Figure 2.3 depicts the evolution of $\mathscr{R}$ and of the reinitialization time as a function of the number of fictive time increments.

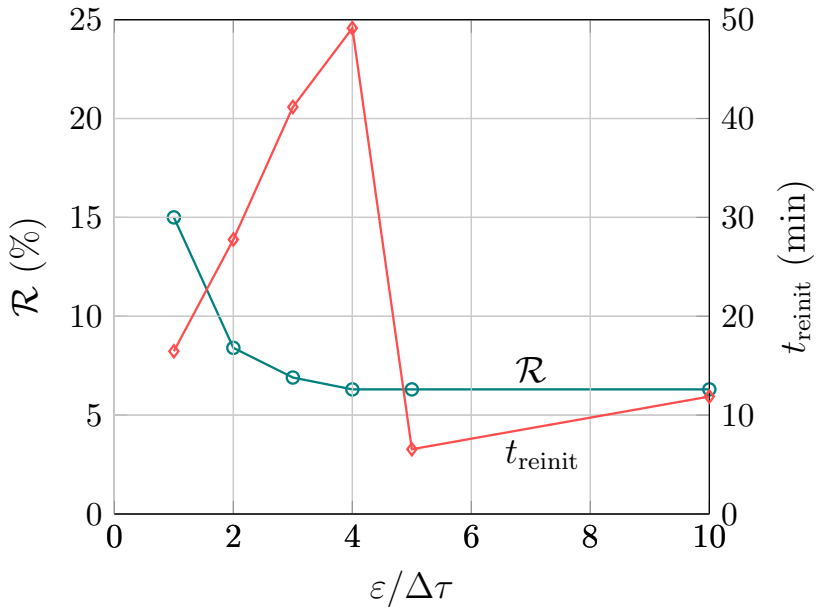


**Fig. 2.3** – Evolution of the reinitialization accuracy and time as a function of the number of fictive time increments (for a single physical time increment).

The residual difference $\mathscr{R}$ becomes stable around 6% for $\varepsilon/\Delta\tau \geq 4$. Effectively the precision of the reinitialization is also determined by the spatial discretization, *i.e.* the refinement of the FE mesh, so a minimal residual error is unavoidable. These results suggest that at least four fictive time increments are needed to properly reinitialize the GLS functions. The computation time is also shown to be extremely sensitive. For $\varepsilon/\Delta\tau \leq 4$ the solver fails to converge and the reinitialization time increases linearly with $\varepsilon/\Delta\tau$. Optimal results in terms of accuracy and numerical efficiency are obtained for $\varepsilon/\Delta\tau = 5$, which was the value adopted in section 1.5.3. So the final conclusion of these two simple studies is that **it is not possible to accelerate the HJ reinitialization without improving the used numerical tools**. Two options are possible at

this point. The former consists in attempting to improve the present HJ approach (solver, FE formulation, stabilization,...). However this HJ approach relies inherently on purely numerical parameters, such as the fictive time step, which are hard to calibrate. Also the HJ reinitialization method remains globally costly from a numerical point of view, regardless of the approach used to solve eq. (2.1), and appears to be hardly optimisable. These are critical issues in the considered context of the development of a robust reinitialization procedure. The second option is to develop a new reinitialization algorithm which outperforms the existing HJ method. Our state of the art about the existing reinitialization methods indicates that DR approaches could be a very interesting alternative to the HJ method due to the fact they are geometric and do not rely on any numerical parameter. However their numerical costs need to be drastically reduced to make them competitive. A new computationally-efficient DR algorithm has therefore been developed. This new reinitialization algorithm is completely generic and is thus able to tackle most problems involving moving interfaces within a LS-FE framework. So it is compared in terms of numerical efficiency with the other reinitialization methods implemented in our numerical library, especially the HJ method presented above and the "reinitialization-free" CR-DF and CR-HTDF solvers.

## 2.4 Development of a new reinitialization algorithm and comparison with other classical methods of the state of the art

### 2.4.1 To a direct reinitialization method

#### Principle and implementation

The basic idea behind DR is to firstly discretize the front and then perform a full reconstruction of the distance function. Let us consider the simple example of fig. 2.4a, composed of five elements, whose four are crossed by the interface of a distance function $\psi$. We note $n_i^k$ the $i^{th}$ node of the mesh element $k$, with $i \in \{1,...,d_s+1\}$, and $x_i^k$ its respective spatial coordinates. The algorithm starts by inspecting the edges of each element. In the frame of P1 (linear by element) interpolation, the distance function is represented by its values at the mesh nodes. So the intersection between an element edge and the front of a distance function is simply calculated by:

$$x^k = x_i^k - \frac{x_i^k - x_j^k}{\psi(n_i^k) - \psi(n_j^k)} \psi(n_i^k). \tag{2.11}$$

After performing this operation, a set of $I^k$ intersection points is obtained for the element $k$, as illustrated on fig. 2.4b. It is obvious that $I^k \geq d_s$ is needed to create a representation of the front in the considered mesh element. A particular case is obtained in 3D for $I^k = 4$, which creates a quad interfacial element. This quad element is then decomposed into two 3D triangles so that only point-to-triangle distance computations are performed. A piecewise linear representation of the interface is finally obtained by inspecting all the mesh elements (see fig. 2.4c). This set of $(d_s - 1)$-simplices, referred to as the *collection*, is therefore composed of segments (in 2D) or triangles (in 3D). Next, a reinitialization of the signed distance function can be performed at any mesh node by searching the closest element in the collection. This is schematically illustrated by fig. 2.4d. As the computation of the distance to a segment (2D) or a triangle (3D) will be a critical operation in this part of the algorithm, we chose to use the optimal implementations detailed in [Schneider et al. 2003]. Obviously the sign of the reinitialized function remains the same because the procedure does not displace the interface. So, given a P1 representation of a distance function, the DR method performs a geometric reconstruction, which provides optimal precision. However this method has an important numerical costs if used as is.

Using the previous notations ($\mathcal{N}$ is the number of mesh nodes and $c$ is the number of facets in the collection), the complexity of the collection construction is linear $\mathcal{O}(\mathcal{N})$. On the other hand the distance computation is of quadratic complexity $\mathcal{O}(\mathcal{N}c)$ which makes this brutal approach hardly compatible with our application, especially in 3D. This explains why HJ method was preferred until now. Based on techniques widely used in computer graphics, data mining, and other domains, we propose hereafter a new DR method where the cost of the distance computation is significantly improved. This optimization is based on a space partitioning technique, which consists in dividing the space into a set of $p$ zones, according to a given criterion. Such a structure is called a *tree*. Then each zone composing the tree is recursively decomposed in the same manner until small regions which can not be further optimized are obtained: *the leaf*. Finally searching operations are performed inside these leaf with much lower computational costs, which is the basic idea behind *divide & conquer* strategies. Here $p$ is a constant number, inherent to the strategy employed to partition the space. Quad-trees in 2D are an example ($p = 4$) wherein the whole space is firstly placed in a bounding box which is divided in fours boxes of identical dimensions, corresponding

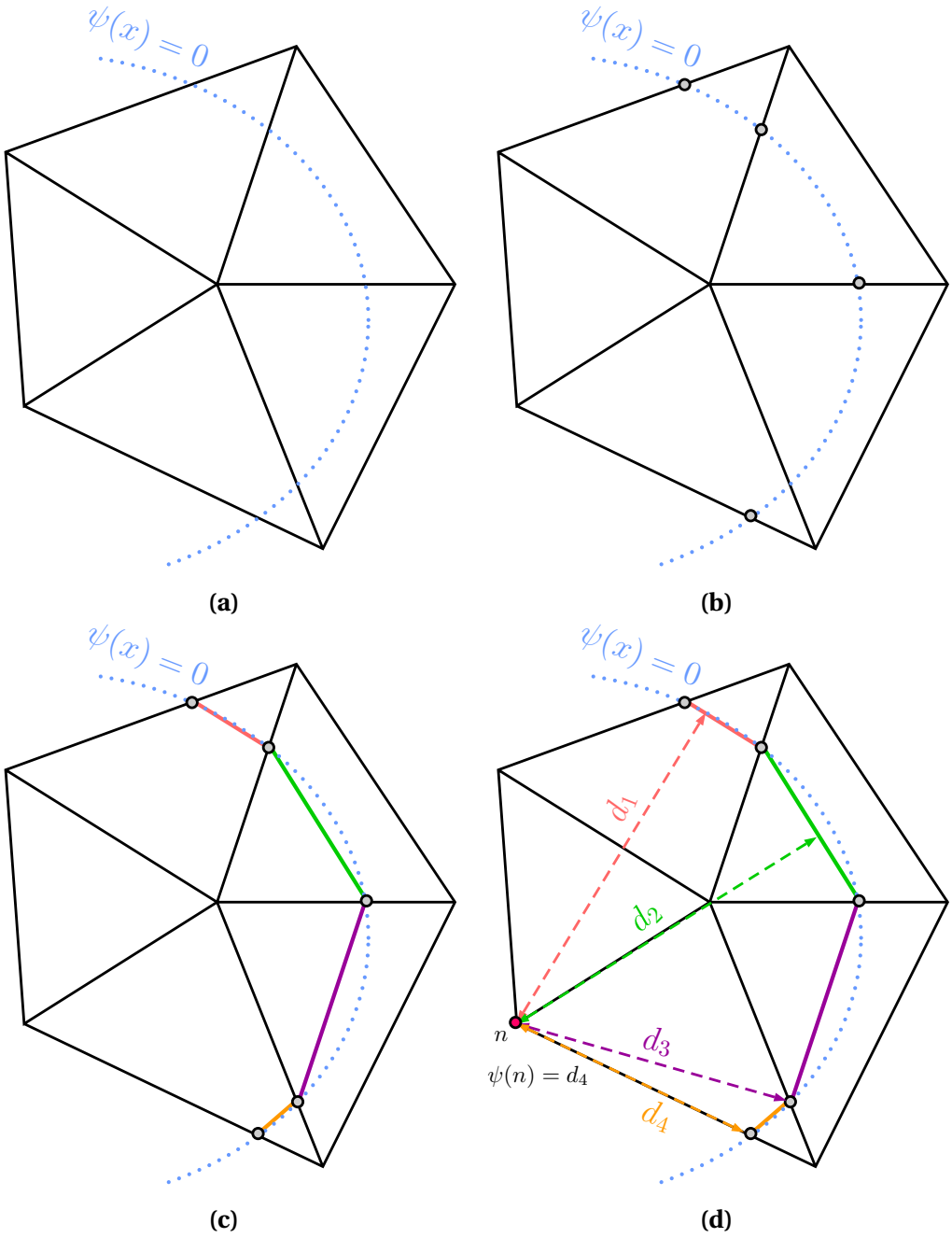


**Fig. 2.4** – DR method performed on a P1 mesh: (a) initial situation; (b) localization of intersections between the interface and the element edges; (c) discretization of the front into a collection of $(d-1)$-simplices; (d) computation of the distances between a reinitialized node and the elements of the collection.

to the four quarters of the initial box. Then each of these boxes is divided into four other boxes, and so on. Using such systematic division, one or several boxes may be empty at some stage, and the division may not be optimal, especially in the present case with unstructured and possibly anisotropic FE meshes. The same statement can be made regarding octrees ($p = 8$) which are the 3D counterparts of quad-trees. That is the reason why it is chosen to partition the space hierarchically using a $k$-dimensional ($k$-d) trees. Here the division is always made into $p = 2$ zones, using a criterion which depends on the elements present in the collection. This structure was firstly introduced in [Bentley 1975], with examples of potential applications. Here we focus especially on the Nearest Neighbor Searches (NNS) whose objective is to find the nearest element in the collection with minimal computations. Hereafter we detail a new algorithm called Direct Reinitialization with Trees (DRT) in which the complexity of the distance computations is reduced to $\mathcal{O}(\mathcal{N} \log c)$.

Unlike systematic methods, the division criterion employed hereafter is based on an analysis of the space that is to be divided. In the present case, this space is the initial collection, or a subset of it, which can be seen as a set of elements. This set is then divided into two parts using a *node*, *i.e.* a division plane. Optimally, this plane should be chosen in such a way that the two subdomains contain the same number of elements. To narrow such result with minimal computation costs, division planes are normal to the Cartesian axis and centered to the set of elements. This centering is obtained by computing the barycenter of each element, and choosing a plane that goes through the barycenter of these points. The whole process of tree construction is given below:

(b.1) set the division plane (line in 2D) as the plane going through the barycenter of all elements and having its direction alternatively defined by the $\vec{x}$, $\vec{y}$ and $\vec{z}$ directions depending on the depth in the tree,

(b.2) compute the signed distance from the vertices of all the elements in the collection to this plane,

(b.3) build a left child to the current tree by going back to (b.1) with all the elements having at least a vertex with negative plane distance,

(b.4) build a right child to the current tree by going back to (b.1) with all the elements having at least a vertex with positive plane distance.

A schematic example is given on fig. 2.5. Starting from fig. 2.5a, a first division plane is introduced on fig. 2.5b, and then a second on fig. 2.5c. The process recursively builds

a binary tree. As observed in fig. 2.5c, the procedure stops when at steps (b.3) and (b.4) one of the two subtrees contains the other. In such situation a leaf is created, which contains (typically) a small subset of the initial collection. Obviously there exist multiple geometric configurations where the strategy employed for defining the division plane does not create two subtrees having the same number of elements. However, such situations are not met in practice and tests have highlighted that this definition leads to a globally well-balanced tree. The final tree structure is given in fig. 2.5d. Regarding costs, the computation of the barycenter is performed in linear time, and the global tree construction is of optimal complexity $\mathcal{O}(c \log c)$ because at each stage the number of considered elements should be divided by around two.

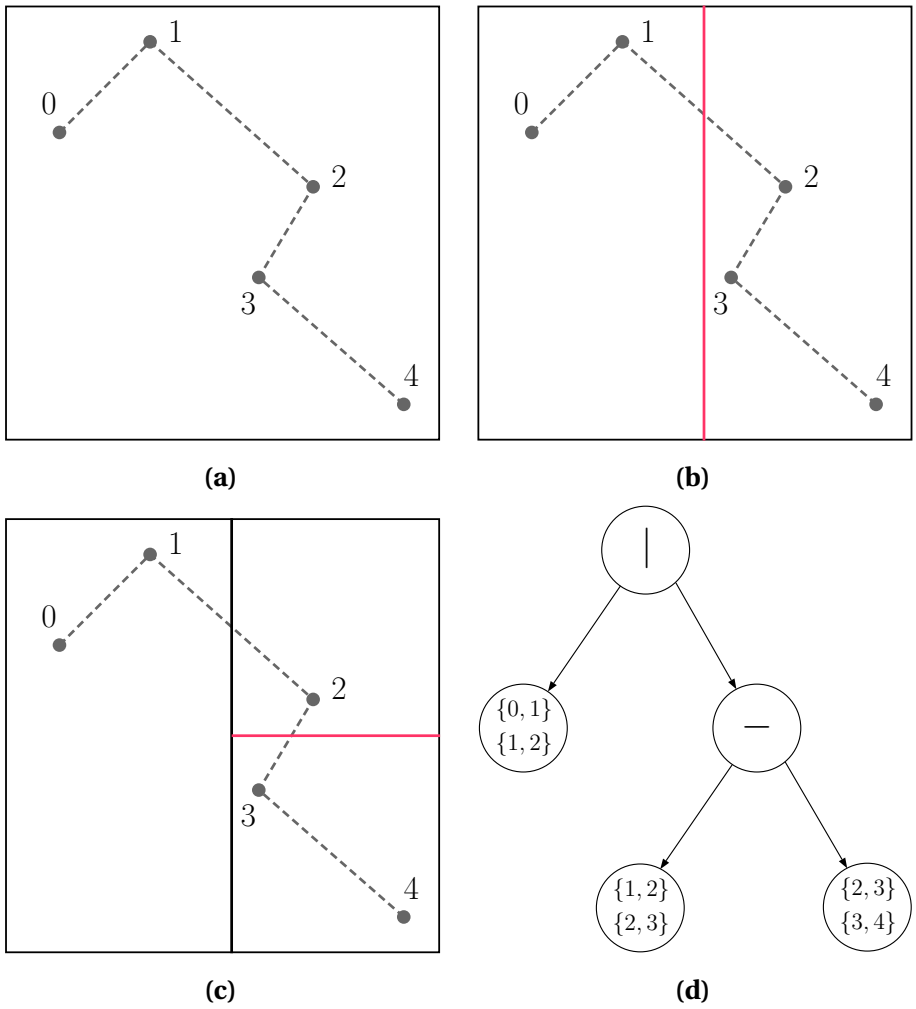


**Fig. 2.5** – Example of recursive tree construction in 2D.

NNS queries can then be performed for each node of the mesh using the following

algorithm at the root of the tree:

(b.5) compute the signed distance from the node to the division plane,

(b.6) if the distance is negative, go back to (b.5) with the left subtree,

(b.7) if the distance is positive, go back to (b.5) with the right subtree.

This recursive process reaches the leaf where the nearest element in the collection is likely to be located. At this point, the smallest distance from the considered node to all the elements contained in that leaf is calculated. It may appear at step (b.6) or (b.7) that the resulting distance is bigger than the distance to the division plane. In such case, it is required to go back to (b.5) with the other subtree. Though this operation is implemented to ensure consistency, it is scarcely met practically if the division planes are well defined, as in our applications. Moreover, due to all the divisions, the set of elements stored in any leaf should be small enough to consider that distance computation is of optimal complexity $\mathcal{O}(\mathcal{N} \log c)$.

The figs. 2.6 and 2.7 illustrate two scenarii for the distance computation at a given node $n$. At each stage of the NNS, the notation $d_p$ designates the distance to a division plane, $d_e$ is the distance to an element of the collection and $d(n)$ is the final result. In the first configuration illustrated on fig. 2.6, the point is optimally located since it is close enough to the interface. Hence, browsing two levels of the tree in figs. 2.6a and 2.6b leads directly to the correct leaf in fig. 2.6c. A first distance $d_e$ is then calculated based on the elements present in that leaf. When browsing back in figs. 2.6d and 2.6e, it is find that $d_e$ is smaller than the distance to any of the division planes. So the final result $d(n) = d_e$ is directly obtained without further computations.

Now a worst case scenario is illustrated on fig. 2.7. Here the leaf containing $n$ returns a distance which is greater than the distance to the first division plane (see figs. 2.7a and 2.7b). So a better (*i.e.* smaller) solution may exist in the other part of the tree. Hence, this has also to be inspected (see fig. 2.7c). In the right subtree, an optimal situation is met as the recursive browsing illustrated on figs. 2.7d and 2.7e provides the final result.

It was mentioned in section 2.3.1 that HJ reinitialization is usually performed only in a small thickness $\pm\varepsilon$ around the interface. Implementing the same optimization in the DRT method can drastically reduce the cost of the distance computations. Then, at step (b.6) and (b.7), if the resulting distance rises a need to look in the other subtree while being greater than $\varepsilon$, this operation can be skipped. Moreover, if all the $d_p$

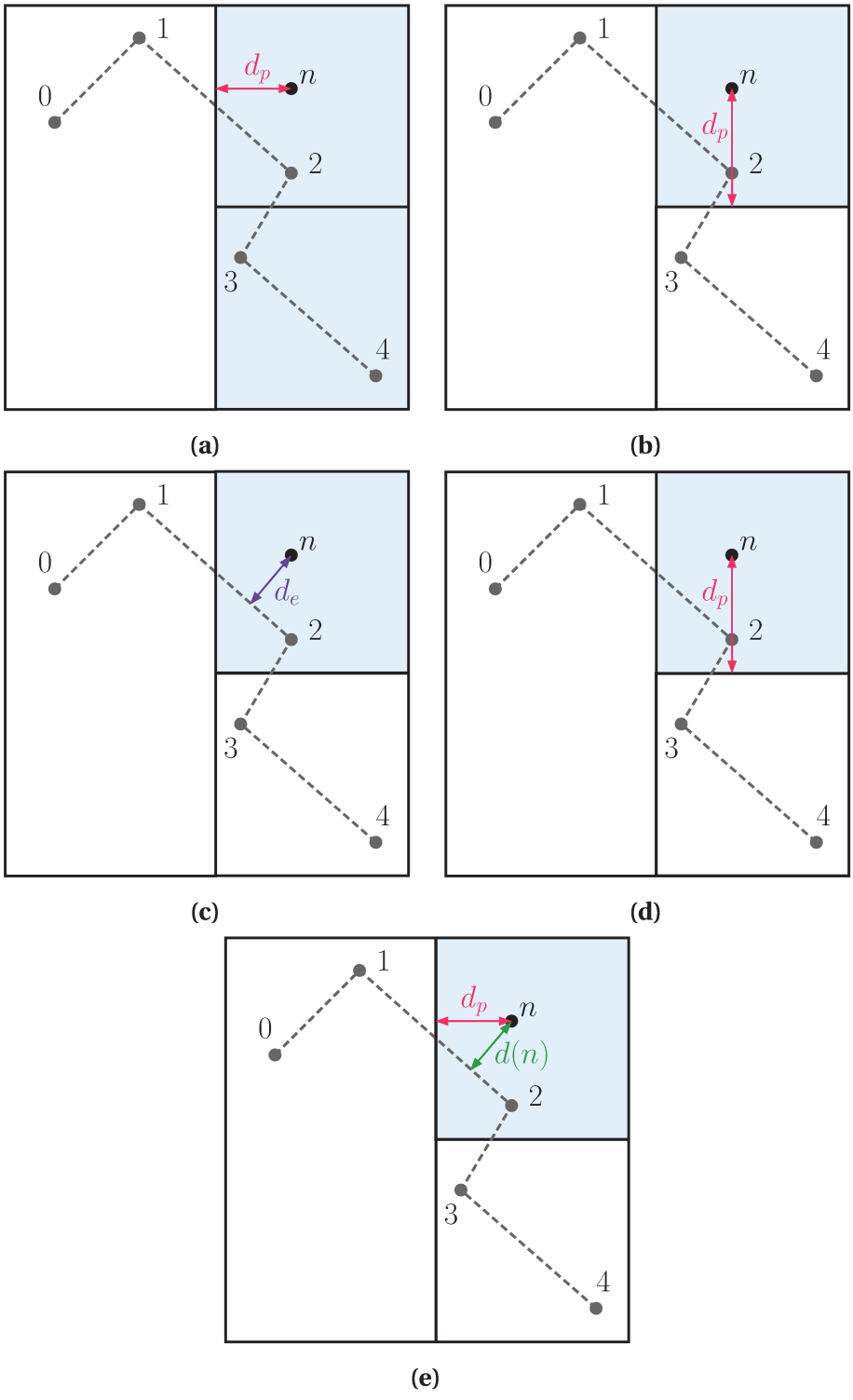


**Fig. 2.6** – Example of recursive distance computation in 2D with the DRT method, best case scenario.

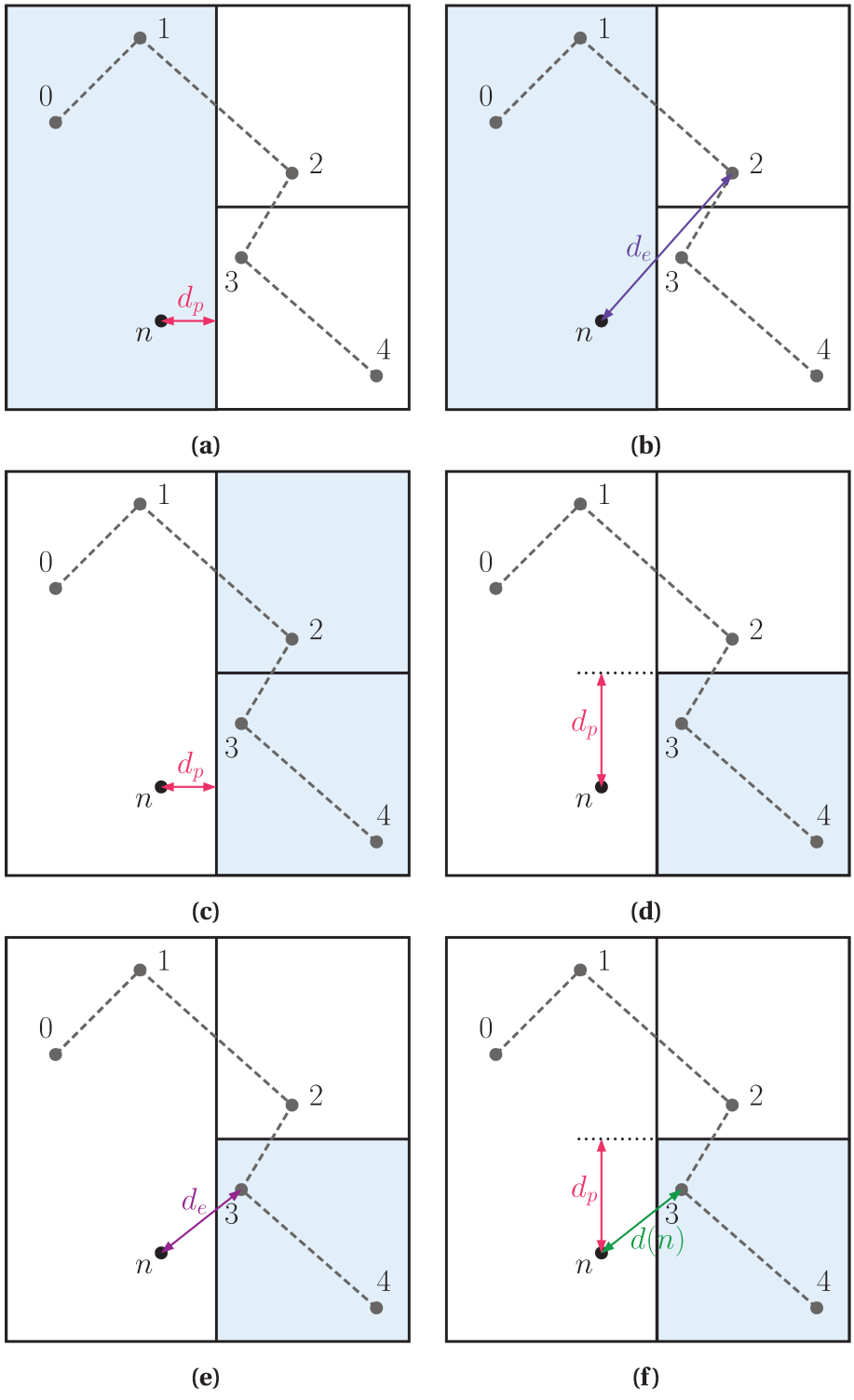


**Fig. 2.7** – Example of recursive distance computation in 2D with the DRT method, worst case scenario.

calculated during the browsing of the tree are greater than $\varepsilon$, no further computation is needed and it falls directly $d(n) = \varepsilon$. So the nodes located far from the interface are rapidly eliminated during the distance computation. Because in practice the reinitialization thickness is small, the number of nodes that have to be reinitialized and $c$ are of the same order, and the final complexity of the new DRT method is expected to be $\mathcal{O}(c \log c)$, on average.

Massively multi-domain simulations often require important numerical resources to obtain sufficient accuracy. The same remark can be drawn for 3D computations. A classical choice in these cases is parallelization using a distributed memory paradigm. Opposed to shared memory, distributed memory paradigm permits to each parallel unit, called *process*, to have its own independent memory which can be possibly located on a different machine. This last point is essential for large scale computations, where it is impossible to store the whole mesh and the corresponding fields on a single machine. In such a paradigm, each process has only access to a part of the mesh, a *partition*, and is only able to build a part of the collection. To solve this issue, a first option is to communicate and gather the full collection on each process, and then build a global $k$-d tree. Experiments have showed that this method performs well for a small number of processes (up to 20) but has a poor parallel speed-up.

To retrieve parallel efficiency, an advanced technique has been developed. In this method, each process builds its own collection and its own tree, ignoring other processes. Then we employ a bounding box strategy. Each process computes the minimal box aligned to the Cartesian axis that contain completely the local collection, *i.e.* the collection associated with this partition. During the distance computation stage, each process computes first the distance using its tree, and then interrogates one by one the other processes to determine if they can improve the result (*i.e.* find an element in their own collection that is closer to the considered node). This parallel implementation is summarized on fig. 2.8. The simulation is here distributed on four processes, noted $P_i$ with $i \in \{0,...,3\}$ and the interface of a distance function is represented by a solid white line. Let us consider the node labeled $i$ located on the $P_0$ process. The recursive NNS queries on this partition provides a first local distance to the interface $d_i^0$. Then the distance to the bounding box of the $P_2$ process, noted $b_i^2$, is evaluated. It is observed that $d_i^0 < b_i^2$ so there is no need to inspect the $P_2$'s collection because no better solution could be find on this process. Considering now the node $j$ located on $P_2$, a first NNS on the local partition returns $d_j^2$. This latter is compared with $b_j^0$, representing the distance between the node $j$ and the bounding box of $P_0$. Because $b_j^0 < d_j^2$, a better solution could eventually be found on $P_0$. If $b_j^0 < \varepsilon$ the coordinates

of $j$ are communicated to the $P_0$ process which performs a new NNS and returns $d_j^0$, the shortest distance between node $j$ and the $P_0$'s collection. Finally it is find that $d_j^0 > d_j^2$, so $d_j^2$ is the final solution.

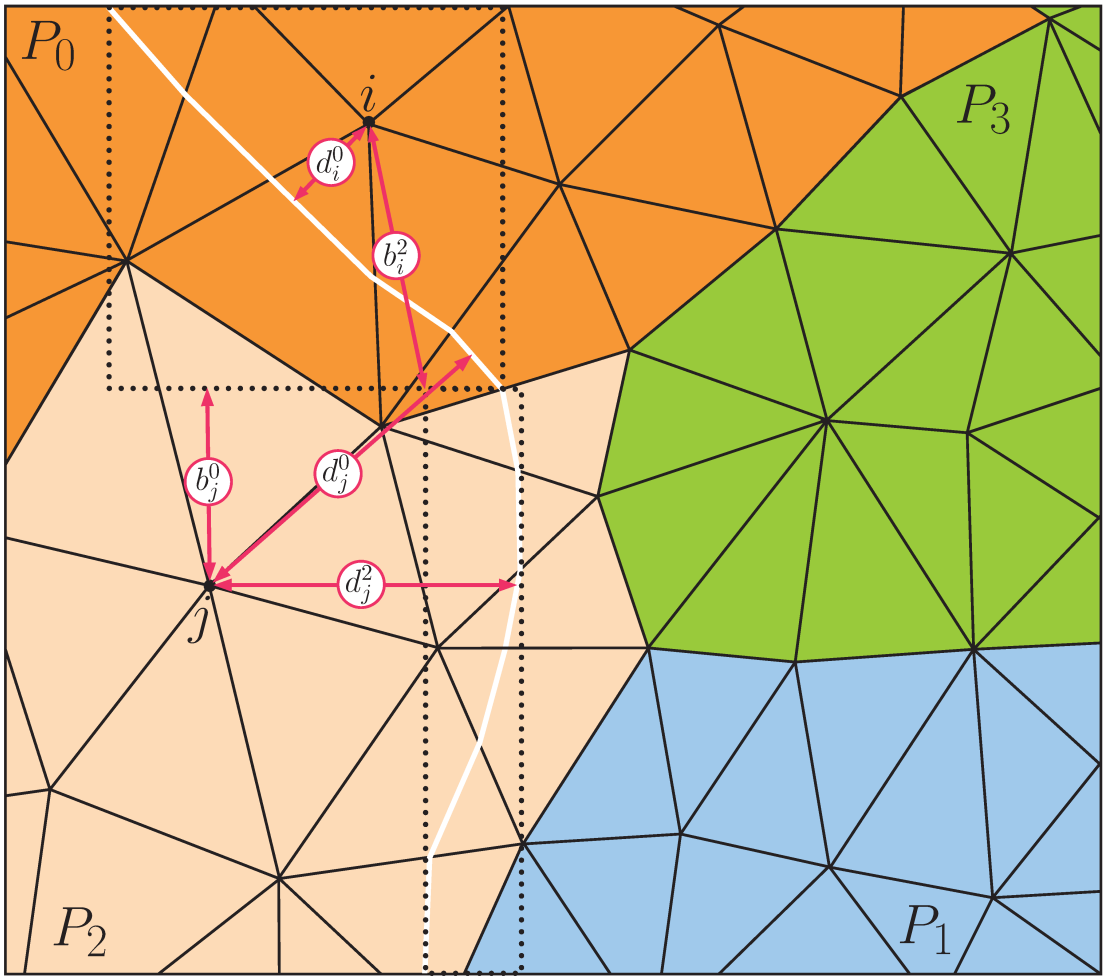


**Fig. 2.8** – Schematic illustration of the bounding box strategy employed in the DRT method for parallel computations. Each process is designated by a given color. The solid white line represents the interface of a distance function and the arrows correspond to the diverse computed distances. The minimal boxes that contain the interface on each partition are represented by dotted black lines.

For a large number of processes and a balanced distribution of the interfaces, communications are expected to be minimal and the optimal parallel efficiency is reached. This bounding box technique at the global level completes the $k$-d tree optimization used at the local level, and the DRT method can now be applied to perform efficient and parallel reinitialization of the LS functions. The method is tested in the next section and compared with the other reintialization approaches described earlier.

### 2.4.2 Academic benchmark and comparison with other approaches

Both DR and DRT methods have been implemented. A comparison between these two methods for a typical GG case in 2D can be found in [Shakoor et al. 2015b]. Regarding the HJ, CR and CR-HTDF methods used for comparison, parallel implementations were already provided by our library. All computations are performed on Intel Xeon CPUs (the number of used CPU units is specified for each simulation).

The first test proposed consists in a square (respecively a cube in 3D) with initial edge length $l_0 = 0.5\text{mm}$ centered in a $[0, 1\text{mm}]^d$ domain. This square (cube) is represented by a distance function $\psi$ and is subjected to a velocity field equals its gradient $\vec{v} = \nabla\psi$. The theoretical instantaneous values of the distance function, noted $\psi_\text{t}$, and of the internal area (respectively internal volume in 3D), noted $f_\text{t}$, are given by:

$$\begin{cases} \psi_\text{t}(x,t) = \psi(x,0) - t \\ f_\text{t}(t) = (l_0 - 2t)^d. \end{cases} \tag{2.12}$$

The simulation time steps are calibrated separately for each method so as to ensure a global error on the internal area (volume in 3D) evolution lower than 1%:

$$\sqrt{\frac{\int_{t=0}^{0.25} \left(f_\text{t}(t) - f(t)\right)^2 dt}{\int_{t=0}^{0.25} f_\text{t}^2(t)\,dt}} \leq 0.01. \tag{2.13}$$

#### Square shrinkage (2D)

We use a fixed unstructured mesh composed of 150,000 triangles with average mesh size $h_\text{b} \approx 4\mu\text{m}$ (homogeneous mesh size). We set $\varepsilon = 20h_\text{b} = 80\mu\text{m}$ for all reinitialization methods in order to perform a fair comparison. Simulations are performed on 4 CPUs. The main results are summarized in table 2.1. Obviously for the CR solvers, the distance function is automatically reinitialized during the solving of eq. (2.3) and no distinction can be made between $t_\text{resol}$ and $t_\text{reinit}$.

| Method | HJ | CR-DF | CR-HTDF | DRT |
|---|---|---|---|---|
| $\Delta t$ (ms) | 10 | 0.1 | 0.1 | 10 |
| $t_\text{resol}$ | 6.4s | 1min 25s | 1min 27s | 5.8s |
| $t_\text{reinit}$ | 2min 13s | | | 0.4s |

**Table 2.1** – Results of the shrinking square simulations performed on 4 CPUs.

The new algorithm appears way more efficient than all other methods and is up to 300 times faster than the HJ approach in this configuration. The CR solvers are proved more effective than the HJ method but require a very small time step to guarantee the scheme stability. We plot on fig. 2.9a the discretization error given by:

$$\mathscr{R}(t) = \frac{\|\psi_t(x,t) - \psi(x,t)\|_2^{\mathscr{N}_{\text{int}}}}{\|\psi_t(x,t)\|_2^{\mathscr{N}_{\text{int}}}} \text{ with } \|u(x,t)\|_2^{\mathscr{N}_{\text{int}}} = \sum_{n \in \mathscr{N}_{\text{int}}} u(x_n,t)^2, \tag{2.14}$$

with $\mathscr{N}_{\text{int}}$ being the set of nodes satisfying $\|\psi\| \leq 5h_b$. These results prove again the superiority of the DRT algorithm compared to CR approaches, which fail to properly maintain the metric property, especially in the corner regions (see fig. 2.9b). On the other hand, the DRT and HJ methods exhibit a high level of accuracy. Around 20 iterations are needed to achieve numerical convergence with the HJ approach using the iterative solver described earlier. Finally this first 2D test case demonstrates that the proposed DRT algorithm is both extremely fast (table 2.1) and accurate (fig. 2.9).

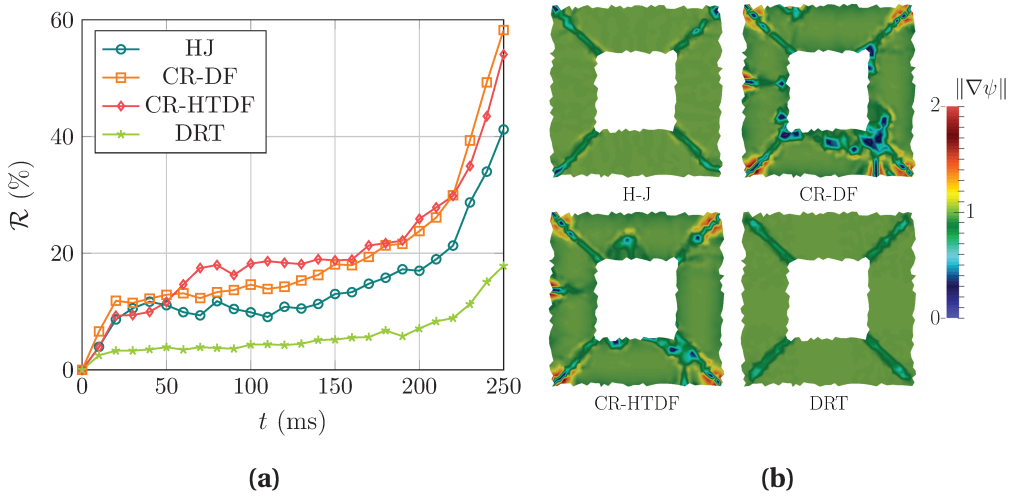


**Fig. 2.9** – (a) Residual error between the exact and calculated values of $\psi$ (see eq. (2.14) for details about the computation of $\mathscr{R}$); (b) $\|\nabla\psi\|$ at $t = 150$ms.

### Cube shrinkage (3D)

Now we investigate the 3D counterpart of the previous test case. Here local anisotropic remeshing is preferred for limiting the number of elements, which is taken constant and equal to 500,000. The resulting FE mesh at different stages of the simulation is depicted on fig. 2.10.

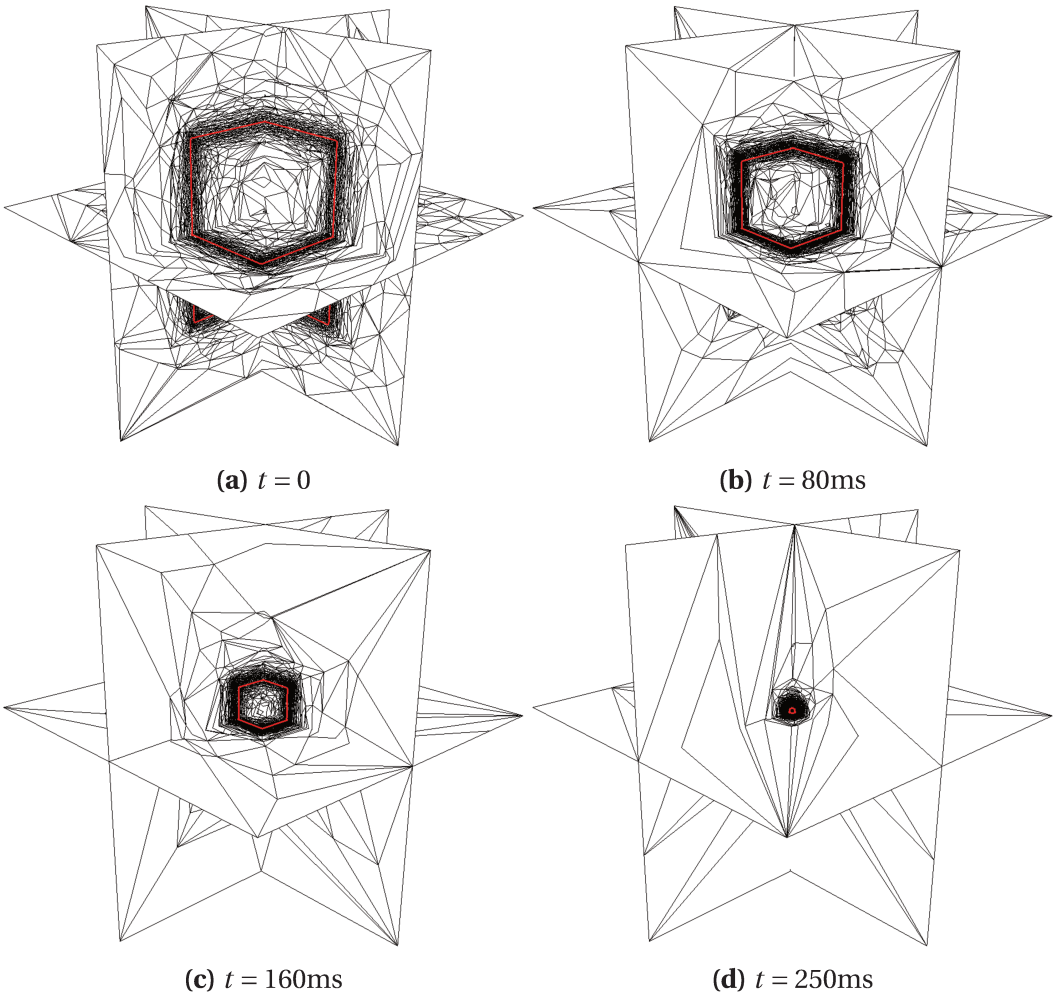

**(a)** $t = 0$ **(b)** $t = 80$ms

**(c)** $t = 160$ms **(d)** $t = 250$ms

**Fig. 2.10** – Anisotropic FE mesh used for the shrinking cube simulation. The interface of $\psi$ is represented by a solid red line.

In addition to the anisotropic mesh, this case is also critical for non-direct approaches (HJ and CR) because the gradient is poorly defined along the bisecting planes and diagonals of the cube. Hence, the linear problems built by the HJ solver are poorly conditioned and around 430 iterations are needed to achieve convergence, on average. We observe also the appearance of a parasite phase outside the cube during the simulation with HJ reinitialization (see fig. 2.11). It proves that the function becomes too irregular to be properly reinitialized with the HJ solver which causes a modification of the sign of the distance function. Furthermore the interface of this parasite phase is automatically detected and captured by the remesher which adapts the mesh around it. As the total number of elements is fixed, the calculation accuracy then falls because fewer elements are used to represent the *real* interface of the cube.

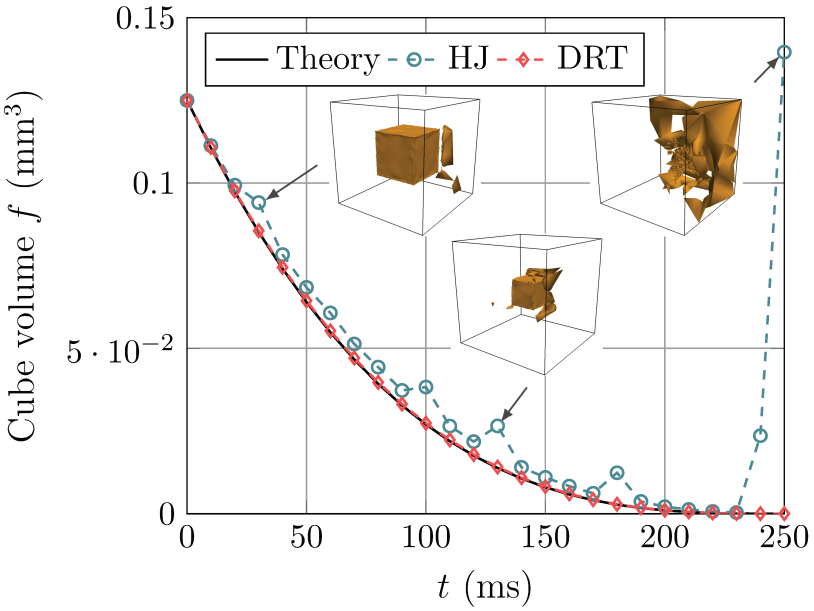


**Fig. 2.11** – Evolution of the cube volume during the simulations with the HJ and DRT approaches. The appearance of a parasite phase with the HJ method is caused by an unsatisfying reinitialization of the distance function.

The CR solvers exhibit unstable behaviors for this test case, although the simulation time step remains an order of magnitude lower than the mesh size in the refined zone (no violation of the stability condition). Despite multiple investigations, we were not able to find a time step value which would satisfy eq. (2.13) with the CR solvers. Finally these approaches seem to be less robust than the HJ and DRT ones. In addition they require a good knowledge of the parameters needed for the stabilization. Results obtained with the DRT and HJ methods are summarized in table 2.2.

| Method | HJ | DRT |
|---|---|---|
| $\mathscr{R}$ (%) | 57 | 0.5 |
| $t_{\text{reinit}}$ | 4min 24s | 52.8s |

**Table 2.2** – Results of the shrinking cube simulations performed on 20 CPUs. CR methods are not reported because eq. (2.13) can not be satisfied with these approaches.

The DRT algorithm is around five times faster than the HJ approach in 3D, while providing much greater accuracy. So the accelerations observed in 3D are smaller than the 2D ones, which suggests there is still room for improvement of the DRT method in 3D.

To summarize, these academic test cases confirm the superiority of the proposed DRT algorithm and demonstrate its robustness. This algorithm is also well-suited with particular triangulations (anisotropic meshes) and does not require any calibration contrary to other classical methods which require, at least, one purely numerical parameter. Next we interest to realistic metallurgical applications in two and three dimensions.

## 2.5 Test on realistic metallurgical cases in two and three dimensions

Let us go back to the 2D GG case presented in section 1.5.3. It has been demonstrated that the HJ reinitialization method was poorly efficient for this application. So the same simulation is now performed with the DRT algorithm. We proved in section 2.3.2 that $\varepsilon = 4E$ is a good compromise, so we conserve this value. Also the same numerical parameters are employed for the simulation. The previous and new computation times are compared in table 2.3.

We observe that the reinitialization of the GLS functions is performed around 70 times faster with the DRT method, which results in a considerable acceleration of the simulation, with a factor close from 9. So this direct approach is proven to be very efficient in 2D. Next we attempt to confirm these promising results in 3D.

A 3D GG case is then considered. A cubic polycrystal with edge length 1.5mm containing around 1000 grains is generated according to a LVT technique. The grain size distribution is representative of a 304L material with initial mean grain size $\langle R_0 \rangle = 92\mu$m.

| | Initial | | With DRT | |
|---|---|---|---|---|
| $t_{\text{remesh}}$ | 4h 11min | (6.4%) | 4h 22min | (57.1%) |
| $t_{\text{resol}}$ | 2h 02min | (3.1%) | 1h 57min | (25.6%) |
| $t_{\text{reinit}}$ | 59h 04min | (89.8%) | 52min | (11.3%) |
| $t_{\text{other}}$ | 28min | (0.7%) | 28min | (6%) |
| $t_{\text{simu}}$ | 65h 45min | | 7h 39min | |

**Table 2.3** – Distribution of the computation time with the HJ and DRT reinitialization methods for the 2D GG simulation detailed in section 1.5.3. Simulations are performed on 6 Xeon Intel CPUs.

The 3D polycrystal is submitted to a $t_{\text{h}} = 5\text{h}$ heat treatment at $T = 1050°\text{C}$. A fixed unstructured FE mesh composed of $150^3$ tetrahedra is used for this simulation, which gives an averaged mesh size $h_{\text{b}} \approx 5\mu\text{m}$. The half reinitialization thickness is $\varepsilon = 4h_{\text{b}}$, which ensures good numerical convergence. We fix also $\delta = 3$ in the same manner it was done in 2D. But satisfying this separation condition in 3D is much more demanding in terms of colors as $N_{\text{p}}^{\delta=3} = 102$ GLS functions are effectively needed to represent this 3D microstructure with this criterion, which is important. The aggregate is depicted on fig. 2.12. This simulation is performed on 12 CPUs and the computation times are detailed in table 2.4.

| | Initial | | With DRT | |
|---|---|---|---|---|
| $t_{\text{remesh}}$ | | No remeshing | | |
| $t_{\text{resol}}$ | 11h 50min | (9.4%) | 11h 50min | (33.1%) |
| $t_{\text{reinit}}$ | 113h 49min | (90.5%) | 23h 48min | (66.6%) |
| $t_{\text{other}}$ | 5min | (0.1%) | 5min | (0.3%) |
| $t_{\text{simu}}$ | 125h 44min | | 35h 43min | |

**Table 2.4** – Distribution of the computation time for the simulation of a 5h heat treatment in 3D using the initial polycrystal of fig. 2.12a. Simulations are performed on 12 Xeon Intel CPUs.

Performing such a simulation with the HJ approach is complicated because of the high numerical costs. However by performing a single increment and by using the evolution of $N_{\text{p}}$ obtained with the DRT method, the time which would have been needed to perform this simulation with the HJ reinitialization method can be estimated. **Based on these simple considerations the simulation time needed with the HJ reinitialization method should be more than five days on 12 CPUs. So the DRT method permits to reduce the global computaton time by a factor 3.5 in 3D, while being at least as accurate.** This new DRT method is therefore a major advance for our

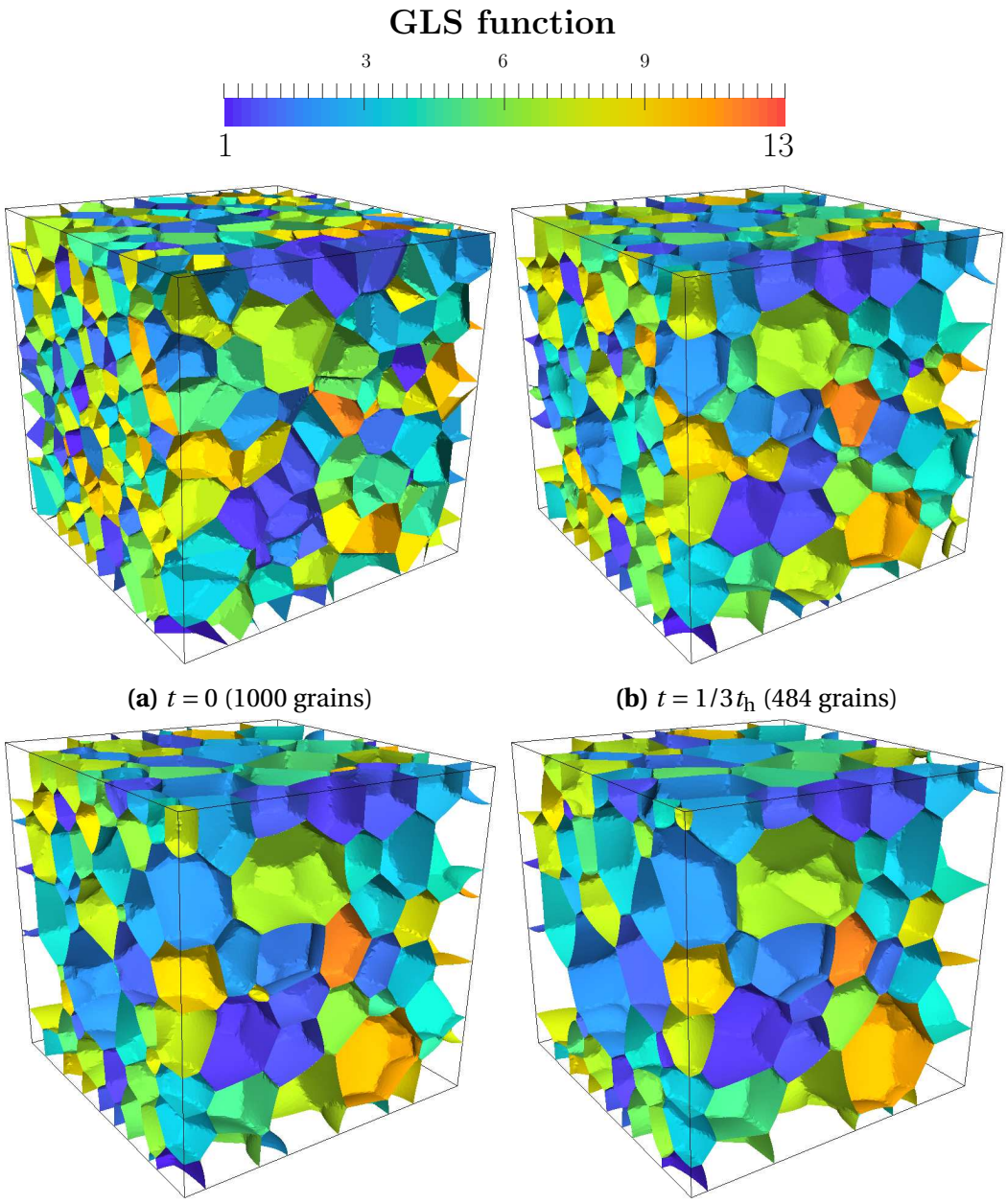


**(a)** $t = 0$ (1000 grains) **(b)** $t = 1/3\,t_h$ (484 grains)

**(c)** $t = 2/3\,t_h$ (293 grains) **(d)** $t = t_h$ (203 grains)

**Fig. 2.12** – Evolution of the 3D grain boundary network during the simulation of a 5h heat treatment at 1050°C for 304L.

applications. But we estimate that the computation time could be further reduced by using less distance fields in the simulation, which involves to improve the present numerical formalism based on GLS functions.

## Summary

In this chapter, the reinitialization of the distance functions is investigated. First the potential of the HJ reinitialization method in the context of our application is evaluated. It is demonstrated that this method can not be improved without significant modifications of the numerical formalism. Furthermore this approach exhibits poor numerical robustness and has numerical parameters whose calibration is not straightforward. These points make the HJ method hardly compatible with the 3D FE-LS modeling of microstructural evolutions with a representative number of grains. So a new method for reinitializing the distance functions has been proposed and implemented in our numerical framework, which relies on a discretization of the front and a geometric reconstruction of the distance functions. This new reinitialization method benefits from an efficient implementation based on a space-partitioning strategy using $k$-d trees and a bounding box technique providing high parallel efficiency. The algorithm has been successfully tested and compared with other reinitialization approaches from the state of the art through diverse academic test cases. Acceleration factors up to 300 have been obtained thanks to this new DRT approach compared with the HJ reinitialization method. It is also much more accurate and robust because it does not rely on any numerical parameter. Finally this method has permitted to accelerate a typical 2D GG simulation by a factor close to 9 and to perform a first 3D large-scale simulation within reasonable simulation times. These developments have allowed to publish [Shakoor et al. 2015b].

# Chapter 3

# Improvement of the numerical formalism based on global level set functions

## Contents


**3.1 Introduction . . . . . 102**

**3.2 Basics about grain coloring . . . . . 102**

3.2.1 Principle . . . . . 102

3.2.2 Limitations . . . . . 102

3.2.3 Existing situation and problem statement . . . . . 103

**3.3 Improvement of the existing situation . . . . . 103**

3.3.1 Literature review . . . . . 103

3.3.2 Development of an efficient recoloring scheme . . . . . 105

**3.4 Evaluation of the numerical efficiency . . . . . 116**

3.4.1 Standard benchmarks . . . . . 116

3.4.2 Massive grain growth computations and topological analysis . 119

**3.5 Immersion of real microstructure from experimental data . . . . . 126**

3.5.1 Procedure . . . . . 126

3.5.2 Illustration . . . . . 132

# Résumé en français

Ce chapitre est consacré à l'étude des limites d'utilisation des fonctions level set globales. Bien que ces dernières permettent d'important gains de temps de calcul et de mémoire vive, il y a aussi des difficultés inhérentes liées à leur utilisation. La première de ces limitations est la possibilité de coalescence numérique entre les grains représentés par une même fonction, qui doit être impérativement évitée afin de garantir la cohérence des résultats. Le deuxième difficulté liée à l'utilisation des fonction level set globales est l'impossibilité d'accéder directement aux propriétés intrinsèques des grains, comme leur taille. Dans les précédents travaux [Fabiano 2013; Cruz-Fabiano et al. 2014], la coalescence était retardée en introduisant une séparation initiale suffisante entre les grains représentés par une même fonction dans la microstructure initiale. Bien que simple à mettre en œuvre, cette approche a été démontrée inefficace d'un point de vue numérique, et ne résout pas le problème concernant l'évaluation des caractéristiques intrinsèques des grains. Une nouvelle méthode a donc été proposé pour répondre à ces problématiques. Elle se compose de deux étapes. D'abord, les composantes connexes d'une même fonction level set globale sont séparées à l'aide d'un nouvel algorithme spécifique capable d'opérer directement dans un cadre éléments finis parallèle. Ensuite, les risques de coalescence sont détectés et traités de façon dynamique à chaque incrément de la simulation. L'implémentation numérique proposée pour cet algorithme tire parti d'une stratégie utilisant des boîtes englobantes pour évaluer la distance séparant les composantes connexes. Cette approche a démontré une très grande efficacité numérique et permet d'importants gains de mémoire. Des facteurs d'accélération proche de deux ont ainsi été obtenus pour des simulations en trois dimensions tout en évitant la coalescence numérique sans aucune hypothèse simplificatrice. En outre le nouvel algorithme développé pour la séparation des composantes connexes permet également de suivre les propriétés de chaque grain. Grâce à ces nouveaux outils, des polycristaux à très grand nombre de grains ont pu être simulés en deux et trois dimensions avec des coûts calcul et mémoire très intéressants. Nous nous sommes intéressés à la topologie et à l'évolution de la microstructure au cours du traitement thermique. Ces évolutions ont été analysées et confrontées avec succès à des modèles en champ moyen. Enfin une nouvelle procédure d'immersion a été proposée afin de représenter des polycristaux réels dans un maillage éléments finis grâce aux fonctions level set globales. Cet algorithme pilote la répartition des grains dans les fonctions level set globales et utilise la méthode de réinitialisation introduite dans section 2.4 pour initialiser les fonctions distances. Une simulation de traitement thermique en trois dimensions à partir de données expérimentales a finalement été

réalisée grâce à ce nouvel algorithme d'immersion. Les résultats numériques obtenus grâce à notre modèle level set/éléments finis doivent maintenant être comparés à des simulations en champ de phase et des observations *in situ* réalisées à l'université d'Ulm dans le cadre d'une collaboration. Les développements numériques présentés dans ce chapitre ont permis la publication d'un article dans une revue internationale à comité de lecture [Scholtes et al. 2015].

## 3.1 Introduction

The DRT reinitialization algorithm introduced in the previous chapter has permitted to reduce significantly the numerical cost of our LS-FE simulations. However it was found that the important number of distance fields needed is still very restrictive, especially in 3D. In the present chapter the objective is to improve this situation by working on the coloring aspect. New numerical tools are introduced to overcome the important limitations of the existing method based on a fixed coloring of the grains. We detail their implementation within the considered FE framework and investigate challenging benchmarks in 2D and 3D to evaluate their efficiency. Finally the immersion of real polycrystals in a FE mesh is explored. We propose a method for initializing the GLS functions based on experimental data, which takes full advantage of grain coloring and of the new numerical tools introduced in the previous chapter. A virtual polycrystal is finally generated and GG mechanism simulated, based on a 3D image obtained by X-Ray tomography.

## 3.2 Basics about grain coloring

### 3.2.1 Principle

The simulation time is strongly related to the number of GLS functions $N_p$. So using a distance function for each grain is unfeasible when several thousand of grains are considered in LS simulations. The simple alternative is grain coloring and consists in using GLS functions, each representing a set of distinct grains in the initial microstructure. This technique reduces drastically the number of needed colors (*i.e.* GLS functions), as shown on fig. 1.14a. Especially in 2D, the *four color theorem* [Appel et al. 1977a; Appel et al. 1977b] states that no more than four colors are required to map a microstructure so that no two adjacent grains have the same color. This theorem has no equivalent in 3D but different tests have shown that around 20 colors are generally sufficient to map a 3D polycrystal for any number of grains. So grain coloring is a very interesting approach for limiting the number of distance functions, the numerical costs and also the memory requirements.

### 3.2.2 Limitations

Given the previous statement, using the strict minimal of colors (4 in 2D, around 20 in 3D) provides optimal numerical efficiency and minimizes the memory requirement. But this radical approach is limited to the cases where the connected components

(*i.e.* the grains in the present application) are static or subjected to very small displacements. In other configurations, the moving child grains (*i.e.* grains sharing the same color) can meet each other during a simulation and merge to form a single one, whose shape is the union of the first two grains. This phenomenon called numerical coalescence is illustrated on fig. 1.14b. A significant amount of coalescence during a simulation alters the kinetics and may have dramatic consequences on the numerical predictions [Fan et al. 1997b]. So it is crucial to avoid (or at least to delay) this purely numerical issue.

### 3.2.3 Existing situation and problem statement

The initial solution adopted in [Fabiano 2013; Agnoli 2013; Jin et al. 2014] was to delay the appearance of coalescence by initializing the microstructure with a number of GLS functions $N_p^\delta$ which ensures a minimal separation of $\delta$ exterior grains between the child grains. Obviously this parameter $\delta$ determines directly the number of colors needed to map the initial microstructure. So it must be chosen small to limit the number of GLS functions and the simulation time while being high enough to prevent a significant amount of coalescence during the simulation. This approach is obviously not systematic and estimating a priori (*i.e.* before the simulation) a correct value for $\delta$ is very complex because it depends on the metallurgical phenomena that are simulated and the considered material. Finally this approach is also numerically not optimal because it uses much more functions than needed to represent the aggregate, which increases the computational costs associated with the resolution of eq. (1.47) and reinitialization. This represents a strong limitation of the existing FE-LS approach that must be addressed. This is the objective of the present chapter.

## 3.3 Improvement of the existing situation

### 3.3.1 Literature review

The objective is to propose a method working within a parallel FE framework which would enable to perform coalescence-free simulations with a minimal number of colors. We opt for a dynamic solution consisting in an automatic reassignment of the grains in the GLS functions (*i.e.* grain recoloring) when coalescence is about to occur. Such an approach has been introduced in 2002 in the context of PF computations with regular grids [Krill III et al. 2002]. The approach proposed by Krill et al. is based on a simple idea: if two child grains are separated by only one exterior grain, there exists a risk of numerical coalescence between these two grains and one of them must

therefore be recolored. Their algorithm maintains for each grain with index $g$ a list of its short-range neighbors (*i.e.* adjacent grains) and long-range neighbors (*i.e.* adjacent grains + neighbors of at least one adjacent grain). At each increment the list is inspected. If one long-range neighbor is represented by the same PF function, then it is reassigned to another PF function. Obviously the same procedure can also be applied to distance functions. This algorithm is relatively simple providing that we are able to separate the connected components, *i.e.* distinguish the grains composing each PF/GLS function. No details are given in [Krill III et al. 2002] concerning the algorithm employed to perform the separation of the connected components (SCC), even if it is worth noting that the problem of the SCC using regular grids is well-addressed in the literature. On the other hand performing such an individual identification of the grains is much more complicated on FE meshes, especially in a parallel framework. Authors mention that thanks to this algorithm, they were able to reduce the number of needed PF functions to 20 and 50 respectively in two and three dimensions.

A variant of the above approach has been proposed recently by Elsey et al. [Elsey et al. 2009] in a LS framework with Fourier transform resolution. This algorithm uses a different criterion and triggers a recoloring operation when two child grains of $\psi_i$ become $\tau$-close, *i.e.* their union is completely contained in the same connected component represented by $\psi_i > -\tau$, where $\tau$ is a distance parameter correlated with the simulation time step. By using this algorithm the authors state that no more than 32 and 64 GLS functions are needed in 2D and 3D, respectively. Again nothing is clearly detailed concerning the strategy employed to perform the SCC and its numerical cost, even if the underlying numerical method relies on regular meshes.

These dynamic approaches are very attractive because they are systematic in the sense that they do not require to estimate *a priori* the number of GLS functions that will be needed for the simulation. Furthermore they permit to avoid coalescence events based on simple considerations concerning the grain neighbourhood or the distance between the child grains. On the other hand, these approaches are, to our knowledge, only employed in the context of regular grids for the time being and no details is given concerning the procedure employed for the SCC and the associated numerical costs. Finally we estimate that, even if the number of functions employed in these previous studies is much less than the number of grains, it can be further improved. Let us recall that **our final objective is to use a minimal number of colors and to prevent coalescence in any case**. We introduce in this chapter a new dynamic algorithm enabling to perform coalescence-free simulations with nearly optimal numerical efficiency. Although this algorithm is here implemented in a LS model work-

ing within a parallel framework using unstructured FE meshes, it is perfectly general and can also be employed for PF-FE simulations.

### 3.3.2 Development of an efficient recoloring scheme

The final objective of this algorithm is to handle dynamically the grain coloring during the simulation. So it must be able to transfer automatically one or more child grains in another GLS functions if these grains become too close from each other. The present algorithm is divided in two steps:

- separate the connected components represented by the GLS functions,
- detect the risks of coalescence and *swap* (*i.e.* reassign) the grains in other GLS functions when coalescence is likely to occur.

#### Separation of the connected components

Before considering the recoloring step itself, it is necessary to distinguish the child grains and identify them individually. More specifically our objective is here to create, for each GLS function $\psi_i$, an index field noted $\mathscr{I}_i$ wherein its grains are represented by a unique identifier. First we perform the procedure entitled TAG_NODE_AND_NEIGHBORS in algorithm 1 on each GLS function. For the sake of clarity let us designate by $\mathscr{M}$ the FE mesh and $\mathscr{V}(n)$ the patch of the $n^{th}$ mesh node, *i.e.* the set of nodes connected to $n$ by an element edge.

When a node located inside the $i^{th}$ GLS function is found (*i.e.* $\psi_i \geq 0$), it is assigned an integer value $id$ (see figs. 3.1a and 3.1b). Then its neighbors are recursively contaminated (see figs. 3.1c and 3.1d) until the interface is reached (see figs. 3.1d and 3.1e). The variable $id$ is finally incremented and the procedure continues with the remaining unlabeled nodes. This first operation has a complexity which is almost linear.

It is obvious that the previous algorithm does not work in parallel because a process cannot access to the mesh nodes located on another partition. Let us consider the example of fig. 3.2a for an illustration.

In this worst case scenario, three partitions $P_0$, $P_1$ and $P_2$ share two components. One is totally located on $P_2$ while the other is shared by the three of them. Moreover the latter is seen as two distinct components by $P_1$. To solve this situation and any other situations that may occur with more processes or components, the following divide and conquer procedure is performed:

**Algorithm 1** Recursive tagging of the connected components

```
function TAG_NODE_AND_NEIGHBORS(Field 𝒮_i, Node n, Patch 𝒱(n), Integer id)
    𝒮_i(n) ← id
    for Node ñ ∈ 𝒱(n) do
        if 𝒮_i(ñ) == −1 then
            TAG_NODE_AND_NEIGHBORS(𝒮_i, ñ, 𝒱(ñ), id)
        end if
    end for
end function
procedure TAG(Field ψ_i)
    Define an integer id ← 1
    for Node n ∈ ℳ do
        if ψ_i(n) ≥ 0 then
            𝒮_i(n) ← −1
        else
            𝒮_i(n) ← 0
        end if
    end for
    for Node n ∈ ℳ do
        if 𝒮_i(n) == −1 then
            TAG_NODE_AND_NEIGHBORS(𝒮_i, n, 𝒱(n), id)
            id ← id + 1
        end if
    end for
    return 𝒮_i
end procedure
```

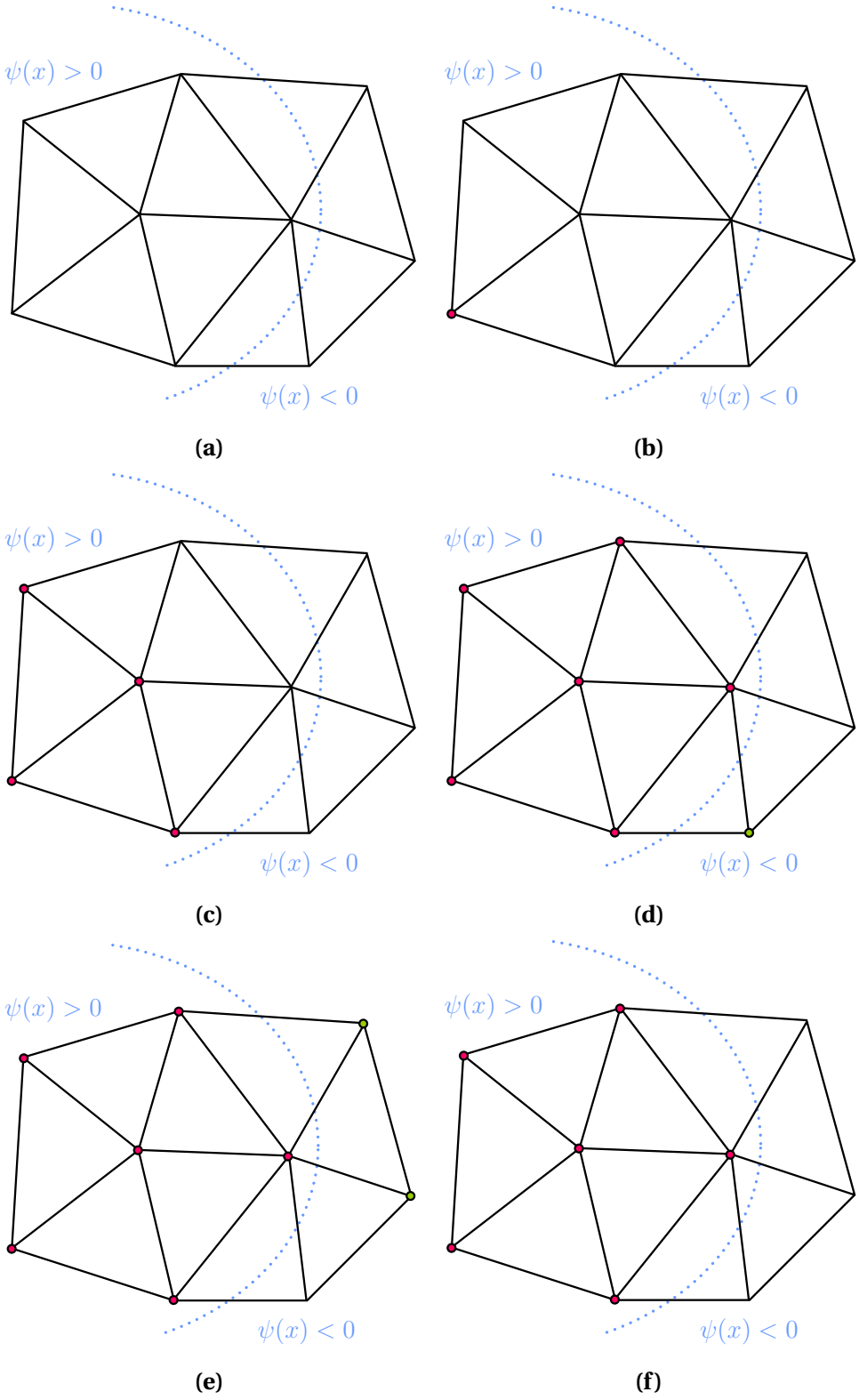


**Fig. 3.1** – Sequential tagging procedure. The recursive propagation stops when a node satisfying $\psi < 0$ is met (represented by the thick green circles), which indicates that the interface has been crossed.

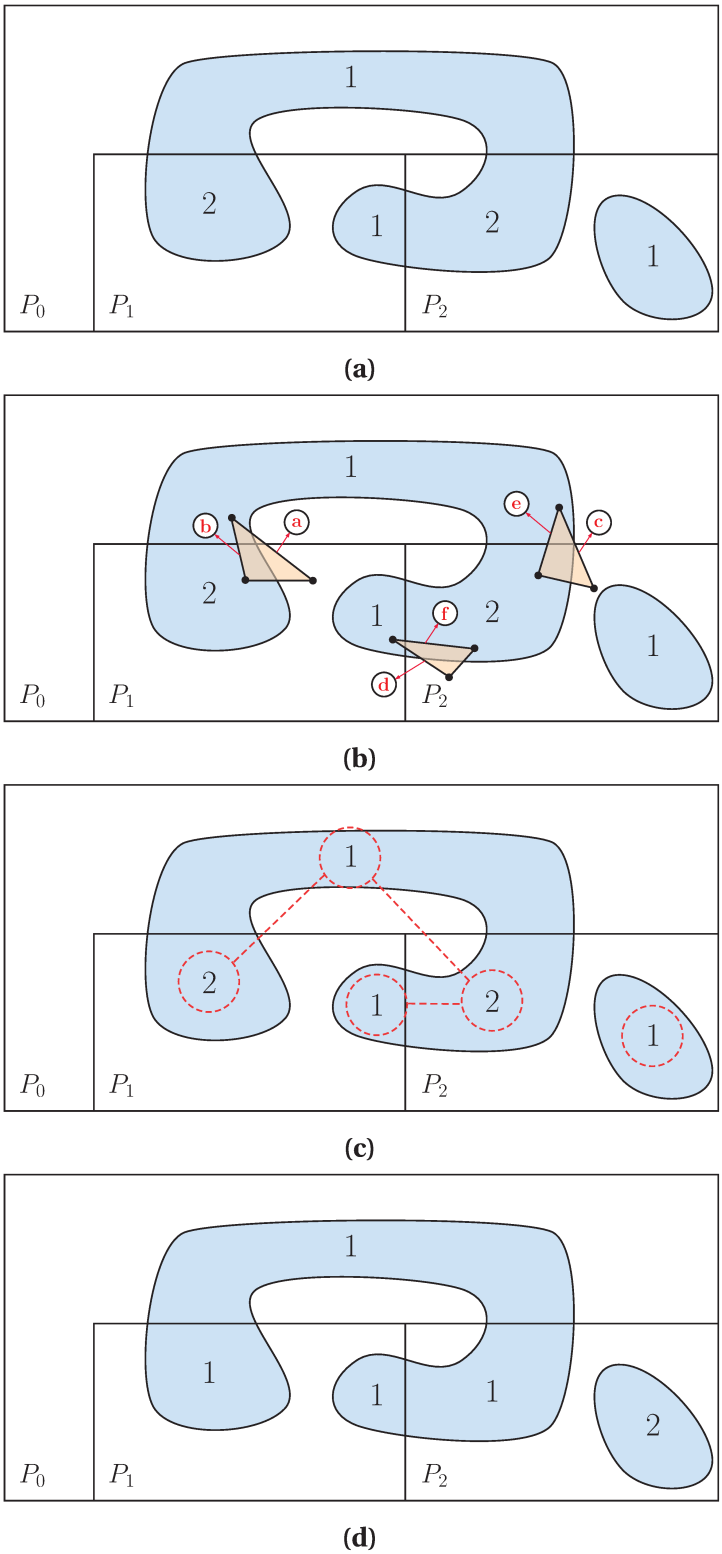


**Fig. 3.2** – (a) Example presenting a worst case scenario for tagging in a parallel context; (b) local tags after performing algorithm 1 independently on each partition; (c) graph giving the tag conflicts; (d) final global tags.

1. each process performs algorithm 1 independently, leading to independent tags, possibly redundant,
2. in algorithm 1, when a node located on another partition is met, it is stored in a set,
3. this set is communicated between the processes,
4. each process receives messages of type "Process $P_i$ wanted to tag your node $n$ with tag $id$"; if node $n$ already has a not null $id$, the conflict is communicated to the root process,
5. the root process solves the conflicts by applying algorithm 1 on the tags instead of the nodes,
6. the root process finally broadcasts the new global tags to the other processes.

Let fig. 3.2b be the result of the first step of this procedure performed on the worst case configuration given by fig. 3.2a. $P_0$ has recognized one connected component, tagged as "$P_0$'s 1", $P_1$ has a number 1 and a number 2 connected components, and $P_2$ has also a number 1 and number 2 connected components. During its tagging loop, $P_0$ has seen that some of its nodes are connected (by an element edge) to nodes located on $P_1$ and $P_2$, and the same for the other two. To prevent redundancy, one chooses to consider there is a conflict only if the identifier of the neighboring partition is higher than the one of the current partition. For example let us consider we are on partition 1 (corresponding to the process $P_1$). If a node of $P_0$ is met, there is no conflict because $1 > 0$. On the other hand, if a node of $P_2$ is met, the conflict is detected and stored in the set. A description of all possible situations can then be established (the item letters correspond to the element edges represented on fig. 3.2b):

(a) $P_1$ has a 0 (unlabeled) node that $P_0$ sees as tag 1 → there is no conflict,

(b) $P_1$ has a 2 node that $P_0$ sees as tag 1 → the conflict "$P_0$'s 1 means $P_1$'s 2" is stored,

(c) $P_2$ has a 0 node that $P_0$ sees as tag 1 → there is no conflict,

(d) $P_2$ has a 0 node that $P_1$ sees as tag 1 → there is no conflict,

(e) $P_2$ has a 2 node that $P_0$ sees as tag 1 → the conflict "$P_0$'s 1 means $P_2$'s 2" is stored,

(f) $P_2$ has a 2 node that $P_1$ sees as tag 1 → the conflict "$P_1$'s 1 means $P_2$'s 2" is stored.

The next step of the algorithm is, for each process, to send its tags along with these conflicts to the root process. All redundancies are then treated by applying algorithm 1 on a specific graph constructed by the root process in which the nodes are the local tags of each process and there exists a connection between two nodes if there is a conflict between them (see fig. 3.2c). After performing the algorithm on such graph, one obtains the global tags which are unique for each connected component. The matching table between local and global tags is finally broadcasted to all processes, which correct their numbering. Figure 3.2d illustrates the final result of the whole procedure.

This step of the algorithm is critical because all the conflicts are treated by the root process. Nevertheless, its complexity depends on the number of connected components represented by the GLS function, which is several order of magnitude lower than the number of mesh nodes. As it will be demonstrated in the last section of this chapter, this sequential procedure does not affect the numerical efficiency of the algorithm in the considered context of polycrystal simulations.

The fig. 1.14a illustrates a concrete microstructure composed of 25 grains ($N_g = 25$). The input is the characteristic function $\chi_i$ of the $i^{th}$ GLS function which is equal to one where $\psi_i \geq 0$ and zero elsewhere. Finally the resulting field $\mathscr{I}_i$ is obtained thanks to the SCC algorithm, wherein each component is labelled by a unique $id$ as depicted on fig. 3.3b.

### Swapping algorithm

After performing the SCC on each GLS function, we are now able to tackle the problem of the automatic grain recoloring. Next the term *swapping* is preferred to *recoloring* because we do not perform a full recoloring of the grains constituting the microstructure. Effectively only the child grains which are getting too close from each other are actually recolored. The algorithm introduced in this section is relatively similar to the one discussed in [Krill III et al. 2002; Elsey et al. 2009] with the exception that it is here developed, described and applied to unstructured FE meshes. It is also further optimized and permits nearly optimal numerical efficiency.

The first step consists in gathering all the $\mathscr{I}_i$ functions with $i \in \{1, ..., N_p\}$ and creating a unique $P_1$ field $\mathscr{I}^{glob}$ wherein all grains of the microstructure are simultaneously represented by a unique *id*:

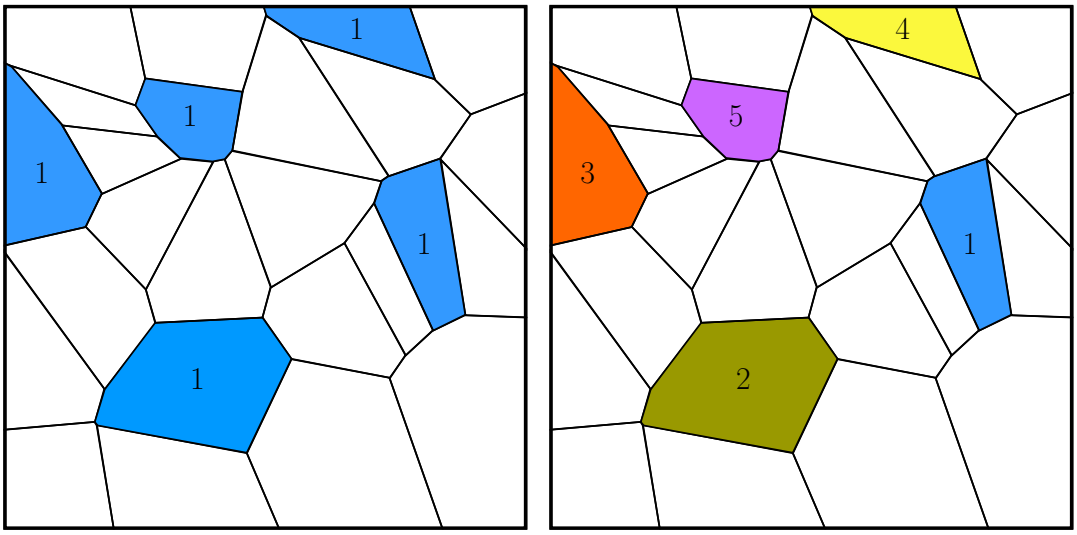


**Fig. 3.3** – (a) Characteristic function $\chi_i$ associated with the $i^{th}$ GLS function which contains five grains; (b) the resulting field $\mathscr{I}_i$ obtained after performing the SCC procedure on the microstructure of (a). The white zone corresponds to a null value.

$$\mathscr{I}^{\text{glob}}(x) = \max_{1 \leq i \leq N_\text{p}} \mathscr{I}_i(x),\ \forall x \in \Omega. \tag{3.1}$$

The $\mathscr{I}^{\text{glob}}$ field calculated for the microstructure of fig. 1.14a is depicted on fig. 3.4. Then, each process scans its element edges and constructs the local *short-range neighborhood* (first neighbors only) associated to each grain. These local tables (one for each process) are then communicated to the root process which handles their association. The global short-range neighborhood $\mathscr{S}(g)$ associated with each grain $g$ is finally built and broadcasted to all processes. In the example illustrated on fig. 3.4, one has $\mathscr{S}(0) = \{8, 11, 20\}$, $\mathscr{S}(6) = \{2, 12, 22, 24\}$...

By mixing the previous tables, the *long-range neighborhood* $\mathscr{L}(g)$ of each grain $g$ can be built which is composed of the first and second neighbors (FSN). Going back to the microstructure of fig. 3.4 one has: $\mathscr{L}(0) = \{3, 5, 7, 8, 11, 16, 17, 18, 20, 23\}$, $\mathscr{L}(6) = \{2, 7, 10, 12, 13, 15, 16, 19, 21, 22, 24\}$... Finally an other table giving the long-range neighborhood (in terms of grains) of each GLS function is also constructed:

$$\mathscr{G}(i) = \Big|\Big| \mathscr{L}(g),\ \ \forall g \in \{1, ..., N_\text{g}\} / \mathscr{C}(g) = i, \tag{3.2}$$

where $\mathscr{C}(g)$ is a corresponding table returning the index $i$ of the GLS function which contains the grain $g$ and $||$ denotes the list concatenation operator. Obviously this

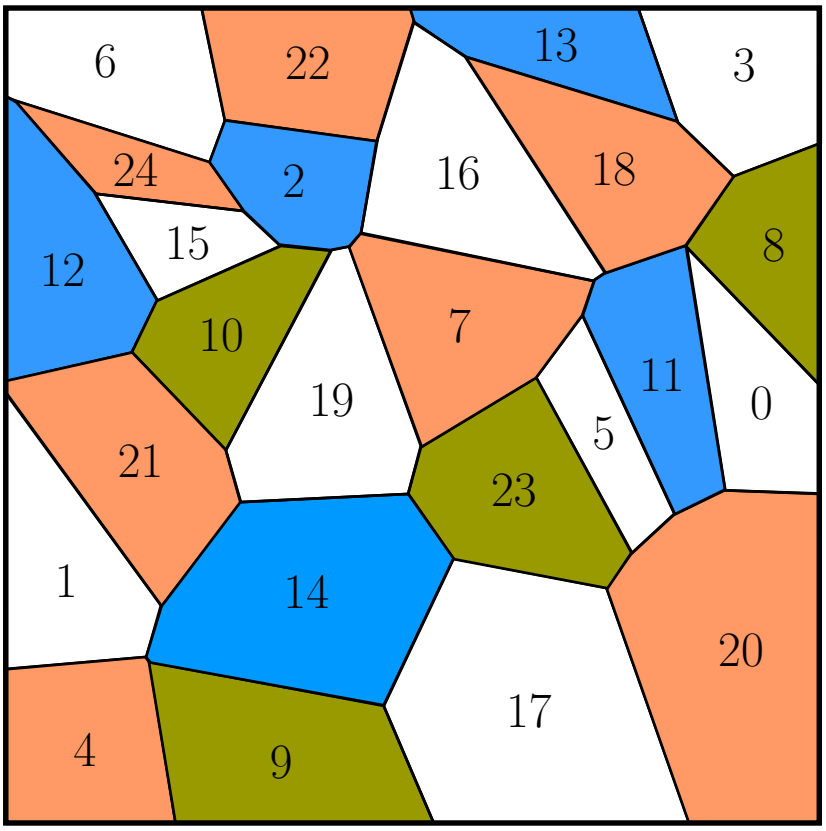


**Fig. 3.4** – $\mathscr{I}^{\text{glob}}$ field wherein each grain of the microstructure has a unique $id$.

table evolves during the simulation due to the swapping operations.

It is worth noting that the long-range neighborhood of the $i^{th}$ GLS function may contain redundancies because an exterior grain of $i$ can be a FSN of several grains represented by $\psi_i$. Conserving these redundancies is crucial in our algorithm. Let us consider the grain labelled 2 on fig. 3.4 for an illustration. This grain is connected five times to the white GLS function (because it is a FSN of grains 5,6,15,16 and 19). So if the grain labelled 6 is transferred from the white to the green function, the grain 2 would remain connected four times to the white function.

After these tables have been created, the sets $\mathscr{L}(g)$ are scanned. If there exists a grain $\tilde{g} \in \mathscr{L}(g)$ which is also a child grain of $g$ (*i.e.* $\mathscr{C}(g) = \mathscr{C}(\tilde{g})$), it is assumed that numerical coalescence is possible. This approach is strictly equivalent to the one introduced by [Krill III et al. 2002] which considers there is a risk when only one exterior grain separates two child grains. Hereafter this simple criterion is referred as $C_1$. In such situation, the following swapping procedure is performed:

**if** $\exists q \neq \mathscr{C}(g)$ / $g \notin \mathscr{G}(q)$ **then**

1. transfer the grain $g$ from $\psi_{\mathscr{C}(g)}$ to $\psi_q$,
2. remove $\mathscr{L}(g)$ from $\mathscr{G}(\mathscr{C}(g))$, add it to $\mathscr{G}(q)$ and finally update $\mathscr{C}$: $\mathscr{C}(g) = q$,

**else if** $\exists q \neq \mathscr{C}(\tilde{g})$ / $\tilde{g} \notin \mathscr{G}(q)$ **then**

execute 1. and 2. by replacing $g$ by $\tilde{g}$,

**else**

initialize a new GLS function $N_\mathrm{p} \leftarrow N_\mathrm{p} + 1$ and execute (2) with $q = N_\mathrm{p}$.

A major advantage of this strategy lies in the fact that it can be easily extended to the needs of ReX modeling. More specifically the values of the fields of interest (dislocation densities, stored energy, orientation...) associated with the swapped grain can also be directly transported in the receipting field. This allows for a grain to keep its properties which are related to its thermomechanical state. This point is further detailed in the next chapter.

The result of this algorithm performed on the microstructure of fig. 1.14a is depicted on fig. 3.5. This is actually a worst case scenario because the microstructure of fig. 1.14a has been initially colored with a minimal separation $\delta = 1$, giving conflicts

everywhere.

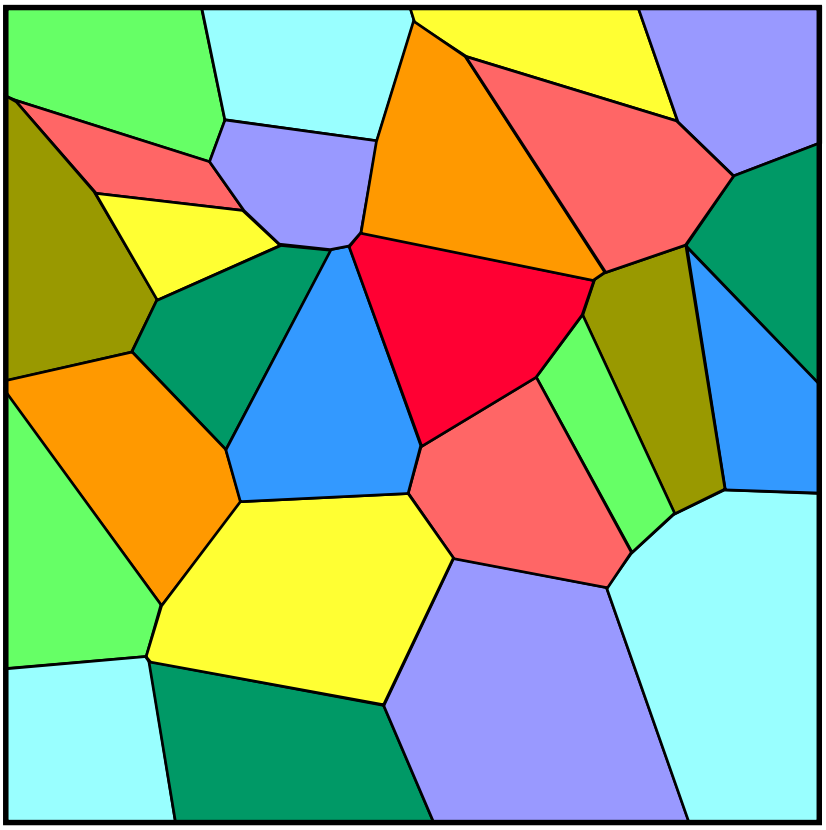

**Fig. 3.5** – New grain coloring after performing the $C_1$ swapping algorithm on the initial microstructure of fig. 1.14a. It is now represented by 10 GLS functions (instead of 4 initially) separated by at least two exterior grains.

The previous algorithm has been extensively challenged and tested in [Scholtes et al. 2015]. Especially a large-scale 2D polycristalline aggregate containing around 50,000 grains has been simulated with less than 20 GLS functions. The computation times associated with the SCC and the swapping algorithm have been demonstrated very low despite the large number of needed swapping operations (18,000 for the present case). A large-scale 3D simulation with 5000 initial grains has also been performed. For this simulation the number of GLS functions never exceed 61 which is in agreement with the conclusions of Krill et al. [Krill III et al. 2002] and Elsey et al. [Elsey et al. 2009]. In 3D the numerical cost associated with the swapping algorithm represents again a very small amount of the computation time (< 1%). On the other hand, the SCC procedure was observed to be much more costly in 3D and represents around 17% of the whole computation time. This was initially attributed to the higher number of needed colors in 3D, which increases the number of operations in the SCC algo-

rithm. Actually the implementation used for this simulation was not fully optimized because the nodal patch of each mesh node was reconstructed for each GLS function. This is obviously not necessary because the patches are only related to the FE mesh and not to the GLS functions. Although this bug has since been corrected, the high number of colors still penalizes the numerical efficiency of the simulation. Especially the resolution of the CDEs for the different GLS functions represents more than the half of the simulation time. Also this case requires a large amount of RAM memory. Hereafter, we propose an optimization of this algorithm based on a redefinition of the long-range neighborhood of the grains.

**Optimization**

We showed that the previous swapping algorithm remains limited, especially when it comes to consider particular microstructures with strong size heterogeneities, such as these obtained when nucleation occurs. Furthermore, we estimate that the number of colors needed in the previous simulations (around 20 and 60 respectively in 2D and 3D) and then the numerical efficiency can be further optimized. A new swapping criterion referred as $C_2$ has therefore been developed.

According to the $C_1$ criterion, $\tilde{g}$ is directly added in $\mathscr{L}(g)$ without any restriction (see eq. (3.2)). So $\mathscr{L}(g)$ contains all the FSN of the $g^{th}$ grain. In practice, if the distance separating two grains is sufficient, there is no risk of coalescence between two consecutive increments, even if there is only one exterior grain between them. So, in the $C_2$ criterion we firstly evaluate the algebraic distance $d(g,\tilde{g})$ separating $g$ and $\tilde{g}$ in order to determine whether $\tilde{g}$ is added in $\mathscr{L}(g)$ or not. Finally by noting $\xi$ a distance parameter, $\tilde{g}$ can be safely ignored if $d(g,\tilde{g}) > \xi$. This has two consequences:

- no conflict can arise between $g$ and $g^\star$, even if $\mathscr{C}(g) = \mathscr{C}(\tilde{g})$,
- by assuming $\mathscr{C}(g) \neq \mathscr{C}(\tilde{g})$ initially, it is perfectly possible that they become child grains after the swapping procedure.

Thus it is obvious that working with $C_1$ is equivalent to use $C_2$ with $\xi = \infty$. In order to maintain high numerical efficiency the exact distance between $g$ and $\tilde{g}$ is not directly computed. Instead we evaluate the distance between their respective bounding boxes in the Cartesian coordinate system used to generate the REV. This box-to-box distance determines whether $\tilde{g}$ is accepted in $\mathscr{L}(g)$ or not. The fig. 3.6 illustrates these two situations: in fig. 3.6a, it is assumed that $d(g,\tilde{g}) < \xi$ which implies $\tilde{g}$ is added in $\mathscr{L}(g)$ ; in fig. 3.6b the grain $\tilde{g}$ is safely ignored because the separation is sufficient.

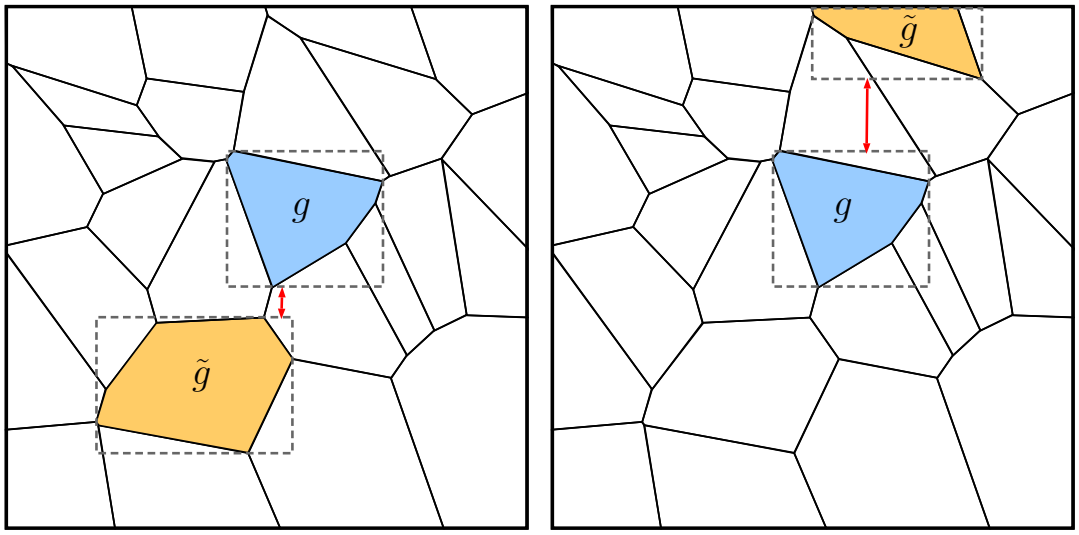


**(a)** $d(g,\tilde{g}) < \xi$ **(b)** $d(g,\tilde{g}) > \xi$

**Fig. 3.6** – Calculation of the distance between the bounding boxes of $g$ and $\tilde{g}$ (represented by the red thick arrow) and decision concerning $\tilde{g}$: (a) $\tilde{g}$ must be included in $\mathscr{L}(g)$ ; (b) $\tilde{g}$ can be safely ignored.

This optimization completes the whole recoloring scheme. Next we challenge its efficiency through diverse simulations in 2D and 3D.

## 3.4 Evaluation of the numerical efficiency

### 3.4.1 Standard benchmarks

Let us reconsider the 2D case previously detailed in section 1.5.3 and section 2.5. It was found that $N_{\mathrm{p}}^{\delta=3} = 27$ are needed to represent this microstructure with an initial separation $\delta = 3$, which is assumed sufficient to prevent a significant amount of numerical coalescence according to Fabiano et al. [Cruz-Fabiano et al. 2014]. Next the same simulation is repeated with the above recoloring scheme. For this purpose, the polycrystal is firstly initialize with the strict minimal number of GLS functions and then we perform a first iteration of the recoloring algorithm in order to solve the coloring conflicts present in the initial microstructure, *i.e.* recoloring of the FSN which satisfy $d(g,\tilde{g}) < \xi$ (see fig. 3.6a). Different tests have demonstrated that fixing $\xi = \langle R \rangle / 2$ is largely sufficient to prevent any coalescence event during the simulation. So we adopt this value hereafter. However let us remind that this parameter is optional, contrary to $\delta$, and stands only for an optimization of the recoloring scheme that allows to use less GLS functions. By using this strategy, only $N_{\mathrm{p}} = 10$ colors are needed for

the whole simulation. We detail the simulation time in table 3.1. The notations $t_{\text{SCC}}$ and $t_{\text{swapping}}$ are introduced to designate the computation times associated with the SCC and swapping algorithms, respectively.

| | Initial | | With DRT | | With DRT + Recoloring | |
|---|---|---|---|---|---|---|
| $t_{\text{remesh}}$ | 4h 11min | (6.4%) | 4h 22min | (57.1%) | 4h 20min | (72.4%) |
| $t_{\text{resol}}$ | 2h 02min | (3.1%) | 1h 57min | (25.6%) | 43min | (12%) |
| $t_{\text{reinit}}$ | 59h 04min | (89.8%) | 52min | (11.3%) | 27min | (7.6%) |
| $t_{\text{SCC}}$ | | - | | | 1min | (0.2%) |
| $t_{\text{swapping}}$ | | - | | | 1min | (0.2%) |
| $t_{\text{other}}$ | 28min | (0.7%) | 28min | (6%) | 28min | (7.6%) |
| $t_{\text{simu}}$ | 65h 45min | | 7h 33min | | 5h 59min | |

**Table 3.1** – Distribution of the computation time with and without the newly developed recoloring scheme for the 2D GG simulation detailed in section 1.5.3. Simulations are performed on 6 Xeon Intel CPUs.

We observe that $t_{\text{SCC}}$ and $t_{\text{swapping}}$ are negligible ($< 1\%$) despite more than 1000 recoloring operations have been performed during this simulation. This demonstrates the efficiency of the present implementation. The global computation time is finally reduced by a factor 1.3 compared to the situation of chapter 2 which is relatively disappointing. So using the recoloring scheme does not increase significantly the numerical efficiency in this case. It is mainly due to the fact that most of the computation time is devoted to the remeshing operations in this 2D case and its complexity is independent of $N_{\text{p}}$. However using the previous recoloring technique presents two great advantages. First, the parameter $\delta$ which translates the initial separation between the colored grain is removed. Effectively, as the coloring of the grain is dynamically handled and the algorithm creates automatically new GLS functions when it is needed, **the microstructure can be simply initialized with the strict minimal number of colors in any case**. This makes the approach completely systematic because it avoids coalescence and does not require any complex calibration or assumptions. Only the parameter $\xi$ remains in the new formulation but the influence of this parameter is actually very small and our numerical investigations have demonstrated that fixing simply $\xi \approx \langle R \rangle / 2$ works fine in all situations that have been tested (GG, SRX). The second advantage is directly related to the SCC algorithm itself. Effectively, as grains are identified by a unique $id$ during the SCC procedure, it becomes very simple to assess their intrinsic properties which is crucial for the post-treatment, analysis of the simulation results or to take into account the properties at the grain scale. This was impossible with the initial implementation of section 1.5.3, so the newly proposed algorithm is a major advance.

Let us now consider the 3D polycrystal of fig. 2.12a. We repeat the 3D simulation of section 2.5 with identical parameters and introduce the dynamic grain recoloring. The evolution of the number of active GLS functions during the simulation is plotted on fig. 3.7 and the new time distribution is given in table 3.2.

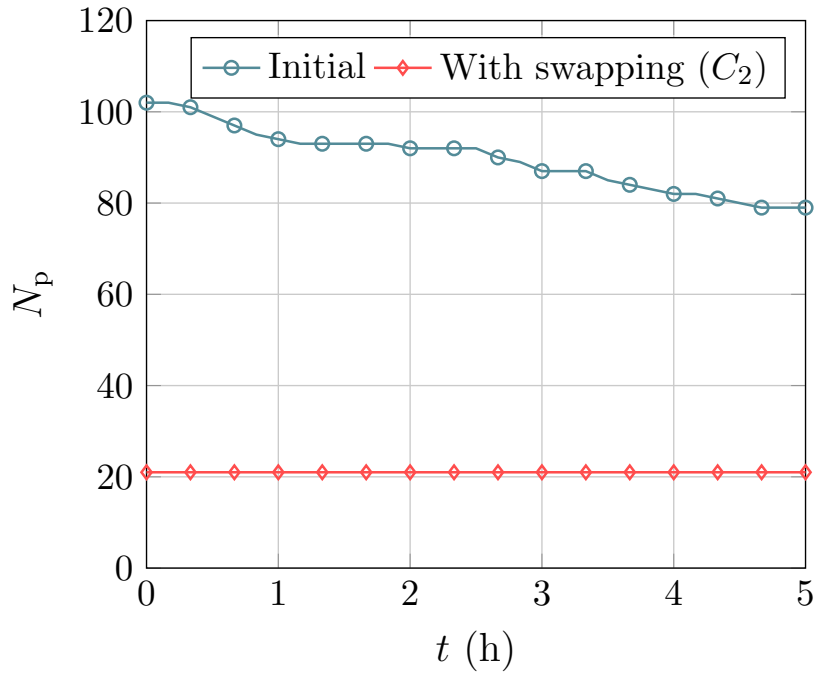


**Fig. 3.7** – Number of active GLS functions during the simulation of a 5h heat treatment using the initial 3D polycrystal of fig. 2.12a.

Because a fixed mesh is used in this 3D case, most computation effort is devoted to the solving of the CDEs and reinitialization. Consequently using much less GLS functions accelerates greatly the simulation in this case. Effectively we observe that $t_{\text{resol}}$ evolves almost linearly with the number of active GLS functions. This is not true for reinitialization, which may seem surprising. But this can be actually easily explained. Let us remind that, for each distance field, a piecewise representation of the interface is firstly constructed at the early stage of the reinitialization algorithm. The complexity of a distance computation is, on average, a logarithmic function of the collection size (see section 2.4). As fewer GLS functions are used when recoloring is active, each contains more grains, which increases the interface length and therefore the size of the associated collection. Consequently the reinitialization of a distance field taken separately requires more efforts when coloration is employed, which justifies that the cost of this operation is not a linear function of $N_p$. However $t_{\text{reinit}}$ is reduced

| | Initial | | With DRT | | With DRT + Recoloring | |
|---|---|---|---|---|---|---|
| $t_{remesh}$ | | | No remeshing | | | |
| $t_{resol}$ | 11h 50min | (9.4%) | 11h 50min | (33.1%) | 2h 47min | (15.2%) |
| $t_{reinit}$ | 113h 49min | (90.5%) | 23h 48min | (66.6%) | 15h 26min | (83.8%) |
| $t_{SCC}$ | | - | | | 3min | (0.2%) |
| $t_{swapping}$ | | - | | | < 1min | (0.0%) |
| $t_{other}$ | 5min | (0.1%) | 5min | (0.3%) | 8min | (0.3%) |
| $t_{simu}$ | 125h 44min | | 35h 43min | | 18h 25min | |

**Table 3.2** – Distribution of the computation time for the simulation of a 5h heat treatment in 3D using the initial polycrystal of fig. 2.12a. Simulations are performed on 12 Xeon Intel CPUs.

by a factor up to 1.5, which remains very interesting. Finally this approach permits great memory savings because around six times less free memory is required for this simulation comparatively with the initial formalism.

To summarize, the numerical developments introduced in section 2.4 and section 3.3.2 have permitted to:

- reduce the overall computation time by a factor of 11 and 7 for the tested configurations in 2D and 3D, respectively,
- increase the robustness of the simulations because less numerical parameters are needed and coalescence is avoided in all simulations,
- assess the properties of the individual grains for the analysis of the simulation results.

In the last section of this chapter, we take advantage of these major advances to perform large-scale GG simulations and analyze the evolutions of the individual grains, which was not possible before these developments. The simulation results are compared with the well-known mean field approximations presented in chapter 1

### 3.4.2 Massive grain growth computations and topological analysis

#### 2D grain growth simulation

First large-scale simulation is performed on a square domain $28 \times 28\text{mm}^2$ composed of 50,000 grains, randomly generated according to a VT method. Consequently the initial mean grain size is around $71\mu$m. The mesh is fixed for numerical convenience with ten million elements. So each grain of the initial microstructure is represented by

approximately 100 elements, on average. A heat treatment of $t_h = 5$h at $T = 1050$°C is simulated. The material is again a 304L austenitic steel, and all the numerical parameters are identical to the ones employed in section 2.5. The calculation of the individual grain sizes uses the index fields returned by the SCC algorithm (see fig. 3.3b). This simulation is performed on "only" 16 CPUs.

Next the predictions of our LS-FE simulation are compared with the classical Hillert mean field theory. Substituting eq. (1.26) in eq. (1.32) gives the surfacic growth rate associated with a grain class in Hillert's formulation:

$$\frac{1}{2\pi M\gamma}\frac{dA_i}{dt} = \beta\left(\frac{R_i}{R_{cr}} - 1\right). \tag{3.3}$$

Here the grain classes are assumed to be directly the grains that compose the virtual aggregate. The theoretical value for the $\beta$ parameter in eq. (3.3) is 0.5 in 2D. Let us remind that this theoretical value relies on diverse assumptions concerning the shapes of the grains in the Hillert's formulation. Especially this model considers that the grains are perfectly circular (respectively spherical in 3D). However, in [Cruz-Fabiano et al. 2014] the offset between the grain size distributions predicted by the full field simulations and eq. (1.26) with $\beta = 0.5$ tends to indicate that $\beta$ could be actually greater than 0.5. We confirm these results on fig. 3.8 where the best fit values calculated at two different stages of the treatment are both greater than 0.5 (respectively 0.61 and 0.57 at $t = 1/3\,t_h$ and $t = 2/3\,t_h$). Approaching the steady-state, $\beta$ becomes stable around 0.55 (see fig. 3.9). According to [Darvishi Kamachali et al. 2015], the adimensional ratio $\langle R\rangle^2/\langle R^2\rangle$ is supposed to be globally constant during GG, which is comforted by our numerical results on fig. 3.9.

The average growth rate of each topological class is plotted on fig. 3.10. A very good agreement is observed between the simulation results and the Von Neumann-Mullins 2D law for $4 \leq n_t \leq 9$, which represents more than 99% of the grains. Also grains having $n_t = 6$ neighbors are found to be stable ($dA/dt \approx 0$), which is comforted by the theory ($n_{cr} = 6$ according to eq. (1.14)).

From a purely numerical aspect, only 10 GLS functions are needed for this simulation with 50,000 initial grains. The overall simulation time is around 6h on 16 CPUs, whose major part is equally distributed between the solving of the PDEs (38%) and reinitialization (45%). Around 10,000 swapping operations are performed, which represents 6% of the simulation time. The SCCs takes less than 1% and the simulation time obtained is outstanding comparatively to the state of the art of full field deterministic

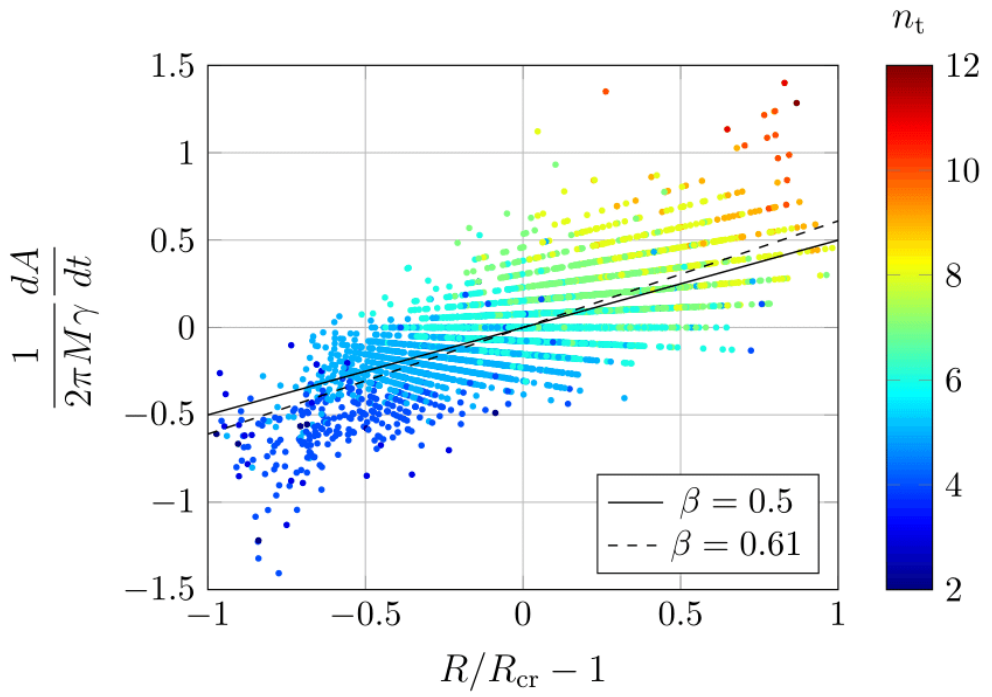


**(a)** $t = 1/3\,t_h$

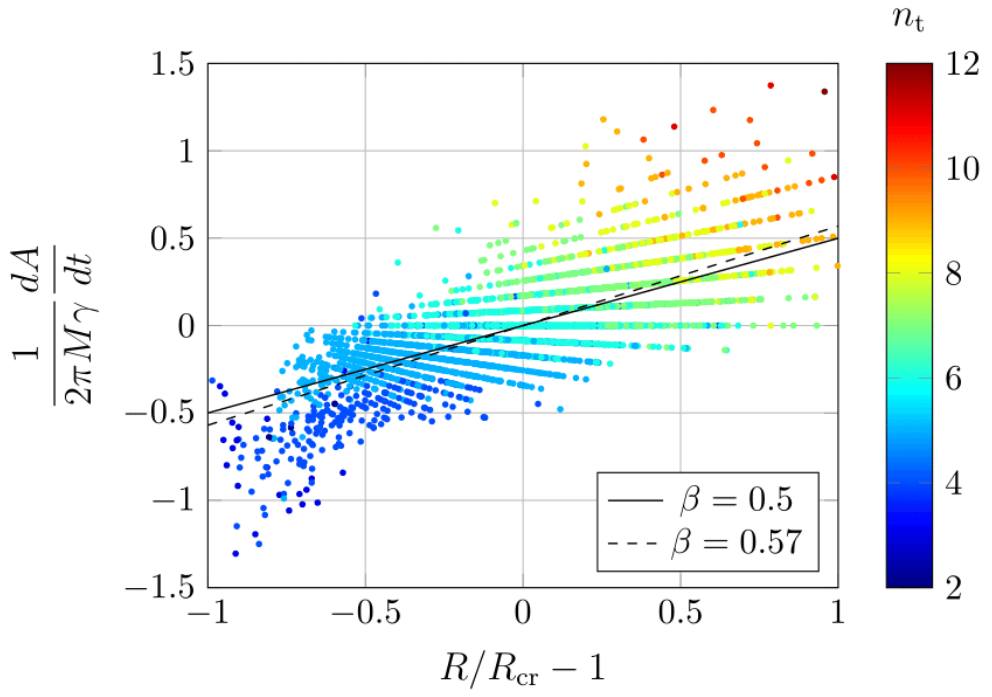


**(b)** $t = 2/3\,t_h$

**Fig. 3.8** – Growth rates of 20,000 grains picked randomly in the 2D polycrystal. The black lines represent eq. (3.3) with two different values for the $\beta$ parameter (Hillert's value [Hillert 1965] and best fit).

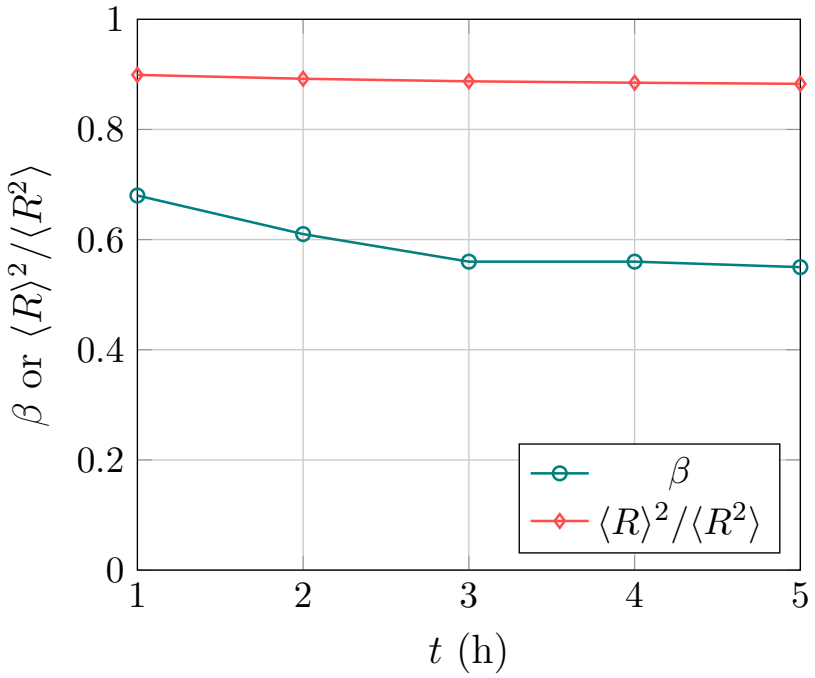


**Fig. 3.9** – Best fit values for $\beta$ in eq. (3.3) calculated from the full field simulation results. As observed by Kamachali et al. [Darvishi Kamachali et al. 2015] the ratio $\langle R\rangle^2/\langle R^2\rangle$ remains stable.

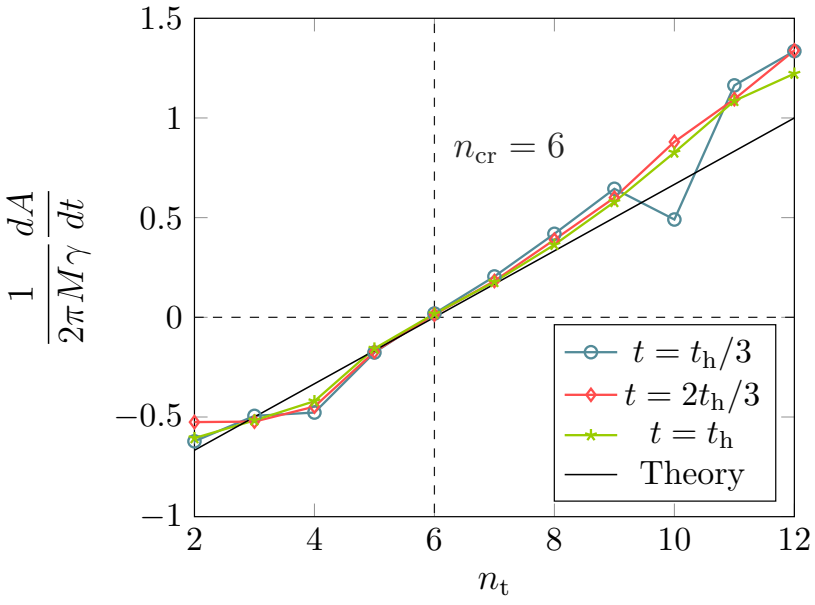


**Fig. 3.10** – Average growth rate associated with each topological class in the 2D simulation. The solid black line refers to the Von Neumann-Mullins law (see eq. (1.14)).

approaches.

### 3D grain growth simulation

The same analysis is now performed in 3D using a cubic REV with edge length 3.5mm and composed of 10,000 grains (see fig. 3.11a). We simulate a heat treatment of $t_h = 5$h at $T = 1050$°C. The FE mesh is fixed and consists of $310^3$ tetrahedral elements. The numerical parameters are identical to the ones employed for the 3D simulation in section 2.5. Figure 3.11 depicts the evolution of the aggregate during the treatment. Around 2000 grains are still present inside the domain after 5h.

The growth rate of a 3D grain can also be expressed in Hillert's formulation by substituting eq. (1.26) in eq. (1.32):

$$\frac{1}{M\gamma} R_i \frac{dR_i}{dt} = \beta \left( \frac{R_i}{R_{cr}} - 1 \right). \tag{3.4}$$

This analytic result is confronted with the simulation results on fig. 3.12. Again the kinetics predicted by the full field model indicates that $\beta > 1$. Same conclusions have been drawn by Kamachali et al. [Darvishi Kamachali et al. 2012] which found $\beta \approx 1.25$ based on the results of large-scale PF simulations. More recently, a 3D analysis using the present LS-FE model has exhibited that $\beta = 1.4$ provides the better predictions for different initial grain size distributions [Maire et al. 2016]. This value ($\beta = 1.4$) is also in good agreement with the present simulation results as the best fit values obtained at $t = t_h/3$ and $t = 2t_h/3$ are respectively $\beta = 1.49$ and $\beta = 1.48$ (see fig. 3.12).

Finally the respective evolution of each topological class is investigated on fig. 3.13. A very good agreement with the 3D Mullins law (see eq. (1.16)) is obtained in the interval $5 \leq n_t \leq 20$, which represents more than 93% of the grains present in the simulation domain. The deviation observed for $n_t \geq 25$ can be due to the small number of grains in these topological classes, which are typically represented by less than 10 grains. The stable topological class is found to be $n_{cr} \approx 13.75$ according to this simulation, which is very close to the value $n_{cr} = 13.39$ obtained by Rios and Glicksman [Rios et al. 2006] (see eq. (1.18)) and in the range $13.5 \leq n_{cr} \leq 14$ proposed by Kamachali et al. [Darvishi Kamachali et al. 2012].

This 3D simulation requires 2 days and 17 hours of computations using 48 CPUs whose major part is devoted to reinitialization (85%). The rest is divided between the solving of the CDEs (11%) and the diverse post-treatment operations (3%). The SCC and swapping algorithms represent less than 1%. Given the acceleration factors

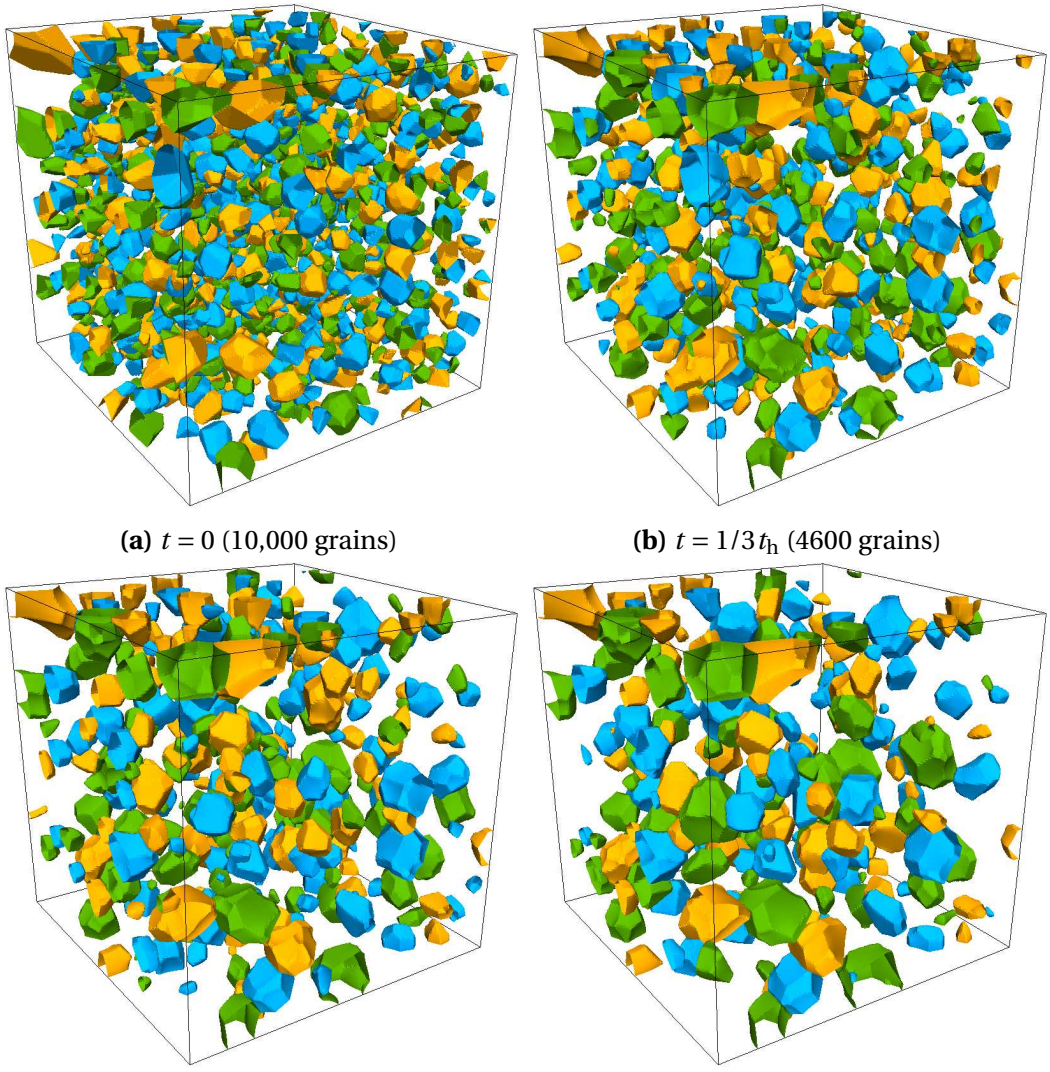

**(a)** $t = 0$ (10,000 grains) **(b)** $t = 1/3\,t_h$ (4600 grains)

**(c)** $t = 2/3\,t_h$ (2750 grains) **(d)** $t = t_h$ (1950 grains)

**Fig. 3.11** – Evolution of the grain boundary network during the simulation of a 5h heat treatment at 1050°C. Only the interfaces of three GLS functions are displaced to facilitate the visualization (shown in different colors).

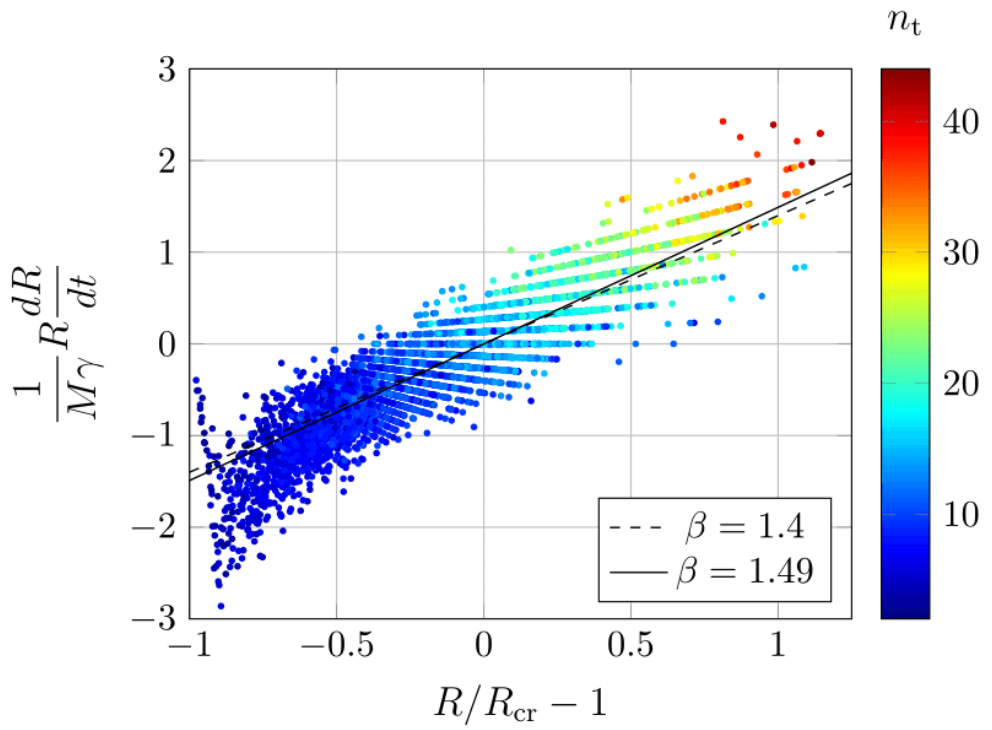


**(a)** $t = 1/3\,t_h$

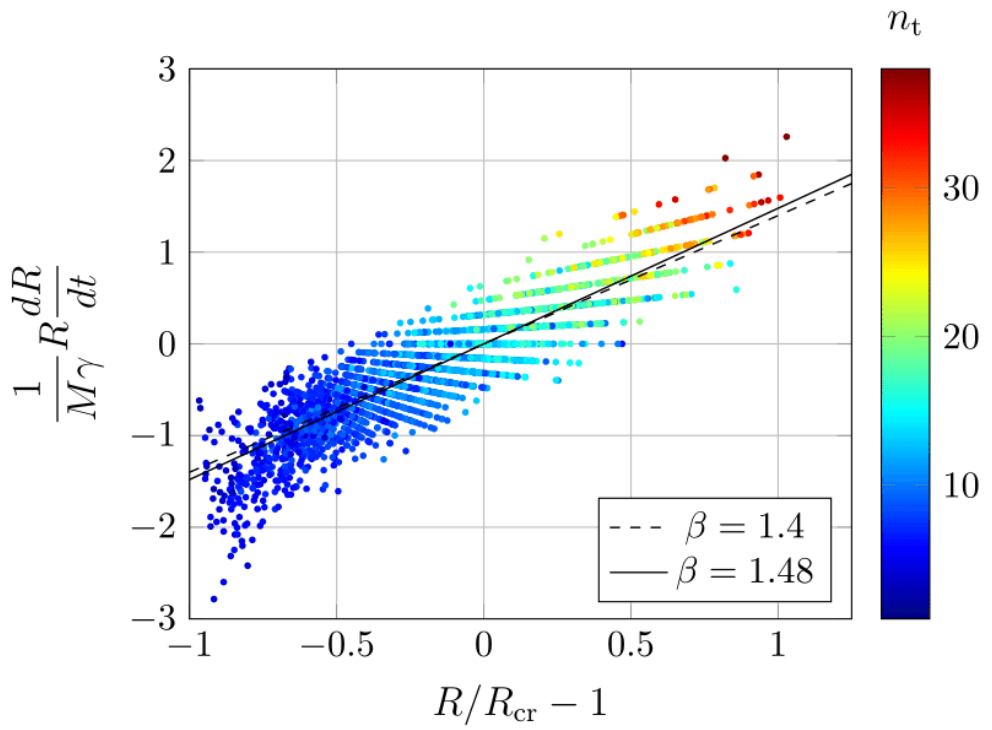


**(b)** $t = 2/3\,t_h$

**Fig. 3.12** – Growth rates of the individual grains in the 3D polycrystal. The black lines represent eq. (3.4) with two different values for the $\beta$ parameter (Maire et al. [Maire et al. 2016] and best fit).

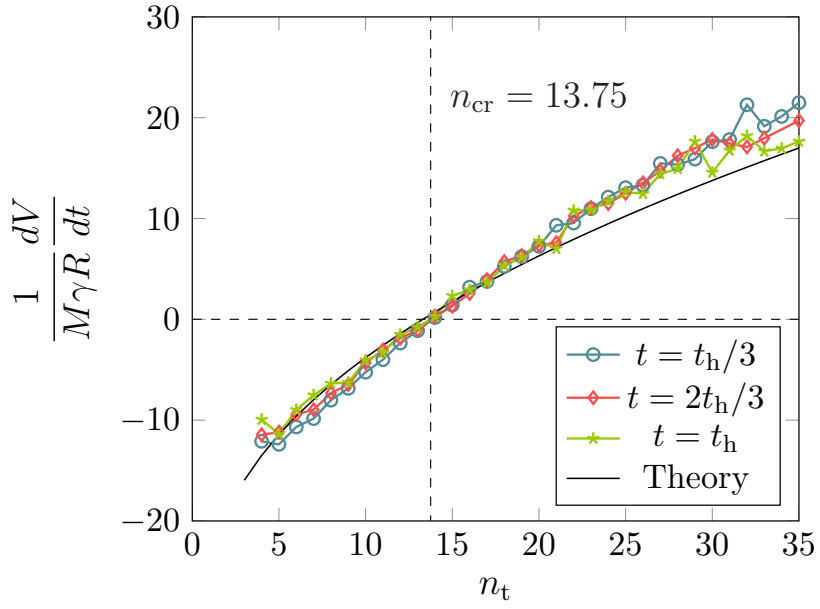


**Fig. 3.13** – Average growth rate associated with each topological class in the 3D simulation. The solid black line refers to the 3D Mullins law (see eq. (1.16)).

mentioned at the end of the previous section (11 in 2D, 7 in 3D), the simulation time needed for such a 3D simulation with the initial formalism of section 1.5.3 can be estimated around 19 days using the same number of CPUs. The initial situation has been therefore drastically improved.

As mentioned in the introduction chapter, the use of periodic BCs for such 2D/3D GG simulations would probably have permitted to obtain as-good numerical results with smaller number of grains.

## 3.5 Immersion of real microstructure from experimental data

### 3.5.1 Procedure

Sometimes creating a virtual polycrystal which is only statistically representative of the real material is not sufficient. Especially the real grains may have particular shapes that can not be represented accurately by standard generation techniques such as the VT and LVT methods. Also strong local heterogeneities of the grain size may be hard to obtain with these methods. In such cases, create a polycrystal based on an experimental image is very useful because it gives an (almost) exact representation

of the real material. An other interesting feature of this approach is the possibility to compare easily the experimental and numerical results. A possible approach is to, first, fit the Voronoï/Laguerre tesselation directly on the experimental data, and secondly, use the classical formula for immersing the grains within the FE mesh as it is done in [Spettl et al. 2016]. Although very interesting, these methods can be long to converge and do not permit to describe the possible curved shape of the grains boundaries because Voronoï/Laguerre cells are polyhedra. In this part, we interest to the direct immersion of the real material without any approximation.

Advanced observation techniques have greatly improved during the last decades. 2D representation of microstructure can be quite easily obtained thanks to EBSD facilities. Moreover, new experimental techniques, such as those presented in the introduction chapter, are also able to provide a 3D image of the polycrystal (see fig. 3b). Basically an experimental image is a regular lattice of cells. We note $r_i$ the resolution of the image (*i.e.* the number of cells) along the $i^{th}$ axis of the Cartesian coordinate system, with $i \in \{1,...,d_s\}$. Each cell has a spin, represented by a vector of values $\langle s_1,...,s_D \rangle$. Here $D$ denotes the dimensions of the spin, that can be, a scalar for $D = 1$ (*e.g* dislocation density), or a vector/tensor for $D > 1$ (*e.g* crystalline orientation, quaternion). This representation of the microstructure is actually very similar to the one used in MC/CA models (see fig. 1.6). So using experimental data as input in these approaches is straightforward. This is not so obvious in our framework because it requires preliminary operations, such as the mapping of the image on the FE mesh and the construction of the distance fields. This section aims to provide a complete method for the immersion of real polycrystals in a LS-FE framework. Our objective is here to take maximum advantage of the tools introduced in the previous sections in order to maximize the numerical efficiency of the immersion procedure. Particularly the proposed approach must be able to represent the real polycrystal in a FE mesh in 2D or 3D with an optimized number of GLS functions and to handle coloring.

Hereafter we detail the immersion procedure. After obtaining the 2D or 3D experimental image, the first step is to treat it, in order to fade the small spin discrepancies inside the grains. Effectively a grain is typically described as the set of adjacent cells whose spins are *close* from each other. This operation can be performed by applying standard treatment techniques implemented in analysis softwares, like DREAM.3D [Groeber et al. 2014]. Undetermined voxels can also be treated to define a parent grain. The result is an image wherein the spin is homogeneous inside a given grain, as illustrated with the gray levels on fig. 3.14. In this image each gray level corresponds to a crystallographic orientation, given by three Euler angles. Using this representation,

the grain boundaries are simply defined by the straight lines (respectively surfaces in 3D) which separate two adjacent cells with different spins.

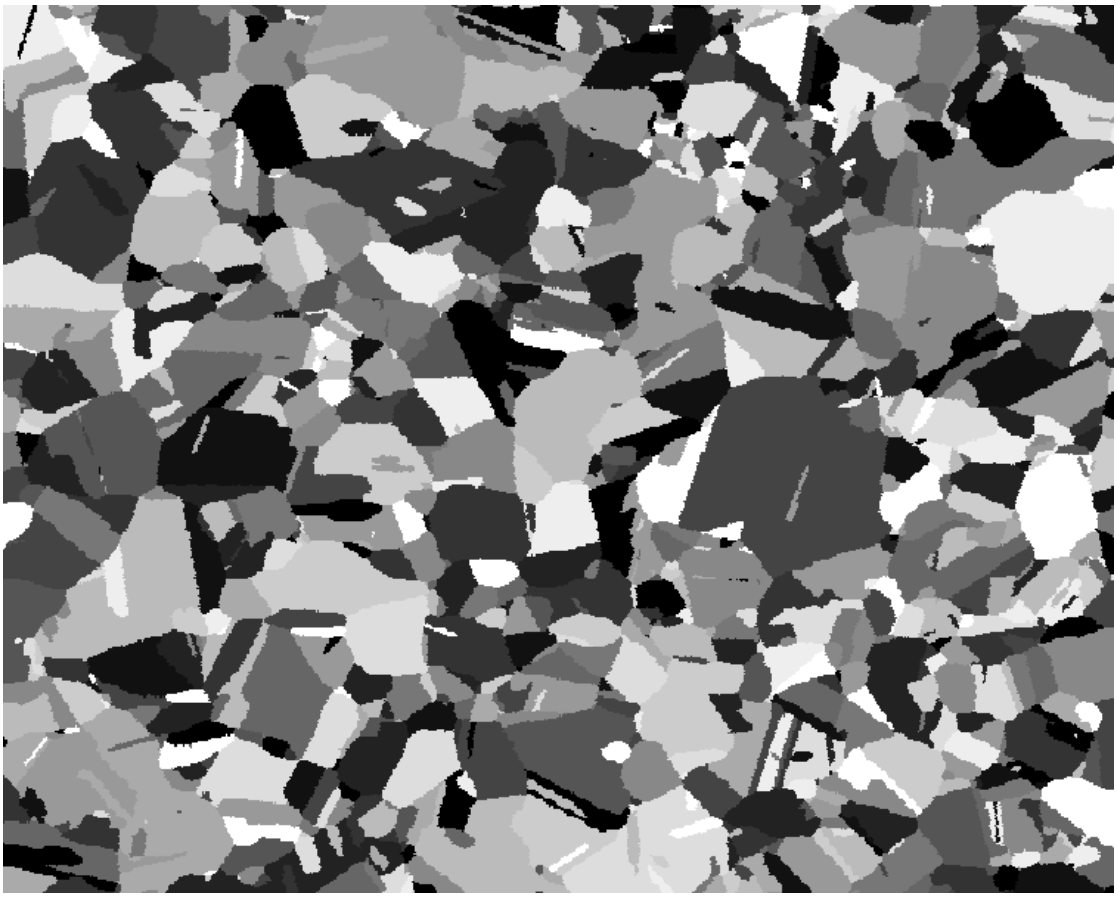

**Fig. 3.14** – 2D image of a microstructure obtained by EBSD. The gray scale refers to the crystallographic orientation.

The second step of the algorithm is to inspect the individual cells of the lattice and their respective spins. When a new spin is met (*i.e.* which has not been found in another cell inspected previously) it is stored in a set. After inspecting all the lattice, this set contains all the possible spins, and its size is therefore equal to the number of spins present in the image. The maximal number of spins is the number of grains as two separated grains can have the same spin. For the sake of simplicity, we associate a unique scalar identifier to each spin which is here simply the position of the considered spin in the set.

Now the objective is to determine how the grain are connected to each others in order to determine their distribution inside the GLS functions. This operation re-

quires to construct firstly the short-range neighborhood of each grain, composed of all the grains that are adjacent to the considered grain. This step is globally equivalent to what it is done at the beginning of the swapping algorithm when the table $\mathscr{S}$ is constructed (see chapter 3), with the exception that the operation is here directly performed on the regular lattice and not on the FE mesh. The other approach would be to first interpolate the spins on the FE mesh, and then construct the grain neighborhoods as it is done in chapter 3. However, in our numerical library the generation of the microstructure is performed prior to the mesh initialization, which makes, at yet, this second approach impracticable.

A second scan of the lattice is thus performed to construct the short-range neighborhood. If an identifier $\tilde{g}$ is met in the neighborhood of a cell whose identifier is $g$, with $g \neq \tilde{g}$, then $\tilde{g}$ is added in $\mathscr{S}(g)$. In the end, $\mathscr{S}(g)$ contains all the identifiers of the grains that are adjacent to $g$. The complete graph $\mathscr{S}$ is obtained after all the lattice cells have been inspected. Next the grains are distributed inside the GLS functions with respect to this graph, thanks to the coloring algorithm described in [Hitti 2011; Hitti et al. 2012]. This algorithm returns a table $\mathscr{A}(g)$ which gives, for each grain with identifier $g$, the index $i$ of the GLS function that will represent this grain. So this table is globally equivalent to the corresponding table $\mathscr{C}$ introduced in chapter 3. However a distinction must be made between these tables. Effectively $\mathscr{A}$ defines how the grain *will be* distributed inside the GLS functions. On the other hand $\mathscr{C}$ only describes the microstructure and the coloring at a given time. In other words, $\mathscr{C}$ and $\mathscr{A}$ describes *what we have* and *what we want to obtain*, respectively. Using $\mathscr{A}$, each grain can now be represented with the index of its GLS function. This is illustrated on fig. 3.15 for the initial microstructure of fig. 3.14, where each color designs the index of a GLS function.

Next algorithm 2 is performed on each GLS function $\psi_i$ with $i \in \{1, ..., N_\mathrm{p}\}$ and each mesh node $n$. It relies on two main functions. The former, GET_CELL($n$) uses a simple localization algorithm to determine the number of the lattice cell of the experimental image, noted $C$, that contains the considered mesh node $n$, which is given by:

$$C = \sum_{i=1}^{d_\mathrm{s}} \mathrm{floor}\left(\frac{n_i}{d_i} r_i\right), \tag{3.5}$$

where $n_i$ and $d_i$ are respectively the coordinate of the node $n$ and the dimension of the experimental image along the $i^{th}$ axis of the Cartesian coordinate system. The function floor($x$) is a simple rounding down.

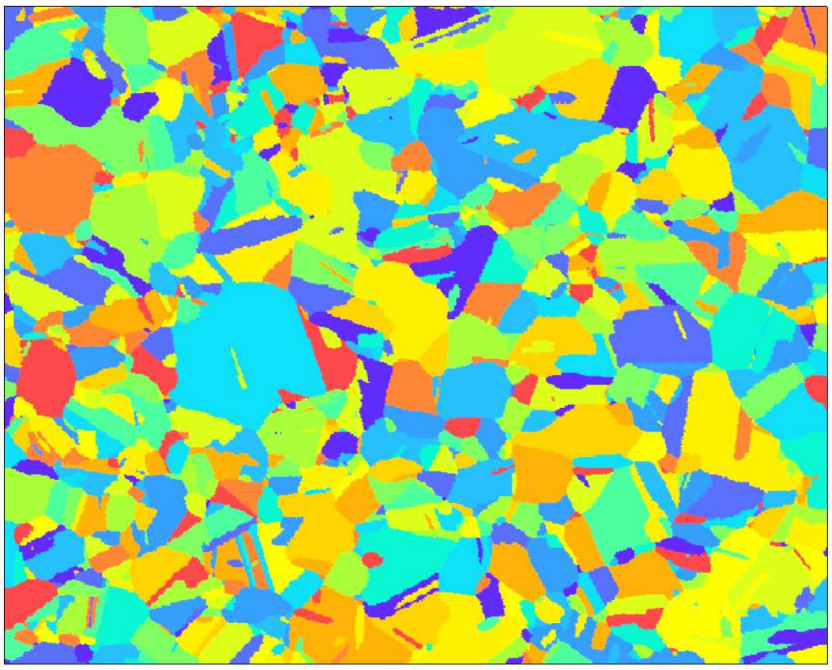

**Fig. 3.15** – Coloring of the initial immersed microstructure defined by the table $\mathscr{A}$ calculated with the algorithm of [Hitti 2011]. The color of each grain refers to the index of the GLS function that represent this grain.

Then the function GET_IDENTIFIER($C$) is performed, which determines the spin and the related identifier $g_c$ of the $C^{th}$ cell.

**Algorithm 2** Initialization of a GLS function from an experimental image

```
procedure INITIALIZE_GLS_FUNCTIONS(Field ψ_i, Table 𝒜)
    Define two integers C and g_c
    for Node n ∈ ℳ do
      C = GET_CELL(n)
      g_c = GET_IDENTIFIER(C)
        if 𝒜(g_c) == i then
            ψ_i(n) = 0.5
        else
            ψ_i(n) = −0.5
        end if
    end for
    return ψ_i
end procedure
```

After these preliminary operations, the $i^{th}$ distance field is initialized. If the considered mesh node $n$ is located inside a grain represented by $\psi_i$ (*i.e.* if $\mathscr{A}(g_c) == i$), then

$\psi_i = 0.5$. Otherwise $\psi_i$ is set to $-0.5$. This gives a binary representation of each GLS function, as depicted on fig. 3.16, which is very similar to a Heaviside function.

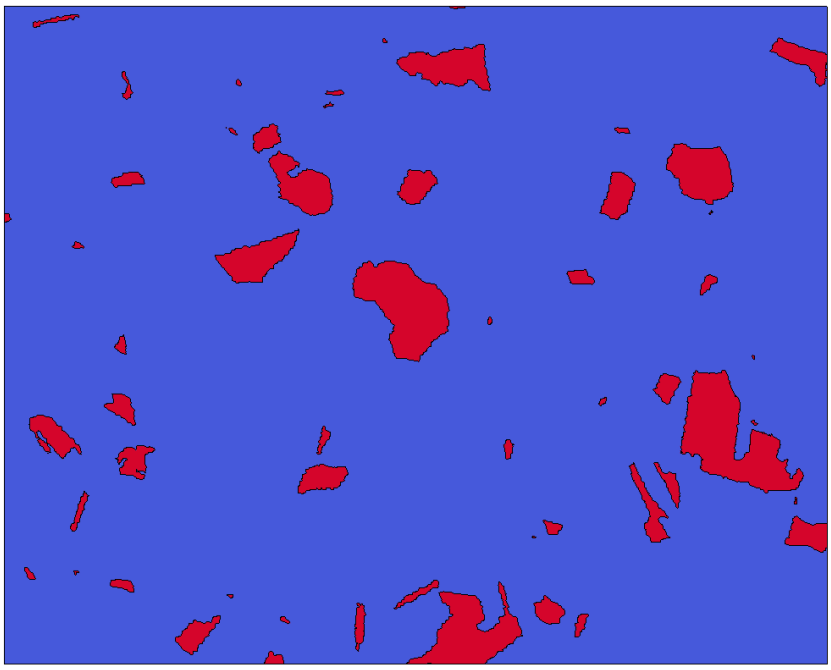

**Fig. 3.16** – Binarization of the grains represented by a GLS functions. Red and blue zones represent respectively 0.5 and $-0.5$.

The interface, given by $\psi_i = 0$, can then be obtained by simple interpolations (see eq. (2.11)). Obviously due to the binary representation, the precision of this approach is limited to the mesh size, which induces a faceting of the grain boundaries as illustrated on fig. 3.17. An alternative would be to apply standard processing operations [Schindelin et al. 2012; Schneider et al. 2012] directly on the experimental image to smooth the data, threshold the grains belonging to the same GLS functions and then convert these binary data to a signed distance function that is finally imported on the FE mesh. This method is much more precise [Shakoor et al. 2015a] but the pre-treatment applied on the image does not benefit from the distributed computing capabilities of the FE code and is highly memory-consuming. Effectively it requires to create an image for each GLS function. So an option would be to implement directly the pre-treatment operations within our FE library with an adequate management of the memory. These points will be investigated further in future works.

After the GLS functions have been initialized to binary fields, the DRT algorithm of section 2.4 is simply performed to convert them into *real* distance fields, based on the

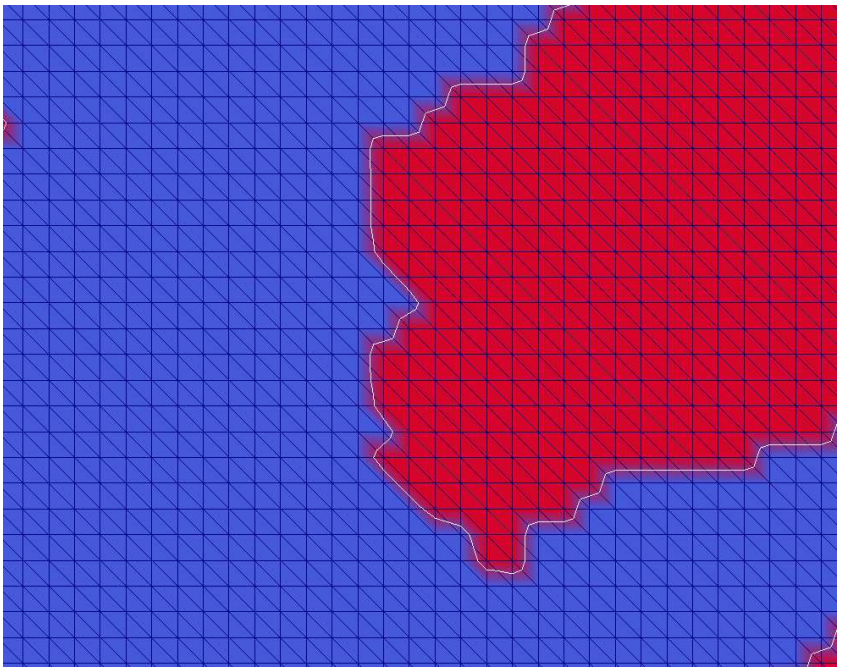

**Fig. 3.17** – Faceting of the grain boundaries due the binary representation and the limited mesh size.

interpolated zero-isovalue (see fig. 3.18). This reinitialization operation concludes the immersion procedure.

### 3.5.2 Illustration

A real practical case is now investigated for illustrating the capabilities of the above immersion procedure. Here we use a 3D experimental image of an aluminum material obtained by the research team of Carl E. Krill III (University of Ulm, Germany) in the context of the thesis work of Mingyan Wang, thanks to a X-ray diffraction technique. The material sample, represented in red on fig. 3.19, has a cylindrical shape and contains around 1300 grains. It is embedded in a $321 \times 321 \times 531$ data box by inserting a virtual phase all around with a specific spin, depicted in blue on fig. 3.19. The voxel size is assumed to be $1\mu$m. Each voxel is represented by three Euler angles. A cylindrical FE mesh is then generated, whose axis is aligned with the material sample. We encountered numerical difficulties during the resolution of eq. (1.48) when attempting to simulate the whole material sample, that are probably caused by the cylindrical shape of the FE mesh. To avoid this issue and limit the numerical cost, we choose to study only a part of the sample and therefore to use a cylindrical FE mesh which is smaller than the material sample (see fig. 3.19). This mesh is composed of

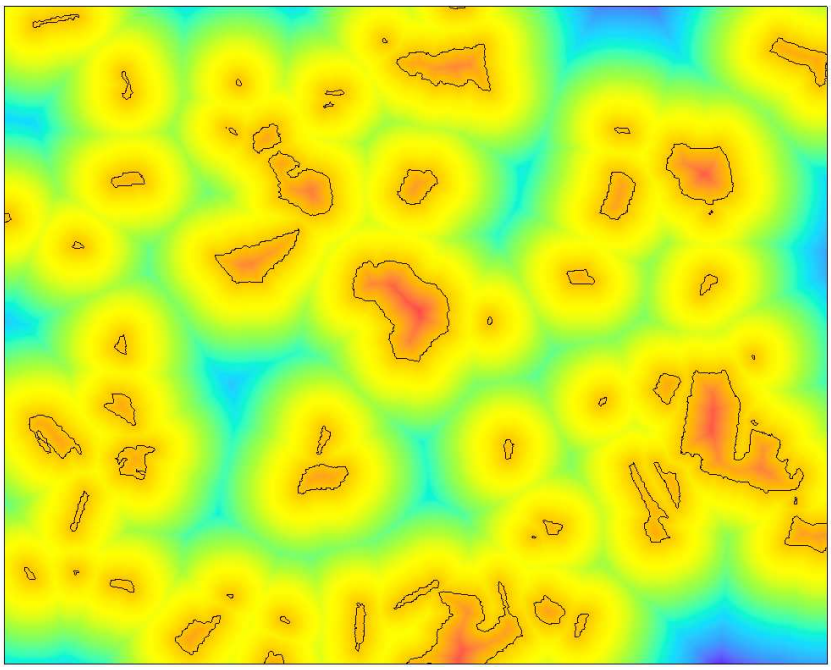

**Fig. 3.18** – Distance field obtained by performing the DRT algorithm on the binary field of fig. 3.16. The solid black line indicates the interface of the GLS function.

1.3 million tetrahedral elements, and its height and radius are 100$\mu$m and 90$\mu$m, respectively.

Then we perform the immersion procedure detailed previously. Around 150 grains of the material sample are initially present in the simulation domain and 18 GLS functions are needed for the mapping of this microstructure. Figure 3.20 depicts the grain boundary network obtained after performing algorithm 2 on all the GLS functions.

As mentioned earlier, the limited precision in terms of mesh size induces a faceting of the grain boundaries. A heat treatment of 17min with $M\gamma = 1 \times 10^{-6}$ mm$^2$/s (arbitrary value) is finally simulated with a fixed time step $\Delta t = 2$s (510 time increments). The evolution of the polycrystal is depicted on fig. 3.21. We observe on fig. 3.21a that the virtual faceting disappears immediately during the first time increment. After this, the grain boundaries adopt a smooth shape. An interesting point would be to evaluate the impact of the initial faceting on the microstructure predicted after the first increment.

The calculation time for this simulation is around 9h using 6 CPUs, which is very reasonable.

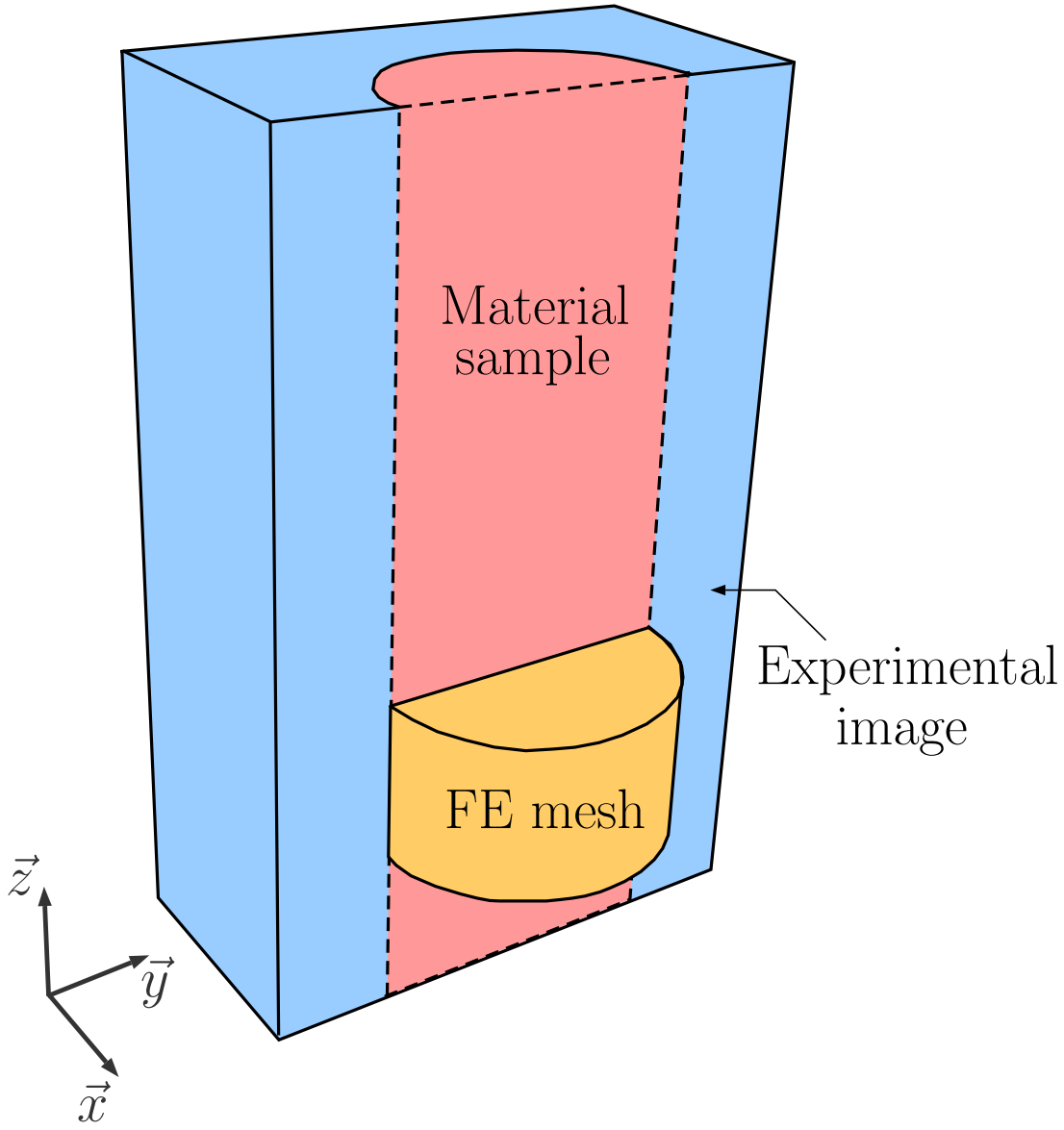


**Fig. 3.19** – Schematic illustration of the immersion case from the 3D experimental image.

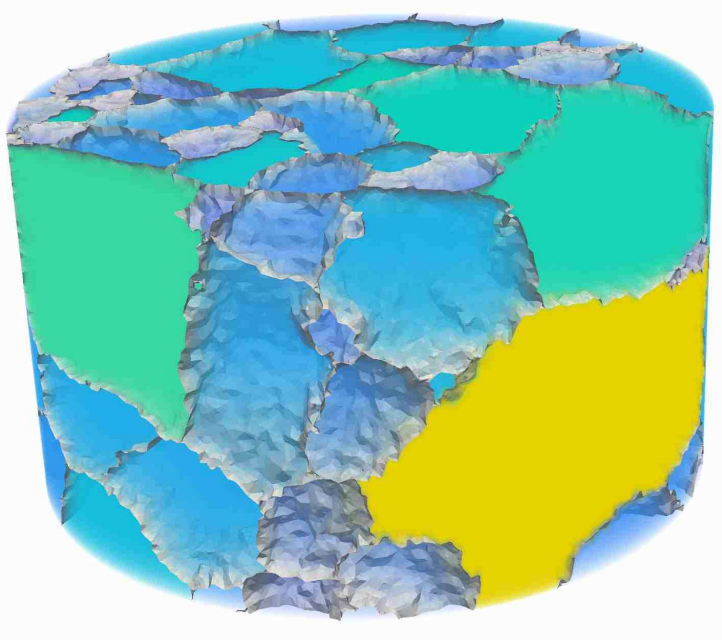

**Fig. 3.20** – Grain boundary network obtained after the immersion of the 3D experimental image on a reduced simulation domain (see fig. 3.19).

Although these first results are interesting, several points should now be investigated. First of all, it important to solve the numerical issues related to the FE solver used to treat eq. (1.48) in order to be able to simulate the whole material sample with our LS-FE approach. It would be also very interesting to compare these LS-FE simulation results with PF simulation tools developed at the university of Ulm. *In situ* observations of the considered material during the TT are also available thanks to the thesis work of Mingyang Wang and should be compared with the numerical results in the context of a collaboration. More particularly it has been observed by Mingyang Wang that the anisotropy of the grain boundary features in the considered aluminum material, and especially the grain boundary energy, may influence the microstructure evolutions. Comparison of numerical and experimental *in situ* results could thus permit to calibrate a model, for example a Read-Schokley relationship, that describes the heterogeneity of the grain boundary energy for this material in the considered thermomechanical conditions.

## Summary

In this chapter, the limitations of the GLS functions have been investigated. Despite it permits significant computation time and memory savings, GLS functions come ef-

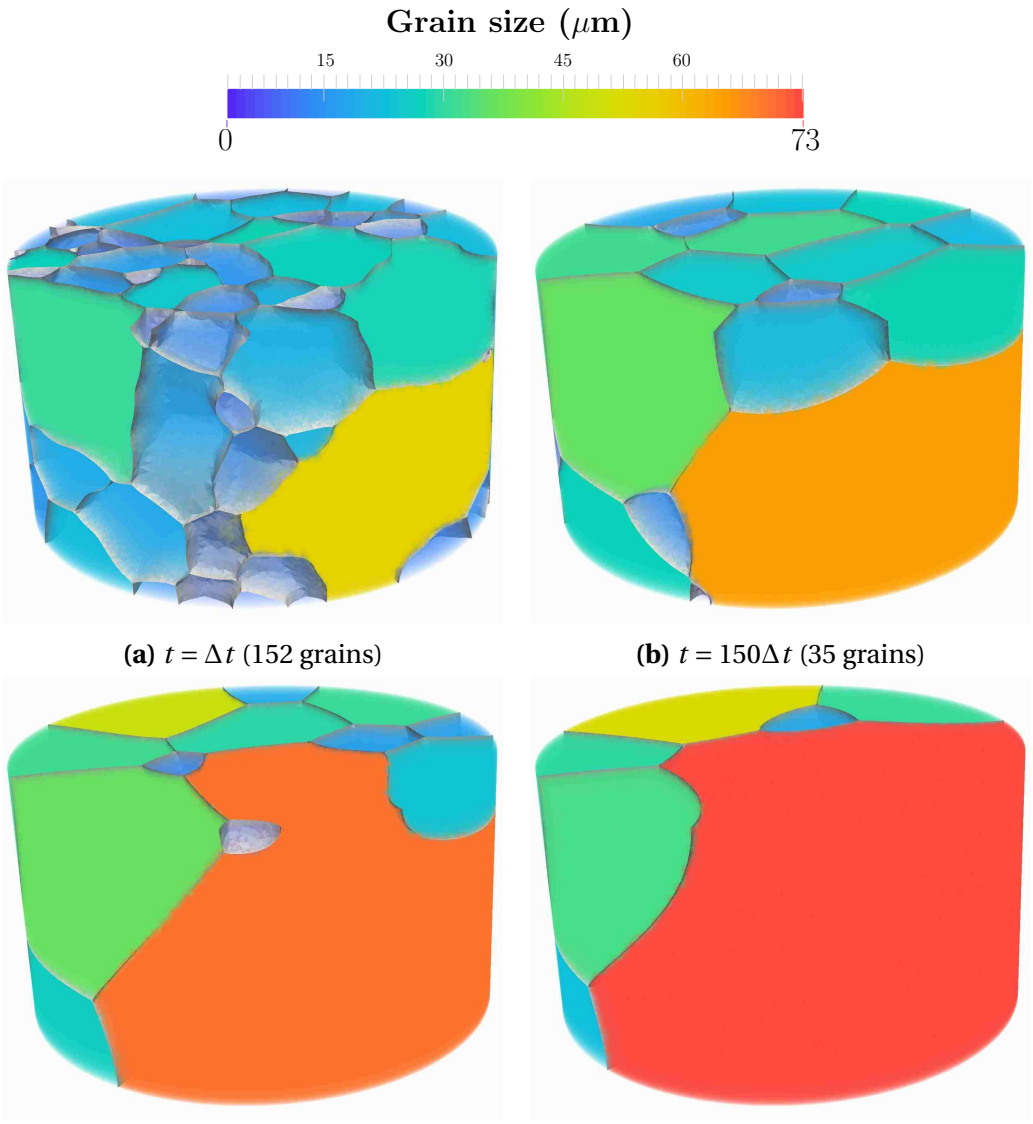


**(a)** $t = \Delta t$ (152 grains)

**(b)** $t = 150\Delta t$ (35 grains)

**(c)** $t = 300\Delta t$ (22 grains)

**(d)** $t = 450\Delta t$ (10 grains)

**Fig. 3.21** – Evolution of the aggregate during the heat treatment simulation based on the initial microstructure of fig. 3.20.

fectively with inherent difficulties. The former is the possible numerical coalescence between the child grains, which must be absolutely avoided to ensure the consistency of the simulation results. Second limitation is the impossibility of assessing directly to the individual properties of the grains, like the grain size. In previous works, an initial separation was introduced between the child grains of the initial microstructure in order to delay coalescence [Fabiano 2013; Cruz-Fabiano et al. 2014]. This approach was demonstrated to be numerically insufficient and does not address the problem concerning the assessment of the individual grain features. A new method has therefore been proposed to address these issues. It is composed of two steps. First the connected components are distinguished using a specific algorithm working within a parallel finite element framework. Then the coalescence risks are detected and eliminated dynamically at each increment. An efficient implementation has been proposed which takes advantage of a bounding-box strategy for the evaluation of the separation distance between the child grains. This approach has been demonstrated to be nearly optimal in terms of memory requirements and numerical efficiency. Especially acceleration factors around two have been obtained in 3D while ensuring coalescence-free simulation without any assumption. The newly proposed algorithm for the separation of the connected components permits also to track the properties of each grain. Large aggregates with several thousand of grains have been simulated in two and three dimensions thanks to these new developments. The topology and evolution of the simulated microstructures have been analyzed and successfully confronted with mean field approximations. Finally an algorithm has been introduced for the immersion of real polycrystals within a LS-FE framework. This algorithm handles the distribution of the grains inside the GLS functions and uses advantageously the DRT method introduced in section 2.4 for the initialization of the distance fields. A first heat treatment simulation based on a 3D experimental image has finally been performed thanks to this new immersion algorithm. The results of this LS-FE simulation should now be compared with PF simulations and *in situ* observations carried out at the university of Ulm in the context of a collaboration. The numerical developments presented in this chapter have allowed to publish [Scholtes et al. 2015].

# Chapter 4

# A new efficient model of static recrystallization based on stored energy field

## Contents


**4.1 Introduction . . . . . 141**

**4.2 Modeling of static recrystallization using the level set/finite element method: first approach and limitations . . . . . 141**

**4.3 New implementation of the recrystallization model . . . . . 143**

4.3.1 Objective . . . . . 143

4.3.2 Initialization of the energy fields . . . . . 143

4.3.3 Calculation of the recrystallization velocity field . . . . . 144

4.3.4 Tracking of the grain energies . . . . . 147

4.3.5 Improvement of the nucleation algorithm . . . . . 150

4.3.6 Evaluation of the numerical efficiency and comparison with the initial implementation . . . . . 152

**4.4 Large-scale simulations of static recrystallizaton in three dimensions . . . . . 156**

4.4.1 Static recrystallization simulation from a deformed state . . . 156

4.4.2 Simulation of static recrystallization in site-saturated conditions 160

# Résumé en français

Ce chapitre est consacré à la modélisation du phénomène de recristallisation statique par une approche level set/éléments finis. Premièrement, le modèle de recristallisation introduit par Bernacki et al. [Bernacki et al. 2008] a été discuté. Ce dernier utilise un niveau d'énergie constant et homogène pour chaque fonction distance. Ensuite, nous avons mis en évidence les limitations de ce modèle, et plus particulièrement l'impossibilité d'utiliser la coloration et la recoloration à la volée des grains. Il est donc limité à des configurations simples à faible nombre de grains, car chacun d'entre eux doit être représenté par une fonction distance. Sur cette base, notre objectif était d'étendre ce formalisme numérique pour tirer pleinement parti des fonctions level set globales et du nouvel algorithme de recoloration automatique introduit dans section 3.3.2. Pour cela, une nouvelle implémentation du modèle de recristallisation statique a été développée. Cette dernière repose sur l'utilisation de champs d'énergie stockée qui permettent de gérer des énergies indépendantes pour chaque grain tout en utilisant très peu de fonctions distances. Dans cette approche, l'énergie est complètement indépendante des fonctions level set globales. Elle est donc parfaitement compatible avec l'algorithme de recoloration introduit dans le chapitre précédent car les énergies peuvent être réassignées en même temps que les grains lors d'une opération de recoloration. Un nouvel algorithme de germination a également été introduit. Celui-ci détermine les sites potentiels et gère l'affectation des nouveaux grains à l'intérieur des fonctions level set globales. Ces nouveaux outils numériques ont été implémentés de façon générique dans notre librairie numérique afin qu'ils puissent manipuler n'importe quelle quantité (scalaire, vecteur, tenseur) associée aux grains. Cette nouvelle implémentation a été testée au travers de différentes simulations de recristallisation statique à grand nombre de grains en trois dimensions. Son efficacité, avec des facteurs d'accélération pouvant atteindre 45 pour certaines configurations, a ainsi été démontrée. Enfin l'influence du scénario de germination sur la cinétique globale de recristallisation a finalement été étudiée en s'appuyant sur des résultats de simulations de recristallisation statique de type *sites saturées*. Les développements numériques présentés dans ce chapitre ont permis la publication d'un article dans une revue internationale à comité de lecture [Scholtes et al. 2016a].

## 4.1 Introduction

The two previous chapters focused on the improvement of the LS methodology itself. Especially we introduced a new DRT algorithm (see chapter 2) and a dynamic recoloring scheme (see chapter 3) which have both demonstrated high numerical efficiency in the context of pure GG without stored energy (*i.e.* $\vec{v}^{\mathrm{e}} = \vec{0}$ in eq. (1.47)). Obviously real materials are rarely free of deformation energy and local energy gradients must be addressed for capturing the real kinetics of the grain boundaries, especially during and after the deformation stage. So the objective of this chapter is to propose an efficient approach for the modeling of the SRX phenomenon. After introducing the initial LS-FE model of SRX developed in [Logé et al. 2008; Bernacki et al. 2009], we highlight its limitations. Then we propose a new implementation which takes advantage of the numerical tools introduced in the previous chapters.

## 4.2 Modeling of static recrystallization using the level set/finite element method: first approach and limitations

According to eq. (1.4), the normal velocity of a grain boundary consists of a capillarity term $\vec{v}^{\mathrm{c}}$ and a recrystallization term $\vec{v}^{\mathrm{e}}$. This latter is related to the jump in stored energy across the grain boundaries as the stored energy is averaged per grain in the discussed numerical framework. Effectively, if different methods can be used to compute this term, the initial approach was proposed by Bernacki et al. in 2008 [Bernacki et al. 2008]. This approach works around a homogeneous energy level inside the grains, which implies that the energy gradient is non-zero only at the grain boundaries. In other words, this model does not consider intragranular heterogeneities and assumes that energy is spatially constant inside a given grain. Also this formulation lies on a constant energy values $e_i$ for each GLS function, which can be eventually time-dependent. Given the previous statements, a natural way to compute the term $\vec{v}^{\mathrm{e}}$ at the interface between two grains with indexes $i$ and $j$ could be:

$$\vec{v}^{\mathrm{e}}(x) = M_{ij} f\left(\psi_i(x), l\right)\left(e_j - e_i\right)\frac{\nabla\psi_i(x)}{\|\nabla\psi_i(x)\|}, \tag{4.1}$$

where $f$ is a decreasing function varying from 1 (for $\psi_i = 0$) to 0 (for $|\psi_i| = l$), and $M_{ij}$ is the interface mobility between grains $i$ and $j$. Here we assume a homogeneous mobility throughout the microstructure with a constant $M$ value, so $M_{ij}$ is simply replaced by $M$. The time variable is still omitted in the notation for simplicity but let

us remind that all the considered quantities are (or can be seen as) time-dependant.

However, this formulation generates discontinuities at multiple junctions which result in ill-conditioned problems. The alternative proposed by Bernacki et al. [Bernacki et al. 2008] is to use the weighted contributions of all GLS functions and their respective energies at each node of the FE mesh:

$$\vec{v}^{\mathrm{e}}(x) = M \sum_{i=1}^{N_\mathrm{p}} \sum_{\substack{j=1 \\ j\neq i}}^{N_\mathrm{p}} \chi_i(x) f\left(\psi_j(x), l\right)\left(e_i - e_j\right) \frac{\nabla\psi_j(x)}{\|\nabla\psi_j(x)\|}, \tag{4.2}$$

which presents the advantage of avoiding the identification of the neighboring grains and leads to a smooth velocity field also at the multiple junctions.

The above approach has been extensively tested and validated in [Bernacki et al. 2008; Bernacki et al. 2009]. However no grain coloring was used in these works (*i.e.* $N_\mathrm{p} = N_\mathrm{g}$) so that an independent energy level can be considered for each grain. As mentioned in the previous chapter using a distance field for each grain of the aggregate is infeasible in 3D because the computational cost is strongly related to $N_\mathrm{p}$. So using a coloring technique seems to be a logical choice in this situation. But this is actually not so simple. Effectively there are major incompatibilities between the grain coloring technique and the above ReX formalism:

- considering that the stored energy level $e_i$ is a constant quantity for the $i^{th}$ GLS function, all the child grains of $\psi_i$ have necessarily the same energy, which makes no sense from a metallurgical point of view,
- if recoloring is used, each swapping operation (see chapter 2 for details) would inevitably modify the energy of the recolored grain, which would receive the energy corresponding to the recipient GLS function and lose the energy associated with its own mechanical state.

We propose in this section a new implementation of the ReX model to overcome these difficulties. This latter employs stored energy fields and is fully compatible with the recoloring scheme introduced in the previous chapter. Although this approach is strictly equivalent to the existing one from a metallurgical point of view, it will be proven much more numerically efficient and permits massive computation time savings. Different large-scale simulations of SRX in three dimensions have been performed within very interesting CPU times thanks to these improvements.

## 4.3 New implementation of the recrystallization model

### 4.3.1 Objective

Our objective is to create a new description of the polycrystal wherein each grain has its own energy, which is completely independent of the GLS functions. The most natural way to achieve this goal consists in replacing the energy $e_i$ of each GLS function (constant for the whole FE mesh) by an energy field $\mathscr{E}_i$ evaluated at the interpolation points. We will see that such an extension is not straightforward and requires the development of new algorithms to:

1. initialize the energy fields by assigning an energy level to each grain of the microstructure at an early stage of the simulation, with respect to a prescribed energy field,
2. compute the velocity field $\vec{v}^{\mathrm{e}}$ with an energy which is no more constant for a given GLS function,
3. track the respective grain energies during the simulation,
4. handle efficiently nucleation events in order to limit the number of GLS functions and maintain low computational costs.

It is worth emphasizing that, even if the present study deals only with scalar energy fields, the algorithms introduced in this section are completely general and address also problems involving vector and/or tensor fields. The interested reader may find an other example of application in [Boulais-Sinou et al. 2016], in which the same tools handle the crystal orientation fields (vector with dimension 3) in the context of DRX.

### 4.3.2 Initialization of the energy fields

The first step consists in initializing the energy fields. This operation is performed in two stages:

1. SCC in order to identify the grains represented by the same GLS function,
2. generation and assignation of the grain energies.

The SCC algorithm has been detailed extensively in section 3.3.2. It returns an index field associated with each GLS function, wherein the grains are marked with a unique identifier (see fig. 3.3b).

Let us designate by $G_i$ the number of grains represented by the $i^{th}$ GLS function at a given time. After performing the SCC algorithm, an energy value is generated for each grain of index $g \in \{1, ..., G_i\}$. These values can be directly imported from CPFEM calculations or experimental data. In both cases, this procedure is designated by the function GENERATE_VALUE() in algorithm 3. Once the energies have been defined, the mesh nodes are scanned and the procedure detailed in algorithm 3 is performed.

**Algorithm 3** Initialization of the energy fields at an early stage of the simulation

```
procedure INITIALIZE_ENERGY_FIELD(Field 𝒥_i)
    Create a Table E with size G_i
    for Integer g ∈ {1, ..., G_i} do
        E[g] ← GENERATE_VALUE()
    end for
    for Node n ∈ ℳ do
        if 𝒥_i(n) > 0 then
            ℰ_i(n) ← E[𝒥_i(n)]
        else
            ℰ_i(n) ← −1
        end if
    end for
    return ℰ_i
end procedure
```

When a node $n$ satisfying $\mathscr{J}_i(n) > 0$ is met, the corresponding energy field receives the value previously generated for this grain identifier. In the zones where $\mathscr{J}_i = 0$, the energy field $\mathscr{E}_i$ is set to an arbitrary negative value ($-1$ for simplicity), which indicates that it is an undefined region. Figure 4.1 illustrates the result obtained by executing this procedure on the microstructure shown in fig. 3.3b.

### 4.3.3 Calculation of the recrystallization velocity field

Considering that in our new formalism energy is no longer a constant but a space-dependent variable, it seems obvious to reformulate eq. (4.2) as follows:

$$\vec{v}^{\mathrm{e}}(x) = M \sum_{i=1}^{N_\mathrm{p}} \sum_{\substack{j=1 \\ j\neq i}}^{N_\mathrm{p}} \chi_i(x) f\left(\psi_j(x), l\right) \left(\mathscr{E}_i(x) - \mathscr{E}_j(x)\right) \frac{\nabla \psi_j(x)}{\|\nabla \psi_j(x)\|}. \tag{4.3}$$

However, this extension makes no sense if used as such because all the energy fields $\mathscr{E}_j$ (with $j \neq i$) are not defined inside the $i$-th GLS function (*i.e.* where $\chi_i = 1$). Let us

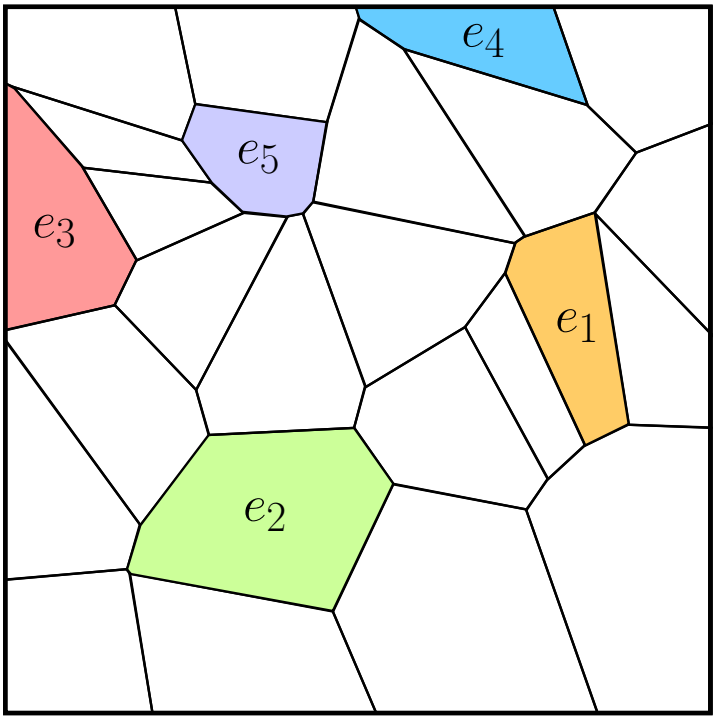


**Fig. 4.1** – Energy field $\mathscr{E}_i$ associated with the $i^{th}$ GLS function. This represents five grains which all have their own independent energy. The white zone corresponds to an arbitrary negative value ($-1$ for the sake of simplicity).

illustrate this situation with the simple two-grain microstructure depicted in fig. 4.2a. These grains are respectively represented by two GLS functions, $\psi_1$ and $\psi_2$, and two energy fields $\mathscr{E}_1$ and $\mathscr{E}_2$ (see figs. 4.2b and 4.2c).

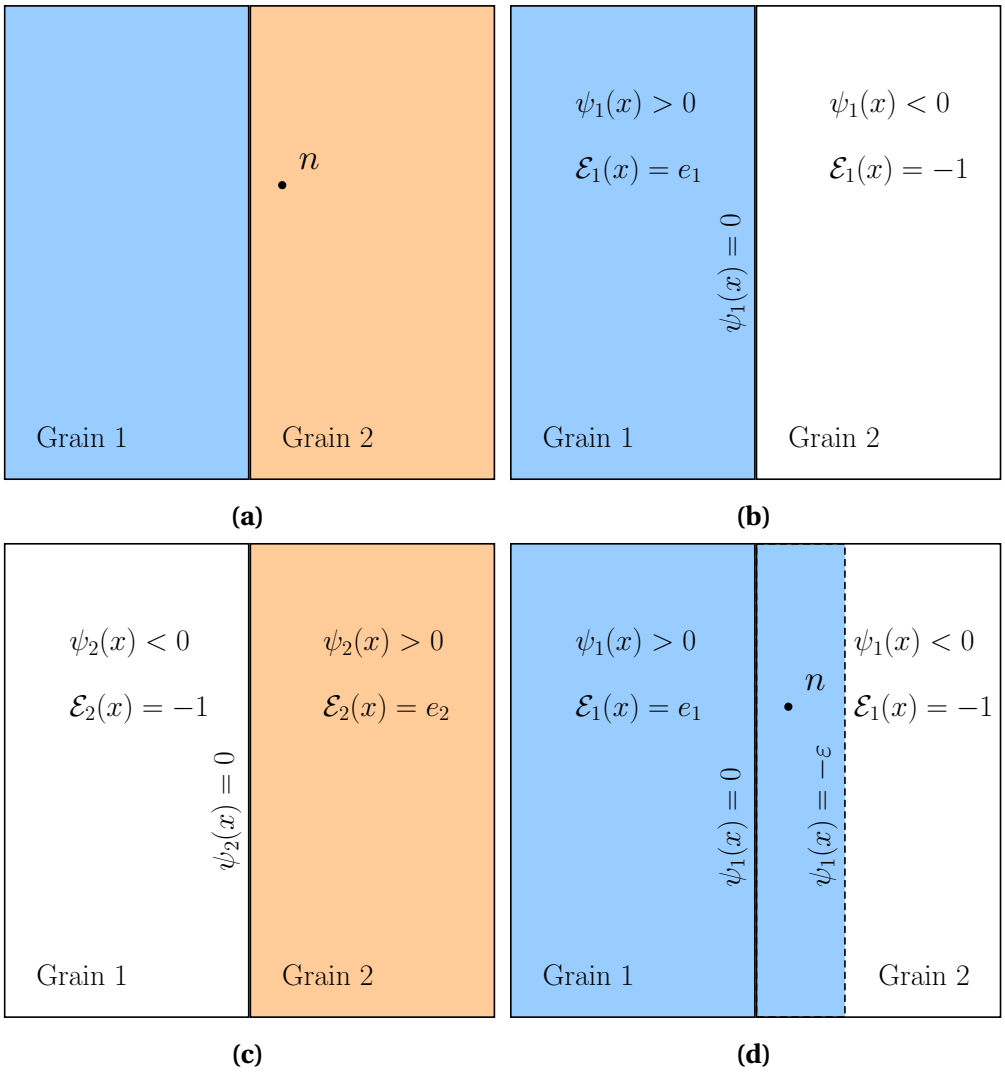


**Fig. 4.2** – Simple two-grain microstructure illustrating the problem of computing the recrystallization velocity term with the new formulation given by eq. (4.3).

At the node $n$ represented in fig. 4.2a, $\chi_1$ is naturally null and eq. (4.3) boils down to:

$$\vec{v}^{\,e}(n) = Mf\left(\psi_1(n), l\right)\left(\mathscr{E}_2(n) - \mathscr{E}_1(n)\right)\frac{\nabla\psi_1(n)}{\|\nabla\psi_1(n)\|}. \tag{4.4}$$

However $\mathscr{E}_1$ is not defined at this node, *i.e.* $\mathscr{E}_1 = -1$.

To solve this issue, the energy fields must be extended outwards their respective GLS functions before computing the velocity field $\vec{v}^{\mathrm{e}}$. When coloring is employed we have $G_i > 1$ and the nodal value of a GLS function represents the distance from this node to the nearest grain it contains. The energy fields must therefore be extended in $\psi_i \in [-\varepsilon, 0]$ with the energy value of this nearest grain. So this field extension procedure is basically a pure NNS problem which can be elegantly addressed by the DRT algorithm introduced in chapter 2. Next the extension of the energy fields is coupled with reinitialization in order to maintain high numerical efficiency. For this purpose we modify the previous implementation of the DRT algorithm in such a way that it returns the nearest element itself, and not only the distance to this nearest element as it was proposed in section 2.4. This approach enables to assess all the features associated with this nearest element (coordinates of the delimiting nodes, normal vector, field values,...). Considering that the only quantity of interest in the context of SRX is the stored energy, we attach a unique scalar value to each facet during the construction of the collection (see section 2.4). Obviously this value is the energy level of the grain surrounded by this facet. Then during the reinitialization stage, the energy attached to the nearest element of the collection is used to complete the stored energy field in $\psi_i \in [-\varepsilon, 0]$. This operation is schematically illustrated on fig. 4.3a where the field $h$ (which can be a scalar, a vector or a tensor) receives at the FE node $n$ the value attached with the nearest facet. Also a great advantage of this new implementation is the possibility to compute the exact P1 gradient of the GLS function, by projecting the reinitialized node on the nearest facet (see fig. 4.3b). Finally the nodal value of $\nabla\psi_i$ is used to compute the velocity field $\vec{v}^{\mathrm{e}}$ according to eq. (4.3).

The reinitialization of the distance functions and the extension of the energy fields are thus performed simultaneously, which involves few additional computations compared to a classical reinitialization, *i.e.* without field extension. The impact of the field extension procedure on the computation time is discussed in the next section. Going back to the previous two-grains microstructure, the result of the reinitialization/extension procedure performed on the energy field $\mathscr{E}_1$ is depicted on fig. 4.2d. After performing the algorithm, the energy field *lives* also in $[-\varepsilon, 0]$, which allows a correct evaluation of the velocity field $\vec{v}^{\mathrm{e}}$ at node $n$ through eq. (4.4).

### 4.3.4 Tracking of the grain energies

After the velocity field $\vec{v}^{\mathrm{e}}$ has been computed, the GLS functions $\psi_i$ evolve accordingly to the system of CDEs defined by eq. (1.47).

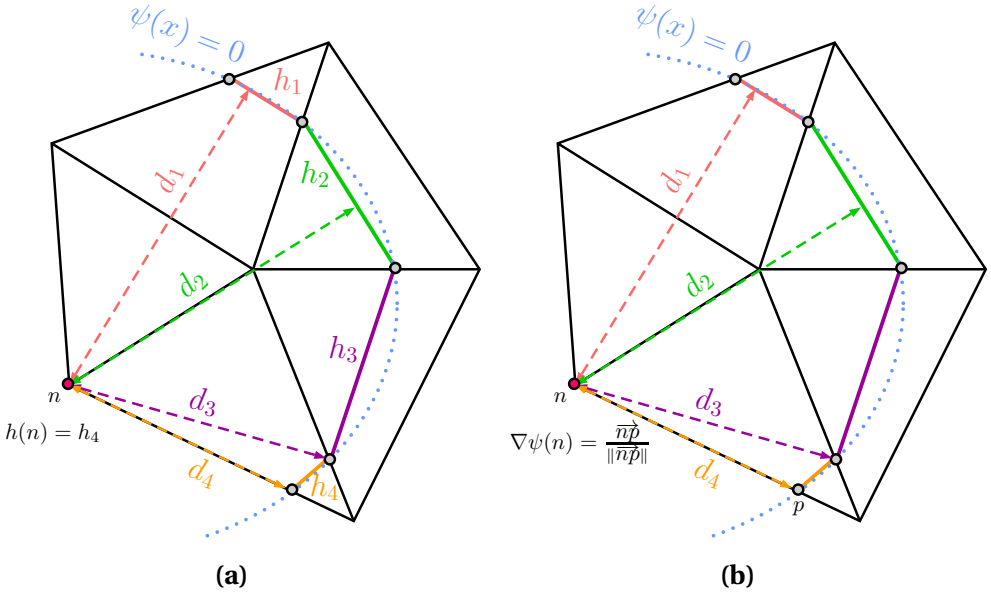


**(a)** **(b)**

**Fig. 4.3** – Extension of an arbitrary field $h$ (a), and computation of the exact P1 gradient $\nabla\psi$ (b) with the new implementation of the reinitialization algorithm.

For convenience, we introduce the notation $\mathcal{N}_{g,i}$ to represent the set of FE nodes located inside the grain with index $g \in \{1,...,G_i\}$, represented by the function $\psi_i$. Also the superscripts $\cdot^t$ and $\cdot^{t+\Delta t}$ are employed to designate the values of a field before and after the solving of the CDEs, respectively.

After displacing the GLS interfaces, the energy fields must be updated to ensure the energies remain fitted on their respective grains between two consecutive increments. The employed procedure is relatively simple and consists in two steps:

- for each grain of index $g \in \{1,...,G_i\}$, search for the maximal positive energy value of the field $\mathscr{E}_i^t$ in the set of nodes $\mathcal{N}_{g,i}^{t+\Delta t}$,
- perform a second loop and assign this maximal energy to all the nodes of the field $\mathscr{E}_i^{t+\Delta t}$ belonging to $\mathcal{N}_{g,i}^{t+\Delta t}$,
- tag all the other nodes (*i.e.* $n \notin \mathcal{N}_{g,i}^{t+\Delta t}$) with $-1$ (undefined region).

It is obvious such an algorithm requires the existence of an overlap region between the old and updated positions of each grain in order to perform the identification, which can be formulated as follows:

$$\mathcal{N}_{g,i}^{t} \cap \mathcal{N}_{g,i}^{t+\Delta t} \neq \emptyset. \tag{4.5}$$

In other words, at least one node having a positive energy value must be found in $\mathcal{N}_{g,i}^{t+\Delta t}$. In practice, eq. (4.5) is not satisfied in the two following configurations:

(a) $\mathcal{N}_{g,i}^{t+\Delta t} = \emptyset$, *i.e.* when the grain with index $g$ disappears,

(b) $\mathcal{N}_{g,i}^{t+\Delta t} \neq \emptyset$ but the displacement of $g$ during $t$ and $t+\Delta t$ is so important that $\mathcal{N}_{g,i}^{t} \cap \mathcal{N}_{g,i}^{t+\Delta t} = \emptyset$,

Case (a) is actually not problematic as the energy of a dying grain must necessarily be removed from the energy field, which is what it is done by the algorithm. On the other hand, the scenario (b) must absolutely be avoided. If it occurs, the considered grain would lose its energy and would receive a negative value instead, as illustrated by the pink grain on fig. 4.4. To prevent this issue, it appears crucial to ensure a proper identification of all the grains between two consecutive increments. The satisfaction of this condition is actually strongly related to the time step $\Delta t$. As a simple example, let us consider a grain and the sphere centered on its centroid, which have a sufficient radius $R_{\text{eq}}$ to contain this grain. In this configuration, it is obvious that eq. (4.5) is always verified between two consecutive increments as long as:

$$\Delta t < \frac{R_{\text{eq}}}{v_{\max}}, \tag{4.6}$$

where $v_{\max}$ is the maximal grain boundary velocity at the interface of the considered grain. A worst case scenario for the satisfaction of this inequality comes when a shrinking grain becomes very close from the the mesh size $R_{\text{eq}} \sim h$. However, given the typical values of $v_{\max}$ and $h$ used in our simulations, the condition $\Delta t < h/v_{\max}$ is always easily verified, even with the large time steps permitted by our implicit numerical scheme. Figure 4.4 illustrates the updating of an energy field. In this example, the grain with energy $e_4$ disappears during the resolution of the CDEs. The grain having the energy $e_5$ illustrates what happens when eq. (4.5) is not satisfied, even if it has been demonstrated above that this scenario does not occur in practice.

We summarize the global algorithm for the updating of the energy fields in algorithm 4.

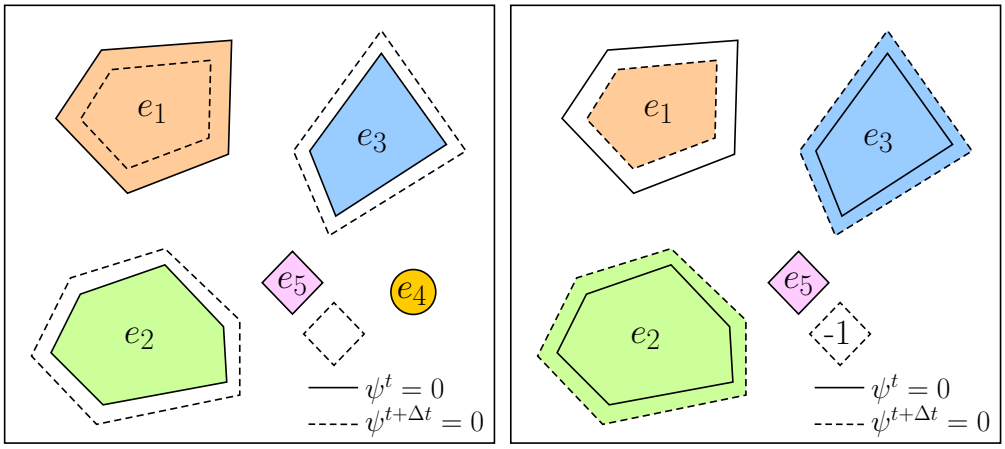


**(a)** **(b)**

**Fig. 4.4** – An energy field before (a) and after (b) the updating procedure. The grain with energy $e_4$ disappears between $t$ and $t+\Delta t$. The white zone corresponds to an arbitrary negative value.

**Algorithm 4** Updating of the energy fields between two consecutive increments

**procedure** UPDATE_ENERGY_FIELD(Field $\mathscr{I}_i$, Field $\mathscr{E}_i^t$)
  Create a Table $E$ with size $G_i$ and initialize its components $E[\cdot] \leftarrow -1$
  **for** Node $n \in \mathscr{M}$ **do**
    **if** $\mathscr{I}_i(n) > 0$ **then**
      $E[\mathscr{I}_i(n)] \leftarrow \max\left(E[\mathscr{I}_i(n)], \mathscr{E}_i^t(n)\right)$
    **end if**
  **end for**
  Process synchronization → keep the maximal value in $E$ component by component
  **for** Node $n \in \mathscr{M}$ **do**
    **if** $\mathscr{I}_i(n) > 0$ **then**
      $\mathscr{E}_i^{t+\Delta t}(n) \leftarrow E[\mathscr{I}_i(n)]$
    **else**
      $\mathscr{E}_i^{t+\Delta t}(n) \leftarrow -1$
    **end if**
  **end for**
  **return** $\mathscr{E}_i^{t+\Delta t}$
**end procedure**

### 4.3.5 Improvement of the nucleation algorithm

During annealing at elevated temperatures, a deformed microstructure usually recrystallizes discontinuously, through the appearance and growth of new grains with low dislocation density, the *nuclei*. This process is known as *discontinuous recrystal-*

*lization.* On the other hand, the microstructure may also evolve relatively homogeneously throughout the material, with no recognizable 'nucleation' and 'growth' of the recrystallized grains. In these conditions, the process can reasonably be classified as *continuous recrystallization.* The microstructural mechanisms involved during discontinuous and continuous recrystallization are actually similar and the difference between these terminologies is purely phenomenological, referring only to the spatial and temporal heterogeneity of microstructural evolution [Humphreys et al. 2004].

During SRX, DRX or PDRX, nuclei can appear continuously during the treatment or in site-saturated conditions. When a nucleus emerges in the microstructure, it can grow or shrink, depending on the capillarity force, the local energy gradient and the mobility of the surrounding grain boundaries. In the present study, a constant mobility is assumed for all grain boundaries, which means that the behavior of a nucleus is only dictated by the balance between capillarity effects and stored energy gradients. In our LS framework, introducing new grains in the microstructure is straightforward because it relies on simple arithmetic operations on the distance functions. In this section, we propose a new nucleation algorithm. The latter can be seen as an improved version of the algorithm introduced in [Bernacki et al. 2008; Bernacki et al. 2009] which takes full advantage of GLS functions and of the numerical tools introduced in chapters 2 and 3. Although only SRX in site saturated condition is considered hereafter, this algorithm can address also continuous recrystallization at the subgrain scale.

An important aspect of recrystallization is heterogeneity, especially as influenced by the placement of the nuclei [Cahn 1956; Rickman et al. 1997]. The present algorithm must therefore be able to handle the distribution of the nuclei inside the microstructure. To do so, a set $\mathscr{P}$ of all the potential nucleation sites is firstly constructed at the early stage of the algorithm. This set can contain all the nodes of the FE mesh or just a subset of them (*e.g.* nodes located inside a layer around the grain boundaries, energy greater than a threshold value,...). A nucleation site with coordinates $x_g$ is then picked in $\mathscr{P}$, randomly or according to an eventual selection criterion (highest stored energy, closest point from the grain boundaries,...). For simplicity we assume that nuclei are perfectly circular with radius $r$. Then the distance function $\phi$ of the new nucleus is calculated:

$$\phi(x) = r - \|x_g - x\|. \tag{4.7}$$

Next the new grain is affected to a GLS function. The index $k$ is used hereafter to

designate the GLS function which receives the nucleus. To determine $k$, we firstly evaluate, for each GLS function $i$, the minimal distance $\rho_i$ between this nucleus and the grains already represented by $\psi_i$. The GLS function $\psi_k$ which satisfies:

$$\rho_k = \max_{\forall i \in \{1,\dots,N_\mathrm{p}\}} (\rho_i), \tag{4.8}$$

is finally chosen to host the germ, provided that $\rho_k \geq s$, with $s$ a positive security distance. If $\rho_k < s$, no existing GLS function can receive the nuclei. A new function is therefore created $N_\mathrm{p} \leftarrow N_\mathrm{p} + 1$ and initialized such as $\psi_{N_\mathrm{p}} = \phi$.

All the nodes where $\phi > 0$ are finally removed from $\mathscr{P}$ to prevent the appearance of an other germ in the recrystallized region and the following arithmetic operations are performed on the GLS and stored energy fields:

$$\tilde{\psi}_i(x) = \begin{cases} \max\left(\psi_i(x), \phi(x)\right) \\ \min\left(\psi_i(x), -\phi(x)\right) \end{cases} \quad \text{and} \quad \tilde{\mathscr{E}}_i(x) = \begin{cases} e_0 & \text{if } i = k \\ -1 & \text{if } i \neq k \end{cases} \quad \forall i \in \left\{1, \dots, N_\mathrm{p}\right\}, \tag{4.9}$$

with $e_0$ the assumed stored energy level in the recrystallized material.

This procedure is repeated until the desired number of created nuclei is achieved or until the set $\mathscr{P}$ becomes empty (which corresponds to a fully recrystallized microstructure).

### 4.3.6 Evaluation of the numerical efficiency and comparison with the initial implementation

By using the new implementation using stored energy fields, the recoloring scheme introduced in section 3.3.2 can now be also employed in ReX simulations. We propose in this section to evaluate the gains in numerical efficiency permitted by the new implementation. Let us remind that two versions of the recoloring algorithm were proposed in section 3.3.2. The former ($C_1$) generates a coloring conflict when two child grains are separated by only one exterior grain. The second version ($C_2$) evaluates also the distance separating the child grains before considering there is a conflict between them. These two approaches are tested and compared with the implementation of [Bernacki et al. 2008; Bernacki et al. 2009] wherein grain coloring is static (*i.e.* $N_\mathrm{p} = N_\mathrm{g}$).

Let us consider the polycrystal of fig. 4.5a with dimensions $0.3 \times 0.3 \times 0.3\text{mm}^3$, composed of 48 grains and represented by $N_\text{p} = 15$ colors.

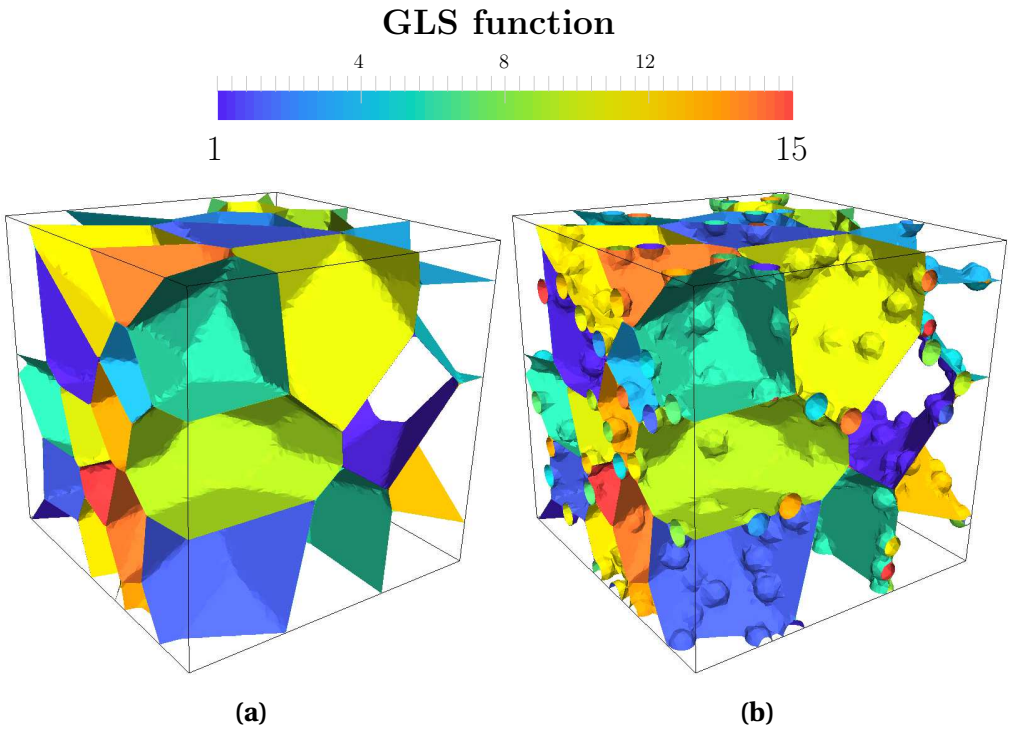


**Fig. 4.5** – (a) 3D polycrystal of 304L composed of 48 grains and represented by 15 GLS functions; (b) the same microstructure after nucleation at grain boundaries ($N_\text{g} = 348$).

300 nuclei are then introduced at the grain boundaries following the procedure detailed in section 4.3.5, giving $N_\text{g} = 348$. Here the set $\mathscr{P}$ is initialized with the nodes satisfying $\psi^\text{glob} \leq h$ in order to restrict nucleation in a narrow band around the grain boundaries. The minimal security distance $s$ is set to $2r$ (see section section 4.3.5 for explanations).

Obviously such a microstructure presents strong grain size heterogeneities. More precisely, the larger grains act like bounds between the nuclei, creating a large number of conflicts if the criterion $C_1$ is used for the swapping procedure. By executing this version of the algorithm (as it is done in [Scholtes et al. 2015]) on the microstructure of fig. 4.5b, 69 new GLS functions are initialized to solve the conflicts, leading to $N_\text{p} = 84$, which is critically high. Using $C_1$ is therefore inefficient in ReX simulations with nucleation. On the other hand if $C_2$ is employed with $\xi = \langle R \rangle_\text{ReX}/2$ (with $\langle R \rangle_\text{ReX}$ being the mean recrystallized grain size), all the coloring conflicts can be treated without creating any GLS function. Next, a heat treatment of $t_\text{h} = 5\text{min}$ at $T = 1000°\text{C}$ is simulated

on the obtained microstructure. A null stored energy is affected to the nuclei while the deformed grains present in fig. 4.5a receive a value of $3.3 \times 10^{-4}$ J/mm$^3$, which is a realistic order of magnitude. The material and simulation parameters are summarized in table 4.1. The time step is set to 5s. The FE mesh is fixed and composed of $90^3$ tetrahedral elements. Simulations are performed on 6 CPUs.

| Parameter | Value | Units |
|---|---|---|
| $T$ | 1000 | °C |
| $M$ | $5 \times 10^{-13}$ | $m^4.J^{-1}.s^{-1}$ |
| $\gamma$ | 0.6 | $J.m^{-2}$ |
| $r$ | 11 | $\mu$m |
| $e_0$ | 0 | $J.m^{-3}$ |

**Table 4.1** – Input parameters for the simulation of a 5min heat treatment using the polycrystal of fig. 4.5b.

As illustrated on fig. 4.6, the number of needed GLS functions remains much lower all along the simulation with the $C_2$ criterion, which is again proven more efficient that $C_1$. In the simulation with static grain coloring, the number of distance fields is naturally equal to the number of grains.

Table 4.2 provides the computation time and its distribution. The average number of active distance fields during a simulation is noted $\langle N_p \rangle$. It is equal to 343 without coloring and falls down to 21 with $C_2$, which results in a great improvement of the simulation time. Effectively, an acceleration factor around 9 is obtained.

| | Without coloring | $C_1$ criterion | $C_2$ criterion |
|---|---|---|---|
| $\langle N_p \rangle$ | 343 | 90 | 21 |
| Solving of CDEs | 7h09min | 1h56min | 27min |
| Reinitialization | 2h01min | 1h02min | 38min |
| Others | 37min | 8min | 3min |
| Total simulation time | 9h47min | 3h06min | 1h08min |

**Table 4.2** – Distribution of the computation time for the simulation of a 5min heat treatment at 1000°C using the polycrystal of fig. 4.5b. Simulations are performed on 6 Intel Xeon CPUs.

Hereafter, the optimized simulation using the $C_2$ swapping criterion is defined as reference configuration. The computation time and the average number of needed GLS functions for this simulation are noted, $t_{\text{simu}}^{\text{ref}}$ and $\langle N_p \rangle^{\text{ref}}$, respectively, and table 4.2 provides $t_{\text{simu}}^{\text{ref}}$ = 1h08min and $\langle N_p \rangle^{\text{ref}} = 21$. Based on the results of table 4.2, a simple

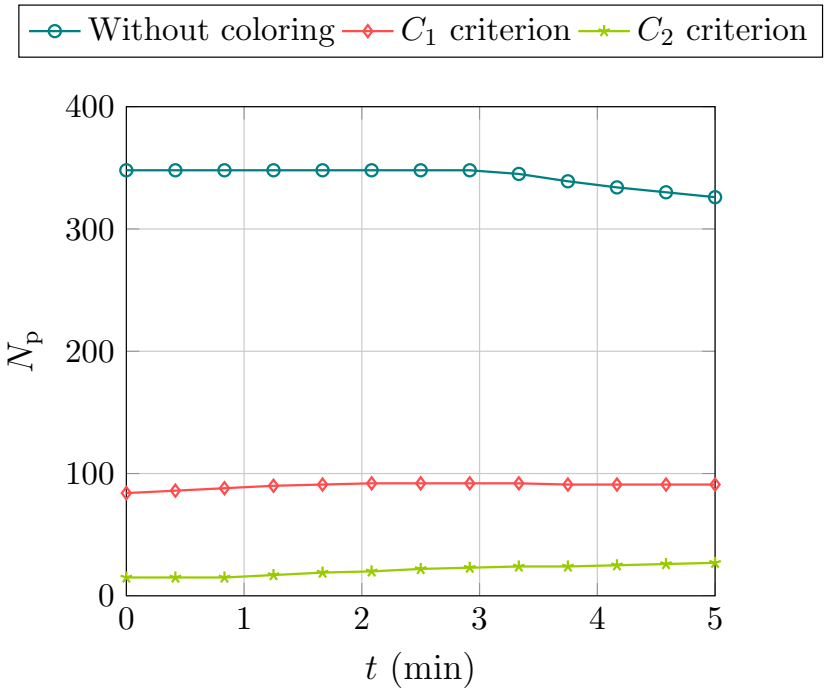


**Fig. 4.6** – Number of active GLS functions during the simulation of a 5min heat treatment at 1000°C using the initial polycrystal of fig. 4.5.

linear relationship with slope 0.5 can be exhibited between the number of active GLS functions and the simulation time:

$$\frac{t_{\text{simu}} - t_{\text{simu}}^{\text{ref}}}{t_{\text{simu}}^{\text{ref}}} = 0.5 \frac{\langle N_p \rangle - \langle N_p \rangle^{\text{ref}}}{\langle N_p \rangle^{\text{ref}}}. \tag{4.10}$$

Again we observe that the global computation time is not proportional to the number of distance fields. This was justified in chapter 3 as the execution time of the reinitialization algorithm depends also on the number of grains represented by each GLS function. However the time devoted to reinitialization is reduced by a factor greater than three thanks to the new implementation, which remains very interesting. Hereafter eq. (4.10) is used to roughly estimate the computation times that would have been obtained with more GLS functions.

The new implementation is finally demonstrated much more efficient. Next we challenge our optimized ReX model through different large-scale simulations of SRX in 3D (with and without nucleation) and confront the numerical results with mean field approximations.

## 4.4 Large-scale simulations of static recrystallizaton in three dimensions

This last section focuses on realistic applications. Especially we study two different SRX configurations. The former is a pure ReX simulation from a deformed state without nucleation wherein each grain is initially affected a given energy. Here recovery is not considered, which can be a strong assumption. So the grain energies remain constant during a simulation. In the second application, the deformation of a polycrystal is firstly simulated using a classical CPFEM code. Then different SRX simulations in site-saturated conditions are performed based on the post-deformation microstructure. Especially the dislocation density fields predicted by the CPFEM simulation are used to initialize the energy fields and to determine the potential nucleation sites.

### 4.4.1 Static recrystallization simulation from a deformed state

During SRX, there is a competition between capillarity effects and stored energy gradients. We introduce a ratio $\Lambda = \langle R \rangle \langle e \rangle / 2\gamma$, which reflects the balance between the averaged capillarity and pure recrystallization forces. $\Lambda > 1$ means that, on average, recrystallization forces outperform the capillarity effects. We pointed out in chapter 1 that these capillarity forces are commonly neglected in mean field models of ReX [Montheillet et al. 2009; Cram et al. 2009] because they are assumed to be one order of magnitude lower than the stored energy gradients. Next we attempt to challenge this assumption based on our new LS-FE SRX model.

First, we introduce $e_i = \tau \rho_i$ the stored energy level of the $i^{th}$ grain to reformulate eq. (1.28):

$$\frac{dR_i}{dt} = bM\langle e \rangle \left(1 - \frac{e_i}{\langle e \rangle}\right) \quad \forall i \in \{1, ..., N\}, \tag{4.11}$$

with $b$ the slope supposed to be unity according to eq. (1.28).

Then we perform a large-scale SRX simulation using the same 3D polycrystal of section 3.4.2, composed of 10,000 grains, and the same fixed FE mesh containing $310^3$ tetrahedral elements. This configuration without nucleation mainly applies to cases where the plastic strain is less than about 15%. Consequently each grain receives initially a random energy level comprised between $1 \times 10^{-4}$ and $5 \times 10^{-4}$ J.mm$^{-3}$, which is a representative order of magnitude. A heat treatment of $t_h = 17$min at $T = 1000$°C is simulated. The simulation parameters are the same than before (see table 4.1). The

average energy inside the material at the early stage of the simulation is $\langle e \rangle = 3 \times 10^{-4}$ J.mm$^{-3}$.

The evolution of the polycrystal during the TT is depicted on fig. 4.7.

The ratio $\Lambda$ evolves between 13 and 19 during the full field simulation, which undermines that stored energy gradients are at least 13 times greater than the averaged capillarity forces in the present case. On fig. 4.8 we compare the growth rates of the individual grains predicted by the LF-FE simulation with the mean field law given by eq. (4.11) at two different stages of the treatment (7min and 14min). The best slopes obtained by linear regression of the full field simulation results are 1.04 at $t = 7$min and 0.96 at $t = 14$min, which is very close from the unitary slope $b = 1$ given by eq. (1.28).

In this first case, the errors induced by the inherent approximations in the mean field formulation of eq. (1.28) are justified and sufficient to describe properly the grain evolutions. However let us remind that neglecting the capillarity effects impacts the shapes of the grains as it was demonstrated in 2D in [Fabiano 2013]. Especially the equilibrium angle at multiple junctions is no longer satisfied. The weakness of eq. (1.28) is then that it does not consider the microstructure topology and the way grains interact with each others. Even if this has not a significant influence in this first case, we will illustrate how topology may affect the predictions in the next section.

This 3D SRX simulation requires 50h of computation using 48 CPUs. The computation time for a single time increment is of the same order than for the same case without stored energy, detailed in section 3.4.2 (pure GG). The average number of grains present in the domain during the treatment is 9130 and $\langle N_\mathrm{p} \rangle = 23.7$. Using eq. (4.10), the computation time for this simulation without coloring can be estimated at more than one year. Also in section 3.4.2 an acceleration factor of 3.5 were obtained in the context of 3D pure GG with the DRT method comparatively to the HJ approach. Here the same acceleration factor can be reasonably expected as the extension of the energy fields (see section 4.3.3) takes less than 1% of the whole computation time. So this simulation would have required around four years at the beginning of this thesis work, using the same numerical facilities. This gives a global reduction of the simulation time by a factor close to 700, which is outstanding. This result is particularly exciting because it demonstrates our model is now very efficient for SRX simulations.

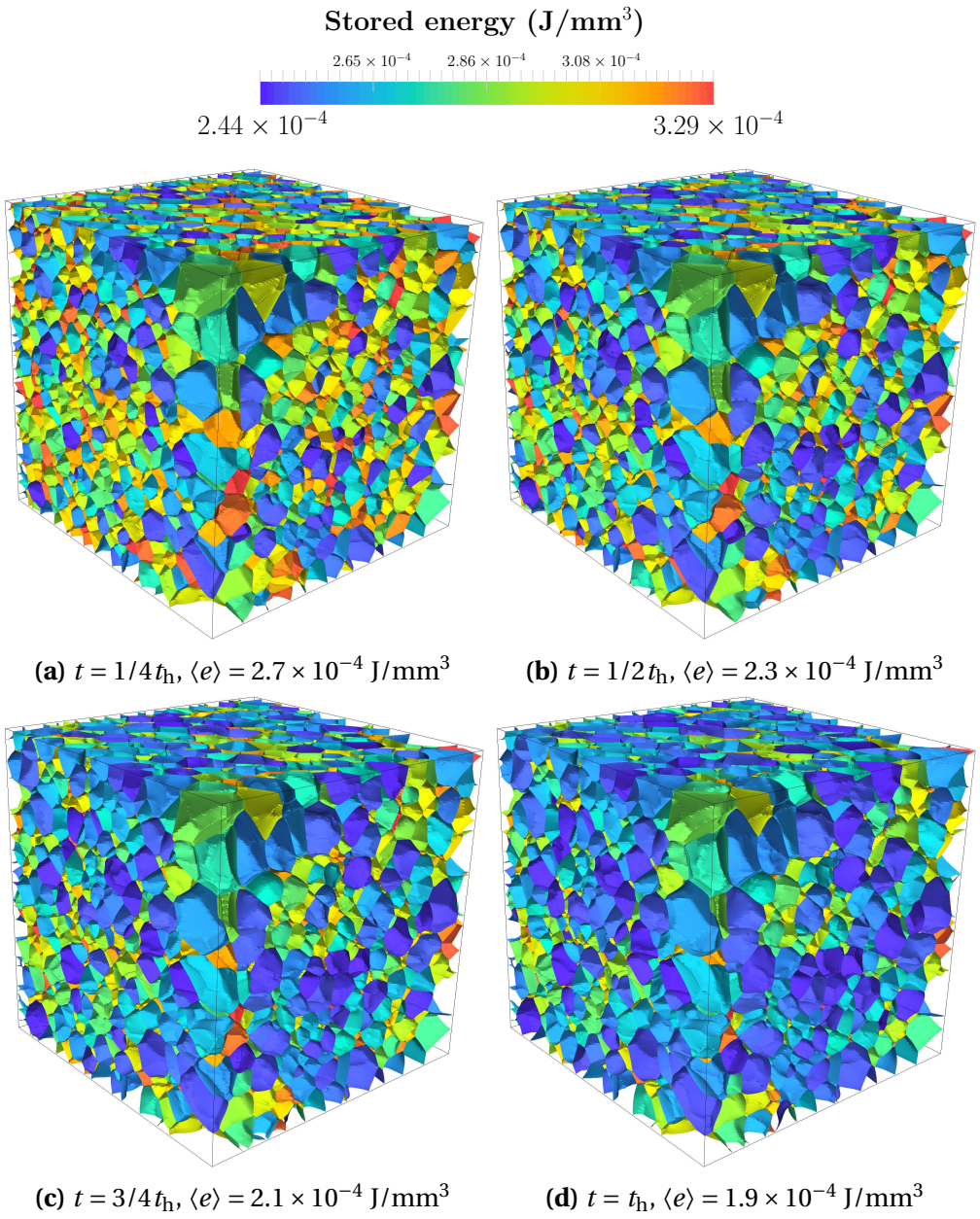


**(a)** $t = 1/4\,t_h$, $\langle e \rangle = 2.7 \times 10^{-4}$ J/mm$^3$ **(b)** $t = 1/2\,t_h$, $\langle e \rangle = 2.3 \times 10^{-4}$ J/mm$^3$

**(c)** $t = 3/4\,t_h$, $\langle e \rangle = 2.1 \times 10^{-4}$ J/mm$^3$ **(d)** $t = t_h$, $\langle e \rangle = 1.9 \times 10^{-4}$ J/mm$^3$

**Fig. 4.7** – Evolution of the grain boundary network during the 3D SRX simulation with an initial random energy level for each grain comprised between $1 \times 10^{-4}$ and $5 \times 10^{-4}$ J/mm$^3$. The color code refers to the stored energy level.

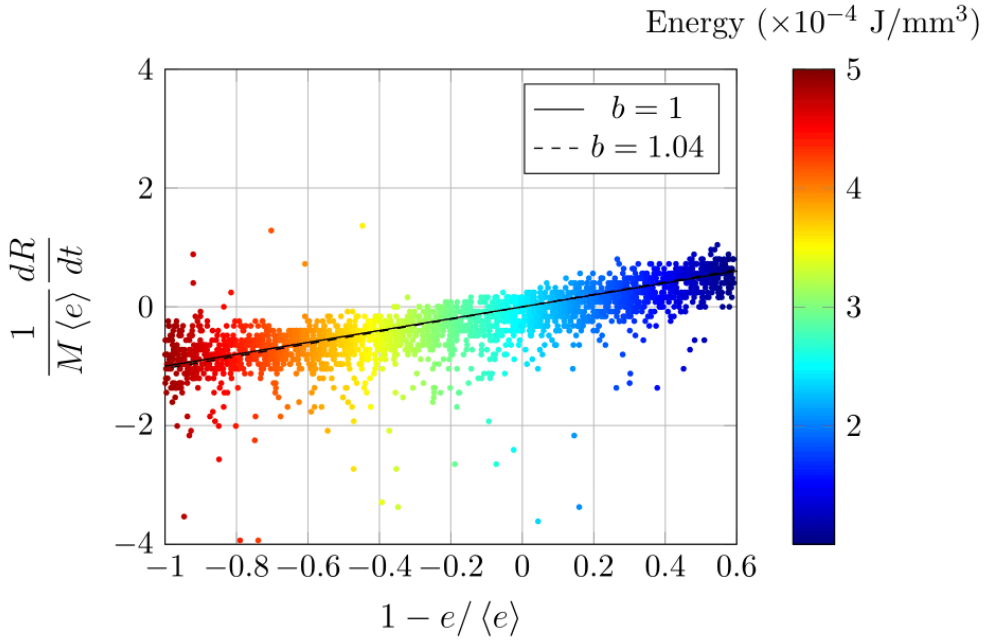


**(a)** $t = 7$min

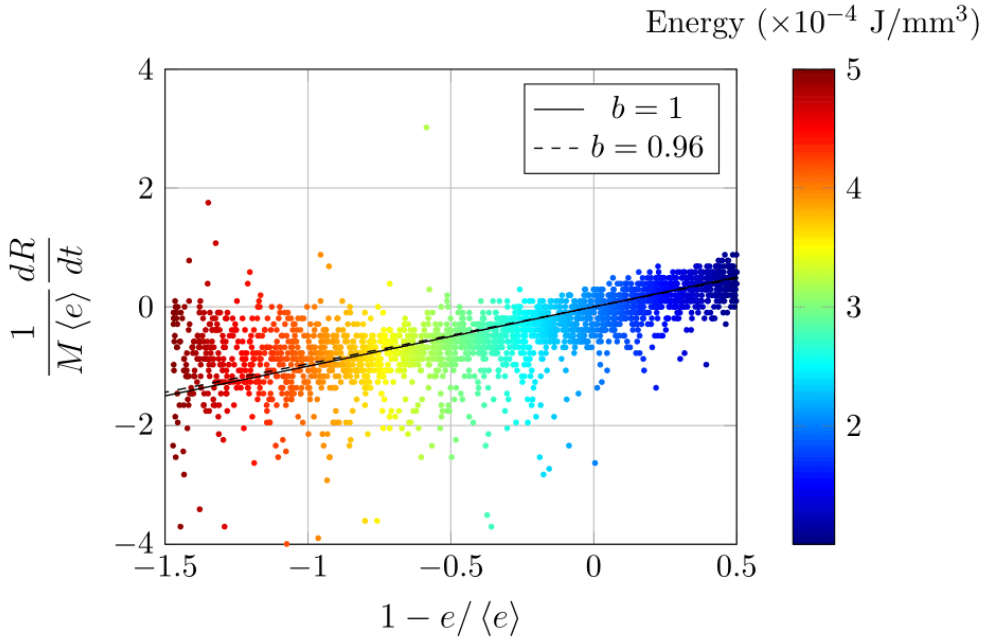


**(b)** $t = 14$min

**Fig. 4.8** – Growth rates of 2500 grains picked randomly in the 3D polycrystal. The solid and dotted lines refer respectively to eq. (1.28) with two different values for $b$ (theoretical and best fit).

### 4.4.2 Simulation of static recrystallization in site-saturated conditions

In this second application we investigate the deformation of a 3D polycrystal with subsequent SRX in site-saturated conditions. A REV is firstly submitted to a channel-die compression test and its mechanical state after deformation is used as input to perform several SRX simulations. Different configurations are investigated in which necklace or bulk nucleation is considered with either heterogeneous or homogeneous stored energy distribution. The model predictions are confronted with the experimental work of Huang [Huang 2011], wherein a 304L material has been submitted to hot torsion tests with subsequent heat treatment in various thermomechanical conditions, in order to investigate DRX, PDRX or SRX.

#### Deformation of the polycrystal

The mechanical behavior of the 304L aggregate during deformation is described by a CPFEM model based on a classical elasto-viscoplastic formulation. This model assumes that elastic strains are infinitesimal and plastic deformation is achieved by dislocation slip along the $\{111\}\langle 110\rangle$ crystallographic system, as expected in FCC crystals deforming at low temperature. The details and validation of the constitutive time integration scheme can be found in [Delannay et al. 2006; Logé et al. 2008]. A viscoplastic exponential flow-rule is used to relate the slip rates to the applied stress [Hutchinson 1977]:

$$\dot{\gamma}^{\alpha} = \dot{\gamma}_0 \left| \frac{\tau^{\alpha}}{\tau_c} \right|^{1/m} \operatorname{sgn}\left(\tau^{\alpha}\right), \tag{4.12}$$

where $\dot{\gamma}^{\alpha}$ and $\tau^{\alpha}$ are respectively the rate of dislocation slip and the resolved shear stress of the slip system $\alpha$. The coefficient $\dot{\gamma}_0$ is a reference slip rate, $m$ is the sensitivity exponent and $\tau_c$ is the critical resolved shear stress which is assumed for the considered 304L material to be identical for all slip systems [Resk et al. 2009]. This model also considers two populations of dislocations:

- the *statistically stored dislocations* which are the dislocations accumulated in the material during homogeneous plastic deformation,
- the *geometrically needed dislocations* which appear in areas of strain gradient and thus ensure the crystal lattice continuity.

The total dislocation density inside the material $\rho$ is naturally the sum of the dislocation densities related to these two populations. The critical resolved shear stress evolves with $\rho$ according to the following hardening law:

$$\tau_c = \tau_0 + \frac{1}{2}\mu b\sqrt{\rho}, \tag{4.13}$$

We refer the interested reader to [Delannay et al. 2006; Logé et al. 2008; Resk et al. 2009; Boulais-Sinou et al. 2016] for further details concerning the temporal evolution of the dislocation densities, the CPFEM model and the FE formulation.

The initial polycrystal is composed of 100 grains with dimensions $0.62\times0.62\times0.62\text{mm}^3$. It is submitted to a planar compression test and deformed until the averaged strain inside the material reaches a value of 30%. The FE mesh is composed of $100^3$ unstructured tetrahedral elements and remeshing operations are performed every 5% of deformation in order to ensure good element qualities all along the CPFEM simulation. At the end of the deformation, we compute the stored deformation energy field $\mathscr{D}$ from the dislocation density field $\mathscr{D} = \tau\rho$.

The final FE mesh and the GLS functions obtained at the end of the CPFEM simulation are then used as input for the SRX simulations. Considering the initialization of the energy fields, two different distributions are studied. In the former, the average value of the field $\mathscr{D}$ is affected to all the grains of the polycrystal, giving a homogeneous distribution of the stored energy. This first simplified configuration permits comparisons with the JMAK theory, which assumes a homogenized deformation energy throughout the microstructure. Hereafter the term "Homogeneized Energy" designates this configuration.

In the second distribution, the energy of a given grain is obtained by averaging the values of $\mathscr{D}$ inside this grain. In this configuration, the function GENERATE_ENERGY() of algorithm 3 can be described by algorithm 5. Obviously this representation, referred as "Heterogeneous Energy", is much more realistic because it also considers energy gradients between deformed grains.

**Algorithm 5** Generation of a grain energy in configuration "Heterogeneous Energy"

**procedure** GENERATE_ENERGY(Field $\mathscr{I}_i$, Field $\mathscr{D}$, Integer $g$)
  Create Floats $e \leftarrow 0$ and $k \leftarrow 0$
  **for** Node $n \in \mathscr{M}$ **do**
    **if** $\mathscr{I}_i(n) == g$ **then**
      $e \leftarrow e + \mathscr{D}(n)$
      $k \leftarrow k + 1$
    **end if**
  **end for**
  Process synchronization → sum the values obtained by each process for $e$ and $k$
  **return** $e/k$
**end procedure**

The dislocation density in the annealed material is around $10^{11}$ m$^{-2}$ and is more than three thousand times smaller than the average dislocation density resulting from the CPFEM simulation. It can thus be reasonably assumed that $e_0 \approx 0$.

Let us remind that our ReX formalism is only able to consider a homogeneous energy level inside a given grain for the time being, which remains a strong assumption. In real materials, intragranual heterogeneities may result in different migration rates for the grain boundaries. Ongoing studies attempt to address this limitation by considering heterogeneous stored energy fields inside the grains within the LS formulation [Ilin et al. 2016]. Furthermore, grain energies remain constant during the simulation. Thus in our framework, when a migrating grain boundary sweeps into the interior of a neighbor grain, the energy of this advancing grain is naturally affected inside the migration region, which is not the case practically. However this approach has the advantage of avoiding a specific treatment in the migration zone. On the other hand, updating the crystal orientation fields in the context of DRX requires much more attention and a specific approach has then been developed very recently [Boulais-Sinou et al. 2016]. The latter relies on an extension of the crystal orientation fields, which is performed during reinitialization, as detailed in section section 4.3.3.

It is well known that nucleation plays an important role in the kinetics of recrystallization. In this study we consider nucleation in site-saturated conditions with different spatial distributions for the nuclei. In "Bulk" nucleation, $\mathscr{P}$ contains all the mesh nodes, while it is only composed of the nodes close from the grain boundaries in "Necklace-Type" nucleation. Two different approaches are also tested for the determination of the nucleation site:

- "Site of Highest Energy" in which the node $n \in \mathscr{P}$ having the highest energy

value (related to the field $\mathscr{D}$) is chosen as nucleation site,

- "Random Nucleation" wherein the nucleation site is randomly picked in $\mathscr{P}$.

After one nucleus has been created, all the mesh nodes located inside ($\phi > 0$) are removed from $\mathscr{P}$. Five configurations are thus simulated, which are summarized in table 4.3.

| Configuration | Energy distribution | Nucleation |
|---|---|---|
| 1 | Homogeneous Energy | Bulk / Random Nucleation |
| 2 | Homogeneous Energy | Necklace-Type / Site of Highest Energy |
| 3 | Heterogeneous Energy | Bulk / Random Nucleation |
| 4 | Heterogeneous Energy | Necklace-Type / Site of Highest Energy |
| 5 | Heterogeneous Energy | Bulk / Site of Highest Energy |

**Table 4.3** – Description of the simulated SRX configurations.

#### Determination of the nucleation parameters, a multiscale approach

In [Kerisit 2012], the critical dislocation density needed to trigger SRX is identified through experimental tests. However, a large number of experiments has to be performed with different strain rates and annealing temperatures in order to correctly estimate this threshold value. Recently a mean field model of DRX [Bernard et al. 2011] and its adaptation to SRX [Fabiano 2013] have been proposed. Hereafter the equations of this SRX model are used to estimate the nucleation parameters $\rho_{\text{cr}}$, $\Upsilon$ and $r$ which are needed inputs for our LS-FE SRX simulations.

The mean dislocation density at the beginning of SRX is $\langle\rho\rangle = 2.01 \times 10^{14}$ m$^{-2}$. By using the data of table 4.4 representative of the 304L steel in the considered processing conditions, eq. (1.9), eq. (1.31) and eq. (1.12) provide respectively $\rho_{\text{cr}} = 5.7 \times 10^{13}$m$^{-2}$, $\Upsilon = 3224$ for $q = 2$ (necklace nucleation), $\Upsilon = 3235$ for $q = 3$ (bulk nucleation) and $r_c = 3.89\mu$m. We choose $r \approx 2h_{\text{b}} > r_c$ in the simulations, which is a minimum to have a correct description of the nuclei.

Figure 4.9 illustrates the initial microstructure before and after the nucleation stage for the different configurations (see table 4.3). It is worth emphasizing that, thanks to the new ReX formalism detailed in the previous section, each grain of the microstructure (deformed grain or nucleus) has its own energy, represented by a given color in

| Parameter | Value | Units |
|---|---|---|
| $T$ | 1000 | °C |
| $\dot{\varepsilon}$ | 0.01 | $s^{-1}$ |
| $b$ | $2.54 \times 10^{-10}$ | m |
| $\mu$ | $4.55 \times 10^{10}$ | Pa |
| $M$ | $5 \times 10^{-13}$ | $m^4.J^{-1}.s^{-1}$ |
| $\gamma$ | 0.6 | $J.m^{-2}$ |
| $K_1$ | $1.01 \times 10^{15}$ | $m^{-2}$ |
| $K_2$ | 3.3 | |
| $\tau$ | $1.47 \times 10^{-9}$ | N |
| $\theta$ | 0.3 | |
| $K_g$ | $7 \times 10^8$ | $m^{-2}.s^{-1}$ |
| $b_g$ | 3 | |
| $r$ | 11 | $\mu$m |
| $e_0$ | 0 | $J.m^{-3}$ |

**Table 4.4** – Processing conditions and input parameters for the SRX simulations.

fig. 4.9. This energy is also completely independent of the GLS functions.

### Simulation results and discussion

After deformation the dimensions of the REV are $0.8 \times 0.62 \times 0.48 mm^3$. The FE mesh is homogeneously refined in order to limit the initial size of the nuclei. It contains finally $200^3$ elements. A heat treatment of $t_h = 17$min at $T = 1000$°C is finally simulated. The time step is set to 5s.

The evolution of the recrystallized fraction is plotted on fig. 4.10. In site-saturated conditions, the Avrami exponent in eq. (1.13) is expected to be 2 for necklace-type nucleation and 3 for bulk nucleation. As the JMAK theory assumes a homogeneous deformation energy throughout the microstructure, only configurations 1 and 2 are considered for this first comparison. Figure 4.10 illustrates that the present LS-FE model captures greatly the recrystallization kinetics, as the calculated Avrami exponents fall very close from the theoretical values.

The numerical results are finally confronted with the experimental observations of [Huang 2011]. Figure 4.11a depicts the evolution of the bulk recrystallized fraction during the heat treatment for configurations 3, 4 and 5 (see table 4.3).

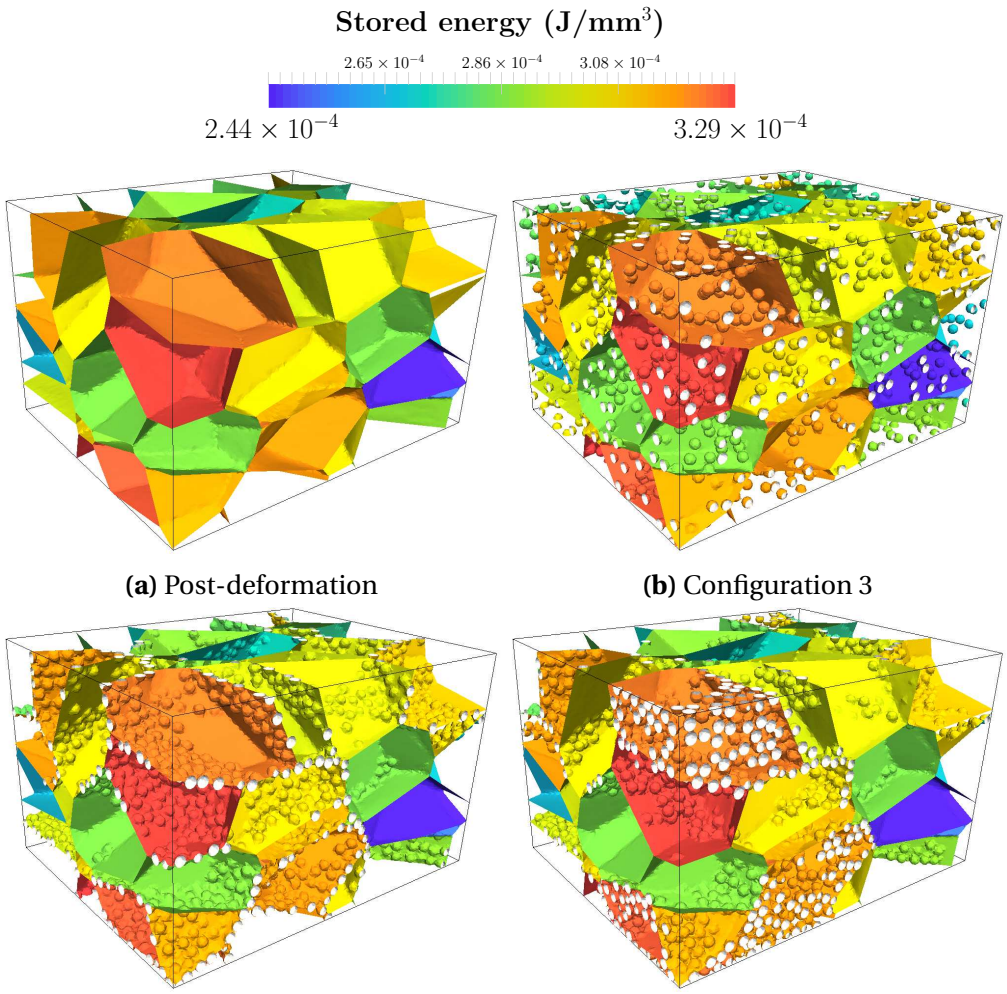


**(a)** Post-deformation

**(b)** Configuration 3

**(c)** Configuration 4

**(d)** Configuration 5

**Fig. 4.9** – Initial microstructure before (a) and after (b-c-d) nucleation with the "Heterogeneous Energy" representation. The color code corresponds to the stored energy level. Recrystallized regions are colored in white.

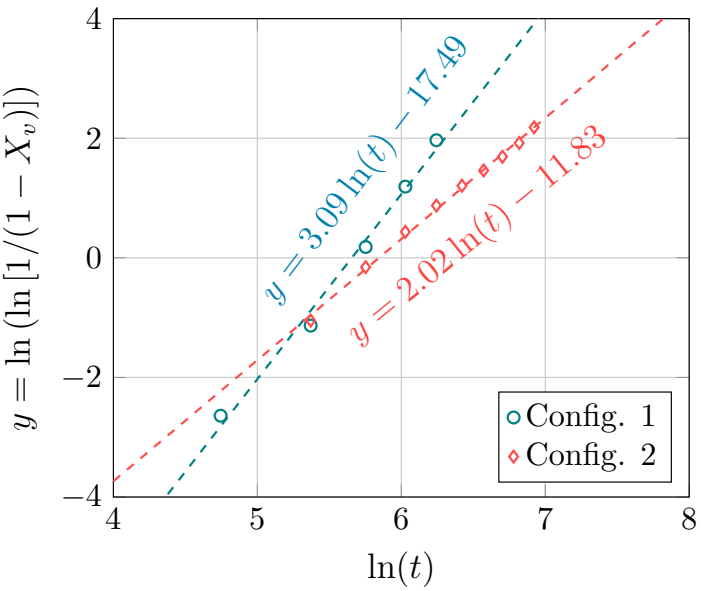


**Fig. 4.10** – Numerical predictions concerning the recrystallized fraction and calculation of the Avrami exponent for configurations 1 and 2 (see table 4.3).

Figure 4.11a illustrates that configuration 4 (necklace-type nucleation with selection of the highest energy node) provides the most realistic prediction in terms of recrystallized fraction. These results are in agreement with the experimental observations of Huang [Huang 2011], where nuclei appeared mainly at the grain boundaries during the recrystallization of the considered 304L steel. With bulk nucleation, the recrystallization kinetics is accelerated because nuclei have more space to grow and do not interfere with each other in the initial microstructure. In configuration 5, the progression of the recrystallized front is slowed down due to the formation of clusters in regions of highest energy.

In [Huang 2011], the recrystallization fraction is measured on slices of the material. One great advantage of the present numerical model lies on the possibility to easily interpolate the 3D distance and energy fields on a planar mesh in order to construct a 2D representation of the microstructure from the volume results (see fig. 4.12). Thus, 10 equally-spaced cutting planes of the virtual polycrystal are analyzed. We compute the respective surface recrystallized fractions of these 10 slices and then the average value $\langle X_s \rangle$. The evolution of this quantity is plotted on fig. 4.11b for the configuration 4 and compared with the bulk recrystallized fraction. It appears that the surface recrystallized fraction slightly overestimates the volumetric one, despite the number of cutting grains is relatively important (> 1000 for the 10 slices considered). This tends to indicate a small space anisotropy of the recrystallized fraction. Moreover, these

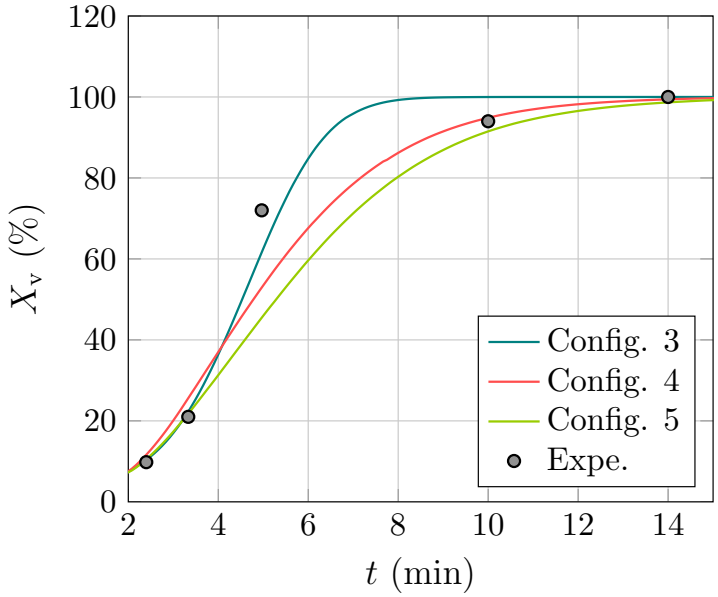


**(a)**

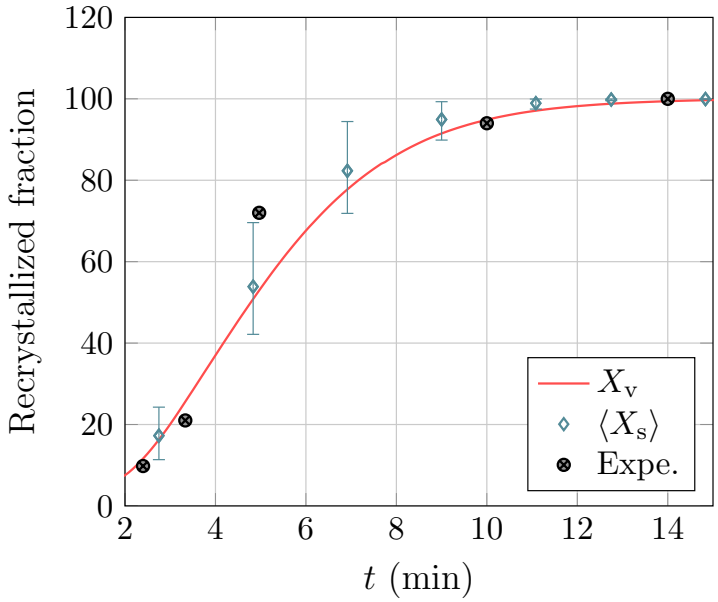


**(b)**

**Fig. 4.11** – (a) Bulk recrystallized fraction $X_v$ during the heat treatment at 1000°C for the configurations 3, 4 and 5 (see table 4.3) and comparison with the experimental observations of [Huang 2011]; (b) comparison of the bulk and surface recrystallized fractions simulated for configuration 4. The error bars indicate the minimal and maximal values measured among the 10 slices.

results also demonstrate that the recrystallized fraction may fluctuate from a cutting plane to another (see the error bars in fig. 4.11b), especially if the number of grains in the cutting plane is not sufficient. This numerical tool could thus be wisely used to size correctly the samples used for the experimental observations *a priori* and not *a posteriori* (determination of the minimal number of cutting grains) in order to ensure that the observed slice(s) is/are representative of the bulk behavior of the material.

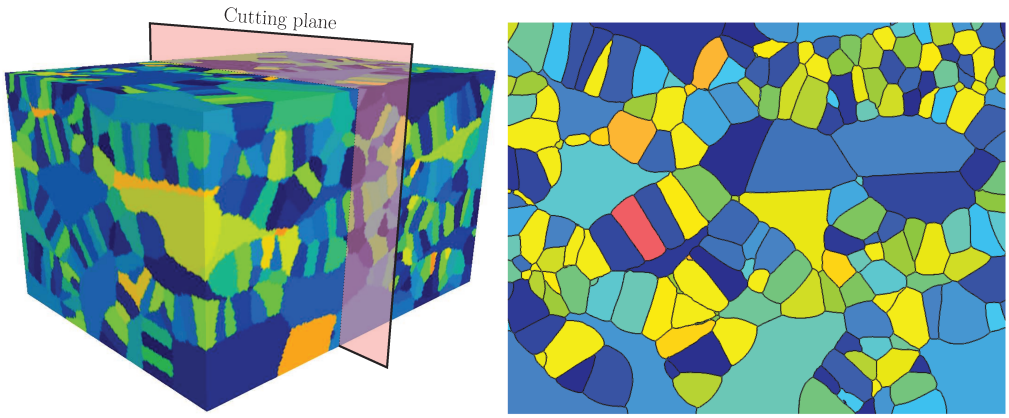


**(a)** 3D results **(b)** 2D extrapolation (slice view)

**Fig. 4.12** – Creation of a 2D representation of the microstructure (slice) from the 3D simulation results. The color code corresponds to the GLS functions.

Starting from the mean field equation given by eq. (4.11), all the recrystallized grains (*i.e.* $e_i \approx 0$) are assumed to grow at the same rate in the mean field model:

$$\frac{1}{M}\frac{dR_i}{dt} = \langle e \rangle. \tag{4.14}$$

The average growth rate of the nuclei obtained in the full field simulation is plotted on fig. 4.13 for comparison. As expected in this context, we observe that this mean field expression describes poorly the numerical predictions.

Effectively, there a two strong assumptions behind eq. (4.14). First, no capillarity term is considered which makes sense only if stored energy gradients prevail on capillarity forces. Secondly it does not take into account the interactions between the recrystallized grains, which is strongly related to their initial distribution. By examining the ratio $\Lambda$ on fig. 4.14a, we observe that capillarity and recrystallization forces are globally in balance for this configuration, and none of them can be safely neglected. Even after 6min the growth regime becomes essentially driven by capillarity, as $\Lambda$ is smaller than unity.

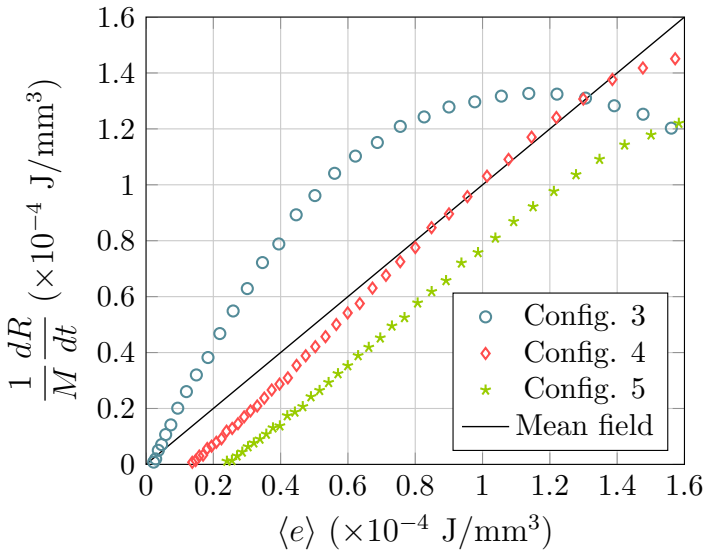


**Fig. 4.13** – Average growth rate of the nuclei during SRX as a function of the critical stored energy level. Here recovery is not considered, so recrystallized grains have a constant null energy.

Taking into account the microstructure topology is then important in this case. In configuration 3 considering random nucleation it is logically expected that germs have more space to grow because they are homogeneously distributed. On the other hand in configuration 4 and 5, nuclei are packed within high-energy regions and/or around the grain boundaries. Consequently they rapidly interact with each others which eliminates one or more growing direction(s) and slows down the coarsening. These conjectures are confirmed by fig. 4.14b which depicts the average number of neighbors for the recrystallized grains. The average number of facets is initially less than two for configuration 3 and around five for configuration 4 and 5. This number of neighbors remains also much lower in configuration 3 during the first stage of the heat treatment $t \leq 5$min which explains why the recrystallization kinetics is faster in this case.

This second study illustrates the importance of considering also the microstructure topology which is often omitted in mean field models. Full field approaches are extremely interesting in this context because they provide a complete representation of the grain interactions and can help to better understand the kinetics at the grain scale. Thus they can be advantageously employed to enrich/improved the mean field representations. Ongoing studies are part of this topic (PhD work of Ludovic Maire, MINES ParisTech, 2015-2018).

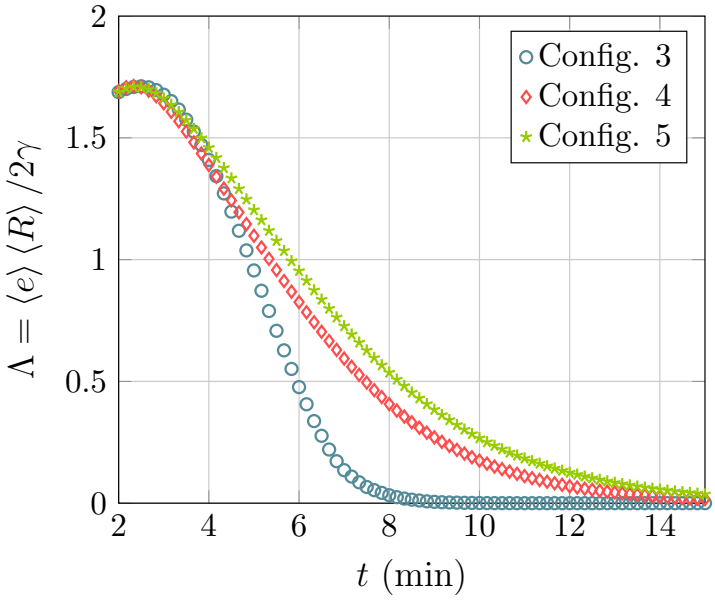


**(a)**

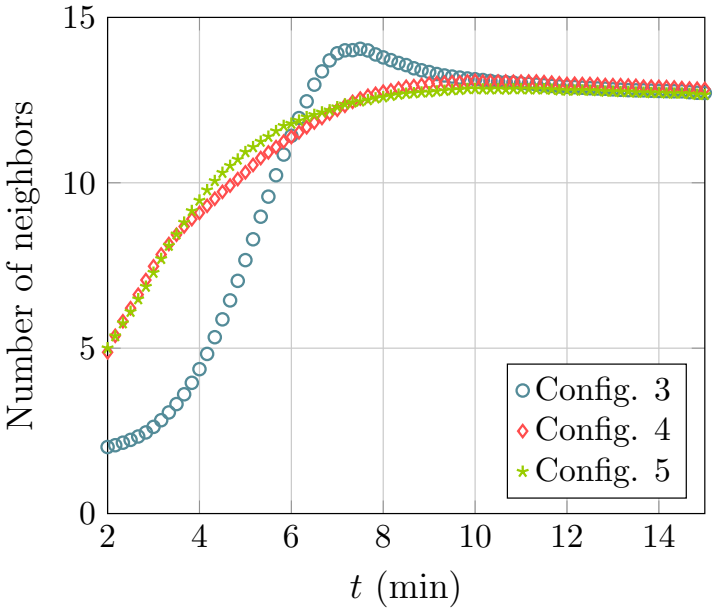


**(b)**

**Fig. 4.14** – (a) Ratio between average capillarity and recrystallization forces ; (b) average number of neighbors for the recrystallized grains.

Considering the capacities of the present LS-FE model, an exciting perspective would be to challenge the numerical predictions with more sophisticated experimental characterisations in terms of volume recrystallized fraction and grain size. Although obtaining these quantities is straightforward numerically (see fig. 4.15), estimating the recrystallized grain size inside the material is rather complex experimentally. Generally, the 3D grain size is estimated from the observed one by the mean of stereological considerations, which relies on assumptions.

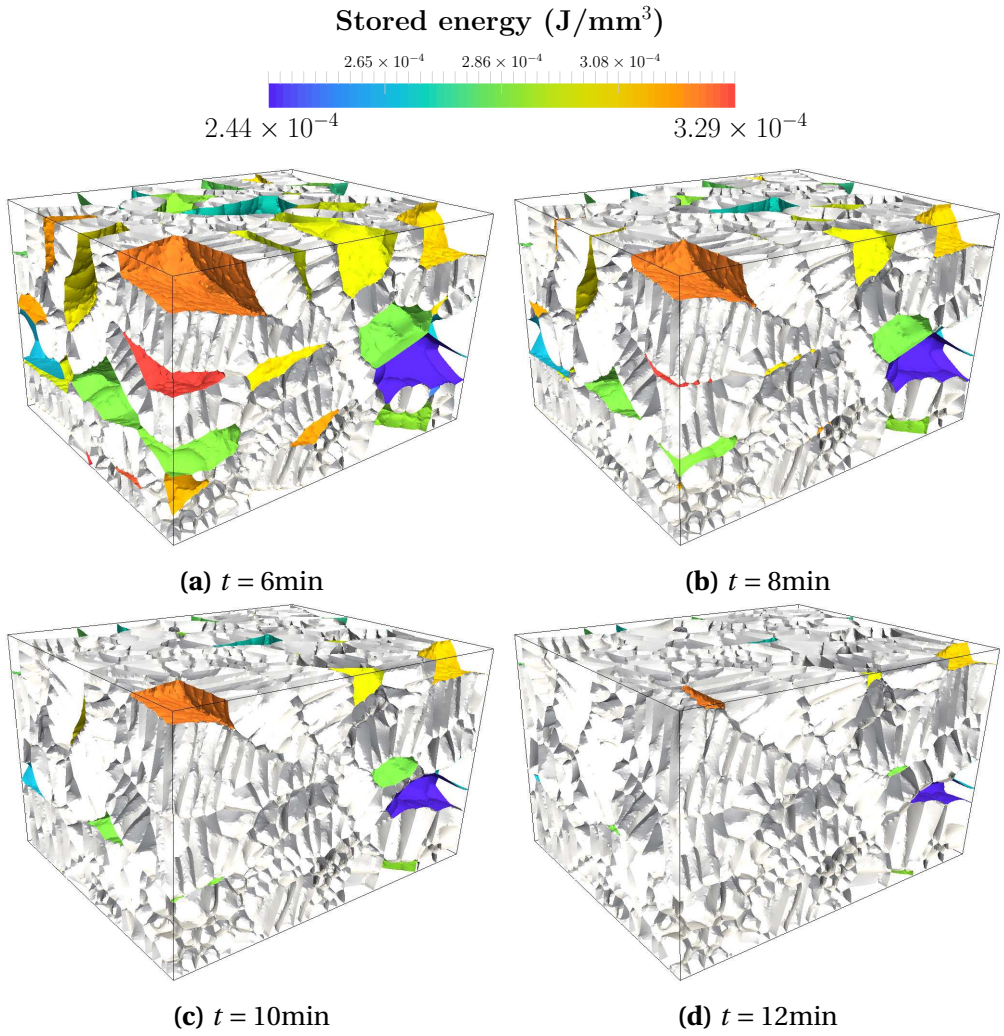


**(a)** $t = 6$min **(b)** $t = 8$min

**(c)** $t = 10$min **(d)** $t = 12$min

**Fig. 4.15** – Simulated microstructure at different stages of the heat treatment (configuration 4). The color code corresponds to the stored energy. Recrystallized regions are represented in white.

As illustrated in table 4.5 for configuration 4, each 3D simulation requires around one

day of computations using 24 CPUs, distributed as follows:

| | Related section | Computation time | Percentage |
|---|---|---|---|
| Solving of CDEs | eq. (1.47) | 8h24min | 31.4% |
| SCCs | section 3.3.2 | 2min | 0.1% |
| Initialization of energy fields | section 4.3.2 | < 1min | 0% |
| Reinitialization | section 2.4 | 17h21min | 64.9% |
| Field extension | section 4.3.3 | 10min | 0.6% |
| Tracking of grain energies | section 4.3.4 | < 1min | 0% |
| Nucleation | section 4.3.5 | < 1min | 0% |
| Post treatment operations | | 57min | 3.5% |

**Table 4.5** – Distribution of the computation time for a 3D large scale SRX simulation (configuration 4). The simulation is performed on 24 Intel Xeon CPUs.

The extension of the energy fields detailed in section 4.3.3 is performed simultaneously with reinitialization and entails an additional cost of around 1% compared with a classical reinitialization (without field extension), which is negligible.

As the nucleation algorithm and the initialization of the energy fields are only executed one time at the early stage of the simulation, they represent a very small amount of the global computation time. In the same way, the numerical costs associated with the SCC procedure, the nucleation algorithm, the initialization and the tracking of the energy fields are negligible compared with the reinitialization and the solving of the CDEs.

On average, 34 GLS functions are active during this simulation (22 and 37 at the early and final stages of the simulation, respectively) and the average number of grains present in the microstructure is equal to 3067. By using eq. (4.10) the computation time needed for such a simulation without coloring can be estimated around 1 month and 20 days. So the computation time is reduced by 45 thanks to the new implementation, which is quite satisfying. By considering again an acceleration factor of 3.5 in 3D between the HJ and DRT reinitialization methods (see section 2.5), one can estimate around 5 months and 25 hours the computation time needed to perform this simulation at the beginning of this work.

Although very promising, the present model should be further improved in order to capture the complexity of microstructural mechanisms involved during the forming process. First of all, the influence of anisotropy in terms of grain boundary energy

and mobility should be considered. More specifically, it is well known that the real 304L material contains twin boundaries, which are currently omitted in the simulations. Some recent studies using the LS method have investigated the influence of anisotropic grain boundary features in the context of 2D grain growth [Jin et al. 2015; Hallberg 2014; Mießen et al. 2015]. To our knowledge, this topic has never been investigated in 3D with stored energy for the time being. Next, the intragranular heterogeneity in terms of stored energy and its evolution during the migration of the grain boundaries should also be considered. This point is currently under study [Ilin et al. 2016; Boulais-Sinou et al. 2016]. Also in the present study, only SRX is considered, which means that recrystallization starts only after the deformation stage. First efforts to model DRX in a LS framework with consideration of the polycrystal deformation are very recent [Boulais-Sinou et al. 2016]. The numerical approach employed in [Boulais-Sinou et al. 2016] for the modeling of DRX works around a coupling between the CPFEM and GG/ReX models and uses the numerical tools detailed in this manuscript. Further experimental investigations should also be carried out in order to verify the values of the input parameters needed for the full field simulations (number and size of the nuclei, critical dislocation density,...). Finally, as nucleation models suitable for SRX conditions are relatively scarce in the literature, using the present model to develop and/or calibrate an accurate SRX nucleation law is a very interesting prospect.

## Summary

The LS-FE modeling of SRX has been covered in this chapter. First we have discussed the recrystallization model introduced by Bernacki et al. in [Bernacki et al. 2008] which uses a given energy level for each distance field. Then we pointed out that this model is not effective enough from a numerical point of view because of the impossibility to use grain coloring and swapping. It is therefore limited to simple configurations with small number of grains because each grain needs to be represented by a distance field. Based on this initial situation, our objective was to extend this first formalism to take full advantage of GLS functions and of the new recoloring scheme introduced in section 3.3.2. For this purpose we developed a new implementation of the recrystallization model based on stored energy fields which permit to handle the energies without using a distance field for each grain. In this approach the energy is completely independent of the GLS functions. Consequently it is perfectly compatible with the recoloring scheme introduced in the previous chapter because the energies can be swapped simultaneously with the grains when a recoloring oper-

ation has to be performed. Also a new nucleation algorithm which determines the potential nucleation sites and handles the affectation of the new grains inside the GLS functions has been developed. These new numerical tools have been implemented in our numerical library in a completely general manner in such a way that any kind of quantity (scalar, vector, tensor) associated with the individual grains can be handled in the same way it is done for the stored energy (crystal orientation is an example). We challenged this new implementation through different large-scale SRX simulations in 3D. The new approach was observed to be far more efficient with acceleration factor up to 45 for the considered cases. The influence of the nucleation scenario on the overall recrystallization kinetics has finally been studied based on different full field simulations of SRX in site-saturated conditions. The numerical developments presented in this chapter have allowed to publish [Scholtes et al. 2016a].

# Chapter 5

# To an efficient modeling of microstructural evolution under consideration of Zener pinning

## Contents


**5.1 Introduction . . . . . 177**

**5.2 Level set modeling of the Zener pinning phenomenon within a finite element framework . . . . . 177**

5.2.1 Description of the numerical approach . . . . . 177

5.2.2 Limitations . . . . . 179

5.2.3 Improvement of the algorithm for the generation of finite element meshes . . . . . 182

**5.3 Numerical investigations of the Zener pinning phenomenon . . . . 187**

5.3.1 Literature review . . . . . 187

5.3.2 Discussion of a classical limiting mean grain size equation in 2D188

5.3.3 First 3D simulation of Zener pinnning using a level set approach within a finite element framework . . . . . 193

# Résumé en français

Dans ce chapitre, la modélisation du phénomène d'ancrage par une méthode level set/éléments finis a été étudiée. L'approche numérique développée par Agnoli et al. [Agnoli 2013] pour la modélisation des précipités inertes a d'abord été présentée. Celle-ci repose sur la construction de maillages éléments finis spécifiques contenant des trous, qui représentent les précipités et freinent les joints de grains. Même si cette méthode est très précise, elle est incompatible avec les simulations industrielles en raison de temps de calcul très importants. La situation a été considérablement améliorée par l'introduction des nouveaux algorithmes de reinitialisation et de recoloration dynamique (cf. sections 2.4 and 3.3.2) dans les simulations du phénomène d'ancrage. Cependant, les temps de simulation étaient toujours pénalisés par la génération des maillages éléments finis troués, qui est très longue. Une nouvelle méthode de génération a donc été développée. Cette approche se base sur la géométrie des objets à mailler (les particules de seconde phase en l'occurrence) pour construire un maillage éléments finis conforme à l'interface des précipités. Un mailleur externe est utilisé pour mailler les entités géométriques dans l'ordre de leur dimension spatiale. Beaucoup plus efficace, cette nouvelle méthode permet de générer des maillages éléments finis adaptés à un grand nombre de particules en trois dimensions avec des temps de calcul raisonnables. Ces développements ont été mis en pratique pour réaliser plusieurs simulations du phénomène d'ancrage en deux dimensions et pour discuter une loi classique à champ moyen prédisant la taille de grains moyenne finale à partir des résultats de simulation en champ complet. Enfin une première simulation réaliste du phénomène d'ancrage en trois dimensions a été réalisée en s'appuyant sur des données expérimentales pour l'Inconel 718. Les développements numériques et résultats présentés dans ce chapitre ont permis la publication d'un article de conférence [Scholtes et al. 2016b].

## 5.1 Introduction

As presented in the introduction chapter, the ZP phenomenon is a dragging effect exerted by the precipitates on the grain boundaries, which may hinder GG or eventually stop it completely under certain conditions. In the case where GG stops, the microstructure reaches a steady-state and a limiting mean grain size $\langle R_f \rangle$ is obtained. The ZP phenomenon is largely exploited in the industry for many alloys and especially for superalloys, where SPPs are used to control the grain size of the material. Because it can dramatically impact the grain boundary kinetics, this phenomenon must be taken into account in numerical models in order to predict accurately the microstructure evolutions and the underlying physical mechanisms. Our main objective in this chapter is to propose an efficient LS-FE method for the modeling of microstructural evolutions in presence of dragging precipitates. We start from the numerical approach developed by Agnoli during its PhD work (MINES ParisTech, 2010-2013) for the modeling of *inert* SPPs (*i.e.* whose shape, size and position do not evolve during the TMT/TT) and improve drastically its numerical efficiency through the recent numerical developments. We introduce also a new methodology for the efficient generation of the specific FE meshes needed for such simulations. These developments are put into practice to discuss the fitting parameters of a classical limiting mean grain size equation in 2D and to perform a first realistic 3D LS-FE simulation of the ZP phenomenon.

## 5.2 Level set modeling of the Zener pinning phenomenon within a finite element framework

### 5.2.1 Description of the numerical approach

#### Basics

The LS modeling of ZP is quite recent comparatively to the other full field approaches presented in chapter 1 [Agnoli et al. 2012; Agnoli et al. 2014]. When coupled with FE, this approach can be very interesting to address this phenomenon. Effectively, no assumption is required concerning the shape or the dragging force exerted by the SPPs. The balance of the surface tensions at the interface between a particle and a grain boundary, given by eq. (1.22), can here be imposed thanks to a boundary condition:

$$\frac{\nabla\psi}{\|\nabla\psi\|}\cdot\vec{p}=\nabla\psi\cdot\vec{p}=\sin(\alpha)=\frac{\gamma_2^p-\gamma_1^p}{\gamma}, \tag{5.1}$$

where $\vec{p}$ represents the unit outward vector perpendicular to the interface of the precipitate (see fig. 1.3). Then, when a grain boundary passes through a particle, its shape adapts to satisfy eq. (5.1), which modifies its local curvature and therefore its kinetics. Coherent or incoherent SPPs can thus be considered by applying the suitable boundary conditions. If null boundary conditions are applied at the SPP/grain boundary interfaces, then we have $\nabla\psi\cdot\vec{p}=0$ and $\alpha=0°$, which represents a precipitate incoherent with the matrix, *i.e.* $\gamma_1^p=\gamma_2^p$ in fig. 1.3. In practice, the SPPs are represented by voids in the FE mesh and the boundary condition defined by eq. (5.1) is directly integrated in the weak formulation of eq. (1.47):

$$\int_\Omega\frac{\partial\psi_i}{\partial t}u+\int_\Omega\gamma M\nabla\psi_i\cdot\nabla u+\int_\Omega\vec{v}^{\,\mathrm{e}}\cdot\nabla\psi_i u=\int_{\partial\Omega}\gamma M\nabla\psi_i\cdot\vec{s}\,u,\ \ \forall u\in H^1(\Omega). \tag{5.2}$$

Let us remind that $\vec{s}$ is the unit outward vector normal to the boundary of the simulation domain. At the interface of a precipitate $\vec{s}=-\vec{p}$ (see fig. 1.3), and the second member term in eq. (5.2) can be rewritten as follows:

$$\int_{\partial\Omega}\gamma M\nabla\psi_i\cdot\vec{s}\,u=-\int_{\partial\Omega}\gamma M\sin(\alpha)u \tag{5.3}$$

Using this approach, the only adaptation needed to include SPPs in the simulation is to, first, create a FE mesh that contains voids, each void representing a precipitate, and secondly, apply the desired Neumann boundary conditions (only needed for coherent precipitates).

In [Agnoli 2013], an approach is presented to generate these FE meshes with holes. The first step is to create a binary field that represents the precipitates, equals to unity inside the SPPs and zero elsewhere, as illustrated on fig. 5.2a. This field can be generated according to an experimental image or a virtual dispersoïd of precipitates that follows a prescribed size distribution. Then the mesh is refined in the zones where the binary field varies from zero to one in order to increase the precision at the precipitate interfaces (see fig. 5.2b). After the mesh has been refined, all the elements that have at least one node inside a particle are *killed*, *i.e.* removed from the FE mesh. The holes formed by the killed elements represent the SPPs, as depicted on fig. 5.2c.

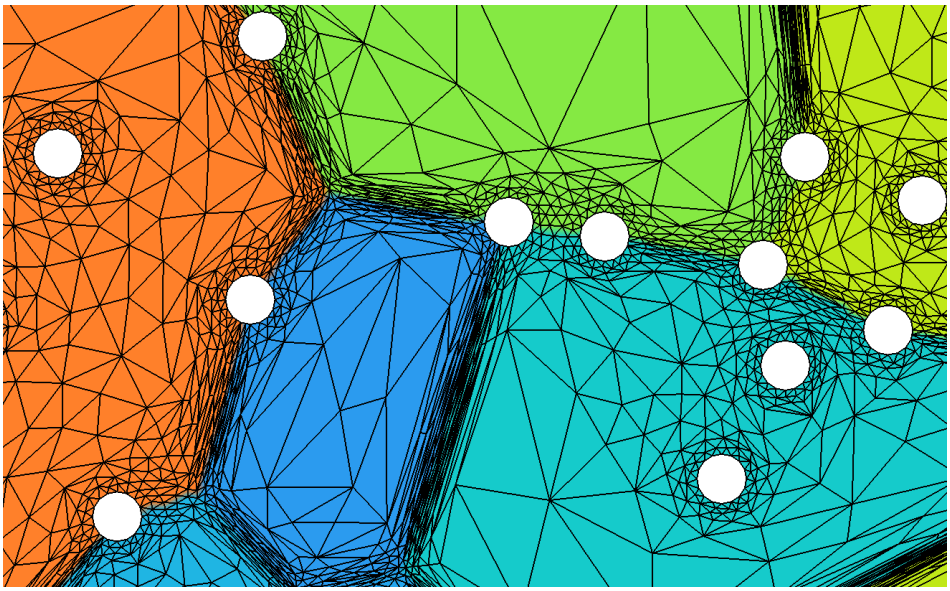

**Fig. 5.1** – View of a FE mesh used for a ZP simulation. The voids (white disks) represent the SPPs.

### 5.2.2 Limitations

This LS-FE approach for the modeling of ZP has been demonstrated very precise [Agnoli et al. 2014]. However different issues have also been reported in the thesis work of Agnoli [Agnoli 2013]. First, such Zener pinning simulations require to adapt (*i.e.* reduce) the time step in order to describe properly the interactions between the grain boundaries and the SPPs. If we use the same time step than for a classical GG simulation without SPP, then the dragging effect exerted by the precipitates can be drastically underestimated and the above approach loses its interest. Agnoli proposed a calibration procedure for the time step in the context of an Inconel 718 material in [Agnoli 2013]. But reducing the time step impacts directly the simulation time because more time increments are needed to simulate the TMT/TT. This was especially problematic when a HJ approach was used for the reinitialization of the LS functions because this method was proven inefficient in the context of our application (see chapters 1 and 2).

The second issue is related to the description of the SPPs within the FE mesh. Effectively, before killing the mesh elements located inside the SPPs, the mesh must generally be refined to better describe the precipitate interfaces. However, if a coarse mesh size is fixed near the SPPs, the obtained interfaces can be sharp and irregular, which alters the kinetics of the boundaries. It may also rise different numerical difficulties concerning the resolution of the HJ equation (see eq. (2.6)) and increase the number of needed iterations [Agnoli 2013]. On the other hand, if the prescribed mesh

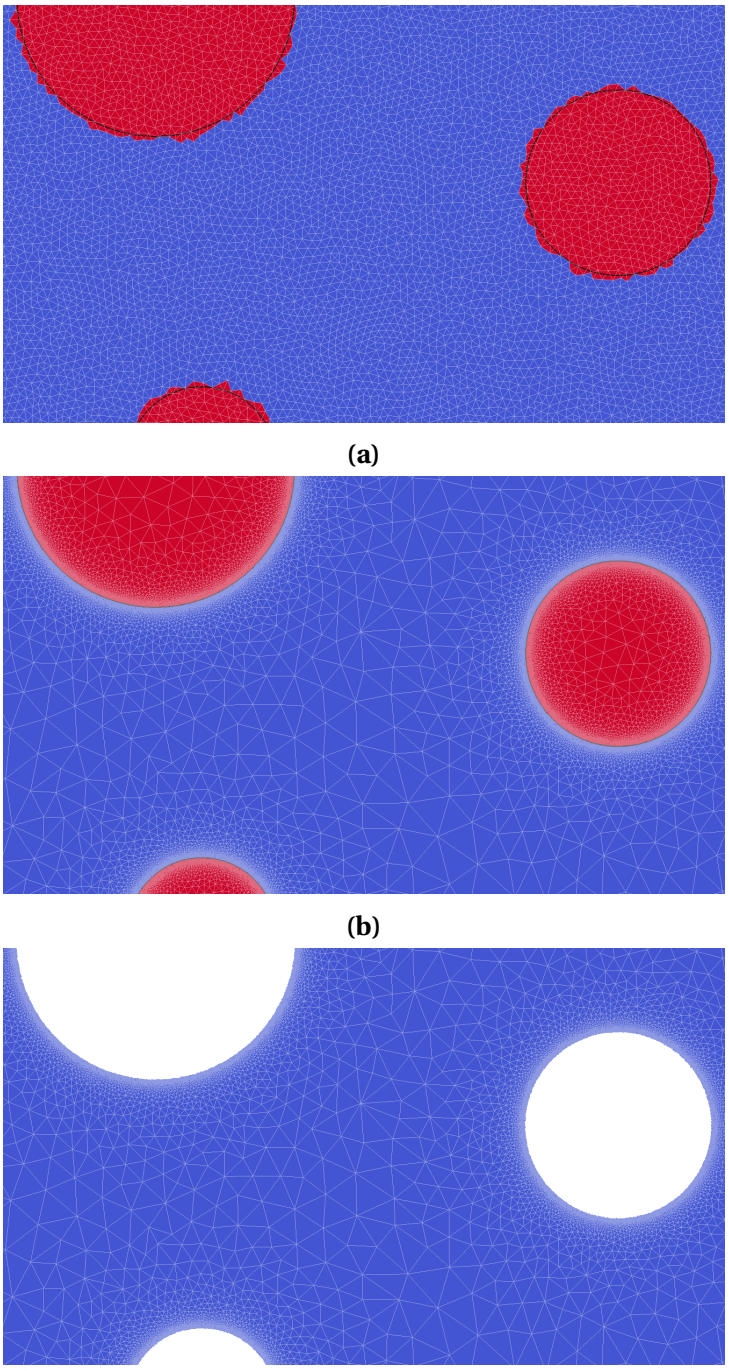

**(a)**

**(b)**

**(c)**

**Fig. 5.2** – Generation of a FE mesh with holes with the method presented in [Agnoli 2013], based on a kill-element strategy. The blue and red colors represent respectively the zero and unity values of the binary field.

size around the SPPs is very fine then the generation of the initial FE mesh with holes is more time demanding.

Finally, the possibility of numerical coalescence imposed to Agnoli et al. to use the same approach than in [Cruz-Fabiano et al. 2014], consisting in introducing an initial separation between the child grains (see parameter $\delta$ in section 1.5.3. Obviously this approach is catastrophic in terms of numerical efficiency because all the GLS functions must be reinitialized at each time step.

Consequently the computation times reported in [Agnoli 2013] for the different 2D simulations of the ZP phenomenon are extremely high. Several weeks are effectively required, even for reasonable 2D microstructures with one thousand initial grains. Obviously these simulation times are not compatible with our expectations and must be drastically improved.

The first problem concerning the reinitialization stage in these ZP simulations has been directly addressed here by replacing the HJ reinitialization method used in [Cruz-Fabiano et al. 2014; Agnoli et al. 2014] by the DRT algorithm introduced in section 2.4, which is far more efficient and robust. The problem of numerical coalescence has also been directly solved by using the dynamic recoloring scheme of section 3.3.2 in the ZP simulations. These two algorithms are effectively completely generic and can be directly employed in ZP simulations without any adaptation. Finally, even if our developments have not permitted to use greater time steps in ZP simulations, it is worth noting that the computation time per increment has been greatly reduced thanks to the previous developments.

The last problem concerns the generation of the specific FE meshes needed in the ZP simulations, which can be very time-consuming. Let us consider a simple 3D case for an illustration. In [Agnoli 2013; Agnoli et al. 2014], the volume fraction of $\gamma$ precipitates measured in the considered Inconel 718 material is around 2%, with an average radius of particles $\langle r_p \rangle = 0.35\mu$m. For this test case, we generate a single precipitate with radius $0.35\mu$m, centered in a $2 \times 2 \times 2\mu m^3$ cubic simulation domain, which gives $f_v = 2\%$. Then the SPP and the domain are meshed by using local refinement with the kill-element strategy detailed previously [Agnoli 2013]. Three different mesh sizes are tested near the SPP $h_n = r_p/2$ (coarse), $r_p/5$ (medium) and $r_p/10$ (fine). Far from the precipitates the mesh size is set to $h_b = 5h_n$. We depict on figs. 5.3a to 5.3c the FE meshes generated in the different configurations with the corresponding element qualities. Table 5.1 provides the number of elements composing each mesh and the

computation times needed for their generation, using 1 CPU.

| | Coarse | Medium | Fine |
|---|---|---|---|
| Number of mesh elements | 718 | 3324 | 32,354 |
| CPU time for one particle | 9.2s | 12.8s | 52.2s |
| Estimated CPU time for 10,000 particles | 1 day 2h | 1 day 12h | 6 days 1h |

**Table 5.1** – Generation of FE meshes for one precipitate with the approach of [Agnoli et al. 2012]. Simulations are performed on 1 CPU.

It is shown that, the aspect of the precipitate remains irregular, even with the finest mesh size. Now, if a real polycrystal composed of around 500 grains with a mean grain size $\langle R \rangle = 3.35\mu$m (which is representative of the Inconel 718 considered in [Agnoli 2013; Agnoli et al. 2014] is considered, 10,000 SPPs with radius $r_p = 0.35\mu$m must be generated to obtain $f_v = 2\%$. In terms of numerical cost, this problem is globally equivalent to mesh 10,000 distinct small domains, each with dimensions $2 \times 2 \times 2\mu m^3$. In the last row of table 5.1, we estimate the computation times needed to generate the FE mesh for such a particle cloud with the different precision levels, using 1 CPU. Even by assuming a perfect speed-up of the parallel mesh adaptation procedure (which is very far from the real speed-up observed in practice [Coupez et al. 2000]), the computation times needed to generate these FE meshes with the kill-element approach are impracticable in 3D, regardless the number of used CPUs. This is a main reason why no 3D LS-FE simulation of the ZP phenomenon has been performed for the time being. We attempt to improve the situation in the next section by introducing a new algorithm for generating the FE meshes.

### 5.2.3 Improvement of the algorithm for the generation of finite element meshes

In the approach of [Agnoli 2013], the particles are firstly immersed within the FE mesh, then the mesh is refined, and finally the holes are created by killing the elements. This approach is the most generic because any kind of particles can be considered, and especially real-shaped SPPs. However, Agnoli [Agnoli 2013] has demonstrated that the real particles can, most of the time, be reasonably approximated by simple geometrical entities, especially spheres. Thus the dispersoïd of SPPs can be modeled by a cloud of spheres (respectively disks in 2D), each represented by the spatial coordinates of its centroïd and a radius. Using this geometrical description, the above strategy based on mesh adaptation for the construction of the initial FE mesh is not

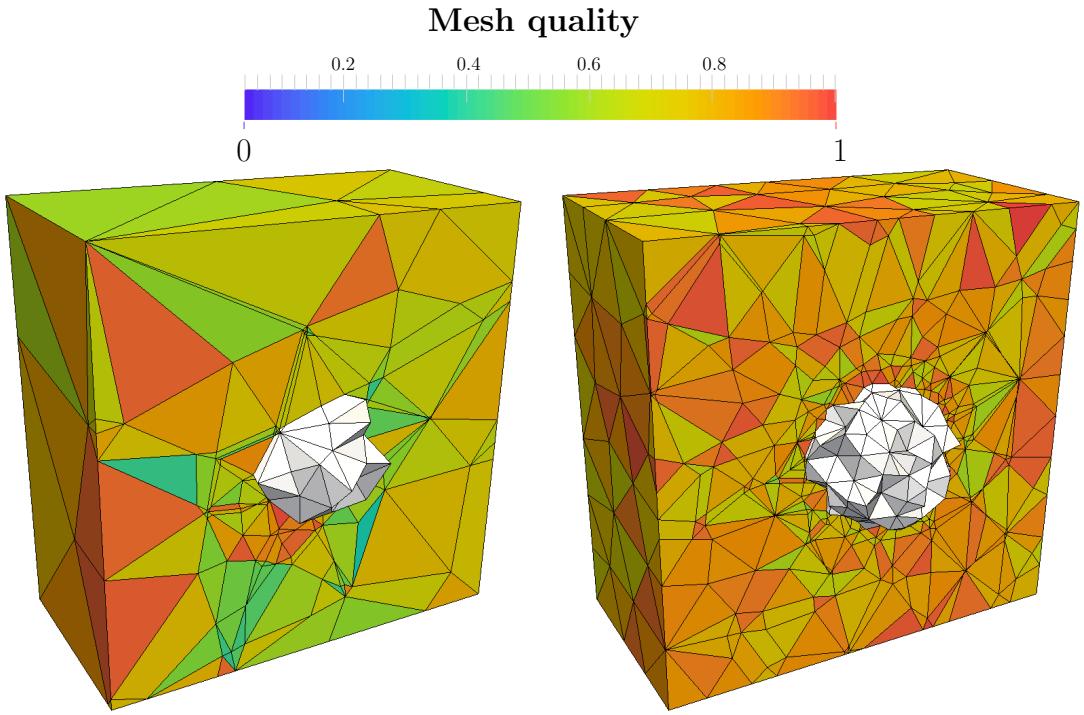


**(a)** Coarse (718 elements) **(b)** Medium (3324 elements)

**(c)** Fine (32,354 elements) **(d)** GBMG (755 elements)

**Fig. 5.3** – Representation of a SPP within the FE mesh using different refined mesh sizes with the kill-element strategy of [Agnoli 2013] and the new geometry-based one. The interface of the precipitate is depicted in white.

optimal because we know in advance where and how the mesh must be refined.

In most engineering problems, and especially in mechanics, the part is generally designed in a first time. Then a virtual representation of the part is created thanks to a CAD (Computer Assisted Design) software and finally the geometry is meshed in order to perform the different simulations. This is the *Geometry-based* approach, which relies on a simple idea: *if we know in advance (before creating the FE mesh) the shape of the entity that has to be simulated, then it is preferable to use its geometry as a support for the mesh adaptation.*

Next we will work around this concept of Geometry-based mesh generation (GBMG) and introduce a new method for generating the FE meshes with holes much more efficiently. The objective is to generate *body-fitted* FE meshes, wherein the interfaces of the particles are explicitly represented. The most simple way to achieve this description is to generate first the mesh of low dimensional entities and then build on top of them higher dimensional entities. This approach is classically referred to as *bottom-up* mesh generation. In other words, in the 3D case, the point (0D) are meshed first, then the lines and splines (1D), then the surfaces (2D) and, finally, the cavities (3D). There are existing solutions to generate the FE meshes according to a geometry. Hereafter we use the open-source GMSH 3D mesh generator [Geuzaine et al. 2009] which is very efficient. Especially we employ the *frontal* algorithm implemented in GMSH to generate the FE meshes (see [Rebay 1993] for details concerning the frontal algorithm). GMSH uses as input a ***.geo*** file that contains the geometrical entities and generates the FE mesh according to these prescriptions. It returns a ***.msh*** files composed of the spatial coordinates of the FE nodes and the connectivity table. This file is finally post-treated in such a way that it can be read and understood by our numerical library. The newly developed GBMG procedure can then be summarized as follows:

1. generate a dispersoïd of spheres (respectively disks in 2D) in the simulation domain, that satisfies the prescribed volume (respectively surface in 2D) fraction and the prescribed size distribution of the SPPs. Hereafter we use the algorithm detailed in [Hitti 2011; Hitti et al. 2016] to generate the centers and radii of the precipitates which alloys to reach easily high densities but also to handle particle clustering,

2. create a geometric description of the particle cloud (points, lines, splines, surfaces, volumes) that can be understood by the mesh generator (*.geo* file for GMSH),

3. mesh the geometric entities in the order of dimensionality according to a frontal algorithm,

4. post-treat the generated mesh file in order to make it compatible with our C++ library.

The key-point in this algorithm is the generation of the geometry file (***.geo***), that needs to be constructed very quickly to ensure efficiency. A C++ code has been developed to perform this operation. Basically, this code converts the data from the files containing the spatial coordinates of the centers and the radii of the SPPs into a collection of geometrical entities (points, splines, surfaces, volumes) that are then used by GMSH to generate the mesh.

Now we repeat the previous test with a unique SPP centered in a cubic domain and use this GBMG approach to generate the mesh. The mesh sizes close and far from the interface are respectively set to $h_n = r_p/2$ and $h_b = 5h_n$, which corresponds to the coarse configuration described earlier. The resulting FE mesh is depicted on fig. 5.3d

The description of the precipitate is here much more accurate. It demands also a small number of elements to achieve this precision (around 750). Finally the CPU time is extremely interesting because only 117ms are needed to generate this mesh, giving an acceleration factor around 79 compared with the kill-element approach (coarse configuration).

Now we use the GBMG approach to generate 10,000 homogeneously distributed SPPs with radius $0.35\mu$m in a $44 \times 44 \times 44\mu m^3$ simulation domain, which gives $f_v = 2\%$. As illustrated on fig. 5.4, the obtained precision is very good and the computation time is also very satisfying because less than 40min are needed on 1 CPU to generate the final 3D mesh with holes which contains more than 7 million elements. Obtaining such a massive 3D FE mesh with equivalent precision and CPU time would be impossible with the kill-element strategy [Agnoli 2013].

Hereafter we take advantage of the numerical developments introduced in the previous chapters (DRT algorithm, dynamic recoloring scheme, optimized FE mesh generation) to discuss a classical limiting mean grain size equation in 2D and to perform a first 3D LS-FE simulation of the ZP phenomenon.

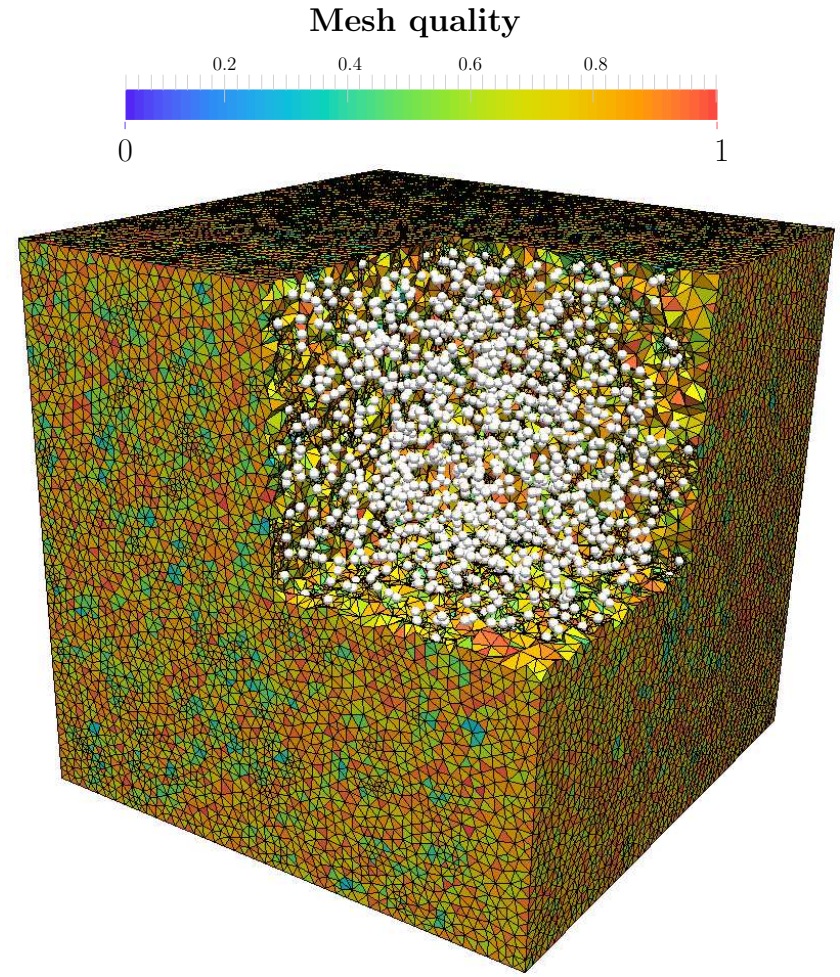


**(a)**

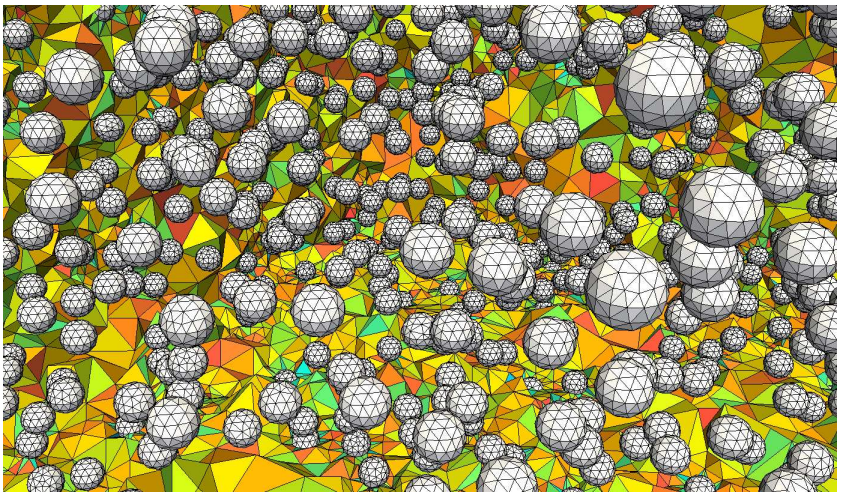

**(b)**

**Fig. 5.4** – 3D FE mesh of a $44 \times 44 \times 44 \mu m^3$ simulation domain containing 10,000 SPPs with radius $r_p = 0.35 \mu m$. The mesh is composed of 7 million elements approximately. The color code refers to the mesh element quality. Precipitates are shown in white.

## 5.3 Numerical investigations of the Zener pinning phenomenon

### 5.3.1 Literature review

As presented in chapter 1, the limiting mean grain size obtained when the dragging precipitates hinder GG is generally predicted by a Zener-type law (see eq. (1.25)). This relationship contains two fitting parameters $(K;m)$ which have been extensively discussed in the last six decades. First analytic investigations were based on many approximations (idealized microstructure topology, simplified shape of the precipitates, estimation of the dragging force, isotropy of the interface energies) and are thus rather limited. More recently, these parameters have been investigated in more details thanks to sophisticated full field models (see chapter 1). A rapid overview of the proposed values for the pair of parameters $(K;m)$ is given in table 5.2.

| Year | Refs. | $K$ | $m$ | Comments |
|---|---|---|---|---|
| 1945 | [Smith 1948] | 4/3 | 1 | Analytical study |
| 1975 | [Hellman et al. 1975] | 4/9 | 0.93 | Analytical study |
| 2000 | [Miodownik et al. 2000] | 0.728 | 1.02 | MC simulations (3D) |
| 2005 | [Couturier et al. 2005] | 0.606 | 1 | FE simulations (3D) |

**Table 5.2** – Brief review of the values proposed for the parameters $K$ and $m$ in eq. (1.25).

In 2006, Moelans and al. [Moelans et al. 2006] proposed to consider only the SPPs located at the grain boundaries to estimate $\langle R_f \rangle$, because only these precipitates really hinder the grain boundaries. Especially the authors introduced a new quantity, noted $f_{gb}$, which represents the volume (respectively surface in 2D) fraction of precipitates in contact with a grain boundary and reformulated eq. (1.25):

$$\langle R_f \rangle = K \frac{\langle r_p \rangle}{f_{gb}^m}, \tag{5.4}$$

Interestingly, even if the relevance of eq. (5.4) comparatively to eq. (1.25) was proved in 2D [Agnoli et al. 2014], quite surprising results were obtained concerning eq. (5.4). It has thus been found that eq. (5.4) can not predict exactly the limiting mean grain size in microstructures characterized by different grain/precipitate size ratios (see fig. 5.5).

However in this study, the important simulation times limited the number of considered grains and the numerical difficulties encountered, especially those concerning

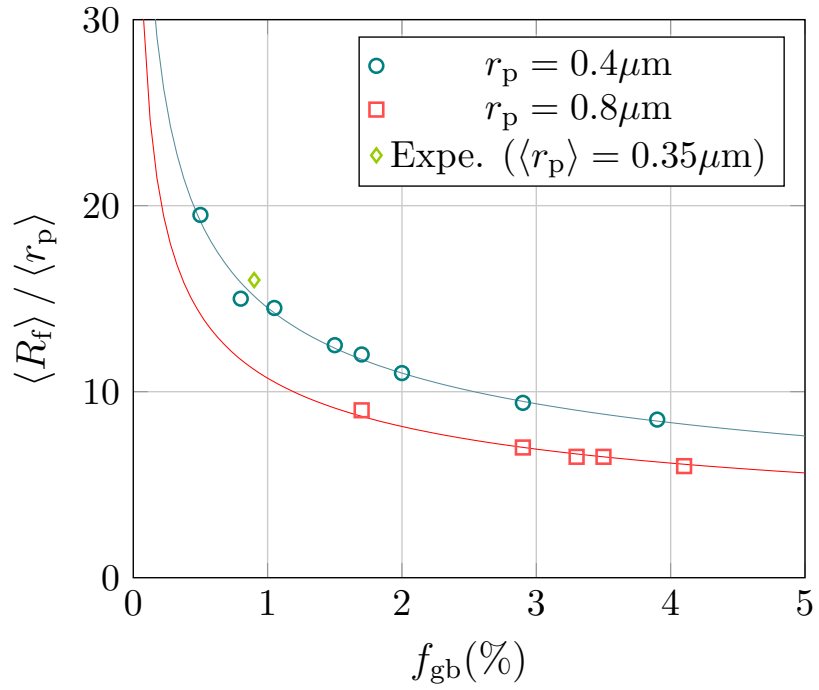


**Fig. 5.5** – Results obtained by Agnoli et al. [Agnoli et al. 2014] for the limiting mean grain size.

the HJ reinitialization solver, have not permitted to determine if these results are founded or just caused by numerical artifacts. This is the question we attempt to address in the next section, wherein we use our new numerical tools to reinvestigate eq. (5.4) and the previous 2D study of Agnoli et al. [Agnoli et al. 2014].

### 5.3.2 Discussion of a classical limiting mean grain size equation in 2D

We perform a set of 2D GG simulations with different distributions of SPPs in order to investigate the influence of the precipitate size and surface fraction on the limiting mean grain size.

#### Simulation parameters

On average, 16 CPUs are used for the simulations and the simulation times are around one or two days, depending on the configuration, which is considerably less than the ones from the previous study [Agnoli et al. 2014]. Furthermore, around twice as many grains are now considered, which enables more statistically representative predictions by limiting the impact of the edge effects.

The initial polycrystal follows the grain size distribution measured experimentally in Inconel 718. The values of the GB mobility and energy are respectively fixed to $M = 2.3 \times 10^{-13}$ m$^4$/J/s and $\gamma = 0.6$ J/m$^2$, which is representative of this material at a sub-solvus temperature (around 985°C) [Agnoli et al. 2014]. The simulated domain is a square with dimensions $0.3 \times 0.3$mm$^2$, leading to an initial number of grains close to 2600. The initial mean grain size is $\langle R_0 \rangle = 3.35\mu$m. All SPPs are perfectly circular with identical radius $r_p$ and assumed incoherent ($\alpha = 0°$ in eq. (1.22) and eq. (5.1)).

In [Agnoli 2013], Agnoli calibrated the time step for Inconel 718 by performing different ZP simulations of a circular (2D) shrinking grain passing through a dispersoid of particles. He compared the grain shapes obtained at steady state (*i.e.* when its boundary is hindered by the SPPs) with the different time steps and observed that the grain adopts globally the same final shape for $\Delta t \leq 0.1$s, which indicates numerical convergence is achieved. According to this study, we use $\Delta t = 0.1$s hereafter for all ZP simulations.

#### Results and discussion concerning the limiting mean grain size equation

The initial FE meshes with voids are generated using the GBMG strategy described earlier. Then the interfaces of the precipitates are blocked to ensure they do not move during the simulation, and anisotropic remeshing is performed at the grain boundaries in order to improve the description of the interfaces (see fig. 5.1).

Hereafter the results of the LS simulations are constantly confronted with the work of Moelans et al. [Moelans et al. 2006], wherein eq. (5.4) is discussed based on the results of PF simulations with different particle and grain sizes. As these PF results show good agreement with experimental observations, it is assumed they stand for a reliable comparison.

In the present study, four particle radii $r_p$ are tested ($0.2\mu$m, $0.4\mu$m, $0.8\mu$m and $1\mu$m) with surface fractions of 1% to 8%. For each simulation, the values of $f_{gb}$ and $\langle R_f \rangle$ are measured at the steady state (when the mean grain size becomes stable). The fig. 5.6 illustrates the microstructure for the configuration $r_p = 0.4\mu$m / $f_v = 3\%$ at the early and final stages of the simulation.

The evolution of the mean grain size during the heat treatment is plotted on fig. 5.7 for different pinning configurations. It appears that, for a given surface fraction, the

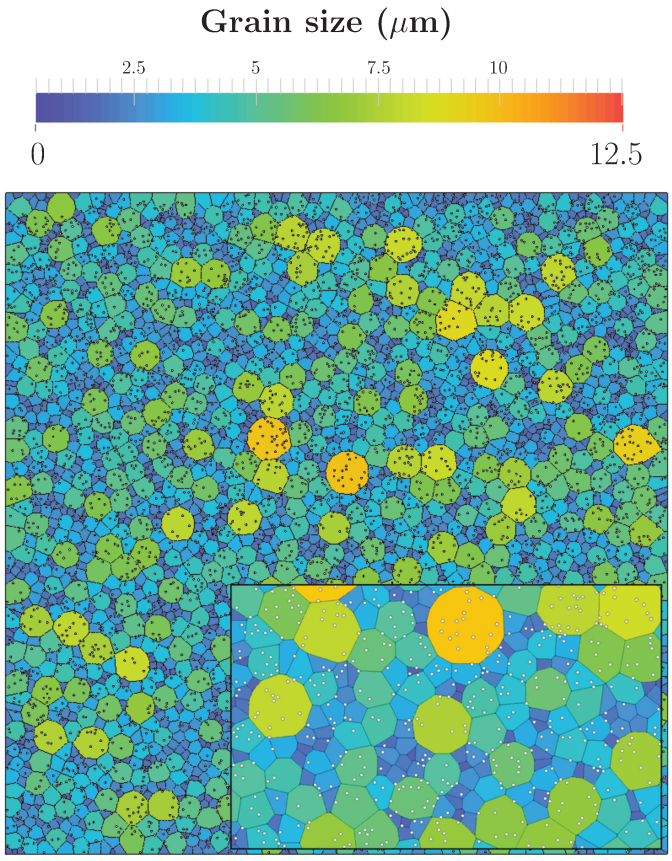


**(a)** $t = 0$

**(b)** $t = 9$min

**Fig. 5.6** – Microstructure at the early and final stage of the simulation for the ZP configuration $r_p = 0.4\mu$m / $f_v = 3\%$. The color code corresponds to the grain size.

radius of the precipitates influences drastically the GG kinetics. For example, with $r_p = 1\mu$m, 20min are needed to reach the steady state while the mean grain size becomes globally stationary after less than 5min with $r_p = 0.2\mu$m. The fig. 5.8 summarizes the results obtained at steady state for all the simulated configurations.

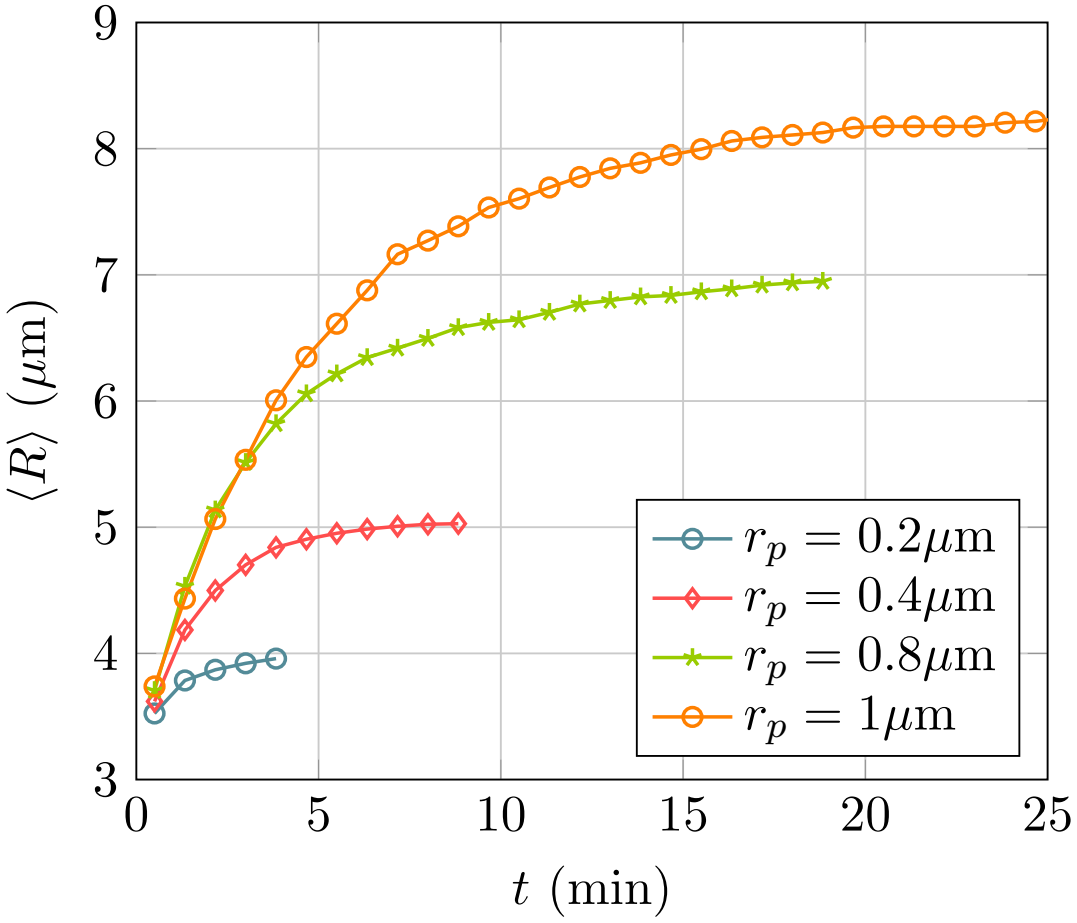


**Fig. 5.7** – Mean grain size during the heat treatment for different particle radii with a surface faction $f_v = 1\%$.

As previously observed by Agnoli et al., all the data plotted on fig. 5.8 can not be represented by a single master curve, which corroborates the idea that the formalism of eq. (5.4) must be enhanced to predict the limiting mean grain size in microstructures presenting different grain/SPP size ratio. For this purpose we plot on fig. 5.9 the evolution of the parameters $K$ and $m$ (see eq. (5.4)) obtained with the present LS simulation results as a function of the initial grain/SPP size ratio. It is obvious that this normalization makes sense only for microstructures wherein the grain size distribution is relatively regular (relatively small deviation from the mean grain size),

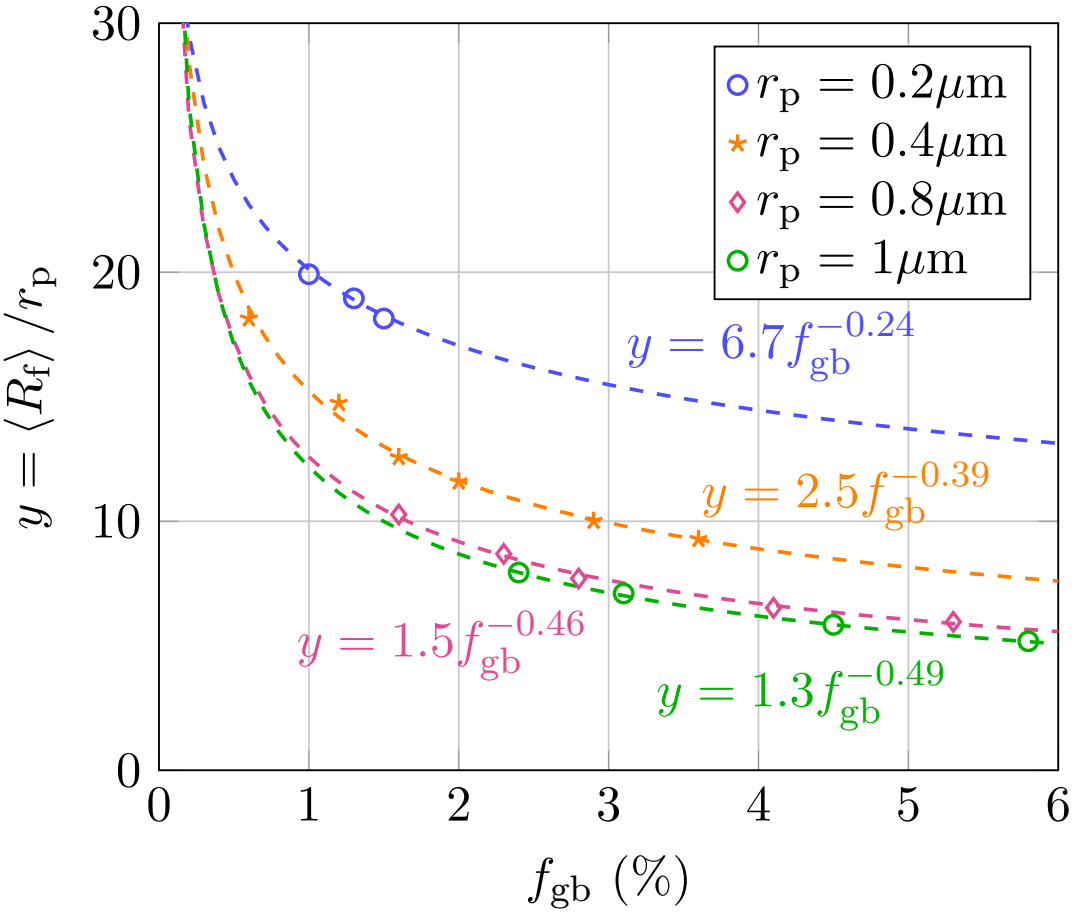


**Fig. 5.8** – Results of the LS simulations at the steady state. Each dashed line corresponds to the best first satisfying eq. (5.4) for a given particle radius.

which is the case in the considered Inconel 718 material.

By using power regressions for these two parameters, the two following expressions are obtained:

$$K = \frac{0.362}{(r_p/\langle R_0\rangle)} \quad \text{and} \quad m = 0.853\left(\frac{r_p}{\langle R_0\rangle}\right)^{0.428}. \tag{5.5}$$

As illustrated on fig. 5.9, the PF results of [Moelans et al. 2006] fall very close from the trend lines given by eq. (5.5).

Substituting eq. (5.5) in eq. (5.4) gives finally a new expression for the limiting mean grain size:

$$\langle R_f\rangle = 0.362\langle R_0\rangle f_{gb}^{-0.853(r_p/\langle R_0\rangle)^{0.428}}. \tag{5.6}$$

Figure 5.10 illustrates the quality of the proposed model comparatively to the obtained LS results and the PF simulations of [Moelans et al. 2006].

### 5.3.3 First 3D simulation of Zener pinnning using a level set approach within a finite element framework

Finally we apply the main developments of this thesis work for a realistic 3D simulation of ZP without stored energy. For this purpose we use the FE mesh of fig. 5.4 whose dimensions are $44 \times 44 \times 44\mu m^3$. Then a polycrystal of 530 grains is immersed inside this domain, following the grain size distribution measured experimentally in Inconel 718 [Agnoli et al. 2012]. Then the initial mean grain size is $\langle R_0\rangle \approx 3.35\mu m$.

No remeshing is performed in the simulation. In first approach, we fix the same time step than in 2D, *i.e.* $\Delta t = 0.1s$ and stop the simulation after 2400 time increments where the steady-state is achieved. The evolution of the microstructure is depicted on fig. 5.11 and fig. 5.12 offers a more precise description of the interaction between a grain boundary and the precipitates. The shape of the interface is close from a catenoid of revolution, as detailed in [Hellman et al. 1975; Harun et al. 2006].

The limiting mean grain size obtained is $\langle R_f\rangle = 7\mu m$ (see fig. 5.13). This value is compared with the predictions of the other models in table 5.3.

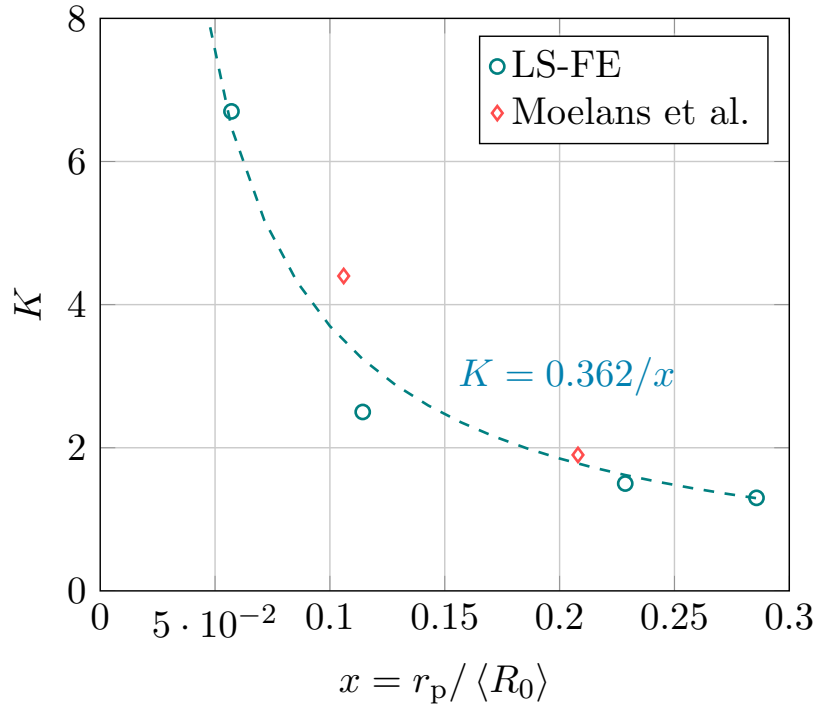


**(a)**

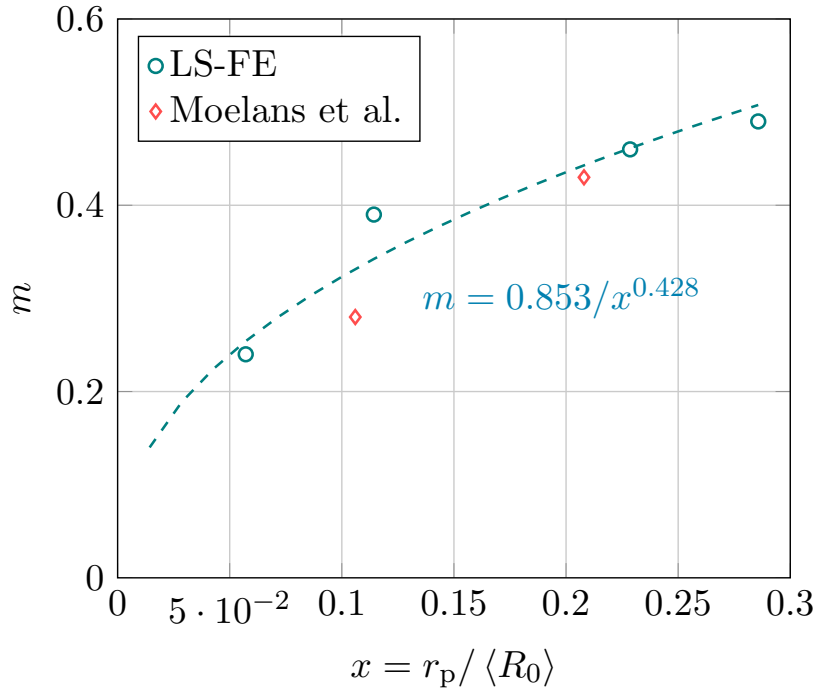


**(b)**

**Fig. 5.9** – Values of $K$ and $m$ (see eq. (5.4)) obtained with full field simulations. The dashed lines correspond to the best power fits. Diamond data points are taken from [Moelans et al. 2006].

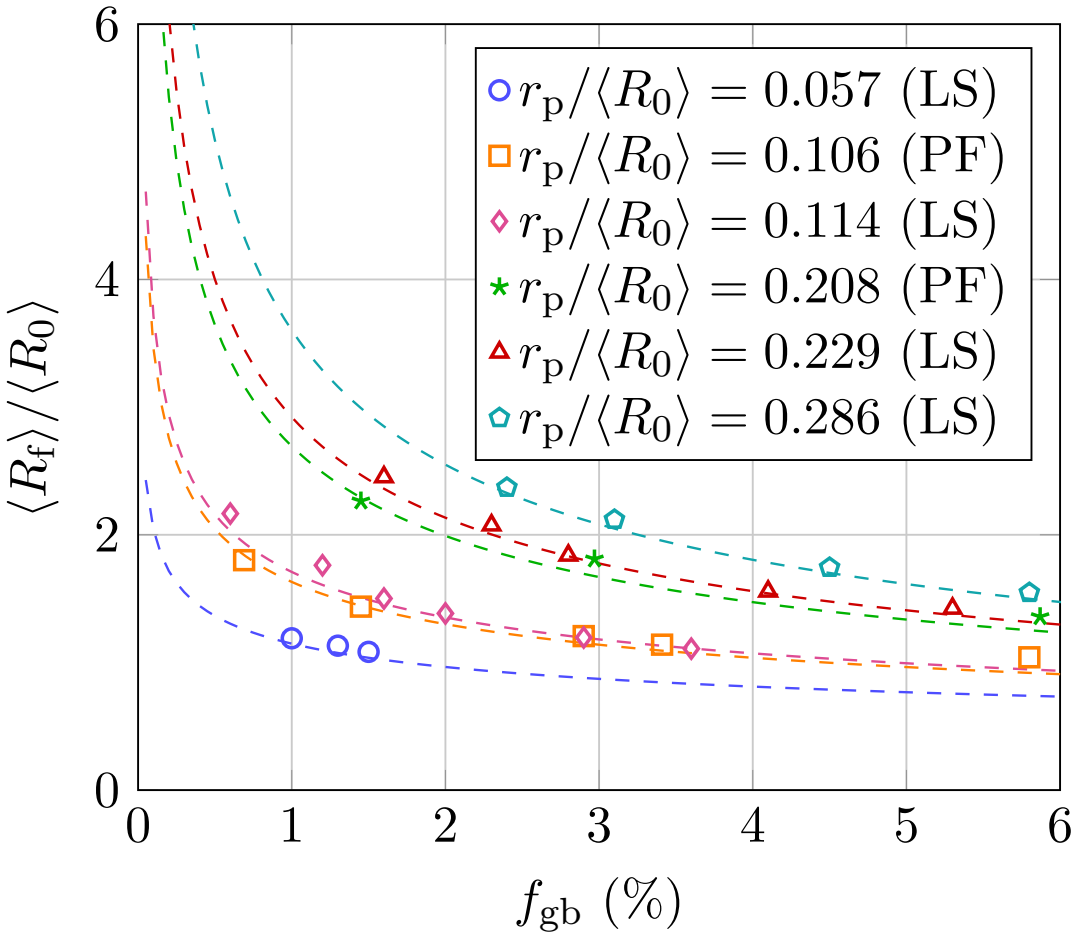


**Fig. 5.10** – Predictions concerning the limiting mean grain size obtained with eq. (5.6) (represented by the dashed lines) for different SPP/grain size ratios and comparison with the full field simulation results (PF simulations from [Moelans et al. 2006] and LS-FE simulations).

| Model | $\langle R_f\rangle$ ($\mu$m) | Comparison |
|---|---|---|
| LS-FE approach | 7 | |
| [Smith 1948] | 23.3 | +70% |
| [Hellman et al. 1975] | 5.9 | -18.4% |
| [Miodownik et al. 2000] | 13.8 | +49.2% |
| [Couturier et al. 2005] | 10.6 | +34% |
| Equation (5.6) | 7.44 | +1.7% |

**Table 5.3** – Mean grain size predicted by the present LS-FE model and comparison with other works.

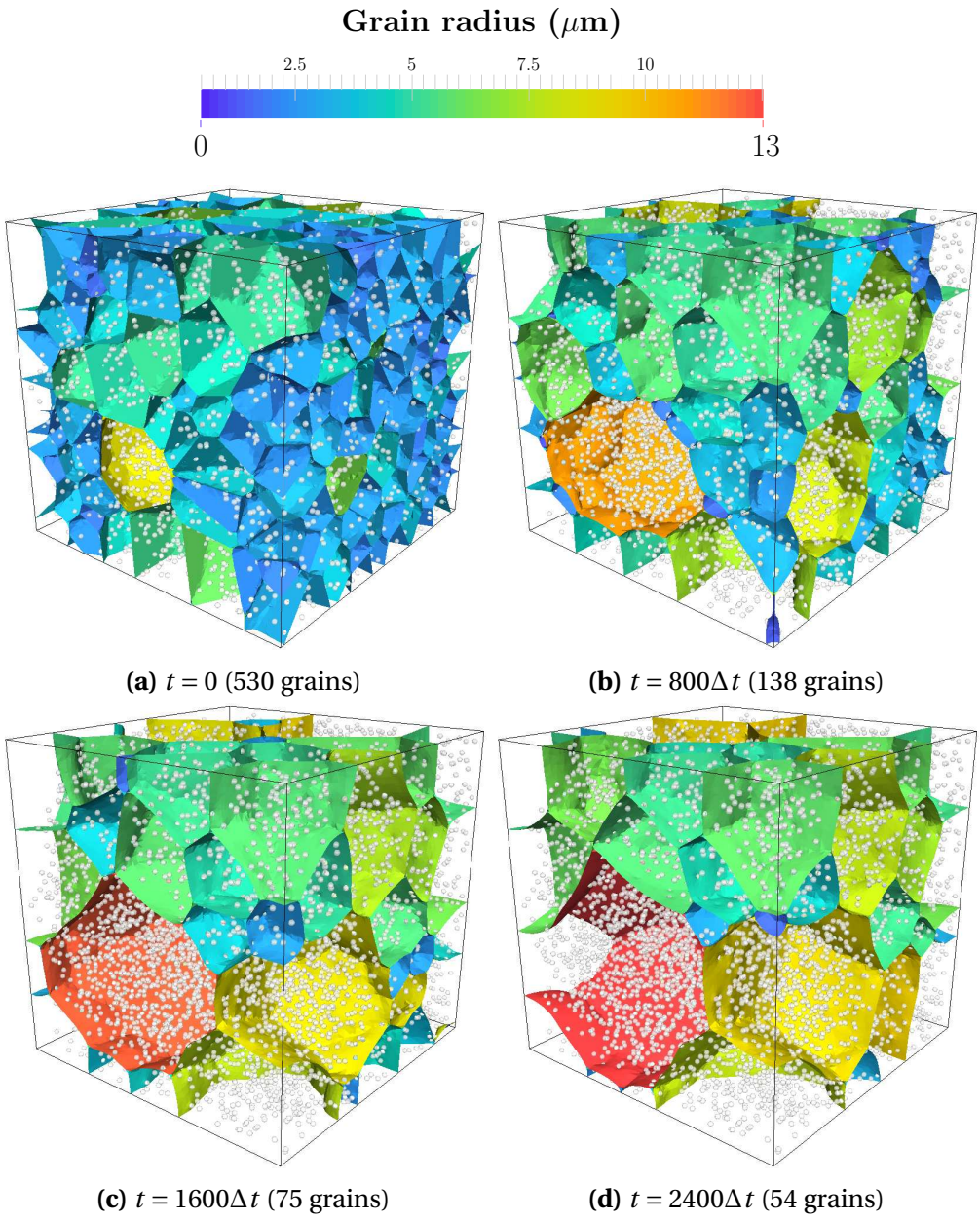


**(a)** $t = 0$ (530 grains)

**(b)** $t = 800\Delta t$ (138 grains)

**(c)** $t = 1600\Delta t$ (75 grains)

**(d)** $t = 2400\Delta t$ (54 grains)

**Fig. 5.11** – Evolution of the grain boundary network during the 3D ZP simulation. The color code refers to the grain size and SPPs are represented in white.

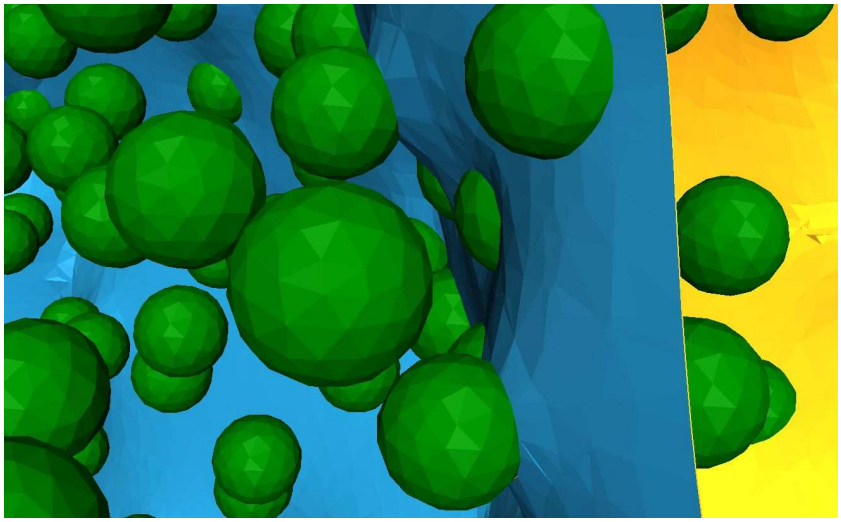

**Fig. 5.12** – Zoom on the interaction between a grain boundary and the cloud of SPPs.

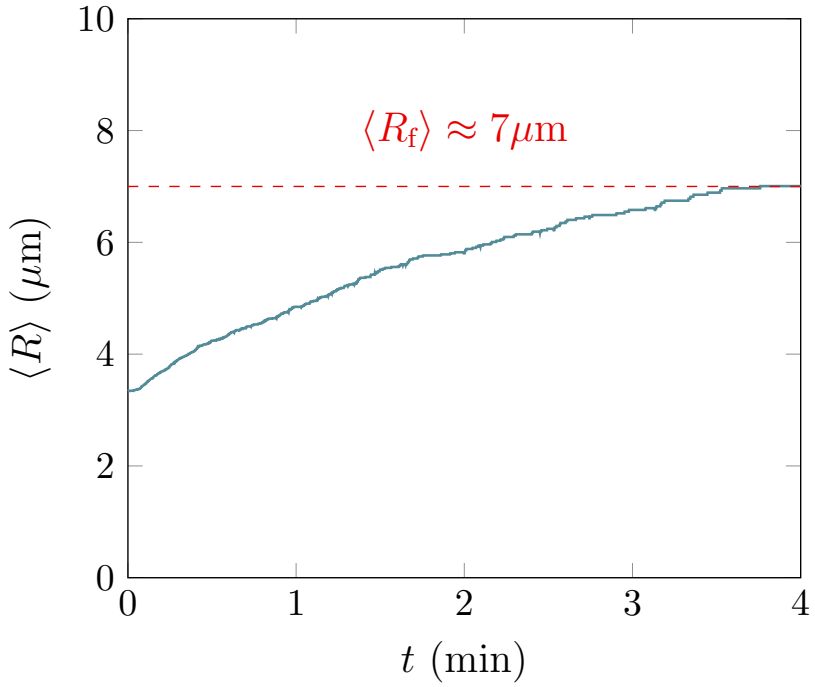


**Fig. 5.13** – Mean grain size in the polycrystal during the 3D ZP simulation.

It appears that the predicted mean grain size at the steady is much smaller than the one obtained with the classical Zener & Smith's set of parameters [Smith 1948]. Despite a very small number of grains are still present in the domain at the end of the simulation (around 50), the calculated mean gain size falls between the predictions of Hellman et al. [Hellman et al. 1975] and of Couturier et al. [Couturier et al. 2005], which tends to validate the consistency of our results.

1770 SPPs are in contact with the grain boundaries at the steady-state, giving $f_{gb} = 0.37\%$. Using this value, eq. (5.6) provides $\langle R_f \rangle = 7.44\mu$m which is in very good agreement with the full field predictions, even if eq. (5.6) has been built on 2D ZP simulation results. This interesting result should be confirmed through additional 3D simulations of ZP with different particle distributions.

Such simulation requires 2 days and 10 hours of computations using 24 CPUs, which is remarkable compared to the state of the art. It is worth noting that performing this simulation would have been hardly possible before this thesis work due to the numerical requirements. That being said, computation times for ZP simulations remain relatively important and require to be further optimized in order to discuss the classical limiting mean grain size equations in 3D.

## Summary

In this chapter the LS-FE modeling of the ZP phenomenon has been investigated. First we have detailed the numerical approach developed by Agnoli et al. [Agnoli 2013] for the modeling of inert precipitates. The latter is based on the construction of specific FE meshes containing holes that represent the precipitates and hinder the movement of the grain boundaries. Even if it is very precise, this approach was demonstrated to be incompatible with industrial simulations due to the colossal computation times. The situation has been drastically improved by introducing the DRT algorithm and the dynamic recoloring scheme (see sections 2.4 and 3.3.2 for details about these algorithms) in ZP simulations. However the simulation times were still penalized by the generation of the FE meshes with holes which is highly time-consuming. So we developed a new method for generating these specific FE meshes. This approach uses the geometry of the objects that have to be meshed (the SPPs in the present context) in order to built a FE mesh conform with the interfaces of the precipitates. An external frontal mesh generator is used to mesh the geometrical entities in the order of dimensionality. This new method was demonstrated much

more efficient and able to tackle large 3D particle clouds within reasonable computation times. These developments have been put into practice to perform a set of 2D ZP simulations and to improve a classical limiting mean grain size equation based on the full field simulation results. Finally we performed a first realistic 3D LS-FE simulation of ZP based on experimental data of Inconel 718. The numerical developments and results presented in this chapter have allowed to publish [Scholtes et al. 2016b].

# Chapter 6

# Conclusion and outlooks

The objective of this PhD work was to improve the numerical performances of a LS-FE model devoted to the simulation, at the polycrystal scale, of microstructural evolutions in metallic material formed at high temperature.

It has been illustrated in the introduction chapter that the recent metallurgical problems faced by the industrials require precise modeling tools in order to limit the cost and time needed for the development/improvement of materials and processes. So these modeling tools need to be extremely precise and versatile in order to capture the complex physical mechanisms involved during hot metal forming. They must also be very efficient and robust to enable industrials to perform the simulations by themselves with their own numerical facilities in reasonable computation times (typically less than few days with standard workstation). Developing such numerical models is a main challenge of today's materials science, and especially in metallurgy where the economic, security and environmental concerns are more and more bindings. The reduction of aircraft engines, for example, requires the improvement or development of materials able to endure higher service temperatures. The modeling approaches are of great interest to support the technological decisions of the engineers in order to address these challenges.

The development of HPC in metallurgy is thus supported by the European institutions at the highest level to encourage the development of new numerical solutions and their implementation directly in the industry. This PhD work, by proposing efficient numerical tools able to predict the microstructure evolutions during hot forming, is then fully in line with these recommendations.

As presented in chapter 1, different approaches have been developed in the last

decades to model microstructure evolutions. Analytical and enriched mean field models which use a homogeneized/simplified description of the material have the advantage of simplicity and rapidity, but rely on many limiting assumptions. On the other hand, full field approaches provide a complete description of the material and are very precise. They are also more greedy in terms of computation time.

The CEMEF and the company Transvalor have therefore initiated the development of a global software package, called DIGIMU® , able to conciliate the most attracting features of mean field and full field approaches in order to tackle the whole manufacturing process of metallic parts and the subsequent microstructural evolutions. Especially a LS-FE approach is employed in DIGIMU® to address the microstructure evolutions at the polycrystal scale. Even if this is not the most rapid or straightforward method, the LS-FE approach presents the great advantage to be more versatile as the approach is able to treat most of the physical phenomena taking place during hot metal forming in a global, robust and unified numerical framework. However the numerical cost of this method remains its main drawback, especially in 3D where simulation times are usually counted in days, or even weeks.

The first step in the development of DIGIMU® was therefore to improve drastically the numerical efficiency of full field simulations, and more specifically of the used LS-FE formalism.

## 6.1 Achievement

After analyzing the distribution of the simulation times for a classical GG simulation in 2D, the first efforts were devoted to the improvement of the reinitialization method. A review of the existing approaches in the literature led us to develop the DRT algorihtm which is based on a geometric approach and uses optimized searching procedures coupled with an efficient bounding-box strategy, ensuring high parallel efficiency. This method was proven far more efficient with acceleration factors up to 300, but also more robust as it requires no numerical parameter and does not rely on the resolution of PDE systems. Colleagues apply this new DRT algorithm to other applications using the LS method, especially phase changes and solidification during welding of additive manufacturing processes [Nguyen 2015; Saad 2016; Chen et al. 2016]. More generally this DRT algorithm is able to address most of the numerical problems based on the LS-FE method, such as fluid mechanics or image treatment.

The second aspect treated in this work was the optimization of the numerical formalism based on GLS functions. Two objectives were particularly sought. The former was to accelerate the simulation times and to reduce the memory requirements by using less GLS functions for representing the polycrystals. The second point was to avoid numerical coalescence and to assess the properties of the individual grains contained in the GLS functions. These two objectives have been addressed by developing and implementing a dynamic recoloring scheme which separates the connected components of each distance field, detects the risks of coalescence and redistributes the grains inside the GLS functions when numerical coalescence is about to occur. This algorithm has permitted to reduce drastically the memory requirements, to improve the efficiency, to prevent coalescence in all simulations, and finally to assess the intrinsic properties of each grain. Based on these developments, a new algorithm was also proposed to immerse real polycrystal within a FE mesh thanks to GLS functions. This algorithm was successfully applied to immerse a real 3D polycrystal from an experimental image and to perform a GG simulation based on this image. Although they have been only used in the context of GG and ReX in this work, these algorithms are completely general and can be directly applied to a variety of multiphase problems relying on coloring. Hot powder compaction [Zouaghi 2013] and fracture mechanics [Trejo et al. 2016] are examples of application where these developments have been, or will be, applied.

After improving the LS formalism itself, special attention has been paid to the SRX phenomenon, and more particularly to the SRX model introduced in [Bernacki et al. 2008]. Effectively this formulation of the ReX model suffers from inherent limitations due to fact it does not handle coloring and thus requires to use as many GLS functions as grains in order to handle the different stored energy levels of the grains. Numerical tools have therefore been developed in order to propose a new efficient formulation of the SRX model working around stored energy fields. These stored energy fields enable to handle independent energy for each grain while taking full advantage of grain coloring and recoloring. This new implementation has permitted to reduce drastically the computation times of SRX simulations. Accelerations up to 45 have effectively been achieved for the considered 3D cases with important number of grains. Also the algorithm used in the new SRX model have been developed in a generic manner, and was recently used by colleagues to model DRX [Boulais-Sinou et al. 2016], and also to handle heterogeneous stored energy inside the grains [Ilin et al. 2016].

Last chapter of the manuscript was finally devoted to the LS-FE modeling of the ZP phenomenon. This problem was tackled previously in [Agnoli 2013; Agnoli et al.

2014] where a LS-FE numerical approach has been developed to model inert precipitates without any simplifying assumption concerning the dragging effect exerted on the grain boundaries. This method relies on, firstly, the construction of specific FE meshes with holes that represent the SPPs, and secondly, the use of suitable boundary conditions that hinder the migration of the grain boundaries. It has been illustrated that the generation of the FE meshes needed in ZP simulations can be extremely time consuming in 3D. This is particularly problematic because a new FE mesh has to be created for each distribution of precipitates. A new approach has therefore been proposed to improve the situation. The latter uses a geometrical representation of the precipitates that supports the mesh generation and enables to build large FE meshes with several million elements in few minutes. Different 2D simulations of ZP have been performed with different particle distributions in order to discuss a classical limiting mean grain size equation. A new formulation of this law has then been proposed based on the full field simulations results. The main developments of this PhD thesis work have finally been applied to a realistic LS-FE simulation of the ZP phenomenon in 3D which is, to the author knowledge, a first time for this approach. The method developed in the context of this work for generating the FE meshes with holes has been recently applied to the simulation of the HIP bounding process [Bernacki et al. 2016]. Especially under certain conditions of loading and/or temperature, the roughness of the initial surfaces in contact during diffusion welding may result in porosities at the interface, that can hinder the movement of the grain boundaries. A simple way to account for this phenomenon is to add holes in the FE mesh near the initial welding interface. Using this approach, grain boundaries are naturally slowed down when they cross the interface. A PhD work based on this development is already planned (CEA/MINES ParisTech 2017-2020).

This project was particularly important to develop all the necessary numerical tools for the modeling of GG and SRX in an accurate way within reasonable computation times. These tools are now being or will be used in other works, and especially in the context of the industrial ANR Chair DIGIMU, started in October 2016 at the CEMEF, whose one objective is to develop and extend the capacities of the DIGIMU® package. It is worth noting that the quality of the present work gave rise to four papers published in peer-reviewed international journals, and conferences (11 international and 10 national).

## 6.2 Suggestions for future works

Although very promising, the present numerical model should however be further improved in order to capture the complexity of microstructural mechanisms involved during the forming process. First, the influence of anisotropy in terms of grain boundary energy and mobility should be considered. Particular grain boundaries, and especially twin boundaries, must also be modeled. These are basically particular grain boundaries that have a very low energy and thus migrate much slower than the regular boundaries. Recent LS studies focused on the influence of anisotropic grain boundary features in the context of 2D GG [Jin et al. 2015; Hallberg 2014; Mießen et al. 2015]. To our knowledge, these works have no 3D equivalent for the time being. Such topic is an obvious perspective of this PhD work.

Next the intragranular heterogeneities in terms of stored energy and their evolutions during the migration of the grain boundaries should also be considered. This point is currently under study [Ilin et al. 2016; Boulais-Sinou et al. 2016]. Again the approach developed by colleagues uses the numerical tools developed in the present work applied to heterogeneous energy fields inside the grains. Especially the algorithm introduced in section 4.3.4 has been adapted to affect a stored energy level representative of the recrystallized material in the zone swept by the grain boundaries during a time increment. This approach is effectively much more relevant from a physical point of view [Boulais-Sinou et al. 2016].

Another global challenge might be to compare MC simulations with the LS-FE simulations for the same GG and ReX problems. This would expose both the differences in computational cost and (perhaps) differences in accuracy. This could be done with, *e.g.* the Sandia SPPARKS code [Plimpton et al. 2009], which is very efficient (fully parallelized).

Although the experimental results obtained by Huang [Huang 2011] for SRX have been used in this work, the current available data are not sufficient for a quantitative discussion of the obtained numerical results. It is then important to perform new experimental investigations of the materials that are considered in the simulations (mainly the 304L material in the present work). As discussed in section 3.5, the collaboration that is being initiated with the university of Ulm offers also a great opportunity to compare the results of the present LS-FE model with *in situ* observations and PF simulations. Especially it was observed that the aluminum material considered in the PhD work of Mingyang Wang presents important anisotropy of the grain boundary

energy. Such collaboration could thus permit to validate the numerical tools needed to consider anisotropic boundary features.

Considering the ZP phenomenon, the numerical results obtained in section 5.3 are quite satisfying. However they shall be substantiated with additional experimental validations. Moreover it appears important to investigate the variability of the fitting parameters in eq. (5.6). More precisely it has been found in this study that the proposed values are in good agreement with the results of Moelans et al. [Moelans et al. 2006] even if the material (grain size distribution, grain boundary energy/mobility) and the TT conditions are different. This new model seems therefore quite generalizable. But further investigations should be conducted in order to corroborate these first remarks. The enrichment of this mean field equation in order to consider more realistic microstructure (anisotropy of grain boundary energy, presence of twin boundaries,...) is also an exciting perspective.

Finally the 3D aspect must also be further considered, as the real interaction between a grain boundary and a precipitate can only be described in 3D. The 3D simulation of ZP phenomenon is now possible thanks to the developments introduced in this manuscript, as illustrated by the simulation of Inconel 718 presented in section 5.3. However discussing the limiting mean grain size equations in 3D remains complicated for the time being due to the high computational cost of these simulations. Effectively, even if the above developments have grandly improved the situation, 3D ZP simulations require a fine spatial discretization near the SPPs and small simulation time steps all along the simulation in order to correctly describe the interaction between the precipitates and the grain boundaries. Given the current numerical tools available in our library, performing mesh adaptation in 3D is extremely costly for the time being, and even counterproductive in the context of our application. This imposes to use fixed isotropic FE meshes with a relatively fine mesh size everywhere inside the domain, which increases obviously the number of DOFs in the FE problem and the memory requirements. Moreover, as we need to simulate a large number of grains to prevent domain-size effects, performing statistically-representative LS-FE simulations of ZP in 3D remains a real challenge for the time being, even with our new numerical tools. The situation could however be improved, as mentioned earlier, by using periodic BCs which enable to limit the RVE sizes, providing that we are able to generate and maintain periodic microstructures and FE meshes. This point has not been investigated in the present work but will be the topic of a planned PhD work in the context of the DIGIMU Chair. Finally, it is worth noting that the above approach for ZP simulations enables to simulate *only* inert SPPs and should then be extended

to account also for evolving precipitates during non-isothermal TMT/TT.

The above remarks rise three main planned area for improvements:

- improvement of the time step management,
- work on 3D mesh adaptation,
- extension of the numerical model of ZP presented in chapter 5 to evolving precipitates.

### 6.2.1 Management of the time step in simulations

As illustrated by the example of ZP, different levels of precision may be needed inside the simulation domain. This concept was introduced in chapter 1 for the spatial discretization with mesh refinement and can also be extended to the time variable. Effectively, it has been discussed earlier that a fine time step is needed to describe properly the interactions between the grain boundaries and the SPPs. However this remarks is only true in the regions where these interactions effectively occur. Elsewhere, and especially in the grain interiors, the needs in terms of accuracy are not the same and using this fine step is a waste of numerical resources. This introduces nicely the complex concept of space-time FE method. In this approach, the time is also meshed in the same manner than space, and different time steps may be adopted simultaneously in the same simulation domain. This approach, currently investigated by colleagues at the CEMEF, requires a mesher/remesher able to perform mesh adaptation both in space and time, a space-time error estimator for the construction of the metric fields and finally 4D solvers adapted to the space-time FE formulation. Even if the Fitz mesher/remesher available in Cimlib is under development to be compatible with the 4D formulation, this is not the case of most numerical tools implemented in the numerical library. Many adaptations are thus needed to investigate this method.

More simply it is also possible to adapt dynamically the time step during the simulation while keeping it homogeneous. Let us consider a simple GG simulation with long treatment time for an illustration. Following the method used in this work, a time step value is chosen for the entire simulation at the early stage, based on the estimation of an average displacement $\langle d \rangle$ of the grain boundaries during one time increment:

$$\langle d \rangle = \int_{t'}^{t'+\Delta t} \langle v \rangle \, dt, \tag{6.1}$$

where $\langle v \rangle$ is an average migration rate of the grain boundaries. Classically, the time step is fixed in such a way that $\langle d \rangle$ does not exceed an arbitrary fraction of the refined layer $E$ (when local mesh adaptation is used) or of the mesh size (in the case of homogeneous mesh refinement). Using classical mean field approximations, $\langle v \rangle$ can be estimated from eq. (1.4):

$$\langle v \rangle = M\left(\gamma \frac{d_s - 1}{\langle R \rangle} + \langle e \rangle\right). \tag{6.2}$$

During GG and SRX in site saturated conditions, $1/\langle R \rangle$ and $\langle e \rangle$ decreases, so as $\langle v \rangle$, and finally $\langle d \rangle$. An alternative in this situation can be to adapt the time step in such a way that the average displacement of the grain boundaries $\langle d \rangle_{\text{lim}}$ remains constant during the treatment. By assuming $\langle R \rangle$ and $\langle e \rangle$ are constant between two consecutive times $t'$ and $t' + \Delta t$, and by substituting eq. (1.6) in eq. (6.2), the time step must therefore satisfy this condition:

$$\langle d \rangle_{\text{lim}} \geq \left(\gamma \frac{d_s - 1}{\langle R \rangle} + \langle e \rangle\right) \int_{t'}^{t'+\Delta t} M_0(T) \exp\left(-\frac{Q_m}{\mathscr{R} T}\right) dt. \tag{6.3}$$

Using a piecewise linear temperature profile, the trapezoid rule can be used to calculate iteratively the integral term in eq. (6.3) until the greatest value of $\Delta t$ which satisfies eq. (6.3) is found. Then this greatest value gives the time step for the next time increment.

This method, referred to as *dynamic time step adaptation* (DTSA), has been recently integrated to our numerical framework. To illustrate its interest, we reinvestigate the SRX simulation referred as "Configuration 4" in section 4.4.2 with DTSA. The evolution of the time step and of the recrystallized volume fraction obtained with both methods (fixed time step and DTSA) are depicted on fig. 6.1. Here $\langle d \rangle_{\text{lim}}$ is chosen in such a way that $\Delta t(t = 0) = 5$s with the DTSA method, which was the value adopted in the SRX simulation of section 4.4.2 (with constant time step).

Using this approach, only 66 time increments are needed to simulate the whole TT of 17min at 1000°C instead of 204 with the fixed time step strategy. The simulation time is thus reduced from more than one day to around 9h, still using 24 CPUs. The predictions in terms of volume recrystallized fraction are also almost identical with both methods (see fig. 6.1b), which proves the great potential of this approach. These good results should now be comforted with other comparisons. An interesting point would be now to determine automatically an adequate value for $\langle d \rangle_{\text{lim}}$ as a function of the considered material and of the thermomechanical conditions in order to assist

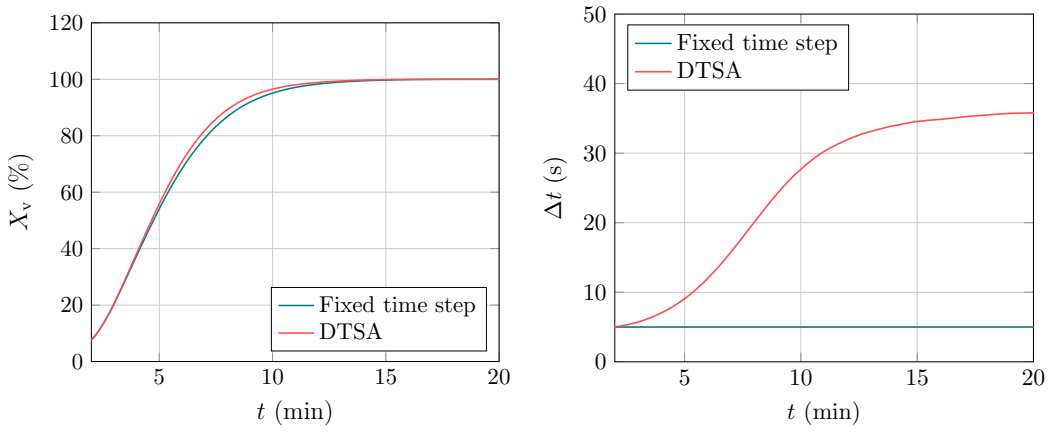


**(a)** **(b)**

**Fig. 6.1** – Evolution of the bulk recrystallized fraction (a) and of the time step (b) for the SRX simulation referred as "Configuration 4" in section 4.4.2 with fixed time step and DTSA methods.

the user. In chapter 5, we mentioned that the time step must also be reduced in ZP simulation to correctly describe the grain boundary/precipitate interactions. So the DTSA approach must be extended to account for the presence of SPPs.

### 6.2.2 Mesh adaptation, perspectives and challenges

The developments introduced in this manuscript have permitted to address many issues of the LS-FE model used to model microstructure evolutions. However some points has not been considered, and especially remeshing. As discussed previously, performing mesh adaptation, even in 2D and with anisotropic elements, has most of the time an important numerical cost. Even in 3D performing remeshing can be counterproductive for the present polycrystal application, as better performances are obtained with fixed fine and homogeneous FE meshes. However, using this kind of FE mesh demands a large amount of free memory available. Also in ZP simulations, the mesh refinement near the precipitates must be correlated to their sizes (see chapter 5), which is generally very small compared to the dimensions of the simulation domain. So, if a fixed FE mesh is used, the mesh size around the SPPs must be kept very small all along the simulation, which increases significantly the computational cost.

An important work must therefore be performed on the remeshing topic. Two approaches are possible. First, it is possible to focus on a better construction of the metric field that supports the mesh adaptation. The latter can effectively be optimized in

such a way that it minimizes the number of needed elements without degrading the precision. An interesting example is pure GG. Effectively during this phenomenon the migration velocity of the grain boundaries is dictated by their local curvature. So the mesh can be unrefined in regions where interfaces are slightly curved, thus saving DOFs. This can be achieved by using curvature-based mesh adaptation as it is done in [Quan et al. 2014]. Recently Shakoor (PhD MINES ParisTech, 2013-2016) adapts this approach to our LS P1 numerical framework and proposed a new error estimator based on interface curvature through gradient and hessian recovery (see [Shakoor 2016] for more details). Obviously this error estimator should be enriched in order to consider also the stored energy gradients in ReX simulations, and not only the interface curvature. The advantage of working on metric fields is that no development has to be made on the core of the remeshing algorithm, *i.e.* the remesher itself.

On the other hand, a work can be made directly on the remeshing tools to improve the global efficiency. Especially other techniques should be investigated to adapt the FE mesh. We refer the interested reader to [Gruau 2004] for a comprehensive review of the existing mesh adaptation techniques. Among all, the approach relying on conform FE meshes, presented in chapter 1 (see fig. 1.10) deserves a particular interest to the opinion of the author. These *body-fitted* approaches are rather similar to Vertex models, with the exception that the grain interiors are also meshed. Using conform FE meshes has two main advantage. First, far less mesh elements are needed to represent a curved interface for an identical level of accuracy. This was nicely illustrated with the meshing of SPPs in chapter 5, where the GBMG is essentially a body-fitted approach. Secondly, thanks to the explicit representation of the grain boundary network obtained with the body-fitted approach, the interface curvature can be explicitly calculated based on geometrical considerations, as it is done in Vertex models. However estimating directly the interface curvature based on the interfacial mesh is more costly numerically than using a diffusive formulation as it was done in the present work (see section 1.5.3). Another advantage of using conform FE meshes is that the decreasing function $f$ in eq. (4.3), that smoothes the recrystallization velocity field $\vec{v}^{\mathrm{e}}$, is not longer needed because the position of the grain boundaries is now known. Finally, as the two terms $\vec{v}^{\mathrm{c}}$ and $\vec{v}^{\mathrm{e}}$ can be explicitly calculated, it is possible to displace directly the nodes located on the grain boundaries so as:

$$x^{t+\Delta t} = x^t + \vec{v}\,\Delta t, \tag{6.4}$$

where $x^t$ and $x^{t+\Delta t}$ design the spatial coordinates of a node located on the boundaries at current time and at the next time step, respectively. Using this approach, the

migration of the grain boundaries, which is treated by solving the system of CDEs given by eq. (1.47) in the present work, boils down here to a remeshing problem. This problem can especially be tackled by the Fitz mesher/remesher [Shakoor et al. 2015a] which allows to preserve the explicit interfaces represented by the zero-isovalue(s) of the distance field(s).

It should be extremely interesting to compare this formulation with the existing implicit one, both in terms of precision and accuracy. The main limitation of the body-fitted approach is related to the handling of grain shrinkage, that relies on specific topological operations on the FE mesh. The problem is actually rather similar than the one encountered in Vertex models. However the problem is here simplified because the grain interiors are also meshed, and not only the interfaces as in Vertex models. Another difficulty could be to handle correctly the quality of the elements near the body-fitted interfaces and mainly at the multiple junctions. Different adaptations and developments seem therefore necessary to make this body-fitted approach very attractive for the modeling of ReX. This point will be investigated in the context of an upcoming PhD work (MINES ParisTech, 2017-2020) during the DIGIMU chair mentioned previously.

More generally the implicit and body-fitted approaches have both their own advantages and limitations. Thus the best option seems to develop them conjointly in order to benefit from their most attractive features and, to choose for each application the most suitable method according to the expectations.

### 6.2.3 Level set modeling of the ZP phenomenon in the presence of evolving second phase precipitates

Chapter 5 focused on the ideal case wherein precipitates are static in space and time. However in most industrial processes, the temperature evolves and the solvus temperature of the SPPs can be reached during the TT/TMT. In this situation the precipitates dissolve and may disappear, fading the dragging effect exerted on the grain boundaries. Being able to model evolving SPPs is thus crucial in order to address real industrial processes. A future thesis work on this topic is already planned in the DIGIMU chair, especially for the LS-FE modeling of phase transformations that may occur during hot metal forming.

Hereafter we propose a first methodology to model dissolving precipitates. The objective is to give some clues and thought on how this phenomenon can be modeled

efficiently by exploiting the numerical tools introduced earlier.

Basically, the proposed methodology works around a dual-mesh strategy, which undermines that two distinct FE meshes are used in the simulations and that the fields of interest will be alternatively transported from one FE mesh to the other. The modeling of the precipitates relies on the same paradigm used for inert precipitates which has, as mentioned earlier, the great advantage of making no approximation concerning the pinning effect exerted by the SPPs (see chapter 5 for more details).

The first step for a ZP simulation with evolving precipitates is to generate a FE mesh in the same way it was done in chapter 5, but this time, the interior of each precipitate must also be meshed. For this purpose an option has been added to the algorithms presented in chapter 5 to define whether the interiors of the precipitates need to be meshed or not, according to the case. As the GMSH mesher handles nicely these two configurations, obtaining such conform FE meshes without void in the precipitates is straightforward.

The result is a body-fitted FE mesh, conform with the interfaces of the precipitates, as illustrated on fig. 6.2a. This first mesh, wherein the particles are fully meshed is designated hereafter as the *support mesh* (SM). The signed distance field of the particle cloud, noted $\Theta$, whose zero-isovalue coincides with the body-fitted mesh of the precipitates is constructed. At this point, a polycrystal is created and the GLS functions $\psi_i$ that represent this polycrystal are initialized. If needed, mesh adaptation can be performed around the grain boundaries. However it is here important that the FE mesh remains fitted on the interfaces of the SPPs during the mesh adaptation. The mesher/remesher Fitz used in this work [Shakoor et al. 2015a; Shakoor 2016] is able to tackle this problem because it has the ability to preserve the zero-isovalue(s) of one or several distance fields while performing the topological operations on the FE mesh.

After SM has been satisfactory adapted, the second FE mesh, called the *pinning mesh* (PM), is built. Its construction consists in three steps. First PM is initialized to SM. Then the GLS functions $\psi_i$ and the field $\Theta$ are transported from SM to PM. As SM and PM coincide at this point, no interpolation is needed and no error is made during the field transport. Then the mesh elements and nodes of PM located inside the SPPs (*i.e.* whose nodes satisfy $\Theta \geq 0$) are killed. Now PM can be seen as a counterpart of SM with no mesh element inside the SPPs (see fig. 6.2b), and this configuration is strictly equivalent to the one described in chapter 5 for inert SPPs.

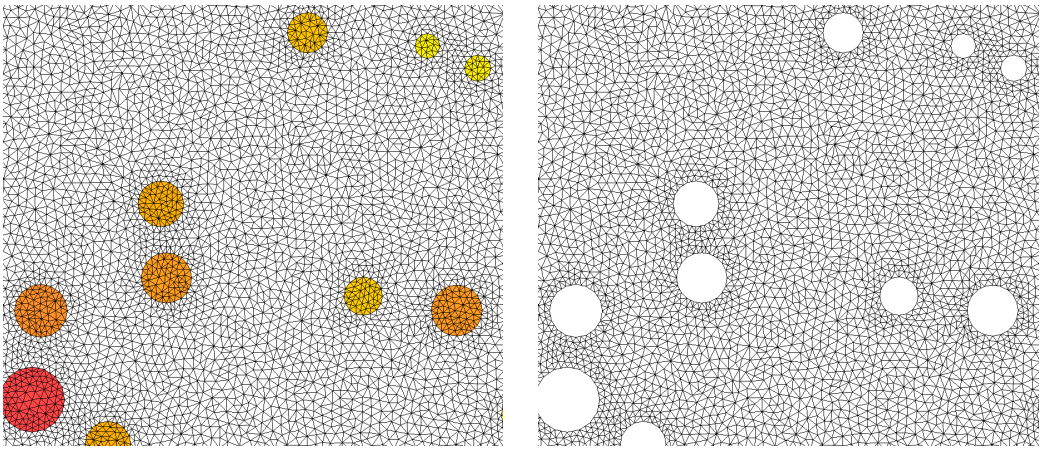

**(a)** **(b)**

**Fig. 6.2** – SM (a) and PM (b) at the early stage of a simulation.

Suitable boundary conditions are then applied around the holes and the FE problem described by eq. (5.2) is solved on PM. Next the vacuum treatment given by eq. (1.50), the swapping algorithm described in section 3.3.2 and the DRT algorithm of section 2.4 are successively performed, still on PM. The $\psi_i$ and $\Theta$ fields are then interpolated from PM to SM. As all the nodes of PM are coincident with the nodes of SM, the transport of the fields from PM to SM is still direct and do not rely on any interpolation. The velocity of the dissolving precipitates is computed and used to update the spatial coordinates of the SM nodes located at the interface of the precipitates. We considered here a fictive dissolving velocity with arbitrary magnitude and oriented toward the centroid of the particles for an illustration. The related evolution of a cloud of SPPs on the FE meshes is depicted on fig. 6.3. After these nodes have been displaced, Fitz adapts SM around the new zero-isovalues of the GLS functions while keeping unchanged the interfaces of the precipitates and the zero-isovalue of $\Theta$. This concludes the sequence of operations for one time step of the simulation, as schematically illustrated on fig. 6.4.

Using this approach, PM is then reconstructed at each time step according to the new positions of the precipitates (see figs. 6.3b, 6.3d and 6.3f). When a precipitate becomes too small and can no longer be accurately represented, it is simply removed from the particle cloud by assigning to $\Theta$ an arbitrary negative value inside this precipitate. As Fitz uses the zero-isovalue of $\Theta$ for the body-fitted mesh adaptation, the interface of this precipitate will no longer be captured and conserved by the remesher. So at the next increment, the PM elements and nodes located inside this precipitate will not be killed, as illustrated on the right column of fig. 6.3.

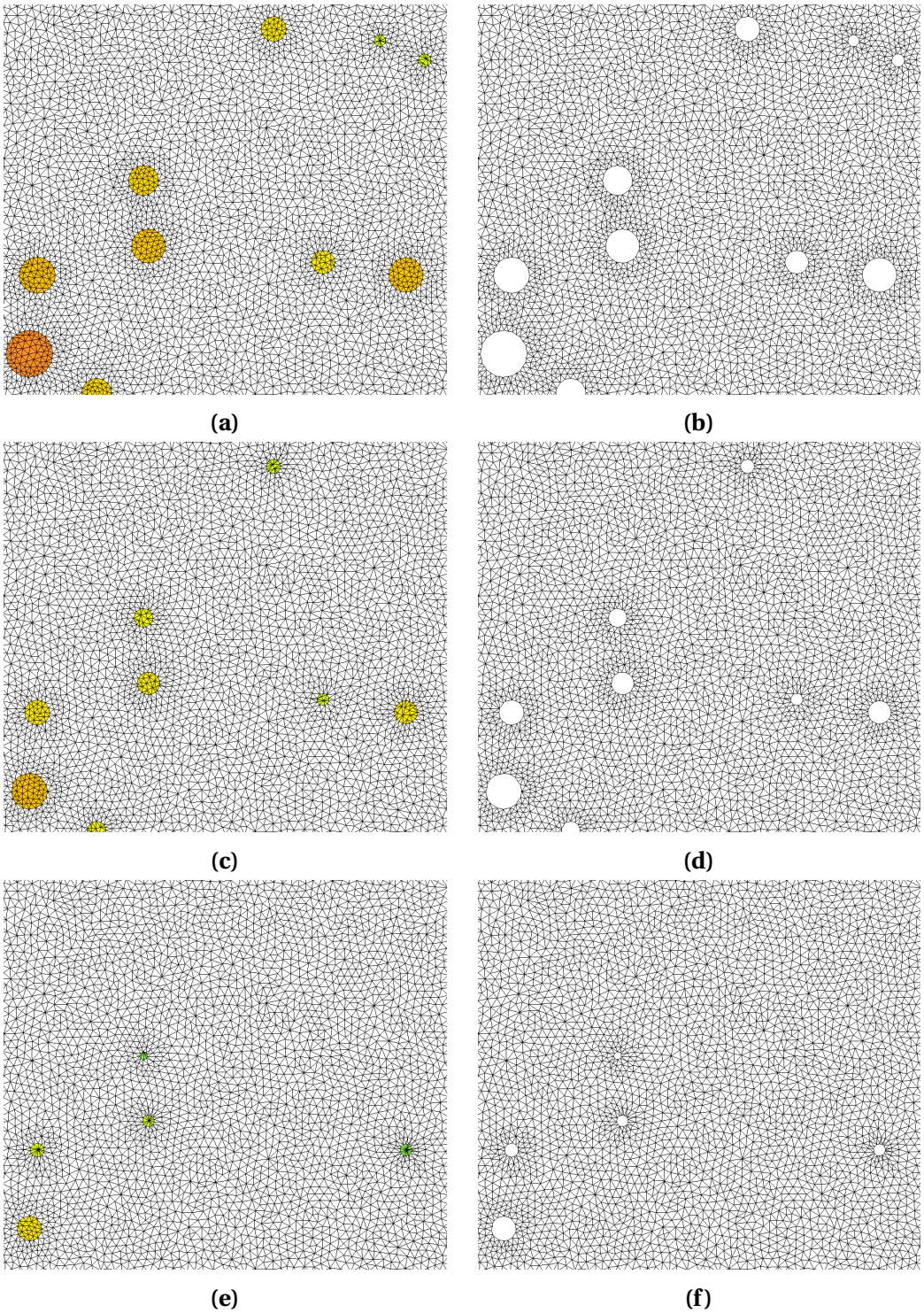


**Fig. 6.3** – Evolution of dissolving SPPs on SM (left column) and PM (right column). A radial velocity with arbitrary magnitude is used to displace the precipitates.

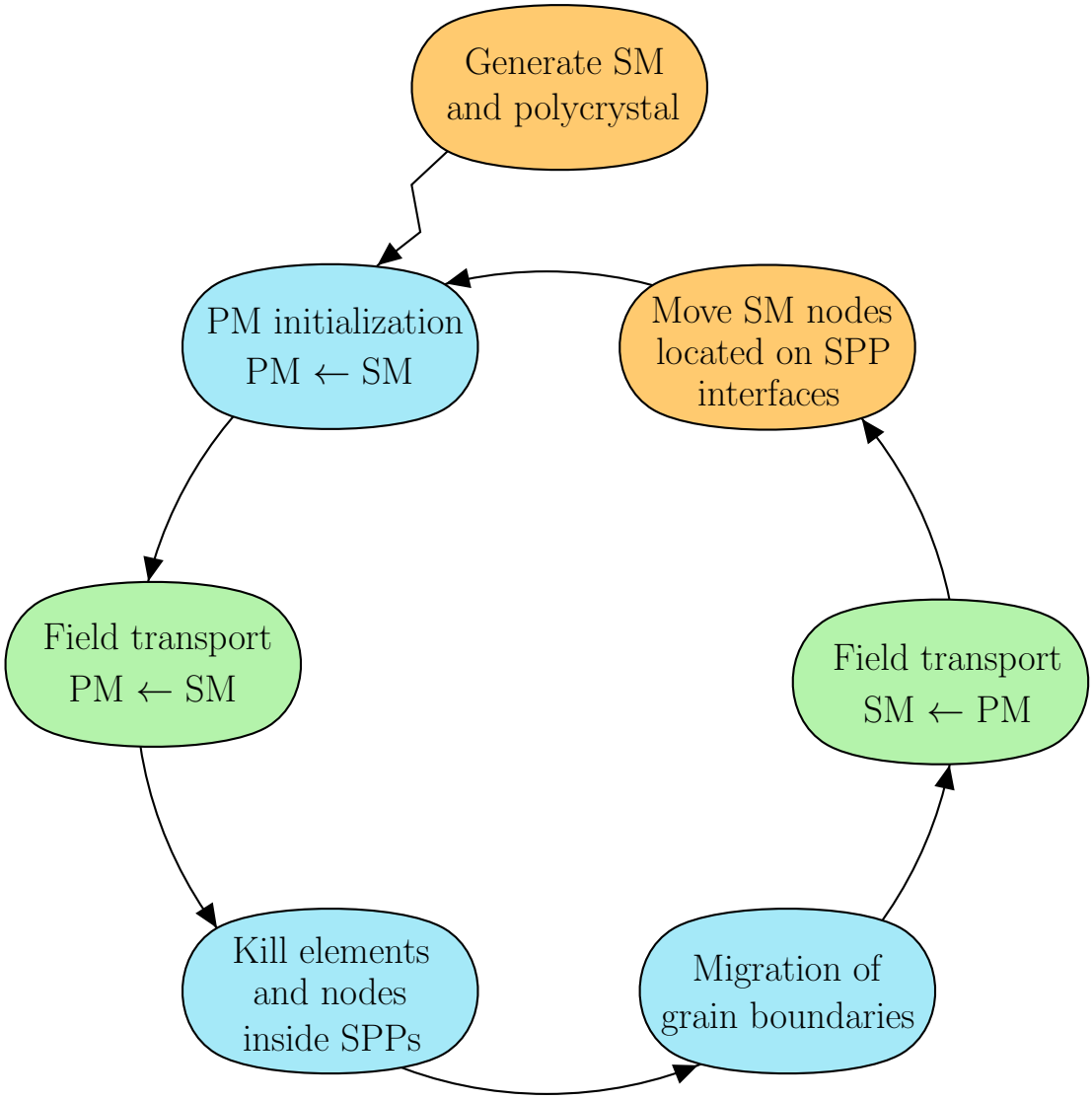


**Fig. 6.4** – Schematic illustration of the sequence of operations for the simulations of ZP with evolving SPPs. Blocks filled in blue and orange are related to the operations performed on PM and SM, respectively. Green blocks stand for the transport of the fields $\psi_i$ and $\Theta$.

However a problem rises when a precipitate is removed. Effectively the values of the GLS functions in its interior are not well-defined because this zone was previously ignored in the computations through the use of the PM mesh (let us remember that a hole was created in this region of the PM mesh to treat it like a precipitate). To address this issue we perform the DRT algorithm at the nodes located inside the dying precipitate(s) before resolving eq. (1.47). This operation recalculates the values of the GLS functions in this zone, that will be now considered as the matrix and no longer as a precipitate. Let us remind that SPPs have small dimensions and so the number of nodes where GLS fields have to be recalculated is sufficiently small to not affect significantly the simulation time. After resolving the CDEs, the vacuum treatment (see eq. (1.50)) is applied to *repair* the vacuum(s) created by the dying precipitates.

This approach can also tackle the formation of SPPs during the simulation. Using the nucleation algorithm introduced in section 4.3.5 on SM, new precipitates can be easily inserted in the distance field $\Theta$. Then the new implicit interface created when a precipitate is added can be explicitly meshed by Fitz, which has the great ability to cut (or split) the elements in order to construct a body-fitted mesh of a (or several) interface(s). We refer the interested reader to [Shakoor 2016] for more details about the strategy adopted to perform this operation and its implementation. Obviously the interfacial mesh of the SPPs that are already present (*i.e.* nodes where $\Theta$ was already zero before inserting the new precipitates) is not affected by the mesh cutting procedure. This numerical approach for the modeling of evolving SPPs has been tested and is numerically robust. Also the few additional numerical tools required to perform such simulations have been developed and validated during the present thesis work. However the evolution law used to calculate the dissolution of the precipitates was here purely virtual and must be improved in order to take into account the chemical composition, the precipitate sizes and shapes, the thermomechanical conditions and the *ad hoc* PDEs describing the SPP evolution [Mei et al. 2015; Masoumi et al. 2016]. Also the PF modeling of precipitate evolution seems more mature at present and can be used advantageously to challenge and validate the future predictions of the LS-FE model [Vaithyanathan et al. 2002; Zhu et al. 2004].

Because the solving of the CDEs, the reinitialization, the dynamic grain recoloring and the vacuum treatment are all performed on PM, no specific treatment is needed for the GLS functions inside the SPPs, as these zones are naturally omitted during these operations. The approach is therefore simple to use but requires to manipulate two FE meshes, which has a memory cost. An interesting prospect would be to impose

the interaction condition between the SPPs and the grain boundaries directly on SM, without having to kill the elements inside the particles. Using this approach, only SM would be needed for the whole simulation.

# Bibliography


**[Abgrall 1996]**
Abgrall, R. (1996). "Numerical discretization of the first-order Hamilton-Jacobi equation on triangular meshes". *Communications on Pure and Applied Mathematics* 49 (12), pp. 1339–1373 (cit. on p. 72).

**[Adalsteinsson et al. 1997]**
Adalsteinsson, D. and J. Sethian (1997). "A level set approach to a unified model for etching, deposition, and lithography". *Journal of Computational Physics* 138 (1), pp. 193–223 (cit. on p. 76).

**[Agnoli 2013]**
Agnoli (2013). "Origin of inhomogeneous grain growth in Inconel 718 forgings". PhD thesis. MINES ParisTech (cit. on pp. 32, 74, 103, 176, 178–183, 185, 189, 198, 203).

**[Agnoli et al. 2012]**
Agnoli, A., M. Bernacki, R. Logé, J. Franchet, J. Laigo, and N. Bozzolo (2012). "Understanding and modeling of grain boundary pinning in Inconel 718". *Proceedings of Superalloys 2012 : The 12th internation symposium on superalloys*. Pennsylvania (cit. on pp. 177, 182, 193).

**[Agnoli et al. 2014]**
Agnoli, A., N. Bozzolo, R. Logé, J. Franchet, J. Laigo, and M. Bernacki (2014). "Development of a level set methodology to simulate grain growth in the presence of real secondary phase particles and stored energy – Application to a nickel-base superalloy". *Computational Materials Science* 89, pp. 233–241 (cit. on pp. 12, 14, 33, 60, 69, 177, 179, 181, 182, 187–189, 203).

**[Alam et al. 1954]**
Alam, M., M. Blackman, and D. Pashley (1954). "High-Angle Kikuchi Patterns". *Proceedings of the Royal Society A: Mathematical, Physical and Engineering Sciences* 221 (1145), pp. 224–242 (cit. on p. 6).

**[Almeida et al. 2000]**
Almeida, R. C., R. A. Feijóo, A. C. Galeão, C. Padra, and R. S. Silva (2000). "Adaptive finite element computational fluid dynamics using an anisotropic error estimator". *Computer Methods in Applied Mechanics and Engineering* 182 (3-4), pp. 379–400 (cit. on p. 56).

[**Anand et al. 1975**]
Anand, L. and J. Gurland (1975). "The relationship between the size of cementite particles and the subgrain size in quenched-and-tempered steel". *Metallurgical Transactions 6A*, pp. 928–931 (cit. on p. 32).

[**Anderson et al. 1984**]
Anderson, M., D. Srolovitz, G. Grest, and P. Sahni (1984). "Computer simulation of grain growth - I. Kinetics". *Acta Metallurgica* 32 (5), pp. 783–791 (cit. on p. 38).

[**Appel et al. 1977a**]
Appel, K. and W. Haken (1977a). "Every planar map is four colorable. Part I: Discharging". *Illinois Journal of Mathematics* 21 (3), pp. 429–490 (cit. on pp. 61, 102).

[**Appel et al. 1977b**]
Appel, K., W. Haken, and J. Koch (1977b). "Every planar map is four colorable. Part II: Reducibility". *Illinois Journal of Mathematics* 21 (3), pp. 491–567 (cit. on pp. 61, 102).

[**Avrami 1939**]
Avrami, M. (1939). "Kinetics of phase change, Part I: General theory". *The Journal of Chemical Physics* 7 (12), pp. 1103–1112 (cit. on pp. 26, 27).

[**Avrami 1940**]
Avrami, M. (1940). "Kinetics of phase change, Part II: Transformation-time relations for random distribution of nuclei". *The Journal of Chemical Physics* 8 (2), pp. 212–224 (cit. on p. 26).

[**Avrami 1941**]
Avrami, M. (1941). "Kinetics of phase change, Part III: Granulation, phase change, and microstructure kinetics of phase change". *The Journal of Chemical Physics* 9 (2), pp. 177–187 (cit. on p. 26).

[**Bailey et al. 1962**]
Bailey, J. and P. Hirsch (1962). "The Recrystallization Process in Some Polycrystalline Metals". *Proceedings of the Royal Society of London A: Mathematical, Physical and Engineering Sciences* 267 (1328), pp. 11–30 (cit. on p. 25).

[**Bammann et al. 1982**]
Bammann, D. and E. Aifantis (1982). "On a proposal for a continuum with microstructure". *Acta Mechanica* 45 (1-2), pp. 91–121 (cit. on p. 24).

[**Basset 2006**]
Basset, O. (2006). "Simulation numérique d'écoulements multi-fluides sur grille de calcul". PhD thesis. MINES ParisTech (cit. on pp. 12, 63, 72, 74–76).

[**Beltran et al. 2015**]
Beltran, O., K. Huang, and R. Logé (2015). "A mean field model of dynamic and post-dynamic recrystallization predicting kinetics, grain size and flow stress". *Computational Materials Science* 102, pp. 293–303 (cit. on pp. 25, 35).

[**Bentley 1975**]
Bentley, J. (1975). "Multidimensional binary search trees used for associative searching". *ACM* 18 (9), pp. 509–517 (cit. on p. 83).

[**Bernacki et al. 2008**]
Bernacki, M., Y. Chastel, T. Coupez, and R. Logé (2008). "Level set framework for the numerical modelling of primary recrystallization in polycrystalline materials". *Scripta Materialia* 58 (12), pp. 1129–1132 (cit. on pp. 11, 14, 60, 72–74, 140–142, 151, 152, 173, 203).

[**Bernacki et al. 2009**]
Bernacki, M., H. Resk, T. Coupez, and R. Logé (2009). "Finite element model of primary recrystallization in polycrystalline aggregates using a level set framework". *Modelling and Simulation in Materials Science and Engineering* 17 (6), p. 064006 (cit. on pp. 11, 14, 51, 55, 57, 72, 141, 142, 151, 152).

[**Bernacki et al. 2011**]
Bernacki, M., R. Logé, and T. Coupez (2011). "Level set framework for the finite-element modelling of recrystallization and grain growth in polycrystalline materials". *Scripta Materialia* 64 (6), pp. 525–528 (cit. on pp. 11, 60).

[**Bernacki et al. 2016**]
Bernacki, M., J. Bruchon, D. Pino Muñoz, M. Bellet, Y. Bienvenu, and E. Rigal (2016). "Numerical FE approach dedicated to microscale modeling of HIP process". *SF2M, Journée HIP 2016*. Dijon (cit. on p. 204).

[**Bernard et al. 2011**]
Bernard, P., S. Bag, K. Huang, and R. Logé (2011). "A two-site mean field model of discontinuous dynamic recrystallization". *Materials Science and Engineering: A* 528 (24), pp. 7357–7367 (cit. on pp. 12, 33, 35, 36, 163).

[**Bois et al. 2012**]
Bois, R., M. Fortin, and A. Fortin (2012). "A fully optimal anisotropic mesh adaptation method based on a hierarchical error estimator". *Computer Methods in Applied Mechanics and Engineering* 209, pp. 12–27 (cit. on p. 56).

[**Boulais-Sinou et al. 2016**]
Boulais-Sinou, R., B. Scholtes, D. Pino Muñoz, C. Moussa, I. Poitrault, I. Bobin, A. Montouchet, and M. Bernacki (2016). "Full field modeling of dynamic recrystallization in a global level set framework, application to 304L stainless steel". *Proceedings of Numiform 2016: The 12th international conference on numerical methods in industrial forming processes* (cit. on pp. 63, 143, 161, 162, 173, 203, 205).

[**Boussetta et al. 2006**]
Boussetta, R., T. Coupez, and L. Fourment (2006). "Adaptive remeshing based on a posteriori error estimation for forging simulation". *Computer Methods in Applied Mechanics and Engineering* 195 (48-49), pp. 6626–6645 (cit. on p. 56).

[**Burke et al. 1952**]
Burke, J. and D. Turnbull (1952). "Recrystallization and grain growth". *Progress in Metal Physics* 3, pp. 220–292 (cit. on p. 30).

[**Cahn 1956**]
Cahn, J. (1956). "The kinetics of grain boundary nucleated reactions". *Acta Metallurgica* 4 (5), pp. 449–459 (cit. on pp. 27, 151).

[**Chang et al. 2009**]
Chang, K., W. Feng, and L. Chen (2009). "Effect of second-phase particle morphology on grain growth kinetics". *Acta Materialia* 57 (17), pp. 5229–5236 (cit. on p. 47).

[**Chang et al. 2014**]
Chang, K. and N. Moelans (2014). "Effect of grain boundary energy anisotropy on highly textured grain structures studied by phase-field simulations". *Acta Materialia* 64, pp. 443–454 (cit. on p. 72).

[**Chang et al. 2015**]
Chang, K. and N. Moelans (2015). "Phase-field simulations of the interactions between a grain boundary and an evolving second-phase particle". *Philosophical Magazine Letters* 95 (4), pp. 202–210 (cit. on p. 47).

[**Chao et al. 2004**]
Chao, W. and L. Guoquan (2004). "Reanalysis of the 3D quasi-stationary grain size distribution based on Hillert's grain growth rate equation". *Science in China Series E Technological Sciences* 47 (1), pp. 112–120 (cit. on p. 33).

[**Chastel et al. 2012**]
Chastel, Y., R. Logé, and M. Bernacki (2012). "Microstructure evolution in metal forming processes". Woodhead Publishing Ltd, first edition. Chap. Modelling, pp. 17–34 (cit. on p. 9).

[**Chen et al. 2015**]
Chen, L., J. Chen, R. Lebensohn, Y. Ji, T. Heo, S. Bhattacharyya, K. Chang, S. Mathaudhu, Z. Liu, and L.-Q. Chen (2015). "An integrated fast Fourier transform-based phase-field and crystal plasticity approach to model recrystallization of three dimensional polycrystals". *Computer Methods in Applied Mechanics and Engineering* 285, pp. 829–848 (cit. on p. 47).

[**Chen et al. 2016**]
Chen, Q., G. Guillemot, C.-A. Gandin, and M. Bellet (2016). "Finite element modeling of deposition of ceramic material during SLM additive manufacturing". *Proceedings of Numiform 2016: The 12th international conference on numerical methods in industrial forming processes*. Troyes (cit. on p. 202).

[**Cheng et al. 2008**]
Cheng, L. and Y. Tsai (2008). "Redistancing by flow of time dependent eikonal equation". *Journal of Computational Physics* 227 (8), pp. 4002–4017 (cit. on p. 71).

[**Cheng et al. 2007**]
Cheng, Y. and C.-W. Shu (2007). "A discontinuous Galerkin finite element method for

directly solving the Hamilton–Jacobi equations". *Journal of Computational Physics* 223 (1), pp. 398–415 (cit. on p. 72).

**[Cheng et al. 2014]**
Cheng, Y. and Z. Wang (2014). "A new discontinuous Galerkin finite element method for directly solving the Hamilton–Jacobi equations". *Journal of Computational Physics* 268, pp. 134–153 (cit. on p. 72).

**[Chopp 1993]**
Chopp, D. (1993). "Computing minimal surfaces via level set curvature flow". *Journal of Computational Physics* 106 (1), pp. 77–91 (cit. on p. 76).

**[Chopp 2001]**
Chopp, D. (2001). "Some Improvements of the Fast Marching Method". *SIAM Journal on Scientific Computing* 23 (1), pp. 230–244 (cit. on p. 70).

**[Chuan et al. 2013]**
Chuan, W., Y. He, and L. Wei (2013). "Modeling of discontinuous dynamic recrystallization of a near-$\alpha$ titanium alloy IMI834 during isothermal hot compression by combining a cellular automaton model with a crystal plasticity finite element method". *Computational Materials Science* 79, pp. 944–959 (cit. on p. 41).

**[Coupez 2007]**
Coupez, T. (2007). "Convection of local level set function for moving surfaces and interfaces in forming flow". *AIP Conference Proceedings* 908, pp. 61–66 (cit. on pp. 72–74).

**[Coupez 2011]**
Coupez, T. (2011). "Metric construction by length distribution tensor and edge based error for anisotropic adaptive meshing". *Journal of Computational Physics* 230 (7), pp. 2391–2405 (cit. on pp. 53, 56).

**[Coupez et al. 2000]**
Coupez, T., H. Digonnet, and R. Ducloux (2000). "Parallel meshing and remeshing". *Applied Mathematical Modelling* 25 (2), pp. 153–175 (cit. on p. 182).

**[Couturier et al. 2003]**
Couturier, G., C. Maurice, and R. Fortunier (2003). "Three-dimensional finite-element simulation of Zener pinning dynamics". *Philosophical Magazine* 83 (30), pp. 3387–3405 (cit. on p. 44).

**[Couturier et al. 2005]**
Couturier, G., R. Doherty, C. Maurice, and R. Fortunier (2005). "3D finite element simulation of the inhibition of normal grain growth by particles". *Acta Materialia* 53 (4), pp. 977–989 (cit. on pp. 44, 187, 195, 198).

**[Cram et al. 2009]**
Cram, D., H. Zurob, Y. Brechet, and C. Hutchinson (2009). "Modelling discontinuous dynamic recrystallization using a physically based model for nucleation". *Acta Materialia* 57 (17), pp. 5218–5228 (cit. on pp. 35, 36, 156).

[**Crandall et al. 1984**]
Crandall, M. and P.-L. Lions (1984). "Two approximations of solutions of Hamilton-Jacobi equations". *Mathematics of Computation* 43 (167), pp. 1–19 (cit. on p. 60).

[**Cruz-Fabiano et al. 2014**]
Cruz-Fabiano, A., R. Logé, and M. Bernacki (2014). "Assessment of simplified 2D grain growth models from numerical experiments based on a level set framework". *Computational Materials Science* 92, pp. 305–312 (cit. on pp. 11, 30, 34, 60, 61, 63, 69, 100, 116, 120, 137, 181).

[**Dancette et al. 2016**]
Dancette, S., A. Browet, G. Martin, M. Willemet, and L. Delannay (2016). "Automatic processing of an orientation map into a finite element mesh that conforms to grain boundaries". *Modelling and Simulation in Materials Science and Engineering* 24 (5), p. 055014 (cit. on p. 49).

[**Darvishi Kamachali et al. 2012**]
Darvishi Kamachali, R. and I. Steinbach (2012). "3D phase-field simulation of grain growth: Topological analysis versus mean-field approximations". *Acta Materialia* 60 (6-7), pp. 2719–2728 (cit. on pp. 30, 33, 37, 46, 123).

[**Darvishi Kamachali et al. 2015**]
Darvishi Kamachali, R., A. Abbondandolo, K. F. Siburg, and I. Steinbach (2015). "Geometrical grounds of mean field solutions for normal grain growth". *Acta Materialia* 90, pp. 252–258 (cit. on pp. 120, 122).

[**Davies 1995**]
Davies, C. (1995). "The effect of neighbourhood on the kinetics of a cellular automaton recrystallisation model". *Scripta Metallurgica et Materialia* 33 (7), pp. 1139–1143 (cit. on p. 40).

[**Davies 1997**]
Davies, C. (1997). "Growth of nuclei in a cellular automaton simulation of recrystallisation". *Scripta Materialia* 36 (1), pp. 35–40 (cit. on p. 40).

[**Davies et al. 1999**]
Davies, C. and L. Hong (1999). "The cellular automaton simulation of static recrystallization in cold-rolled AA1050". *Scripta Materialia* 40 (10), pp. 1145–1150 (cit. on p. 40).

[**Delannay et al. 2006**]
Delannay, L., P. Jacques, and S. Kalidindi (2006). "Finite element modeling of crystal plasticity with grains shaped as truncated octahedrons". *International Journal of Plasticity* 22 (10), pp. 1879–1898 (cit. on pp. 12, 160, 161).

[**Delannay et al. 2009**]
Delannay, L., M. Melchior, J. Signorelli, J.-F. Remacle, and T. Kuwabara (2009). "Influence of grain shape on the planar anisotropy of rolled steel sheets - evaluation of three models". *Computational Materials Science* 45 (3), pp. 739–743 (cit. on p. 49).

[**Demirel et al. 2003**]
Demirel, M. C., A. P. Kuprat, D. C. George, and A. D. Rollett (2003). "Bridging simulations and experiments in microstructure evolution". *Physical Review Letters* 90, p. 016106 (cit. on p. 41).

[**Desmaison 2013**]
Desmaison, O. (2013). "Modélisation numérique d'un procédé de soudage hybride arc/laser en approche level set : application au soudage multi-passes de tôles d'acier de forte épaisseur". PhD thesis. MINES ParisTech (cit. on p. 70).

[**Digonnet et al. 2007**]
Digonnet, H., L. Silva, and T. Coupez (2007). "Cimlib: A fully parallel application for numerical simulations based on components assembly". *AIP Conference Proceedings*. Vol. 908. 1. AIP, pp. 269–274 (cit. on p. 11).

[**Elias et al. 2007**]
Elias, R., M. Martins, and A. Coutinho (2007). "Simple finite element-based computation of distance functions in unstructured grids". *Internation journal for numerical methods in engineering* 72 (May), pp. 1095–1110 (cit. on pp. 70, 74).

[**Elsey et al. 2009**]
Elsey, M., S. Esedoglu, and P. Smereka (2009). "Diffusion generated motion for grain growth in two and three dimensions". *Journal of Computational Physics* 228 (21), pp. 8015–8033 (cit. on pp. 58, 61, 104, 110, 114).

[**Elsey et al. 2011**]
Elsey, M., S. Esedoglu, and P. Smereka (2011). "Large scale simulations and parameter study for a simple recrystallization model". *Philosophical Magazine* 91, pp. 1607–1642 (cit. on p. 58).

[**Elsey et al. 2013**]
Elsey, M., S. Esedoglu, and P. Smereka (2013). "Simulations of anisotropic grain growth: Efficient algorithms and misorientation distributions". *Acta Materialia* 61 (6), pp. 2033–2043 (cit. on p. 58).

[**Estrin 1998**]
Estrin, Y. (1998). "Dislocation theory based constitutive modelling: foundations and applications". *Journal of Materials Processing Technology* 80-81, pp. 33–39 (cit. on pp. 24, 25).

[**Estrin et al. 2007**]
Estrin, Y. and H. Kim (2007). "Modelling microstructure evolution toward ultrafine crystallinity produced by severe plastic deformation". *Journal of Materials Science* 42 (5), pp. 1512–1516 (cit. on p. 23).

[**Fabiano 2013**]
Fabiano, A. (2013). "Modelling of crystal plasticity and grain boundary motion of 304L steel at the mesoscopic scale". PhD thesis. MINES ParisTech (cit. on pp. 12, 27, 61, 63, 73, 74, 100, 103, 137, 157, 163).

[**Fan et al. 1997a**]
Fan, D. and L. Chen (1997a). "Computer simulation of grain growth using a continuum field model". *Acta Materialia* 45 (2), pp. 611–622 (cit. on p. 46).

[**Fan et al. 1997b**]
Fan, D., C. Geng, and L. Chen (1997b). "Computer simulation of topological evolution in 2D grain growth using a continuum diffuse-interface field model". *Acta Materialia* 45 (3), pp. 1115–1126 (cit. on pp. 46, 61, 103).

[**Fan et al. 2004**]
Fan, Z., Y. Wu, X. Zhao, and Y. Lu (2004). "Simulation of polycrystalline structure with Voronoi diagram in Laguerre geometry based on random closed packing of spheres". *Computational Materials Science* 29 (3), pp. 301–308 (cit. on pp. 51, 52).

[**Favre et al. 2013**]
Favre, J., D. Fabrègue, C. Akihiko, and Y. Bréchet (2013). "Nucleation of recrystallization in fine-grained materials: An extension of the Bailey-Hirsch criterion". *Philosophical Magazine Letters* 93 (11), pp. 631–639 (cit. on p. 25).

[**Fortmeier et al. 2011**]
Fortmeier, O. and H. Martin Bücker (2011). "Parallel re-initialization of level set functions on distributed unstructured tetrahedral grids". *Journal of Computational Physics* 230 (12), pp. 4437–4453 (cit. on p. 74).

[**Gao et al. 1997**]
Gao, J., R. Thompson, and B. Patterson (1997). "Computer simulation of grain growth with second phase particle pinning". *Acta Materialia* 45 (9), pp. 3653–3658 (cit. on p. 39).

[**Garcke et al. 1998**]
Garcke, H., B. Nestler, and B. Stoth (1998). "On anisotropic order parameter models for multi-phase systems and their sharp interface limits". *Physica D: Nonlinear Phenomena* 115 (1-2), pp. 87–108 (cit. on p. 46).

[**Geuzaine et al. 2009**]
Geuzaine, C. and J. Remacle (2009). "Gmsh : A 3-D finite element mesh generator with built-in pre- and post-processing facilities". *Internation journal for numerical methods in engineering* (79), pp. 1309–1331 (cit. on p. 184).

[**Gladman 1966**]
Gladman, T. (1966). "On the theory of the effect of precipitate particles on grain growth in metals". *Proceedings of the Royal Society of London A: Mathematical, Physical and Engineering Sciences* 294 (1438), pp. 298–309 (cit. on p. 32).

[**Glicksman 2005**]
Glicksman, M. (2005). "Analysis of 3-D network structures". *Philosophical Magazine* 85 (1), pp. 3–31 (cit. on p. 29).

[**Groeber et al. 2014**]
Groeber, M. and M. Jackson (2014). "DREAM.3D: A Digital Representation Environment

for the Analysis of Microstructure in 3D". *Integrating Materials and Manufacturing Innovation* 3 (cit. on p. 127).

**[Gross et al. 2006]**
Gross, S., V. Reichelt, and A. Reusken (2006). "A finite element based level set method for two-phase incompressible flows". *Computing and Visualization in Science* 9 (4), pp. 239–257 (cit. on p. 70).

**[Gruau 2004]**
Gruau, C. (2004). "Génération de métriques pour adaptation anisotrope de maillages, applications à la mise en forme des matériaux". PhD thesis. MINES ParisTech (cit. on p. 210).

**[Gruber et al. 2005]**
Gruber, J., D. George, A. Kuprat, G. Rohrer, and A. Rollett (2005). "Effect of anisotropic grain boundary properties on grain boundary plane distributions during grain growth". *Scripta Materialia* 53 (3), pp. 351–355 (cit. on p. 41).

**[Hallberg 2011]**
Hallberg, H. (2011). "Approaches to modeling of recrystallization". *Metals* 1 (1), pp. 16–48 (cit. on pp. 38, 40, 42).

**[Hallberg 2014]**
Hallberg, H. (2014). "Influence of anisotropic grain boundary properties on the evolution of grain boundary character distribution during grain growth - A 2D level set study". *Modelling and Simulation in Materials Science and Engineering* 22 (8), p. 085005 (cit. on pp. 173, 205).

**[Hallberg et al. 2010a]**
Hallberg, H., M. Wallin, and M. Ristinmaa (2010a). "Modeling of continuous dynamic recrystallization in commercial-purity aluminum". *Materials Science and Engineering: A* 527 (4-5), pp. 1126–1134 (cit. on p. 23).

**[Hallberg et al. 2010b]**
Hallberg, H., M. Wallin, and M. Ristinmaa (2010b). "Simulation of discontinuous dynamic recrystallization in pure Cu using a probabilistic cellular automaton". *Computational Materials Science* 49 (1), pp. 25–34 (cit. on p. 40).

**[Hallberg et al. 2013]**
Hallberg, H. and M. Ristinmaa (2013). "Microstructure evolution influenced by dislocation density gradients modeled in a reaction-diffusion-system". *Computational Materials Science* 67, pp. 373–383 (cit. on pp. 24, 60, 74).

**[Harten 1989]**
Harten, A. (1989). "ENO schemes with subcell resolution". *Journal of Computational Physics* 83 (1), pp. 148–184 (cit. on p. 71).

**[Harun et al. 2006]**
Harun, A., E. Holm, M. Clode, and M. Miodownik (2006). "On computer simulation methods to model Zener pinning". *Acta Materialia* 54 (12), pp. 3261–3273 (cit. on p. 193).

[**Hefferan et al. 2012**]
Hefferan, C., J. Lind, S. Li, U. Lienert, A. Rollett, and R. Suter (2012). "Observation of recovery and recrystallization in high-purity aluminum measured with forward modeling analysis of high-energy diffraction microscopy". *Acta Materialia* 60 (10), pp. 4311–4318 (cit. on p. 6).

[**Hellman et al. 1975**]
Hellman, P. and M. Hillert (1975). "On the effects of second phase particles on grain growth". *Scandinavian Journal of Metallurgy* 4 (5), pp. 211–219 (cit. on pp. 32, 187, 193, 195, 198).

[**Hesselbarth et al. 1991**]
Hesselbarth, H. and I. Göbel (1991). "Simulation of recrystallization by cellular automata". *Acta Metallurgica et Materialia* 39 (9), pp. 2135–2143 (cit. on p. 40).

[**Hesselbarth et al. 1993**]
Hesselbarth, H., L. Kaps, and F. Haessner (1993). "Two Dimensional Simulation of the Recrystallization Kinetics in the Case of Inhomogeneous Stored Energy". *Materials Science Forum* 113-115, pp. 317–322 (cit. on p. 40).

[**Hillert 1965**]
Hillert, M. (1965). "On the theory of normal and abnormal grain growth". *Acta Metallurgica* 13 (3), pp. 227–238 (cit. on pp. 33, 121).

[**Hitti 2011**]
Hitti, K. (2011). "Direct numerical simulation of complex Representative Volume Elements (VERs): Generation, resolution and homogenization". PhD thesis. MINES ParisTech (cit. on pp. 12, 52, 61, 129, 130, 184).

[**Hitti et al. 2012**]
Hitti, K., P. Laure, T. Coupez, L. Silva, and M. Bernacki (2012). "Precise generation of complex statistical Representative Volume Elements (RVEs) in a finite element context". *Computational Materials Science* 61, pp. 224–238 (cit. on pp. 12, 51, 52, 129).

[**Hitti et al. 2016**]
Hitti, K., S. Feghali, and M. Bernacki (2016). "Permeability computation on a Representative Volume Element (RVE) of unidirectional disordered fiber arrays". *Journal of Computational Mathematics* 34 (3), pp. 246–264 (cit. on p. 184).

[**Hore et al. 2013**]
Hore, S., S. Das, S. Banerjee, and S. Mukherjee (2013). "A multiscale coupled Monte Carlo model to characterize microstructure evolution during hot rolling of Mo-TRIP steel". *Acta Materialia* 61 (19), pp. 7251–7259 (cit. on p. 39).

[**Hore et al. 2015**]
Hore, S., S. Das, S. Banerjee, and S. Mukherjee (2015). "Computational modelling of static recrystallization and two dimensional microstructure evolution during hot strip rolling of advanced high strength steel". *Journal of Manufacturing Processes* 17, pp. 78–87 (cit. on p. 39).

**[Hu et al. 1999]**
Hu, C. and C.-W. Shu (1999). "A Discontinuous Galerkin Finite Element Method for Hamilton–Jacobi Equations". *SIAM Journal on Scientific Computing* 21 (2), pp. 666–690 (cit. on p. 72).

**[Huang 2011]**
Huang, K. (2011). "Towards the modelling of recrystallization phenomena in multi-pass conditions: application to 304L steel". PhD thesis. MINES ParisTech (cit. on pp. 160, 164, 166, 167, 205).

**[Hull 1988]**
Hull, F. (1988). "Plane section and spatial characteristics of equiaxed $\beta$-brass grains". *Materials Science and Technology* 4 (9), pp. 778–785 (cit. on p. 30).

**[Humphreys et al. 2004]**
Humphreys, F. and M. Hatherly (2004). *Recrystallization and related annealing phenomena*. Elsevier (cit. on pp. 4, 5, 23, 26, 27, 31, 151).

**[Hutchinson 1977]**
Hutchinson, J. (1977). "Creep and plasticity of hexagonal polycrystals as related to single crystal slip". *Metallurgical Transactions A* 8, pp. 1465–1469 (cit. on p. 160).

**[Ilin et al. 2016]**
Ilin, D., B. Scholtes, N. Bozzolo, D. Pino Munoz, and M. Bernacki (2016). "Effect of intragranular strain heterogeneity on recrystallization kinetics assessed by numerical simulation at the mesoscopic scale". *Workshop "La métallurgie, quel avenir !"* (Cit. on pp. 162, 173, 203, 205).

**[Janssens 2010]**
Janssens, K. (2010). "An introductory review of cellular automata modeling of moving grain boundaries in polycrystalline materials". *Mathematics and Computers in Simulation* 80 (7), pp. 1361–1381 (cit. on p. 40).

**[Jensen et al. 2013]**
Jensen, M. and I. Smears (2013). "Finite element methods with artificial diffusion for Hamilton-Jacobi-Bellman equations". *Numerical Mathematics and Advanced Applications 2011*. Berlin, Heidelberg: Springer Berlin Heidelberg, pp. 267–274 (cit. on p. 72).

**[Jiang et al. 2000]**
Jiang, G.-S. and D. Peng (2000). "Weighted ENO schemes for Hamilton–Jacobi equations". *SIAM Journal on Scientific Computing* 21 (6), pp. 2126–2143 (cit. on p. 71).

**[Jin et al. 2014]**
Jin, Y., B. Lin, M. Bernacki, G. Rohrer, a.D. Rollett, and N. Bozzolo (2014). "Annealing twin development during recrystallization and grain growth in pure nickel". *Materials Science and Engineering: A* 597, pp. 295–303 (cit. on pp. 74, 103).

**[Jin et al. 2015]**
Jin, Y., N. Bozzolo, A. Rollett, and M. Bernacki (2015). "2D finite element modeling of anisotropic grain growth in polycrystalline materials: level set versus multi-phase-field

method". *Computational Materials Science* 104 (15), pp. 108–123 (cit. on pp. 46, 69, 173, 205).

[**Johnson et al. 1939**]
Johnson, W. and R. Mehl (1939). "Reaction kinetics in processes of nucleation and growth". *Transactions of the American Institute of Mining and Metallurgical Engineers* 135, pp. 416–458 (cit. on p. 26).

[**Jones et al. 2006**]
Jones, M., J. Baerentzen, and M. Sramek (2006). "3D distance fields: a survey of techniques and applications". *IEEE Trans. Visual. Comput. graphics* 12 (4), pp. 581–599 (cit. on p. 74).

[**Karakus et al. 2016**]
Karakus, A., T. Warburton, M. Aksel, and C. Sert (2016). "A GPU accelerated level set reinitialization for an adaptive discontinuous Galerkin method". *Computers & Mathematics with Applications* 72 (3), pp. 755–767 (cit. on p. 72).

[**Kawasaki et al. 1989**]
Kawasaki, K., T. Nagai, and K. Nakashima (1989). "Vertex models for two-dimensional grain growth". *Philosophical Magazine B* 60 (3), pp. 399–421 (cit. on p. 42).

[**Kerisit 2012**]
Kerisit, C. (2012). "Analyse des mécanismes de recristallisation statique du tantale déformé à froid pour une modélisation en champ moyen". PhD thesis. MINES ParisTech (cit. on p. 163).

[**Kimmel et al. 1998**]
Kimmel, R. and J. Sethian (1998). "Computing geodesic paths on manifolds". *Proc. Natl. Acad. Sci. USA* 95 (15), pp. 8431–8435 (cit. on p. 69).

[**Kocks 1976**]
Kocks, U. (1976). "Laws for work-hardening and low-temperature creep". *Journal of Engineering Materials and Technology* 98 (1), pp. 76–85 (cit. on pp. 24, 25).

[**Kolmogorov 1937**]
Kolmogorov, A. (1937). "Statistical theory of crystallization of metals". *Bull. Acad. Sci. USSR Ser. Math.* 24, pp. 355–359 (cit. on p. 26).

[**Kremeyer 1998**]
Kremeyer, K. (1998). "Cellular Automata Investigations of Binary Solidification". *Journal of Computational Physics* 142 (1), pp. 243–262 (cit. on p. 40).

[**Krill III et al. 2002**]
Krill III, C. and L. Chen (2002). "Computer simulation of 3-D grain growth using a phase-field model". *Acta Materialia* 50 (12), pp. 3059–3075 (cit. on pp. 61, 103, 104, 110, 113, 114).

[**Kuprat 2000**]
Kuprat, A. (2000). "Modeling microstructure evolution using gradient-weighted moving finite elements". *SIAM Journal on Scientific Computing* 22 (2), pp. 535–560 (cit. on p. 41).

**[Laasraoui et al. 1991]**
Laasraoui, A. and J. Jonas (1991). "Prediction of steel flow stresses at high temperatures and strain rates". *Metallurgical Transactions A* 22 (7), pp. 1545–1558 (cit. on pp. 24, 25).

**[Lazar et al. 2010]**
Lazar, E., R. MacPherson, and D. Srolovitz (2010). "A more accurate two-dimensional grain growth algorithm". *Acta Materialia* 58 (2), pp. 364–372 (cit. on p. 29).

**[Lazar et al. 2011]**
Lazar, E., J. Mason, R. MacPherson, and D. Srolovitz (2011). "A more accurate three-dimensional grain growth algorithm". *Acta Materialia* 59 (17), pp. 6837–6847 (cit. on pp. 29, 43, 44).

**[Lelièvre et al. 2011]**
Lelièvre, P., C. Farquharson, and C. Hurich (2011). "Computing first-arrival seismic traveltimes on unstructured 3-D tetrahedral grids using the Fast Marching Method". *Geophysical Journal International* 184 (2), pp. 885–896 (cit. on p. 70).

**[Li et al. 2006]**
Li, C., C. Xu, Konwar K.M., and M. Fox (2006). "Fast Distance Preserving Level Set Evolution for Medical Image Segmentation". *Proceedings of 9th International Conference on Control, Automation, Robotics and Vision*. Singapore: IEEE, pp. 1–7 (cit. on p. 72).

**[Li et al. 2005]**
Li, F. and C.-W. Shu (2005). "Reinterpretation and simplified implementation of a discontinuous Galerkin method for Hamilton–Jacobi equations". *Applied Mathematics Letters* 18 (11), pp. 1204–1209 (cit. on p. 72).

**[Lin et al. 2016]**
Lin, Y., Y.-X. Liu, M.-S. Chen, M.-H. Huang, X. Ma, and Z.-L. Long (2016). "Study of static recrystallization behavior in hot deformed Ni-based superalloy using cellular automaton model". *Materials & Design* 99, pp. 107–114 (cit. on pp. 40, 41).

**[Liu et al. 2015]**
Liu, Y.-X., Y. Lin, H.-B. Li, D.-X. Wen, X.-M. Chen, and M.-S. Chen (2015). "Study of dynamic recrystallization in a Ni-based superalloy by experiments and cellular automaton model". *Materials Science and Engineering: A* 626, pp. 432–440 (cit. on pp. 40, 41).

**[Logé et al. 2008]**
Logé, R., M. Bernacki, H. Resk, L. Delannay, H. Digonnet, Y. Chastel, and T. Coupez (2008). "Linking plastic deformation to recrystallization in metals using digital microstructures". *Philosophical Magazine* 88 (30-32), pp. 3691–3712 (cit. on pp. 12, 141, 160, 161).

**[MacPherson et al. 2007]**
MacPherson, R. and D. Srolovitz (2007). "The von Neumann relation generalized to coarsening of three-dimensional microstructures." *Nature* 446, pp. 1053–1055 (cit. on p. 28).

**[Madej et al. 2016]**
Madej, L., M. Sitko, K. Radwanski, and R. Kuziak (2016). "Validation and predictions of coupled finite element and cellular automata model: Influence of the degree of defor-

mation on static recrystallization kinetics case study". *Materials Chemistry and Physics* 179 (15), pp. 282–294 (cit. on p. 41).

[**Maire et al. 2016**]
Maire, L., B. Scholtes, C. Moussa, N. Bozzolo, D. Pino Muñoz, and M. Bernacki (2016). "Improvement of 3-D mean field models for capillarity driven grain growth based on full field simulations". *Journal of Materials Science* 51 (24), pp. 10970–10981 (cit. on pp. 30, 123, 125).

[**Masoumi et al. 2016**]
Masoumi, F., M. Jahazi, D. Shahriari, and J. Cormier (2016). "Coarsening and dissolution of $\gamma$' precipitates during solution treatment of AD730 Ni-based superalloy: Mechanisms and kinetics models". *Journal of Alloys and Compounds* 658, pp. 981–995 (cit. on p. 216).

[**Mei et al. 2015**]
Mei, Y., Y. Liu, C. Liu, C. Li, L. Yu, Q. Guo, and H. Li (2015). "Effects of cold rolling on the precipitation kinetics and the morphology evolution of intermediate phases in Inconel 718 alloy". *Journal of Alloys and Compounds* 649, pp. 949–960 (cit. on p. 216).

[**Mellbin et al. 2015**]
Mellbin, Y., H. Hallberg, and M. Ristinmaa (2015). "A combined crystal plasticity and graph-based vertex model of dynamic recrystallization at large deformations". *Modelling and Simulation in Materials Science and Engineering* 23 (4), p. 045011 (cit. on pp. 42, 43).

[**Merriman et al. 1994**]
Merriman, B., J. Bence, and S. Osher (1994). "Motion of multiple junctions : A level set approach". *Journal of Computational Physics* 112, pp. 334–363 (cit. on pp. 60, 73).

[**Mesri et al. 2008**]
Mesri, Y., W. Zerguine, H. Digonnet, L. Silva, and T. Coupez (2008). "Dynamic parallel adaption for three dimensional unstructured meshes : Application to interface tracking". *Proceedings of the 17th International Meshing Roundtable,* pp. 195–212 (cit. on pp. 12, 56, 57, 63).

[**Metallurgy made in and for Europe 2014**]
Metallurgy made in and for Europe (2014). *Metallurgy made in and for Europe, Publications Office of the European*. Tech. rep. (cit. on p. 10).

[**Mießen et al. 2015**]
Mießen, C., M. Liesenjohann, L. Barrales-Mora, L. Shvindlerman, and G. Gottstein (2015). "An advanced level set approach to grain growth - Accounting for grain boundary anisotropy and finite triple junction mobility". *Acta Materialia* 99, pp. 39–48 (cit. on pp. 58, 173, 205).

[**Min 2010**]
Min, C. (2010). "On reinitializing level set functions". *Journal of Computational Physics* 229 (8), pp. 2764–2772 (cit. on pp. 60, 71).

[**Miodownik et al. 1999**]
Miodownik, M., J. Martin, and A. Cerezo (1999). "Mesoscale simulations of particle pinning". *Philosophical Magazine A* 79 (1), pp. 203–222 (cit. on p. 40).

[**Miodownik et al. 2000**]
Miodownik, M., E. Holm, and G. Hassold (2000). "Highly parallel computer simulations of particle pinning: zener vindicated". *Scripta Materialia* 42 (12), pp. 1173–1177 (cit. on pp. 40, 187, 195).

[**Miyoshi et al. 2016**]
Miyoshi, E. and T. Takaki (2016). "Extended higher-order multi-phase-field model for three-dimensional anisotropic-grain-growth simulations". *Computational Materials Science* 120, pp. 77–83 (cit. on p. 46).

[**Moelans et al. 2005**]
Moelans, N., B. Blanpain, and P. Wollants (2005). "A phase field model for the simulation of grain growth in materials containing finely dispersed incoherent second-phase particles". *Acta Materialia* 53 (6), pp. 1771–1781 (cit. on p. 47).

[**Moelans et al. 2006**]
Moelans, N., B. Blanpain, and P. Wollants (2006). "Phase field simulations of grain growth in two-dimensional systems containing finely dispersed second-phase particles". *Acta Materialia* 54 (4), pp. 1175–1184 (cit. on pp. 187, 189, 193–195, 206).

[**Moelans et al. 2008**]
Moelans, N., B. Blanpain, and P. Wollants (2008). "Quantitative analysis of grain boundary properties in a generalized phase field model for grain growth in anisotropic systems". *Physical Review B* 78 (2), p. 024113 (cit. on pp. 45, 46).

[**Moelans et al. 2009**]
Moelans, N., F. Wendler, and B. Nestler (2009). "Comparative study of two phase-field models for grain growth". *Computational Materials Science* 46 (2), pp. 479–490 (cit. on p. 46).

[**Montheillet et al. 2009**]
Montheillet, F., O. Lurdos, and G. Damamme (2009). "A grain scale approach for modeling steady-state discontinuous dynamic recrystallization". *Acta Materialia* 57 (5), pp. 1602–1612 (cit. on pp. 24, 33, 35, 36, 156).

[**Mullins 1989**]
Mullins, W. W. (1989). "Estimation of the geometrical rate constant in idealized three dimensional grain growth". *Acta Metallurgica* 37 (11), pp. 2979–2984 (cit. on pp. 28–30).

[**Mullins 1956**]
Mullins, W. (1956). "Two-dimensional motion of idealized grain boundaries". *Journal of Applied Physics* 27 (8), pp. 900–904 (cit. on p. 28).

[**Nakashima et al. 1989**]
Nakashima, K., T. Nagai, and K. Kawasaki (1989). "Scaling behavior of two-dimensional domain growth: Computer simulation of vertex models". *Journal of Statistical Physics* 57 (3-4), pp. 759–787 (cit. on p. 42).

[**Nervo et al. 2016**]
Nervo, L., A. King, A. Fitzner, W. Ludwig, and M. Preuss (2016). "A study of deformation

twinning in a titanium alloy by X-ray diffraction contrast tomography". *Acta Materialia* 105, pp. 417–428 (cit. on p. 6).

[**Nguyen 2015**]
Nguyen, T. (2015). "Multiscale finite element modeling of macrosegregation and grain transport". PhD thesis. MINES ParisTech (cit. on p. 202).

[**Noumir et al. 2015**]
Noumir, Y., A. Le Guilcher, N. Lardjane, R. Monneau, and A. Sarrazin (2015). "A fast-marching like algorithm for geometrical shock dynamics". *Journal of Computational Physics* 284, pp. 206–229 (cit. on p. 69).

[**Osher et al. 1988**]
Osher, S. and J. Sethian (1988). "Fronts propagating with curvature-dependent speed : Algorithms based on Hamilton-Jacobi formulations". *Journal of Computational Physics* 79 (1), pp. 12–49 (cit. on pp. 48, 71).

[**Osher et al. 1991**]
Osher, S. and C.-W. Shu (1991). "High-order essentially nonoscillatory schemes for Hamilton–Jacobi equations". *SIAM Journal on Numerical Analysis* 28 (4), pp. 907–922 (cit. on p. 71).

[**Peczak et al. 1993**]
Peczak, P. and M. Luton (1993). "The effect of nucleation models on dynamic recrystallization I. Homogeneous stored energy distribution". *Philosophical Magazine Part B* 68 (1), pp. 115–144 (cit. on p. 25).

[**Peczak et al. 1994**]
Peczak, P. and M. Luton (1994). "The effect of nucleation models on dynamic recrystallization II. Heterogeneous stored-energy distribution". *Philosophical Magazine Part B* 70 (4), pp. 817–849 (cit. on p. 25).

[**Peng et al. 1999**]
Peng, D., B. Merriman, S. Osher, H. Zhao, and M. Kang (1999). "A PDE-Based Fast Local Level Set Method". *Journal of Computational Physics* 155 (2), pp. 410–438 (cit. on p. 76).

[**Piekos et al. 2008**]
Piekos, K., J. Tarasiuk, K. Wierzbanowski, and B. Bacroix (2008). "Generalized vertex model of recrystallization – Application to polycrystalline copper". *Computational Materials Science* 42 (4), pp. 584–594 (cit. on pp. 42, 44).

[**Plimpton et al. 2009**]
Plimpton, S., C. Battaile, M. Chandross, L. Holm, A. Thompson, V. Tikare, G. Wagner, E. Webb, X. Zhou, C. G. Cardona, and A. Slepoy (2009). *Crossing the Mesoscale No-Man's Land via Parallel Kinetic Monte Carlo*. Tech. rep. Sandia SAND2009-6226 (cit. on p. 205).

[**Pokharel et al. 2015**]
Pokharel, R., J. Lind, S. F. Li, P. Kenesei, R. a. Lebensohn, R. M. Suter, and A. D. Rollett (2015). "In-situ observation of bulk 3D grain evolution during plastic deformation in polycrystalline Cu". *International Journal of Plasticity* 67, pp. 217–234 (cit. on pp. 6, 8).

**[Potts 1952]**
Potts, R. (1952). "Some generalized order-disorder transformations". *Mathematical Proceedings of the Cambridge Philosophical Society* 48 (1), pp. 106–109 (cit. on p. 37).

**[Quan et al. 2014]**
Quan, D., T. Toulorge, E. Marchandise, J. Remacle, and G. Bricteux (2014). "Anisotropic mesh adaptation with optimal convergence for finite elements using embedded geometries". *Computer Methods in Applied Mechanics and Engineering* 268, pp. 65–81 (cit. on pp. 55, 60, 210).

**[Quey et al. 2011]**
Quey, R., P. Dawson, and F. Barbe (2011). "Large-scale 3D random polycrystals for the finite element method: Generation, meshing and remeshing". *Computer Methods in Applied Mechanics and Engineering* 200 (17-20), pp. 1729–1745 (cit. on pp. 49–51).

**[Raabe 1999]**
Raabe, D. (1999). "Introduction of a scalable three-dimensional cellular automaton with a probabilistic switching rule for the discrete mesoscale simulation of recrystallization phenomena". *Philosophical Magazine A* 79 (10), pp. 2339–2358 (cit. on p. 40).

**[Raabe 2000]**
Raabe, D. (2000). "Scaling Monte Carlo kinetics of the Potts model using rate theory". *Acta Materialia* 48 (7), pp. 1617–1628 (cit. on p. 39).

**[Raabe et al. 2000]**
Raabe, D. and R. Becker (2000). "Coupling of a crystal plasticity finite-element model with a probabilistic cellular automaton for simulating primary recrystallization in aluminium". *Modelling and Simulation in Materials Science and Engineering* 8, pp. 445–462 (cit. on p. 41).

**[Raabe 2002]**
Raabe, D. (2002). "Cellular automata in materials science with particular reference to recrystallization simulation". *Annual Review of Materials Research* 32 (1), pp. 53–76 (cit. on p. 40).

**[Rabizadeh et al. 2016]**
Rabizadeh, E., A. Saboor Bagherzadeh, and T. Rabczuk (2016). "Goal-oriented error estimation and adaptive mesh refinement in dynamic coupled thermoelasticity". *Computers & Structures* 173, pp. 187–211 (cit. on p. 56).

**[Randrianalisoa et al. 2015]**
Randrianalisoa, J., D. Baillis, C. Martin, and R. Dendievel (2015). "Microstructure effects on thermal conductivity of open-cell foams generated from the Laguerre–Voronoï tessellation method". *International Journal of Thermal Sciences* 98, pp. 277–286 (cit. on p. 51).

**[Rebay 1993]**
Rebay, S. (1993). "Efficient unstructured mesh generation by means of delaunay triangulation and Bowyer-Watson algorithm". *Journal of Computational Physics* 106 (1), pp. 125–138 (cit. on p. 184).

[**Resk et al. 2009**]
Resk, H., L. Delannay, M. Bernacki, T. Coupez, and R. Logé (2009). "Adaptive mesh refinement and automatic remeshing in crystal plasticity finite element simulations". *Modelling and Simulation in Materials Science and Engineering* 17 (7), p. 075012 (cit. on pp. 12, 55, 160, 161).

[**Rickman et al. 1997**]
Rickman, J., W. Tong, and K. Barmak (1997). "Impact of heterogeneous boundary nucleation on transformation kinetics and microstructure". *Acta Materialia* 45 (3), pp. 1153–1166 (cit. on p. 151).

[**Rios et al. 2006**]
Rios, P., T. Dalpian, V. Brandão, J. Castro, and a.C.L. Oliveira (2006). "Comparison of analytical grain size distributions with three-dimensional computer simulations and experimental data". *Scripta Materialia* 54 (9), pp. 1633–1637 (cit. on pp. 29, 33, 123).

[**Roberts et al. 1978**]
Roberts, W and B Ahlblom (1978). "A nucleation criterion for dynamic recrystallization during hot working". *Acta Metallurgica* 26 (5), pp. 801–813 (cit. on p. 24).

[**Rollett et al. 1989**]
Rollett, A. D., D. Srolovitz, R. Doherty, and M. Anderson (1989). "Computer simulation of recrystallization in non-uniformly deformed metals". *Acta Metallurgica* 31 (2), pp. 627–639 (cit. on p. 38).

[**Rollett 1997**]
Rollett, A. (1997). "Overview of modeling and simulation of recrystallization". *Progress in Materials Science* 42 (1-4), pp. 79–99 (cit. on pp. 38, 39).

[**Rollett et al. 1992a**]
Rollett, A., D. Srolovitz, M. Anderson, and R. Doherty (1992a). "Computer simulation of recrystallization—III. Influence of a dispersion of fine particles". *Acta Metallurgica et Materialia* 40 (12), pp. 3475–3495 (cit. on p. 38).

[**Rollett et al. 1992b**]
Rollett, A., M. Luton, and D. Srolovitz (1992b). "Microstructural simulation of dynamic recrystallization". *Acta Metallurgica et Materialia* 40 (1), pp. 43–55 (cit. on p. 38).

[**Rollett et al. 2001**]
Rollett, A. and D. Raabe (2001). "A hybrid model for mesoscopic simulation of recrystallization". *Computational Materials Science* 21 (1), pp. 69–78 (cit. on p. 38).

[**Rollett et al. 2004**]
Rollett, A., D. Saylor, J. Fridy, B. El-Dasher, A. Brahme, S. Lee, C. Cornwell, and R. Noack (2004). "Modeling Polycrystalline Microstructures in 3D". *Proceedings of Numiform 2004*. Columbus, pp. 71–77 (cit. on pp. 38, 49).

[**Rollett et al. 2015**]
Rollett, A., G. Rohrer, and R. Suter (2015). "Understanding materials microstructure and behavior at the mesoscale". *MRS Bulletin* 40 (11), pp. 951–960 (cit. on p. 9).

**[Saad 2016]**
Saad, A. (2016). "Numerical modelling of macrosegregation formed during solidification with shrinkage using a Level Set approach". PhD thesis. MINES ParisTech (cit. on p. 202).

**[Saye et al. 2012]**
Saye, R. and J. Sethian (2012). "Analysis and applications of the Voronoi Implicit Interface Method". *Journal of Computational Physics* 231 (18), pp. 6051–6085 (cit. on p. 69).

**[Schindelin et al. 2012]**
Schindelin, J., I. Arganda-Carreras, E. Frise, V. Kaynig, M. Longair, T. Pietzsch, S. Preibisch, C. Rueden, S. Saalfeld, B. Schmid, J. Tinevez, D. White, V. Hartenstein, K. Eliceiri, P. Tomancak, and A. Cardona (2012). "Fiji: an open-source platform for biological-image analysis". *Nature Methods* 9 (7), pp. 676–682 (cit. on p. 131).

**[Schneider et al. 2012]**
Schneider, C., W. Rasband, and K. Eliceiri (2012). "NIH Image to ImageJ: 25 years of image analysis". *Nature Methods* 9 (7), pp. 671–675 (cit. on p. 131).

**[Schneider et al. 2003]**
Schneider, P. and D. Eberly (2003). "Geometric tools for computer graphics". *The Morgan Kaufmann Series in Computer Graphics and Geometric Modeling* (cit. on p. 81).

**[Scholtes et al. 2015]**
Scholtes, B., M. Shakoor, A. Settefrati, P.-O. Bouchard, N. Bozzolo, and M. Bernacki (2015). "New finite element developments for the full field modeling of microstructural evolutions using the level set method". *Computational Materials Science* 109, pp. 388–398 (cit. on pp. 101, 114, 137, 153).

**[Scholtes et al. 2016a]**
Scholtes, B., R. Boulais-Sinou, A. Settefrati, D. Pino Muñoz, I. Poitrault, A. Montouchet, N. Bozzolo, and M. Bernacki (2016a). "3D level set modeling of static recrystallization considering stored energy fields". *Computational Materials Science* 122, pp. 57–71 (cit. on pp. 140, 174).

**[Scholtes et al. 2016b]**
Scholtes, B., D. Ilin, A. Settefrati, N. Bozzolo, A. Agnoli, and M. Bernacki (2016b). "Full field modeling of the Zener pinning phenomenon in a level set framework - discussion of classical limiting mean grain size equation". *Proceedings of Superalloys 2016 : The 13th international symposium on superalloys*. Pennsylvania (cit. on pp. 33, 176, 199).

**[Schwarze et al. 2016]**
Schwarze, C., R. Darvishi Kamachali, and I. Steinbach (2016). "Phase-field study of zener drag and pinning of cylindrical particles in polycrystalline materials". *Acta Materialia* 106, pp. 59–65 (cit. on p. 47).

**[Sethian 1995]**
Sethian, J. (1995). "A Fast Marching Level Set Method for monotically advancing fronts". *Proceedings of the National Academy of Sciences* 93 (4), pp. 1591–1595 (cit. on p. 69).

[**Sethian et al. 2000**]
Sethian, J. and A. Vladimirsky (2000). "Fast methods for the Eikonal and related Hamilton-Jacobi equations on unstructured meshes." *Proceedings of the National Academy of Sciences of the United States of America* 97 (11), pp. 5699–703 (cit. on p. 70).

[**Shakoor 2016**]
Shakoor, M. (2016). "Three-dimensional numerical modeling of ductile fracture mechanisms at the microscale". PhD thesis. MINES ParisTech (cit. on pp. 210, 212, 216).

[**Shakoor et al. 2015a**]
Shakoor, M., M. Bernacki, and P. Bouchard (2015a). "A new body-fitted immersed volume method for the modeling of ductile fracture at the microscale: Analysis of void clusters and stress state effects on coalescence". *Engineering Fracture Mechanics* 147, pp. 398–417 (cit. on pp. 12, 49, 53, 131, 211, 212).

[**Shakoor et al. 2015b**]
Shakoor, M., B. Scholtes, P.-O. Bouchard, and M. Bernacki (2015b). "An efficient and parallel level set reinitialization method - Application to micromechanics and microstructural evolutions". *Applied Mathematical Modelling* 39 (23-24), pp. 7291–7302 (cit. on pp. 60, 68, 90, 97).

[**Smith 1948**]
Smith, C. (1948). "Introduction to grains, phases and interfaces - An interpretation of microstructure". *Transactions of the Metallurgical Society of AIME* 175, pp. 15–51 (cit. on pp. 6, 31, 32, 187, 195, 198).

[**Spettl et al. 2016**]
Spettl, A., T. Brereton, Q. Duan, T. Werz, C. Krill, D. Kroese, and V. Schmidt (2016). "Fitting Laguerre tessellation approximations to tomographic image data". *Philosophical Magazine* 96, pp. 166–189 (cit. on p. 127).

[**Srolovitz et al. 1984**]
Srolovitz, D., M. Anderson, G. Grest, and P. Sahni (1984). "Computer simulation of grain growth - III. Influence of a particle dispersion". *Acta Metallurgica* 32 (9), pp. 1429–1438 (cit. on pp. 38, 39).

[**Steinbach et al. 1996**]
Steinbach, I., F. Pezzolla, B. Nestler, M. Seesselberg, R. Prieler, and J. Rezende (1996). "A phase field concept for multiphase systems". *Physica D: Nonlinear Phenomena* 94, pp. 135–147 (cit. on p. 46).

[**Steinbach et al. 1999**]
Steinbach, I. and F. Pezzolla (1999). "A generalized field method for multiphase transformations using interface fields". *Physica D: Nonlinear Phenomena* 134 (4), pp. 385–393 (cit. on p. 46).

[**Sussman et al. 1994**]
Sussman, M., P. Smereka, and S. Osher (1994). "A level set approach for computing solu-

tions to incompressible two-phase flow". *Journal of Computational Physics* 114, pp. 146–159 (cit. on pp. 71, 74, 75).

**[Sussman et al. 1999]**
Sussman, M. and E. Fatemi (1999). "An efficient, interface-preserving level set redistancing algorithm and its application to interfacial incompressible fluid flow". *SIAM Journal on Scientific Computing* 20 (4), pp. 1165–1191 (cit. on p. 71).

**[Suwa et al. 2006]**
Suwa, Y., Y. Saito, and H. Onodera (2006). "Phase field simulation of grain growth in three dimensional system containing finely dispersed second-phase particles". *Scripta Materialia* 55 (4), pp. 407–410 (cit. on p. 47).

**[Suwa et al. 2008]**
Suwa, Y., Y. Saito, and H. Onodera (2008). "Parallel computer simulation of three-dimensional grain growth using the multi-phase-field model". *Materials Transactions* 49 (4), pp. 704–709 (cit. on p. 33).

**[Syha et al. 2010]**
Syha, M. and D. Weygand (2010). "A generalized vertex dynamics model for grain growth in three dimensions". *Modelling and Simulation in Materials Science and Engineering* 18 (1), p. 015010 (cit. on p. 44).

**[Syha et al. 2012]**
Syha, M., W. Rheinheimer, M. Bäurer, E. Lauridsen, W. Ludwig, D. Weygand, and P. Gumbsch (2012). "Three-dimensional grain structure of sintered bulk strontium titanate from X-ray diffraction contrast tomography". *Scripta Materialia* 66 (1), pp. 1–4 (cit. on p. 6).

**[Takaki et al. 2007]**
Takaki, T., A. Yamanaka, and Y. Tomita (2007). "Static recrystallization phase-field simulation based on the predicted subgrain structures". *Proceedings of APCOM'07*. Kyoto (cit. on p. 46).

**[Takaki et al. 2009]**
Takaki, T., Y. Hisakuni, T. Hirouchi, A. Yamanaka, and Y. Tomita (2009). "Multi-phase-field simulations for dynamic recrystallization". *Computational Materials Science* 45 (4), pp. 881–888 (cit. on p. 46).

**[Takaki et al. 2010]**
Takaki, T. and Y. Tomita (2010). "Static recrystallization simulations starting from predicted deformation microstructure by coupling multi-phase-field method and finite element method based on crystal plasticity". *International Journal of Mechanical Sciences* 52 (2), pp. 320–328 (cit. on p. 46).

**[Telley et al. 1996]**
Telley, H., T. Liebling, and A. Mocellin (1996). "The Laguerre model of grain growth in two dimensions I. Cellular structures viewed as dynamical Laguerre tessellations". *Philosophical Magazine Part B* 73 (3), pp. 395–408 (cit. on p. 51).

[**Toda-Caraballo et al. 2013**]
Toda-Caraballo, I., C. Capdevila, G. Pimentel, and C. De Andrés (2013). "Drag effects on grain growth dynamics". *Computational Materials Science* 68, pp. 95–106 (cit. on pp. 42, 44).

[**Touré et al. 2016**]
Touré, M. and A. Soulaïmani (2016). "Stabilized finite element methods for solving the level set equation without reinitialization". *Computers & Mathematics with Applications* 71 (8), pp. 1602–1623 (cit. on p. 72).

[**Treister et al. 2016**]
Treister, E. and E. Haber (2016). "A fast marching algorithm for the factored eikonal equation". *Journal of Computational Physics* 324, pp. 210–225 (cit. on p. 69).

[**Trejo et al. 2016**]
Trejo, V., M. Shakoor, M. Bernacki, and P.-O. Bouchard (2016). "Ductile fracture - influence of an heterogeneous microstructure on nucleation, growth and coalescence mechanisms". *Proceedings of Numiform 2016: The 12th international conference on numerical methods in industrial forming processes*. Troyes (cit. on p. 203).

[**Vaithyanathan et al. 2002**]
Vaithyanathan, V., C. Wolverton, and L. Chen (2002). "Multiscale modeling of precipitate microstructure evolution". *Physical Review Letters* 88 (12), p. 125503 (cit. on p. 216).

[**Vanherpe et al. 2010**]
Vanherpe, L., N. Moelans, B. Blanpain, and S. Vandewalle (2010). "Pinning effect of spheroid second-phase particles on grain growth studied by three-dimensional phase-field simulations". *Computational Materials Science* 49 (2), pp. 340–350 (cit. on p. 47).

[**Ville et al. 2011**]
Ville, L., L. Silva, and T. Coupez (2011). "Convected level set method for the numerical simulation of fluid buckling". *International Journal for Numerical Methods in Fluids* 66 (3), pp. 324–344 (cit. on pp. 72, 74).

[**Voyiadjis et al. 2005**]
Voyiadjis, G. and F. Abed (2005). "Microstructural based models for BCC and FCC metals with temperature and strain rate dependency". *Mechanics of Materials* 37 (2), pp. 355–378 (cit. on p. 23).

[**Walgraef et al. 1985a**]
Walgraef, D. and E. Aifantis (1985a). "On the formation and stability of dislocation patterns, Part I: One-dimensional considerations". *International Journal of Engineering Science* 23 (12), pp. 1351–1358 (cit. on p. 24).

[**Walgraef et al. 1985b**]
Walgraef, D. and E. Aifantis (1985b). "On the formation and stability of dislocation patterns, Part II: Two-dimensional considerations". *International Journal of Engineering Science* 23 (12), pp. 1359–1364 (cit. on p. 24).

**[Walgraef et al. 1985c]**
Walgraef, D. and E. Aifantis (1985c). "On the formation and stability of dislocation patterns, Part III: Three-dimensional considerations". *International Journal of Engineering Science* 23 (12), pp. 1365–1372 (cit. on p. 24).

**[Wang et al. 2014]**
Wang, N., Y. Wen, and L. Chen (2014). "Pinning force from multiple second-phase particles in grain growth". *Computational Materials Science* 93, pp. 81–85 (cit. on p. 39).

**[Weinbub et al. 2016]**
Weinbub, J. and A. Hössinger (2016). "Comparison of the Parallel Fast Marching Method, the Fast Iterative Method, and the Parallel Semi-ordered Fast Iterative Method". *Procedia Computer Science* 80, pp. 2271–2275 (cit. on pp. 69, 70).

**[Wejrzanowski et al. 2013]**
Wejrzanowski, T., J. Skibinski, J. Szumbarski, and K. Kurzydlowski (2013). "Structure of foams modeled by Laguerre–Voronoi tessellations". *Computational Materials Science* 67, pp. 216–221 (cit. on p. 51).

**[Werz et al. 2014]**
Werz, T., M. Baumann, U. Wolfram, and C. Krill (2014). "Particle tracking during Ostwald ripening using time-resolved laboratory X-ray microtomography". *Materials Characterization* 90, pp. 185–195 (cit. on p. 6).

**[Weygand et al. 1999]**
Weygand, S., Y. Brechet, and J. Lépinoux (1999). "Zener pinning and grain growth : A two-dimensional vertex computer simulation". *Acta Materialia* 47 (3), pp. 961–970 (cit. on pp. 6, 44).

**[Wu et al. 2000]**
Wu, M. and J. Guo (2000). "Analysis of a sector crack in a three-dimensional Voronoi polycrystal with microstructural stresses". *Journal of Applied Mechanics* 67 (1), p. 50 (cit. on p. 51).

**[Yan et al. 2011]**
Yan, J. and S. Osher (2011). "A local discontinuous Galerkin method for directly solving Hamilton–Jacobi equations". *Journal of Computational Physics* 230 (1), pp. 232–244 (cit. on p. 72).

**[Zhang et al. 2003]**
Zhang, Y.-T. and C.-W. Shu (2003). "High-order WENO schemes for Hamilton–Jacobi equations on triangular meshes". *SIAM Journal on Scientific Computing* 24 (3), pp. 1005–1030 (cit. on pp. 71, 72).

**[Zhao et al. 2016]**
Zhao, P., S. Niezgoda, and Y. Wang (2016). "An integrated full-field modeling of concurrent mechanical deformation of microstructure evolution: Application to 3D simulation of dynamic recrystallization in polycrytalline Cu". *International Journal of Plasticity* 80, pp. 38–55 (cit. on pp. 47, 49).

[**Zheng et al. 2008**]

Zheng, C., N. Xiao, D. Li, and Y. Li (2008). "Microstructure prediction of the austenite recrystallization during multi-pass steel strip hot rolling: A cellular automaton modeling". *Computational Materials Science* 44 (2), pp. 507–514 (cit. on p. 6).

[**Zhu et al. 2004**]

Zhu, J., T. Wang, A. Ardell, S. Zhou, Z. Liu, and L. Chen (2004). "Three-dimensional phase-field simulations of coarsening kinetics of $\gamma$' particles in binary Ni-Al alloys". *Acta Materialia* 52 (9), pp. 2837–2845 (cit. on p. 216).

[**Zouaghi 2013**]

Zouaghi, A. (2013). "Modélisation numérique multiéchelle de la compaction à chaud de poudres métalliques et étude des impacts des paramètres du procédé sur les caractéristiques". PhD thesis. MINES ParisTech (cit. on p. 203).

## Résumé

Les propriétés mécaniques et fonctionnelles des matériaux métalliques sont conditionnées par leurs microstructures, qui sont elles-mêmes héritées des traitements thermomécaniques subis. Etre capable de prévoir et simuler la microstructure et ses hétérogénéités lors des procédés de mise en forme complexes est récemment devenu crucial dans l'industrie métallurgique. C'est également un véritable challenge d'un point de vue numérique qui met en évidence l'importance des matériaux numériques dans les nouvelles méthodes de modélisation. Dans ce travail, nous nous intéressons à un modèle en champ complet récent basé sur la méthode level set (LS) dans un cadre éléments finis (EF) pour la modélisation des mécanismes de recristallisation.

Les points forts de cette approche par rapport à l'état de l'art ont motivé le développement d'un logiciel appelé DIGIMU® par la société TRANSVALOR avec le soutien de grandes entreprises industrielles. Toutefois, le principal inconvénient de cette approche, commun aux autres méthodes en champ complet utilisant des maillages EF non structurés, reste son coût numérique important.

Le principal objectif de ce travail a donc été de réduire considérablement le coût numérique de la formulation LS utilisée dans le contexte de maillages EF non structurés. De nouveaux développements génériques ont été réalisés pour améliorer l'efficacité globale du modèle. La formulation 2D LS existante, déjà utilisée pour modéliser la croissance de grains, la recristallisation statique et l'effet d'ancrage de Smith-Zener, a été étendue et améliorée afin de modéliser ces mécanismes en 3D pour des polycristaux à grand nombre de grains en des temps de calcul raisonnables.



## Mots Clés

Métallurgie numérique, méthode level set, éléments finis, calcul à haute performance



## Abstract

Mechanical and functional properties of metallic materials are strongly related to their microstructures, which are themselves inherited from thermal and mechanical processing. Being able to accurately predict and simulate the microstructure and its heterogeneities after complex forming paths recently became crucial for the metallurgy industry. This is also a real challenge from a numerical point of view which highlights the importance of digital materials in new modeling techniques. In this work, we focus on a recent front-capturing full field model based on the level set (LS) method within a finite element (FE) framework to model recrystallization mechanisms.

The strengths of this approach comparatively to the state of the art have motivated the development of a software package called DIGIMU® by the company TRANSVALOR with the support of major industrial companies. However, the main drawback of this approach, common with other full field approaches working on unstructured FE meshes, remains its important computational cost, especially in 3D.

Main purpose of this work was finally to drastically reduce the numerical cost of the considered LS formulation in context of unstructured FE meshes. New generic numerical developments have been proposed to improve the global efficiency of the model. The existing 2D LS formulation, already used to model grain growth, static recrystallization and the Smith-Zener pinning effect, has been extended and improved in order to model these mechanisms in 3D for large-scale polycrystals with reasonable computational efforts.



## Keywords

Numerical metallurgy, level set method, Finite elements, high performance computing